New insights on the explosion severity of nanopowders: a nano-grain of sand in the gears of the standards

Audrey Santandrea

LABORATOIRE REACTIONS ET GENIE DES PROCEDES, CNRS, UMR 7274

ECOLE DOCTORALE :

Sciences et Ingénieries des Molécules, des Produits, des Procédés et de l'Energie

THESIS

Presented and defended publicly on:

June 15th, 2020

for obtaining a

PhD title from the University of Lorraine
In Process and Product Engineering and Molecules

by

Audrey SANTANDREA

Chemical Engineer - ENSIC

New insights on the explosion severity of nanopowders: a nano-grain of sand in the gears of the standards

---

Composition of the Jury:

Referees:	Mrs. Valérie TSCHAMBER	Pr. Univ. Haute-Alsace
	Mr. Fabien HALTER	Pr. Univ. Orléans
Members:	Mrs. Sophie TRELAT	Dr. Ing. IRSN
	Mrs. Agnès JANES	Dr. Ing. CRAMIF
	Mr. Jean-François BRILHAC	Pr. Univ. Haute-Alsace
	Mr. Arne KRIETSCH	Dr. Ing. BAM Berlin
	Mr. Alexis VIGNES	Dr. Ing. INERIS (Thesis Supervisor)
	Mr. Olivier DUFAUD	Pr. Univ. Lorraine (Thesis Director)
Guest :	Mr. Laurent PERRIN	Pr. Univ. Lorraine (Thesis Co-director)

Remerciements

Je souhaite dans un premier temps remercier l'Institut National de l'Environnement Industriel et des Risques (INERIS) d'avoir financé cette thèse et le Laboratoire Réactions et Génie des Procédés (LRGP) d'avoir rendu ces travaux possibles.

Je tiens à adresser mes plus sincères remerciements à mon directeur de thèse, Olivier Dufaud. Merci pour ta disponibilité, ton soutien permanent, ta patience et ton intérêt pour mes idées parfois farfelues, mais également pour ton côté humain et ta gentillesse. Merci pour tous nos échanges, à la fois professionnels et personnels, et d'avoir cru en moi quand moi-même je ne le faisais pas (sauf peut-être pour Kansas City 😉). Toujours viser le top !

Je remercie également mon co-directeur de thèse, Laurent Perrin, pour sa confiance et sa disponibilité. Merci pour tes petites histoires et anecdotes au café, et surtout d'avoir fourni la preuve que non, je ne « voyais pas des lumières » !

Un grand merci également à Alexis Vignes pour ses encouragements et sa bienveillance. Merci pour ton enthousiasme et ton intérêt, ainsi que pour nos nombreuses conversations, professionnelles ou non, et tes conseils avisés.

Mes remerciements vont aux membres du jury, qui ont eu l'amabilité d'accepter de lire et de juger ce travail de thèse. Un grand merci pour avoir été si conciliants concernant les conditions particulières de la soutenance de thèse.

Je voudrais également remercier le personnel du LRGP, et plus particulièrement les membres de l'équipe SAFE, pour leur accueil lors de cette thèse. Merci, entre autres, à Stéphanie, Léa, Nathalie, Augustin, Dominique et Jean-Christophe pour votre présence, votre gentillesse et votre soutien. Un merci tout particulier à André Laurent pour nos échanges, son support et sa confiance. Merci d'avoir tout fait pour être présent à ma soutenance.

Je tiens également à remercier Stéphanie Pacault et Jean-François Remy pour leur aide au niveau expérimental. Merci également au service électronique et à l'atelier, et plus particulièrement à David Brunello et à Christian Blanchard, pour leur support concernant le développement de nouvelles manips.

Je souhaite remercier toutes les personnes que j'ai eu l'occasion de rencontrer et qui ont rendu ces trois années plus qu'agréables grâce à leur sympathie et leur bonne humeur : Nicolas, Mathieu, Marine, Xiaojin, Eloïse, Florine, Jean-Patrick ainsi que ceux que je n'ai pas cités.

Et enfin, un énorme merci à ma famille, plus particulièrement ma mère et ma sœur, et à Adrien pour m'avoir soutenue et encouragée tout au long de ce projet.

Merci à toutes et à tous !

Abstract

By definition, nanoparticles exhibit at least one dimension below 100 nm. This small size implies a high specific surface area, which induces original properties when compared to micropowders, such as chemical, mechanical, optical or biological properties. Among these new specificities, nanoparticles are subjected to weak cohesion forces, such as van der Waals, electrostatic or capillary forces, which cause them to agglomerate in a reversible way. However, dust explosions require the dispersion of the dust in the air, which can lead to a breakage of these agglomerates. The aim of this work is then to study the influence of nanoparticles specificities, notably the agglomeration, on their ignition sensitivity and explosion severity, and evaluate the adequacy of the international standard methods to determine these parameters when it comes to nanoparticles.

Four types of powders were chosen to highlight the specific behavior of each type of combustible powder, i.e. carbonaceous, organic or metallic: carbon black, nanocellulose, aluminum and carbon-coated silicon. The powders were characterized by Scanning Electron Microscopy (SEM), specific surface measurement and helium pycnometer, and their particle size distribution (PSD) was measured before and after dispersion using different methods. The mean surface diameter, used to consider the high surface area of nanoparticles, considerably decreases after the injection in the 20L sphere, which is the standard equipment to measure the explosion severity of a dust. This observation highlighted the necessity to characterize the dust not only before dispersion, but also after injection in the 20L sphere, to accurately evaluate the explosion risk. Ignition and explosion tests were conducted in standard conditions, but also by varying the powder preparation (aging, drying, sieving, agglomeration), and the operating conditions (dispersion procedure, ignition energy, initial turbulence). Specific behaviors related to the powder nature (carbonaceous, organic or metallic) were then observed, discussed, and alternative measurement methods were proposed. For instance, alternative dispersion nozzles were tested to provide a better cloud homogeneity or to reproduce industrial release conditions. Dispersion procedure and ignition source should be adapted to the minimum ignition energy of the nanopowders to avoid both pre-ignition and overdriving. Variation of the ignition delay time can be helpful to obtain the most conservative results.

One of the main proposals consists in the consideration of the laminar burning velocity as a standard characteristic of the explosion severity. Experiments were conducted in a flame propagation tube and a vented 20L sphere to evaluate the unstretched burning velocity of nanocellulose. The results were then compared to an existing correlation based on the pressure-time evolution during standard experiments. Furthermore, a flame propagation model, initially designed for hybrid mixtures, was adapted to the flame propagation in a cloud of organic nanoparticles, showing consistent results with the experiments.

Résumé

Par définition, les nanoparticules possèdent au moins une dimension inférieure à 100 nm. Cette petite taille induit une grande surface spécifique, qui procure des propriétés inédites, notamment chimiques, mécaniques, optiques ou biologiques, comparées aux particules micrométriques. Parmi ces nouvelles spécificités, les nanoparticules sont soumises à des forces de cohésion plus intenses, telles que des forces de van der Waals, électrostatiques ou capillaires, ce qui les amène à s'agglomérer de manière réversible. Cependant, une explosion de poussières nécessite une dispersion de la poudre dans l'air, ce qui peut mener à une fragmentation de ces agglomérats. L'objectif de ce travail est ainsi d'étudier l'influence des spécificités des nanoparticules, notamment de l'agglomération, sur leur sensibilité à l'inflammation et leur sévérité d'explosion, et d'évaluer l'adéquation des méthodes définies par les standards internationaux pour la détermination de ces paramètres concernant les nanoparticules.

Quatre types de poudres ont été considérées pour mettre en lumière le comportement spécifique de chaque type de combustible, c'est-à-dire les poudres carbonées, organiques ou métalliques : noirs de carbone, nanocellulose, aluminium et silicium enrobé de carbone. Les poudres ont été caractérisées par microscopie électronique à balayage, mesure de surface spécifique et pycnométrie hélium. De plus, leur distribution de tailles de particules a été mesurée avant et après dispersion à l'aide de méthodes complémentaires. Le diamètre moyen en surface diminue significativement après l'injection dans la sphère de 20L, qui est l'équipement standard utilisé pour la mesure de la sévérité d'explosion. Cette observation prouve la nécessité de caractériser la poudre non seulement avant dispersion, mais aussi après injection dans la sphère de 20L, pour évaluer le risque d'explosion de manière fiable. Des essais d'inflammation et d'explosion ont été réalisés dans des conditions standards, mais aussi modifiant la préparation de la poudre (vieillissement, séchage, tamisage, agglomération) ainsi que les conditions opératoires (procédure de dispersion, énergie d'inflammation, turbulence initiale). Des comportements spécifiques liés à la nature de la poudre (carbonée, organique ou métallique) ont été observés, discutés, et des méthodes alternatives de mesure ont été proposées. Par exemple, des buses de dispersion alternatives ont été testées afin de garantir une meilleure homogénéité des nuages poudres/air ou reproduire les conditions réelles de génération. La procédure de dispersion et la source d'inflammation doivent être adaptées à l'énergie d'allumage minimale des nanopoudres pour éviter à la fois les phénomènes de pré-inflammation et 'd'overdriving'. Une variation du délai d'inflammation est également préconisée pour obtenir des résultats les plus conservateurs.

Enfin, l'une des principales propositions consiste à considérer la vitesse laminaire de flamme comme un paramètre standard représentant la sévérité d'explosion. Des tests ont été réalisés dans un tube de propagation de flamme et dans une sphère éventée pour évaluer la vitesse non étirée de la nanocellulose. Les résultats obtenus ont alors été comparés à une corrélation existante basée sur l'évolution de la pression en fonction du temps lors d'essais standards. De plus, un modèle de propagation de flamme, initialement développée pour des mélanges hybrides, a été adapté pour représenter la propagation de flamme dans un nuage de nanoparticules et a montré des résultats en adéquation avec les résultats expérimentaux.

Contents

List of figures

List of tables

Nomenclature

Symbol	*Description*
A (J)	Hamaker constant
A_f (cm^2)	Flame surface
A_s (cm^2)	Flame section
Aw (-)	Water activity
C ($kg.m^{-3}$)	Dust concentration
c_{edge} (m)	Length of the edge notch
C_p ($J.kg^{-1}.K^{-1}$)	Heat capacity
D (-)	Dimension
d_{50} (m)	Mean surface diameter of agglomerates after dispersion
d_{agg} (m)	Diameter of the agglomerate
d_c (m)	Critical diameter of the dust cloud
$d_{min\text{-}VSSA}$ (m)	Smallest particle dimension
d_p (m)	Primary particle diameter
dP/dt_m ($bar.s^{-1}$)	Rate of pressure rise
dP/dt_{max} ($bar.s^{-1}$)	Maximum rate of pressure rise
E_i ($cal.mol^{-1}$)	Activation energy
F_{agglo} (N)	Cohesion forces of the agglomerates
F_{cap} (N)	Capillary forces
F_{disp} (N)	Force required for a total dispersion of the agglomerate
F_{el} (N)	Electrostatic forces
F_{mean} (N)	Force required to break a contact between particles
F_{VdW} (N)	van der Waals forces
h ($W.m^{-2}.K^{-1}$)	Convection heat transfer coefficient
h_p (m)	Interparticle distance
k (-)	Coordination number
K (s^{-1})	Stretching factor
K_a (m^{-1})	Absorption coefficient
K_s (m^{-1})	Scattering coefficient

K_{St} (bar.m.s^{-1})	Explosion index
L_{car} (m)	Characteristic length
m_u (kg)	Mass of the unburnt gases
P_m (bar)	Explosion overpressure
P_{max} (bar)	Maximum explosion overpressure
q (C)	Particle charge
r (m)	Meniscus radius
R (m)	Sphere radius
r_j (kg.m^{-3}.s^{-1})	Molar reaction rate
S_{agg} (m²)	Total surface of the agglomerate
S_S (cm.s^{-1})	Spatial velocity
SSA (m².g^{-1})	Specific surface area
S_u (cm.s^{-1})	Burning velocity
$S_u°$ (cm.s^{-1})	Laminar burning velocity
T (K)	Temperature
u (m.s^{-1})	Fluid velocity
u_{rms} (m.s^{-1})	Root-mean square velocity
V (m^3)	Volume
V_{ej} (m.s^{-1})	Ejection velocity
VSSA (m².cm^{-3})	Volume-specific surface area
V_u (cm^3)	Volume of the unburnt gases
ΔP_{cap} (bar)	Pressure loss in the liquid bridge
μ_{air} (Pa.s)	Dynamic viscosity of air

Dimensionless number	***Description***
Bi (-)	Biot number
B_T (-)	Spalding number
Da_{II} (-)	Damköhler number
Le (-)	Lewis number
Nu (-)	Nusselt number
Re (-)	Reynolds number

Re_p (-)	Particle Reynolds number
St (-)	Stokes number
Sta (-)	Stanton number
We (-)	Weber number
π_i (-)	Dimensionless number

Greek letter	***Description***
γ (-)	Ratio of specific heats
Γ ($J.m^{-2}$)	Equilibrium surface energy
γ ($J.m^{-2}$)	Surface tension
Γ_c ($J.m^{-2}$)	Fracture surface energy
ΔD (%)	Mode diameter variation
ΔH_{comb} ($J.mol^{-1}$)	Enthalpy of combustion of the dust cloud
ΔH_{vap} ($J.mol^{-1}$)	Enthalpy of vaporization of the dust cloud
δ_M (cm)	Markstein length
ε (-)	Agglomerate porosity
ε_0 ($F.m^{-1}$)	Dielectric permittivity of vacuum
λ ($W.m^{-1}.K^{-1}$)	Thermal conductivity
ρ_{air} ($kg.m^{-3}$)	Air density
ρ_p ($kg.m^{-3}$)	Particle density
ρ_{sk} ($g.cm^{-3}$)	Skeletal density
ρ_u ($kg.cm^{-3}$)	Density of the unburnt gases
σ_k (Pa)	Agglomeration cohesion strength (Kendall)
σ_R (Pa)	Agglomerate cohesion strength (Rumpf)
σ_w (Pa)	Agglomerate cohesion strength (Weiler)
τ_c (s)	Characteristic chemical time
τ_s (s)	Relaxation time
φ (-)	Agglomerate solid fraction
ϕ ($N.m^{-1}$)	Surface energy of agglomerates

Chapter 1:
Introduction

Powders are omnipresent in our modern industry. Produced, handled, conveyed, stored, powders are involved along the value chain of various industrial sectors like the chemical industry, the pharmaceutical industry, the cosmetics, the food industry or the metallurgy. However, powders can be hazardous for the workers, the population and the environment, especially when it comes to be released in the air: beyond their potential toxicity, combustible particles can explode when it becomes airborne. Actually, dust explosions frequently occur in industrial facilities and, over the years, led to loss of life and properties. At the European level, two main regulations were implemented to prevent dust fires and explosions through two EU directives. While the first directive, 1999/99/CE directive, is a directive providing minimum requirements (employer obligations) for protecting health and safety at work, especially through zone classification of hazardous areas, i.e. areas where explosive atmospheres may occur, the second directive, 2014/34/UE directive, specifies the equipment to be used in these hazardous zones (Janes et al., 2011; Jespen, 2016). In order to fulfill the regulatory requirements, it is necessary to assess explosion risks and to select appropriate equipment. In order to comply with the ATEX Workplace directive 2014/34/UE, it is generally recommended for dust to refer to standards like EN 1127-1 and EN 60079-10-2. Further guidance can be obtained from "codes of good practice" as NFPA standards in the USA or Non-binding European ATEX guideline or from some industrial specific guidelines. However, despite the efforts provided so far, explosion risk is still threatening industries and innovative products like nanomaterials are posing new challenges that require further investigation from fundamental, experimental and modeling perspectives as stated by Amyotte (2014). Recent work carried out at the European standardization level in CEN TC 352/WG3/PG3 also highlighted the need to consider more carefully the current standards used to evaluate the flammability and explosivity of powders in the case of nanopowders. These standards provide experimental methods to determine the ignitability parameters of a combustible dust (ASTM E1491-06, 2012; ASTM E1515-14, 2014; ASTM E2019-03, 2007), and its explosion severity (ASTM E1226-19, 2019; EN 14034-1, 2004; EN 14034-2, 2006). These international standards describe specific apparatuses to conduct ignition sensitivity and explosion severity measurements, along with specific operating conditions. The tests are considered to provide conservative safety characteristics and, although the testing conditions do not reproduce the industrial conditions of an explosion event, these characteristics are also essential outputs to design adequate safety barriers both for explosion prevention and protection (e.g. design of explosion vent).

Since these standards were elaborated before the industrial development of nanotechnologies, the standard procedures are built to evaluate the explosion characteristics of microparticles and are currently applied to nanomaterials without further considerations. Nanomaterials are mainly used because of their original properties due to the size reduction with regard to microparticles, such as optical, biological or mechanical properties, and an increased reactivity (Stark et al., 2015). Thus, these specificities can induce a combustion behavior different than microparticles, which is not considered by the international standards. The recent publication of a technical specification on the topic (NF CEN TS 17274, 2019) should nevertheless be noted as a first positive step to adapt current experimental approaches though it provides only preliminary recommendations. It then appears essential to get more fundamental knowledge on the safety

profile of nanomaterials and on the tools used to characterize the flammability and explosion safety parameters of nanomaterials.

In that context, this work will focus on the investigation of the potential limitations of the current experimental standardized approaches used to evaluate the explosion characteristics of nanoparticles so that recommendations can be formulated for new approaches based on the specificities of nanoparticles. This work aims at giving the basis of a practical framework for process safety engineers confronted to the evaluation of the flammability and explosion severity of nanomaterials. In order to highlight the diversity of the potential concerns, a variety of combustible nanopowders were selected: a nanocellulose (organic) powder, a carbon black (carbonaceous) powder, two aluminum powders (metallic) and a carbon-coated silicon (metalloid/carbonaceous) powder.

The core of the manuscript is organized in 5 chapters. It is structured so as to reflect the approach that would be adopted by an explosion safety engineer to get relevant safety characteristics for either an explosion risk assessment or the modeling of explosion consequences. The last chapter proposes a new approach to evaluate fundamental safety parameter related to the explosion propagation of a nanodust cloud. More specifically, the manuscript is structured as follows :

- In chapter 2, the industrial context of this work and a literature review are introduced. It first focuses on accidents feedbacks and an overview of ATEX regulatory context. The main parameters related to dust ignition sensitivity and explosion severity are then defined, along with the main influential factors. Nanoparticles specificities, and more specifically the agglomeration phenomenon, are also reviewed. The final part of this chapter summarized the effect of the main influential factors related to nanomaterials characteristics on the ignition sensitivity and explosion severity of nanomaterials.
- The third chapter is dedicated to the characterization of the nanopowders in bulk and in cloud. First, the selected powders are presented and assessed according to the European Commission definition for nanomaterials. Then, the airborne behavior of nanomaterials is investigated through the assessment of the particle size distribution of the dust cloud after high-energy dispersion in the standardized vessel, i.e. the 20L sphere. In order to highlight the role of the different influential factors on the dispersion of the cloud, a dimensional analysis was performed so that to propose a semi-empirical correlation to support future investigations on a broader range of nanomaterials.
- In chapter 4, the ignition sensitivity and explosion severity of the powders is assessed by strictly following the standard procedure. Based on the knowledge acquired in the previous chapter, limitations of the standard procedures are highlighted, and some recommendations are proposed. The first part consists in the presentation of the standard apparatuses and protocols for the determination of the ignition sensitivity parameters. The experimental results obtained for each powder are then discussed and completed by

a dimensional analysis focusing on the ignition phenomenon to support future in-depth investigations and highlight the main influential factors. The second part of this chapter is dedicated to the assessment of the explosion severity of the powders. Limitations of the current experimental approaches are highlighted through a discussion of the procedures and experimental results and some recommendations are finally proposed.

- The fifth chapter is dedicated to an in-depth investigation of the different aspects identified in the previous chapter and requiring further analysis. This chapter deals respectively with the influence of agglomeration, humidity, aging, ignition energy, dispersion procedure and turbulence on the ignition sensitivity and explosion severity of the powders. First, the impact of the agglomeration on the explosion parameters is investigated through powder sieving and mechanical agglomeration. Then, the influence of the moisture content of the powder and atmosphere are evaluated, and a powder aging phenomenon was highlighted. The third part focuses on the ignition energy to supply when performing explosion tests in the standard vessel to avoid an excessive amount of energy that could disturb the flame propagation. Experimental results conducted on aluminum are also discussed, and an investigation on a so-called 'pre-ignition' phenomenon during testing was performed. Another part concerns the effects of the modification of the dispersion procedure on the particle size distribution after dispersion, the initial turbulence and the explosion severity. Finally, the last part evaluates the influence of the initial turbulence on the explosion severity through the modification of the ignition delay time, i.e. the delay between the dust dispersion and the beginning of the explosion.
- Chapter 6 focuses on the development of an approach enabling to determine a more fundamental safety parameter, i.e. laminar burning velocity to get free from the limitations of the experimental standards and provide input of interest for explosion modeling. The first part consists in an experimental estimation using three methods: flame propagation visualization in a tube and in a vented standard apparatus and a semi-empiric correlation based on the pressure-time evolution during a standard test. The second part presents a numerical one-dimensional model considering the radiative heat transfer, initially developed for hybrid mixtures and adapted to the flame propagation of nanoparticles. Finally, turbulent velocity models estimating the burning velocity in specific (industrial) conditions will be applied on the experimental values in the last part.

Chapter 2:
Generalities on dust explosion

In order to assess correctly the risks related to nanoparticles explosion, the process safety engineer must first acquire information on past accidents, current regulatory provisions and explosion phenomenology. This chapter, divided into four parts, then introduces the industrial context of this work, as well as a literature review, and more specifically nanoparticles explosions. The first part presents some feedbacks about industrial dust explosion accidents and an overview of ATEX regulation which aims at preventing and protecting from such incidents. The second part describes the main parameters to consider when evaluating the ignition sensitivity and explosion severity of dusts, and the elements generally influencing dust explosions. A third part is dedicated to nanoparticles specificities, more precisely to the agglomeration phenomenon and considerations on the agglomerate's breakage. Finally, some observations concerning the influence of nanoparticles specificities on their ignition sensitivity and explosion severity are discussed in the last part.

II.1. A glimpse on the industrial context: feedback and regulation

Any dust capable of burning in air, i.e. any combustible dust, can explode when dispersed with a certain degree of subdivision (Eckhoff, 2003). More precisely, an explosion being defined as a fast combustion reaction that induces a sudden release of energy (Eckhoff, 2003; Skjold, 2003), any material that is not already totally oxidized can give rise to a dust explosion. This notably includes carbonaceous compounds, metallic dust and organic materials, either natural or synthetic. This wide range of combustible powders implies that dust explosions can occur in various sectors such as chemical and pharmaceutical industry, metallurgy, petrochemistry…The statistical features shows that dust explosion accidents mainly happen in process units like grinders, mills, dust separators, silos, mixers, driers, grain elevators, cyclones, incinerators and conveyors … (Eckhoff, 2016; Yuan et al., 2015).

Past accidents turned attention to development of systems and devices to better prevent and protect industrial equipment against these events. The development of new applications and new materials require the development of specific knowledge on dust explosion phenomenon in terms of occurrence and consequences, relying both on research activities and accident feedbacks. To this aim, the BARPI (French acronym of Bureau for Analysis of Industrial Risks and Pollutions) collects information and experience feedback on accidents in the ARIA database (Analysis, Research and Information on Accidents). Some accidents are also reported in the literature by different authors (Abbasi and Abbasi, 2007; Eckhoff, 2003; Theimer, 1973; Vijayaraghavan, 2004). Recently, Cloney and Snoeys (2019) provided an extensive review on the main dust explosions incidents that occurred throughout the world.

*An explosion involving **cellulose** occurred in a chemical industry in **Bergerac, France**, in **2004**, on the cellulose supply of the nitration line. The weighing hopper system, the storage hopper, the conveyor belt and the roof were damaged during the explosion, which was caused by a **hot spot** (mechanical friction on the different systems), an **electrical spark** or a **static electricity discharge** due to the hot, dry weather (BARPI database).*

To target the objects on which research activities must focus, it is essential to identify the materials generating dust explosions. When analyzing such incidents, it then appears that a significant part of dust explosion events implies **organic** dust such as grains; for instance, the explosion of a maize silo in Strasbourg, France, in 2018. According to the ARIA database, an explosion of cellulose followed by a fire also occurred in Bergerac, France, in 2004. These accidents led to injuries, but, unfortunately, some explosions caused a lot more damages. For instance, a well-known sugar dust explosion occurred in the Imperial Sugar Company (Georgia, United-States) in 2008, involving several secondary explosions due to a dust accumulation, leading to 14 killed (U.S. Chemical Safety and Hazard Investigation Board, 2009).

Carbonaceous dust explosions are also frequently encountered, such as the explosion in Dongfeng Coal Mine, one of China's national key mines, which caused 171 deaths (Zheng et al., 2009). Another example is the Benxihu colliery disaster that occurred in China in 1942 and cost more than 1500 lives; it is considered as the world's worst coal mining explosion ever (Yuan et al., 2015) and was caused by a mixture of gas and coal. However, coal dust explosions are not restricted to coal mining industries, as evidenced by a recent accident in New Mexico, United States in March 2018, where a coal storage silo collapsed and caused an explosion and fire (Cloney and Snoeys, 2019).

In 2018, in New Mexico, United States, a silo holding more than 600 tons of coal collapsed, thus causing an explosion and a fire. Investigations then led to the conclusion that corrosion and a faulty weld, holding two sections of the silo together, induced its collapse. No injuries, but damages estimated to $15-20 million, were reported (Cloney, 2018).

Since **metallic** materials are widely used in industries, accidents involving explosion of metallic powders are relatively frequent as shown by the analysis of accident databases. In the ARIA database such accidents were reported with major consequences in terms of releases. Aluminum dust was involved for instance in several devastating explosions, such as an explosion that occurred in the mixing section of a premix plant at Gullaug, Norway, in 1973, probably caused by a propagating brush discharge and leading to 5 deaths, 2 injuries and the destruction of a significant part of the plant (Eckhoff, 2003). Another aluminum explosion was mentioned by Eckhoff (2003), concerning an atomized aluminum powder production plant at Anglesey, United Kingdom, in 1983, which led to 2 injuries. More recently, a catastrophic aluminum-alloy dust explosion also occurred in a large industrial plant of

*In 2014, a large industrial plant in **Kunshan, China**, suffered a severe explosion during polishing of aluminum-alloy. The explosion is believed to have been initiated by **self-ignition of contaminated aluminum-alloy** in the **dust collecting barrel** below the external bag filter unit. Due to a heavy rain for days before the accident and the discovery of a hole near the ignition location, **water is supposed to have accelerated the self-ignition** process through an exothermal reaction with the dust (Li et al., 2016).*

Kunshan, China, in 2014, and caused 146 deaths and 114 injuries (Li et al., 2016). This accident probably involved sub-micrometric metallic particles (e.g. process fumes and deposits).

Even though dust explosion accidents involve, in most cases, grain, coal or metal powders, it has to be kept in mind that any combustible dust can cause an explosion, including for instance wood dust and pharmaceutical component. Another example was reported by Eckhoff (2003) concerning a dust explosion in a silicon powder grinding plant at Bremanger, Norway, in 1972, in which 5 workers lost their lives.

To prevent and protect industries from dust explosions, numerous regulations and standards have been elaborated (Center for Chemical Process Safety, 2004; Zalosh, 2019). In Europe, two directives were adopted more specifically for controlling Explosive Atmospheres (ATEX), i.e. fuel-air mixtures prone to ignite: 1999/99/CE directive (ATEX Workplace directive) and directive 2014/34/UE, known as 94/9/CE directive until March 2016 (ATEX Equipment directive). The first directive defines ATEX zones depending on the formation probability of an explosive atmosphere, whereas the second specifies the equipment to use into the previously defined zones through equipment categorization, conformity assessment procedure and CE- and Ex- marking obligations (Janes et al., 2011; Jespen, 2016). Risk areas must then be identified and classified according to the probability of provoking an accident, as presented in Table 2-1 for dusts.

Table 2-1 Definition of ATEX zones concerning dust according to ATEX directive 1999/92/CE

Presence of an explosive atmosphere	ATEX zone	Risk
Continuously, for long periods or frequently in normal operating conditions	20	Permanent
Likely to occur in normal operating conditions	21	Occasional
Accidently, in cause of process failure, for short periods	22	Rare

The equipment to use into these zones must comply with the requirements of ATEX directive 2014/34/UE. The aim of ATEX directives is then to ensure explosion prevention, by avoiding the formation and the ignition of explosive atmosphere, but also to protect worker and industries from the effects of a potential explosion. The explosion prevention, which is given priority, can be achieved by suppressing a condition needed to produce the dust explosion. For instance, removing the combustible through ventilation or frequent cleaning, avoid its dispersion by modifying the process, suppress the oxygen by inerting the process or limiting the oxygen concentration, or even eliminate all potential ignition sources (Amyotte and Eckhoff, 2010; EN 1127-1, 2019; Janes et al., 2011). The implementation of those safety measures mainly relies on the reliable determination of the quantitative explosion characteristics of the dust involved in the process. In this respect, further work must be dedicated to new materials such as nanomaterials (Amyotte, 2014; Vignes et al., 2019).

II.2. Dust explosions phenomenology

This section is dedicated to general aspects on dust explosions and is therefore intended to basic knowledge acquisition on this subject. Dust combustion requires the simultaneous presence of a sufficient amount of combustion agent (generally oxygen from air), a combustible material in a sufficiently divided state and an ignition source providing enough energy to initiate the reaction.

To induce a dust explosion, three more conditions are requested, leading to the diagram presented in Figure 2-1. The first condition is the dispersion of the powder, which can happen during the product treatment (milling, fluidized bed drying…), through handling (discharge of silos, pneumatic transport…), or can even result from a primary explosion. The second condition implies that the combustible concentration must lie within a certain range, often called explosion domain. Finally, some containment is sometimes considered as a necessary condition for a dust explosion to occur. However, accidents in unconfined environment, such as the explosion at the "Color Play Asia Party" in 2015 in Taiwan (Chan and Chong, 2016) disprove this point. The containment can then be considered as a worsening factor increasing pressure effects of the explosion.

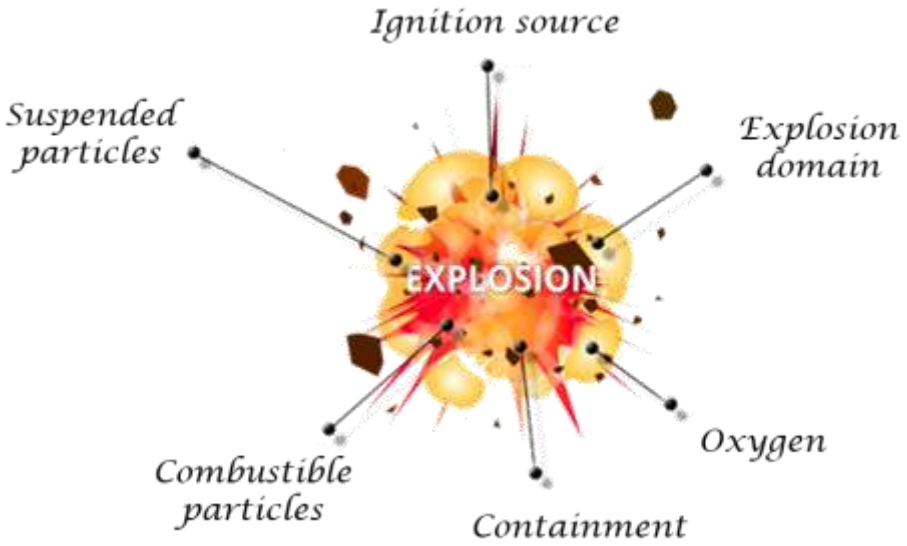

Figure 2-1 Requirements to generate a dust explosion

If the previous conditions are fulfilled simultaneously, an exothermic oxidation reaction occurs, either in gaseous phase or in heterogeneous gas/solid phase depending on the dust nature. Thus, a heterogeneous combustion happens when it comes to carbonaceous compounds. Then, organic compounds undergo a pyrolysis/devolatilization phase before the combustion process itself, which then occurs in the homogeneous gas phase. It is generally assumed that this first step is very fast, although not kinetically negligible, and that combustion of organic compounds occurs mainly in gas phase (Cashdollar et al., 1989; Di Benedetto and Russo, 2007; Dufaud et al., 2012; Eckhoff, 2003). Finally, when considering metallic particles, either the surface oxidation or the vaporization may be predominant depending on the combustion energy,

melting point of the metal and particle size (Bazyn et al., 2007; Levitas, 2013; Lomba, 2016; Moser, 2019; Sundaram et al., 2016).

During the combustion process, the flame propagates gradually, separating the unburnt mixture from the hot combustion gases, whose expansion induces a pressure wave that precedes the flame. This pressure wave is then capable of dispersing the dust upstream of the flame, provoking secondary explosion and, as shown in section II.1, implying a risk for industrial installations, environment, residents and workers. An accurate risk assessment relies both on the evaluation of the probability that a dust cloud would ignite, called ignition sensitivity, and on the estimation of the consequences of a potential explosion scenario, called explosion severity (Abuswer et al., 2013; Lemkowitz and Pasman, 2014). In the following sections (from II.2.1 to II.2.4), the different parameters involved in dust ignition and explosion are defined along with the main factors affecting them. The characterization procedures and apparatuses will be detailed in chapter 4.

II.2.1. Ignition sensitivity

The ignition sensitivity of a powder represents an estimation of the probability that the powder would ignite when submitted to certain conditions. It is then possible to determine this sensibility under specific conditions (e.g. corresponding to an industrial process), or to determine the conditions corresponding to the highest ignition probability. The ignition sensitivity is related to i) the ignition source, ii) the explosion domain and iii) the concentration of oxygen.

i) An ignition source should be sufficiently powerful to ignite the fuel-air mixture. If the ignition source is present but of too low energy, the oxidation reaction will not occur, or too slowly to sustain a flame propagation. The Minimum Ignition Energy (MIE) obviously depends on the dust-air mixture. If this energy is present as a heat source, the term Minimum Ignition Temperature (MIT) is employed.

ii) For an ignition to propagate, the mixture must contain a minimum amount of dust, called the Lower Explosion Limit (LEL). It is also possible to define a maximum explosive concentration above which no explosion can occur, because of a lack of oxygen. However, since it is difficult to generate a stable high concentrated suspension of dust and because of the natural sedimentation phenomenon which tends to decrease the dust concentration of the cloud, this parameter is not usually considered as a safety parameter.

iii) However, the extinction phenomenon due to the lack of oxygen is considered through the Limiting Oxygen Concentration (LOC), corresponding to the lowest oxygen concentration required to produce an explosion.

II.2.1.1. Minimum Ignition Temperature

Increasing the temperature of a dust-air mixture leads to an increase of its energy, implying the existence of a temperature above which the mixture can spontaneously ignite (Eckhoff, 2019a). This temperature generally lies between 150°C and 700°C for a dust cloud and, due to improved heat transfers, is lower for a dust layer (Eckhoff, 2003). Since this work will mainly focus on the explosion risk assessment of dust clouds, the minimum ignition temperature of a dust layer will not be detailed hereafter, but some advanced notions on its determination were previously discussed by Bideau (2010).

Many process units inherently include the presence of flames or hot surface, such as ovens or heat exchangers. If a dust cloud is generated near such units, it will ignite if its minimum ignition temperature is attained by the heat source (Abbasi and Abbasi, 2007). This temperature can vary with the size and the shape of the hot surface, and with the dust cloud concentration and initial turbulence, as those parameters have a direct influence on the heat transfer. These influences are partially considered during the minimum ignition temperature measurement, detailed in chapter 4, performed in normalized ovens, such as the vertical Godbert-Greenwald oven (Eckhoff, 2019b) or the horizontal BAM oven (ASTM E1491-06, 2012; EN 50281-2-1, 2000; IEC 1241-2-1, 1994).

II.2.1.2. Minimum Ignition Energy

Sparks generated mechanically, electrically or electrostatically are also commonly encountered in industrial processes. In the presence of an explosive atmosphere, if a spark with an energy higher than the MIE of the cloud is generated, an ignition will occur (Siwek, 1995).

The MIE of dust clouds is conventionally measured using a modified Hartmann tube for energies between 1 mJ and 1000 mJ (ASTM E2019-03, 2007; ISO/IEC 80079-20-2, 2016). Although it does not allow the measurement of MIE lower than 1 mJ, the "Mike 3" is considered as the standard apparatus (Eckhoff, 2002; Eckhoff and Randeberg, 2007). A dust is considered "normally sensitive" if its MIE is greater than 10 mJ, "particularly sensitive" if its MIE lies between 3 mJ and 10 mJ, and "extremely sensitive" if its MIE is lower than 3 mJ (Gustin, 2004; Janes et al., 2008). Although other parameters than the powder nature must be taken into account, metallic particles generally tend to be particularly to extremely sensitive, whereas carbonaceous compounds are usually not ignitable by a spark of 1 J (Clouthier et al., 2019).

Just like the MIT, the MIE depends on the dust concentration and initial turbulence, and despite the fact that international standards impose the modification of both parameters during the experimental estimation of the MIE, it has been shown that, currently, no experimental method can produce an optimal homogeneous dust cloud for MIE determinations (Eckhoff, 2019c). Moreover, the MIE is also greatly influenced by the ambient temperature, which implies that a specific attention should be paid to the testing and operating conditions (American Institute of Chemical Engineers, 2017).

II.2.1.3. Lower Explosion Limit

The Lower Explosion Limit (LEL) is defined as the concentration below which no flame can propagates. This parameter depends on the initial turbulence, but also on the ignition energy and the volume vessel and shape. It can be measured either in the modified Hartmann tube or in the 20L sphere according to international standards (ASTM E1515-14, 2014; EN 14034-3, 2006). The LEL of dust generally lies between 30 and 125 $g.m^{-3}$ (Babrauskas and Britton, 2018; Clouthier et al., 2019).

II.2.1.4. Limiting Oxygen Concentration

The flame speed and the explosion severity generally tend to increase with the dust concentration, until reaching a concentration generally higher than the stoichiometric concentration. For rich mixtures, the oxygen is lacking, and the flame is no longer able to propagate, inducing a quenching effect. However, the maximum explosible concentration is rarely estimated, both because of the difficulty to generate a homogeneous high concentrated suspension and of the limited interest related to uncertainties due to the dust sedimentation. Indeed, this phenomenon can decrease the concentration back to the explosion domain. Instead, the Limiting Oxygen Concentration (LOC) is generally evaluated, as its knowledge allows inerting the process under the limiting value, thus preventing dust explosion.

As previously mentioned, these safety parameters depend on the operating conditions and methods used for their measurements, implying that standardized conditions, methods and apparatuses must be respected to compare the powders, but also to design the prevention and protection equipment (Clouthier et al., 2019; Eckhoff, 2003; Gustin, 2004; Jespen, 2016). Therefore, the safety parameters obtained through standardized tests must be considered more as references than as process operating parameters, as they also depend on parameters not perfectly controlled, such as the particle size distribution, the initial turbulence and the moisture content. Table 2-2 presents the experimental methods currently accepted as standard tests to evaluate the minimum ignition energy, minimum ignition temperature and lower explosion limit.

Those parameters provide information on the ignition probability of a dust cloud and it supports the design and implementation of ignition prevention strategies. However, explosion prevention cannot rely only on ignition prevention, one needs to firstly focus on reducing the likelihood of formation of an explosive atmosphere. Beyond prevention, it is however also necessary to protect from the explosion by assessing its potential effects.

Table 2-2 Standard test methods and equipment for the determination of ignition sensitivity parameters of dust clouds

Safety parameter	Description	Standard method	Apparatus	Application
MIT	Minimum Ignition Temperature	(ASTM E1491-06, 2012; EN 50281-2-1, 2000; IEC 1241-2-1, 1994)	Godbert-Greenwald Oven BAM Oven	Control of hot surfaces temperatures, fire permit – ATEX 2014/34/UE
MIE	Minimum Ignition Energy	(ASTM E2019-03, 2007; ISO/IEC 80079-20-2, 2016)	Modified Hartmann Tube	Removal of potential ignition sources – ATEX 1999/92/CE
LEL	Lower Explosion Limit	(ASTM E1515-14, 2014; EN 14034-3, 2006)	Modified Hartmann Tube 20L sphere	Control of the dust concentration (cleaning)

II.2.2. Explosion severity

If the ignition sensitivity is related to the probability that a powder ignites and produces an explosion, the explosion severity is linked to the effects and consequences. It usually includes the maximum explosion overpressure P_m as well as the maximum rate of pressure rise $(dP/dt)_m$ recorded during the pressure growth. The maximum overpressure P_{max} and the maximum rate of pressure rise $(dP/dt)_{max}$ correspond to the maximum values of P_m and $(dP/dt)_m$ obtained over a wide range of dust concentration. These parameters are measured by performing controlled explosion tests in a closed vessel, which induces a volume-dependence of the results. Therefore, they must be used as references or indicators for protection equipment design instead of an absolute value necessarily obtained in case of an accident. Indeed, the explosion severity greatly depends on the vessel geometry and volume, which can either increase the rate of pressure rise or disturb the flame propagation and generate quenching phenomenon.

Moreover, other parameters as the particle size distribution or the initial turbulence can also impact the explosion severity. It is then again recommended to perform the explosion severity measurements in normalized conditions and equipment (EN 14034-1, 2004; EN 14034-2, 2006; ISO 6184/1, 1985). Two explosion vessel are mentioned in international standards: a 1 m^3 vessel, which has the disadvantage of handling and consuming great amounts of powders, and a 20L sphere, more generally adopted in process safety labs (Siwek, 1977). However, several authors (Dahoe et al., 2001; Proust et al., 2007; van der Wel et al., 1992) highlighted that, in practice, these two vessels are not perfectly equivalent notably due to different evolutions of the turbulence during the dust dispersion and its combustion. Moreover, the small size of the 20L sphere increases the likelihood of flame quenching to the walls compared to a 1 m^3 vessel.

The maximum overpressure obtained during a gas explosion is generally considered independent from the vessel in which the explosion occurred and from the initial turbulence, as it is mainly affected by the explosion thermodynamics. The maximum overpressure of a dust explosion is commonly considered to behave the same way than gas explosions (Dahoe, 2000), and the knowledge of this parameter then allows the design of pressure resisting equipment as well as vents and rupture discs.

While the explosion severity can be measured in two different equipment of different volumes, the maximum rate of pressure rise depends on the vessel volume. Some experiments were conducted in vessel of different sizes, from 0.020 m^3 to 100 m^3, to evaluate the volume dependency. Based on the propagation of a spherical thin flame in an explosion vessel, some assumptions were then formulated to deduce a new explosion severity parameter, called explosion index K_{St}, independent from the vessel volume. Thus, the combustion rate should be the same in the testing vessel and in the enclosure in which the explosion severity has to be predicted. To fulfill this condition, both vessels must be of the same geometry, ignition must occur in the center of the vessel, the flame thickness must be negligible with respect to the vessel radius and turbulence temporal and spatial variations must be similar in both enclosures (Bartknecht, 1989; Eckhoff, 2003; Lewis and von Elbe, 1987). The explosion index is then defined by the so-called "cube-root law" as follows:

$$K_{St} = V^{\frac{1}{3}} . \left(\frac{dP}{dt}\right)_{max} \qquad 2\text{-}1$$

Based on the value of K_{St} obtained, powders can be classified into different classes, called "St classes" (Table 2-3). This classification provides information for the design of protection equipment against the explosion (Bartknecht, 1989).

Table 2-3 Classification of powders into St classes

St class	K_{St} (bar.m.s^{-1})
St 0	0 (non-explosible)
St 1	$1 < K_{St} \leq 200$
St 2	$200 < K_{St} \leq 300$
St 3	$300 < K_{St}$

Due to the previously quoted assumptions related to the cubic law, this latter should be used carefully. Indeed, in practice, the conditions for its validity are rarely perfectly fulfilled. Moreover, this relation is based on a single point of the pressure evolution curve for a single concentration (among other tested), which does not represent the powder global behavior. For instance, the maximum rate of pressure rise and the maximum overpressure can be obtained at different concentrations (Dahoe et al., 1996). Additionally, the results obtained in labs are extrapolated to industrial situations with unknown turbulence, which can lead to misestimations of the explosion severity, as it greatly depends on the initial turbulence (Dahoe et al., 2002).

Several tests have then been performed to compare the results obtained in the 20L sphere and in the 1 m3 vessel, revealing significant differences between the two vessels, thus questioning the validity of the cube-root law (Proust et al., 2007; van der Wel et al., 1992). Discrepancies have notably been found in terms of turbulence, showing the operating conditions in both vessels do not allow the same initial turbulence of the dust cloud (Amyotte et al., 1988; Dahoe et al., 2001; Pu et al., 1991; van der Wel, 1993). Since the cube-root law is based on results obtained in both apparatus, Dahoe et al. (2001) even claim that the cube-root law should be abandoned. It has also been proven that radiation can play a significant role in dust combustion, which tends to increase the flame thickness and even invalidate the cube-root law, especially for metal particles (Bidabadi and Azad, 2015; Dahoe et al., 1996; Julien et al., 2017; Moussa et al., 2015). To overcome the limitations of the cube-root law, recent studies proposed rather to focus on the determination of flame propagation and related dust explosion burning velocity (Beeckmann et al., 2019; Brequigny et al., 2016; Chanut, 2018; Lomba et al., 2019; Proust et al., 2017). These aspects are further detailed in the next section.

II.2.3. Burning velocity

A flame can be considered as a reaction zone of a given thickness at the interface between the post flame zone composed by the hot burnt gases and the fresh mixture constituted of the combustible and oxygen, as illustrated in Figure 2-2 (Haghiri and Bidabadi, 2010). The combustion occurring in the reaction zone provides the energy required to ignite the adjacent fresh mixture, allowing the flame to propagate by conduction, radical propagation, radiation or even by a shockwave in the case of a detonation. Several theories were developed to study the flame propagation phenomenon, considering mainly the heat transfer (Cassel et al., 1957; Ivanov et al., 2015; Mallard and Chatelier, 1883), the free radicals diffusion (Tanford and Pease, 1947), or both (Dahoe, 2000; Zeldovich and Barenblatt, 1959). More recent studies highlighted that, in the case of dust explosions, the radiative transfer has a great influence on the flame propagation and cannot be neglected (Julien et al., 2017; Proust et al., 2017).

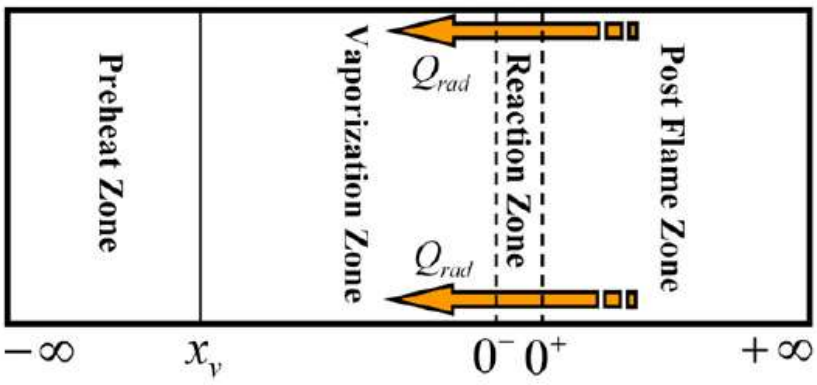

Figure 2-2 Schematic of the front flame propagation divided into four zones for organic particles in air (Haghiri and Bidabadi, 2010)

The burning velocity is not a standardized parameter currently used to define explosion severity. However, the use of this parameter is being increasingly promoted in the domain of gas explosion and also dust explosion. Actually, several studies focusing on flame propagation were conducted to provide inputs for Computational Fluid Dynamics (CFD) simulations of gas or dust explosion development (Di Benedetto et al., 2013; Skjold, 2007, 2003). Request inputs are typically the flame thickness and, more importantly, the laminar burning velocity, which is considered as an intrinsic property of the fuel-air mixture (Belerrajoul, 2019; Miao et al., 2014). Thus, by providing these parameters into CFD simulations or phenomenological tools such as EFFEX (Proust, 2005), the consequences of an explosion scenario in an industrial environment can be better predicted (Skjold et al., 2018; Tolias and Venetsanos, 2018). The determination of burning velocity is also useful for the design of explosion venting but is currently mainly used for gas explosion venting (Daubech et al., 2018). In order to determine burning velocity, it is of importance to be able to measure both the laminar burning velocity and also to evaluate the influence of turbulence on the flame propagation.

From an experimental point of view, the laminar burning velocity of dust-air mixtures is harder to evaluate than for gases. Since a dust cloud can only be formed when a dust is dispersed, i.e. by creating turbulence, the existence of a true laminar burning velocity could even be questioned. However, Bradley and Lee (1984) stated that dust clouds exhibit a measurable laminar burning velocity if the combustible particles produce appreciable amounts of volatile compounds (Dahoe et al., 2002). To perform tests at low turbulence, some experiments were conducted in micro-gravity environment during parabolic flights or using a drop tower to avoid the dust sedimentation (Goroshin et al., 2011; Lee et al., 1993; Pu et al., 1998; Tang et al., 2009). However, the high cost and specific material required to perform such tests makes their application impossible in the framework of normalized tests.

Three more accessible methods for the determination of the burning velocity can be found in the literature: the burner method, with various existing configurations (Dahoe et al., 2002; Julien et al., 2017; Lomba et al., 2019; van der Wel, 1993), the contained explosions method (Silvestrini et al., 2008; Skjold, 2003; van der Wel, 1993) and the tube method (Andrews and Bradley, 1972; Di Benedetto et al., 2011; Proust, 2006). Since those tests are commonly performed in turbulent conditions, the results are extrapolated to laminar conditions to approximate the laminar burning velocity, which limits the accuracy of the obtained values (Bradley et al., 1989) and requires the development of correlations linking this parameter to the turbulent velocity.

Although these methods are more accessible than the micro-gravity tests, experimental issues still exist. Indeed, the stochastic nature of turbulence, the particle agglomeration and the instabilities of the biphasic flow limit the reproducibility of the results, along with the difficulties to visualize the flame front. However, it has been shown that such drawbacks may be limited when studying gas-dust mixtures with low dust concentration (Cuervo et al., 2017; Torrado et al., 2017).

II.2.4. Parameters affecting dust explosions

The ignition sensitivity and explosion severity characteristics depend on the powder specificities such as the composition, initial particle size distribution, shape and moisture content, but also on the operating conditions at stake during the explosion: initial turbulence of the dust cloud, dust concentration, particle size distribution after dispersion, ignition source nature and energy, and vessel volume and shape (Skjold, 2003). In addition to this non-exhaustive list, the influence of other parameters, such as the dustiness, on the powder explosibility is of growing interest (Klippel et al., 2015, 2013; Thomas et al., 2019). Despite the standardization of equipment and protocols, it should be kept in mind that dust explosion behavior is still subjected to a strong interdependency between powder specificities and operating conditions. Thus, the process safety engineer should keep in mind the main parameters affecting dust explosions, which are presented in the next section.

II.2.4.1. Chemical composition

The most intuitive parameter affecting dust explosions is probably the chemical composition of the powder. Indeed, in most cases, the combustion agent implied in the reaction is the oxygen present in ambient air, whose consumption rate directly depends on the chemical composition of the dust, as the powder nature impacts its combustion enthalpy, shape and porosity as well as other physicochemical properties. Although it is technically impossible to accurately estimate the probability of occurrence of an explosion by only knowing the chemical composition of a dust, using QSPR models for instance (Fayet and Rotureau, 2019), the presence of functional grouping can increase (COOH, OH, NH_2, C≡N, C=N, N=N) or decrease (halogen compounds) this risk (Grewer, 1991; Rotureau et al., 2010). In a similar way, the explosivity characteristics of hybrid mixtures cannot be evaluated by only considering the pure separated compounds properties (D'Amico, 2016; Dufaud et al., 2009; Torrado et al., 2017a).

II.2.4.2. Dust concentration

As previously discussed, the dust concentration also has a direct influence on the ignition sensibility and explosion severity. However, the experimental optimal concentration for which the fuel/air mixture would be in equal proportions is generally different from the theoretical stoichiometry. Indeed, in practice, the fuel is not 100% converted, inducing that the experimental optimal concentration is generally higher than the theoretical concentration. Moreover, some quenching effects at the walls can also impact the flame propagation and combustion reactions, thus modifying the optimal concentration.

II.2.4.3. Moisture content

On an intuitive way, it can be considered that the explosion of a wet powder would be less severe than an explosion caused by the same dry powder. However, depending on the powder nature, humidity can either inhibit the reaction or promote it. In most cases, humidity indeed

decreases the explosion severity, as energy is used for the water vaporization reaction, which decreases the flame temperature and thus the explosion overpressure (Eckhoff, 2003). Moreover, agglomeration phenomenon is promoted by moisture and the presence of water in gaseous phase decreases the oxygen concentration in the atmosphere, which induces a decrease of the rate of pressure rise (Yuan et al., 2014).

However, high humidity conditions are not necessarily safer, notably when it comes to metallic particles. Indeed, water can enhance the self-ignition of the dust, such as during the accident in Kunshan, China, in 2014 mentioned in section II.1. (Li et al., 2016). Moreover, Traoré et al. (2009) also showed that a humid atmosphere tends to inhibit the explosion of dry aluminum whereas an explosion of aluminum stored under controlled humidity in ambient atmosphere for a short time leads to an increase of the maximum rate of pressure rise due to hydrogen production.

II.2.4.4. Initial turbulence

The initial turbulence of the dust cloud is recognized to be one of the most important parameter affecting dust explosions (Amyotte et al., 1988; Dahoe et al., 2001; Pu et al., 1991; Tamanini, 1990). Turbulence is closely linked to the dispersion process of the dust and varies from one apparatus or process to another, as a function of the dispersion system, the injection pressure or even the vessel volume and geometry (Amyotte et al., 1988). The turbulence is also affected by the nature of the powder, its particle size distribution and its density, which can lead to concentration heterogeneities in the cloud (Murillo et al., 2018). The initial turbulence of the dust cloud evolves with time and is thus directly affected by the delay between dust injection and ignition, called ignition delay time (Dahoe et al., 2001).

The turbulence intensity can then impact the flame kernel growth and influences the maximum rate of pressure rise and, less significantly, the maximum explosion overpressure. This phenomenon raises some difficulties to extrapolate the data obtained in the 20L sphere to bigger equipment using the “cube-root law” (Equation 2-1). Indeed, one of the main hypotheses of this relation is that similar turbulence levels must be involved in the different equipment, which is questioned by several authors when considering the turbulence in the 20L sphere and the 1 m^3 vessel at the imposed ignition delay times (Amyotte et al., 1988; Dahoe et al., 2001; Pu et al., 1991; van der Wel, 1993).

II.2.4.5. Ignition source and energy

As previously explained, each dust-air mixture has its own minimum energy required to be ignited. Thus, an ignition energy lower than this value will not lead to any explosion, whereas an energy much greater will increase the explosion severity. Indeed, in this case, the additional heat, not used for the dust ignition, would modify the flame propagation and participate to the explosion, leading to a so-called “overdriving” phenomenon which tends to overestimate the

explosion severity (Dastidar et al., 2001; Going et al., 2000; Zhen and Leuckel, 1997). Moreover, using chemical igniters delivering a high energy can modify the initial turbulence of the dust cloud, thus modifying the explosion severity.

II.2.4.6. Particle Size Distribution

The particle size distribution has been long recognized as one of the most important factor influencing dust explosions (Bartknecht, 1989; Soundararajan et al., 1996). Indeed, fine particles tend to easily form a stable dust cloud compared to bigger particles. Moreover, those fine particles develop a high specific surface area, thus presenting a great surface accessible for the oxygen during the combustion. However, the mean volume diameter d_{50} is generally considered to characterize a powder, which does not always provide a correct characterization as big particles, with a high volume, can occult the presence of smaller ones (Harris et al., 2015; Tascón, 2018). Indeed, Vignes (2008) reports several studies showing that the particle size directly impacts the combustion kinetics, which is especially limited by the oxygen diffusion to the particle surface when considering microparticles, whereas it is limited by the reaction itself for smaller particles.

Eckhoff (2012) also pointed out that agglomeration phenomenon can happen and impact the dust explosibility. In such cases, the mean size of the particles involved in the explosion reaction is modified, and the size of the agglomerates is then considered instead of the size of the primary particles. It is generally considered that a dust explosion becomes impossible if the size of the particles exceeds 1 mm (Palmer, 1973). From a safety point of view, agglomeration of particles for dust transport, handling and storage can then constitute a good option to balance a low density and an explosion risk, which will notably be demonstrated in chapter 5.

II.2.5. Decreasing the particle size…

The impact of the particle size on dust explosivity has been illustrated by Jacobson et al. (1964) and Nagy and Verakis (1983), who investigated the evolution of the explosion parameters of an aluminum powder with the particle size (Figure 2-3). It appears that the smaller the particles, the easier the ignition and the more severe the explosion, mainly due to the increased specific surface area. But is this tendency still verified by decreasing even more the particle size, to the nano-range? Are nanoparticles explosion more likely and more destructive than microparticles? Further investigations on the previously mentioned aluminum explosion at Gullaug, Norway, in 1973, revealed that the aluminum thickness was around 100 nm, and MIE of the order of 1 mJ and maximum rate of pressure rise around 2600 $bar.s^{-1}$ were measured, which seems to show an extreme ignition sensitivity and explosion severity (Eckhoff, 2003). However, it has to be noticed that, due to the presence of sulfur in the mixture, the explosion cannot be totally attributed to the aluminum nanoparticles.

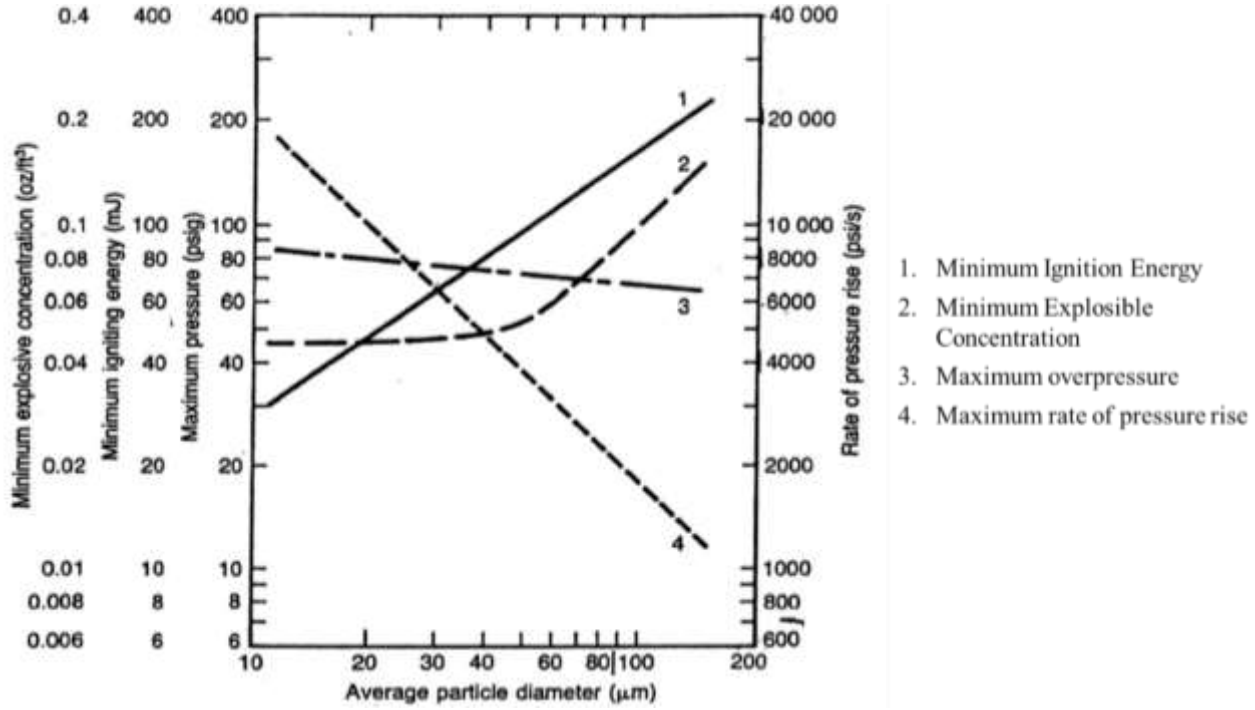

Figure 2-3 Explosion characteristics as a function of aluminum particle size (Baudry, 2007; Jacobson et al., 1964; Nagy and Verakis, 1983)

Furthermore, regulations such as ATEX directives were initially established for microparticles and barely consider the risks related to nanoparticles specificities. For instance, a classification system for the sealing effectiveness of enclosures of electrical equipment against the intrusion of foreign bodies such as dust and moisture is specified by international standards (BS EN 60529, 1992; IEC 60529, 2001). This classification relies on the Ingress Protection (IP), determined by exposing the equipment to a talcum powder of several tens of micrometers diameter during a few hours to verify the sealing of the apparatus. However, a cloud constituted of nanoparticles, even slightly agglomerated, may penetrate the equipment, thus questioning the application of the Ingress Protection. Thus, nanoparticles specificities should be investigated in order to adapt the current regulations and standards.

II.3. Nanomaterials

II.3.1. Generalities on nanomaterials

According to the European Commission (2011/696/EU, 2011), a nanomaterial is "a natural, incidental or manufactured material containing particles, in an unbound state or as an aggregate or as an agglomerate and where, for 50% or more of the particles in the number size distribution, one or more external dimensions is in the size range 1 nm – 100 nm". This recommendation also specifies that any material presenting a volume specific surface area (VSSA) higher than 60 $m^2.cm^{-3}$ must be considered as a nanomaterial. This value is the theoretical VSSA of a non-porous, perfectly monodisperse material consisting of spherical particles with a diameter of 100 nm or cubic particles with an edge length of 100 nm (Rauscher et al., 2019).

In industry, nanomaterials can be produced as by-products or accidentally. In the first case, two production ways are considered: the top-down, consisting in splitting a material to reach the nanodimension, and the bottom-up, in which the material is assembled from the atom to build the molecule. If both approaches enable the production of nanomaterials, their properties (specific surface area, particle size, structure, shape) greatly depend on the production method. The definition of the material application is then essential before the choice of its processing way (Iqbal et al., 2012).

Nanomaterials interest relies on additional, enhanced or different properties of materials when moving from the microscale to the nanoscale. The fundamental properties such as chemical, mechanical, optical or biological properties are then modified and often innovative (Stark et al., 2015). For instance, a material considered inert at the microscale such as gold can become a great catalyst when used at the nanoscale (Thompson, 2007). Those new properties induce numerous applications in different fields, like health, auto, construction, food or electronic sectors. Among the most commonly encountered nanomaterials, carbon blacks, resulting from the incomplete combustion or thermal decomposition of hydrocarbons, can be used as catalyst, absorbents or pigments. When dispersed in a system, this material can also modify its optical, thermal, mechanical and electrical properties (Soares et al., 2014).

The properties differences when moving from the microscale to the nanoscale come from the reduction of the particle size, which increases the specific surface area and the number of surface atoms, and thus the surface energy. For industrial applications, those properties are generally desired, but they also raise numerous questions concerning the toxicity of the materials. Indeed, due to their small size, nanoparticles can easily penetrate the organism, mainly through the respiratory route but also by dermal route. Once inhaled, particles can settle in different zones of the organism depending on their chemical composition, size or shape. Each type of nanoparticles then produces a different impact on health, possibly inducing inflammatory, respiratory, neurological or cardiovascular effects (Oberdörster et al., 2005).

However, the small size of nanoparticles also induces agglomeration and aggregation phenomenon, which are detailed in the next section.

II.3.2. Agglomeration forces

Agglomeration and aggregation can be distinguished by the binding strengths between the particles, although their definition divides the authors who tend to exchange both terms (Nichols et al., 2002). In this work, according to the definition from ISO/TS 80004-2 (2015), agglomeration is considered as a breakable assembly of particles through weak bonding whereas an aggregate consists of strongly bonded particles and cannot be broken (Sokolov et al., 2015; Walter, 2013), as presented in Figure 2-4. The aggregation phenomenon being generally considered irreversible, this work mainly focuses on the agglomerate formation and breakage. Two main agglomeration ways are generally encountered: the cluster-particle agglomeration, where a particle grafts on an existing cluster, and the cluster-cluster agglomeration, where two clusters bond together.

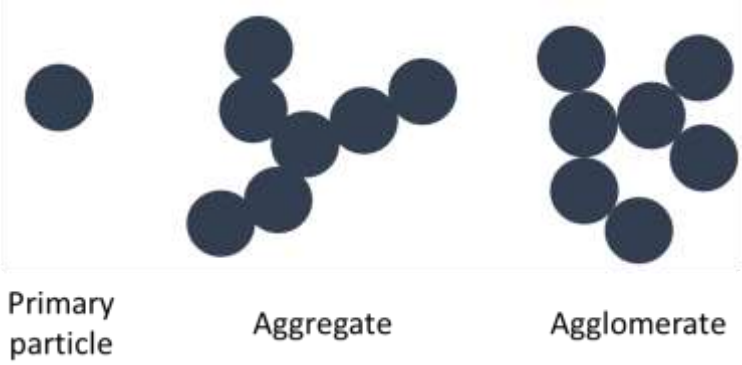

Figure 2-4 Illustration of a primary particle, an aggregate and an agglomerate

The main cohesion forces inducing the agglomeration of nanoparticles are the van der Waals interactions, electrostatic forces and, in the case of wet particles, capillary effects (Debrincat et al., 2008; Hartley et al., 1985). Magnetic forces can also act between the particles, but only on particles presenting a dipole moment, which is not the case of the studied powder (aluminum, carbon black, cellulose and silicon).

II.3.2.1. Van der Waals forces

Van der Waals electromagnetic interactions act between two close particles or between a particle and a surface due to their spontaneous electric and magnetic polarization. In the case of an interaction between a microparticle and a nanoparticle, a sphere-plane contact can be considered because of the size difference between the particles. However, in this work, only contacts between nanoparticles are analyzed in the form of sphere-sphere contacts. In the microscopic scale, the London-van der Waals theory is applied, with the force acting between two symmetric and neutral molecules (Figure 2-5).

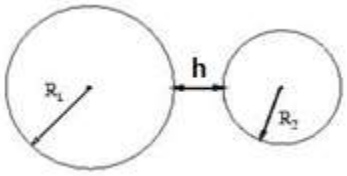

Figure 2-5 Useful geometric considerations to present van der Waals forces between two spherical particles

Van der Waals forces acting on two spherical particles of radius R_1 and R_2 with surfaces separated from a distance h_p can be expressed as follows (Israelachvili, 2011):

$$F_{VdW} = -\frac{AR_1R_2}{6(R_1+R_2){h_p}^2} \qquad 2\text{-}2$$

In the case of particles of the same diameter $d_p = 2\ R_1 = 2R_2$, the previous relation becomes:

$$F_{VdW} = -\frac{Ad_P}{24{h_p}^2} \qquad 2\text{-}3$$

The Hamaker constant A is a parameter which depends on the nature and density of the material as well as the environment in which the interaction takes place. Table 2-4 presents some Hamaker constant values for the compounds of interest in this study.

Table 2-4 Values of Hamaker constant for the considered compounds

System	Hamaker constant (J)	Reference
Cellulose in water	5.8×10^{-20}	(Bergstroem et al., 1996)
Aluminum in water	1.84×10^{-19}	(Jiang and Pinchuk, 2016)
Aluminum in vacuum	2.56×10^{-19}	(Jiang and Pinchuk, 2016)
Graphite in water	1.15×10^{-19}	(Dagastine et al., 2002)
Graphite in air	2.53×10^{-19}	(Dagastine et al., 2002)
Silicon carbide in n-heptane	2.48×10^{-19}	(Médout-Marère, 2000)

It should be noted that, to reach a given concentration, the number of nanoparticles is greatly higher than that of microparticles, which decreases the distance between the particles and thus favorizes the van der Waals interactions. Due to the square factor on the interparticle distance, such forces are non-negligible compared with the gravitational forces for particles smaller than 50-100 µm (Condotta, 2005).

II.3.2.2. Electrostatic forces

Electrostatic interactions result from frequent contacts between particles, thus creating an electrostatic potential. In the case of two different particles, part of the electrons from the surface of one particle is transferred to the other, inducing a triboelectric effect leading to attractive or repulsive interactions. The electrostatic force F_{el} is expressed by Coulomb law, where ε_0 is the dielectric permittivity of vacuum, q the charge of the particles and h the distance between the particles:

$$F_{el} = \frac{1}{4\pi\varepsilon_0}\frac{q_1 q_2}{{h_p}^2} \qquad 2\text{-}4$$

II.3.2.3. Capillary forces

Capillary forces act when the moisture content of the powder is relatively high. The water retention within the solid depends on its hygroscopicity and the relative humidity of atmosphere. This force can thus vary by modifying the available quantity of liquid and its properties (notably the surface tension γ and the viscosity). It is calculated according to relation 2-5, where the first term represents the surface tension force and the second term expresses the force resulting from a pressure loss in the liquid/capillary bridge (Seville et al., 2000). The capillary forces are characterized by the apparition of a meniscus between the particles (Figure 2-6) and can be neglected if the moisture content of the powder is low.

$$F_{cap} = 2\pi r\gamma + \pi r^2 \Delta P_{cap} \quad 2\text{-}5$$

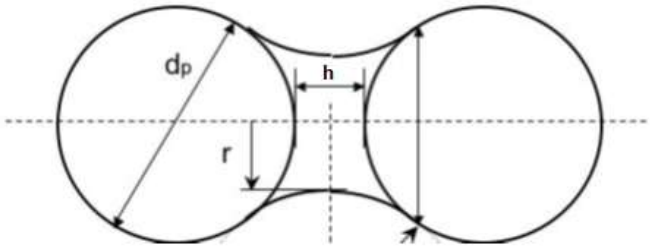

Figure 2-6 Liquid meniscus between two spherical particles (Seville et al., 2000)

II.3.3. Agglomerates breakage

As previously explained, an agglomerate is an assembly of weakly bounded particles. Depending on the cohesion forces, each agglomerate possesses its own cohesion strength, i.e. a force per surface unit to provide for the breakage of the contacts between particles. Over the years, several methods were developed to calculate the cohesion strength of agglomerates.

II.3.3.1. Simultaneous rupture across a fracture plan (Rumpf, 1962)

The oldest and best-known theory was established by Rumpf (1962), who considered spherical particles with the same size. This ideal model assumes that the agglomerate is separated in two parts by a transverse section, without taking into account the actual structure of the agglomerate (Figure 2-7). Several hypotheses were emitted to define a formula allowing the estimation of an agglomerate cohesion strength. First, the stressed section contains a great number of bonds, evenly distributed along this section and in the spatial directions. Then, the particles are statically distributed within the agglomerate: the stressed section is then homogeneous at the macroscopic level and presents an average effective force. Finally, the effective cohesion forces are distributed around a mean value that can be used for calculations and considered equal in every point of the section.

Figure 2-7 Example of ideal (dotted line) and real (solid line) fracture of an agglomerate (Rumpf, 1962)

Rumpf (1962) then defines the agglomerate cohesion strength σ_r as a function of the cohesion forces acting on the agglomerate F_{agglo}, the agglomerate porosity ε, the diameter of the primary

particles d_p and the coordination number k, representing the mean number of contacts between a particle and the neighboring particles:

$$\sigma_r = \frac{9}{8}\frac{(1-\varepsilon)}{\pi} k \frac{F_{agglo}}{{d_P}^2} \quad 2\text{-}6$$

The coordination number can be approximated using equation 2-7 (Smith et al., 1929), leading to the final relation 2-8.

$$k\varepsilon \cong 3.1 \cong \pi \quad 2\text{-}7$$

$$\sigma_r = 1.1\frac{(1-\varepsilon)}{\varepsilon}\frac{F_{agglo}}{{d_P}^2} \quad 2\text{-}8$$

This model implies that the breakage occurs through a simultaneous rupture of all the bonds along the fracture plan. The agglomerate cohesion strength is then calculated as the sum of the inter-particle strengths located in this plan. The whole surface of the agglomerate is thus considered to be used for contacts, which is consistent in the case of large agglomerates for which almost all the particle surface is in contact with another particle. However, the particles on the external layer of the agglomerates present less bonds than the internal particles, which is not considered by the model but can be neglected in the case of big agglomerates.

The model defined by Rumpf (1962) was criticized by Kendall (1988), who claims that, in practice, the bonds on the fracture plan do not break simultaneously. On the contrary, a gradual rupture occurs, leading to the formation of a crack. Moreover, agglomerates constituted of spherical particles of the same diameter are unlikely to be found in practice. Finally, in agglomerates with low porosity, the proximity between particles can lead to frictions, which is not considered in this model (Reynolds et al., 2005).

II.3.3.2. Progressive failure across a fracture plan (Kendall, 1988)

Kendall (1988) claims that Rumpf theory does not allow the calculation of the real cohesion strength of an agglomerate and overestimates it. Indeed, the fracture is due to the propagation of a crack from an edge notch, leading to the sequential separation of the particles, unlike the simultaneous breakage of all the bounds considered in Rumpf model (Figure 2-8).

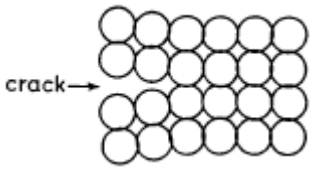

Figure 2-8 Agglomerate fracture model according to Kendall (1988)

Kendall (1988) then established a new model to estimate the agglomerate cohesion strength, noted σ_k, where Γ and Γ_c represent respectively the equilibrium surface energy and the fracture surface energy:

$$\sigma_k = 15.6\ \varphi^4\ {\Gamma_C}^{\frac{5}{6}}\ \Gamma^{\frac{1}{6}}\ (d_P c_{edge})^{-\frac{1}{2}} \quad 2\text{-}9$$

This model shows an influence of the length of the edge notch c_{edge}, a higher dependency on the solid fraction φ and a lower impact of the primary diameter d_p compared to Rumpf model. However, Kendall's work relies on Griffith's (1921) who developed fracture mechanisms for linear elastic material. Considering the inherent heterogeneous nature of agglomerates, nothing proves that they can be characterized by those fracture mechanisms (Reynolds et al., 2005). Moreover, the considered parameters are not easily determined in practice, which makes this model difficult to use.

II.3.3.3. Total breakage of the agglomerate (Weiler, 2010)

The validity of Rumpf's model is limited because of the heterogeneous distribution of strengths, contact surfaces and porosity within the agglomerate. Due to those heterogeneities, the breakage of an agglomerate occurs where the resistance is the lowest. The stress to provide to break the agglomerate calculated by Rumpf (1962) is then overestimated. A new model was then introduced by Weiler et al. (2010) who assumed a total breakage of the agglomerate by considering all the contacts between the particles (Figure 2-9), thus reducing the impact of the heterogeneities within the agglomerate.

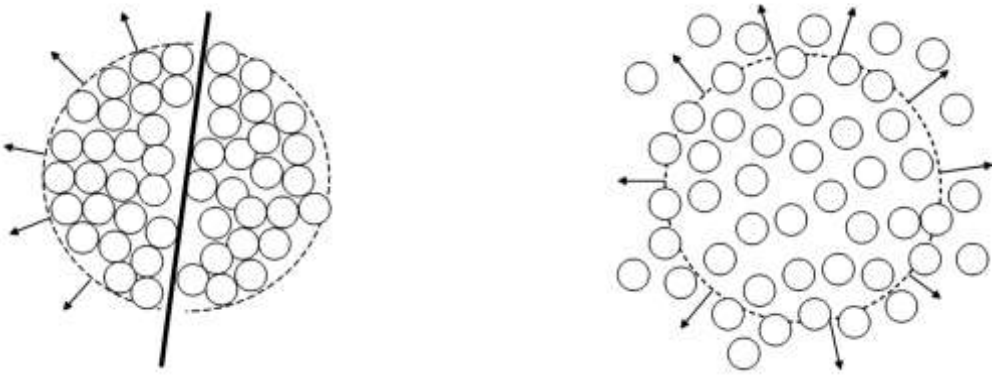

Figure 2-9 Theoretical models of agglomerate fracture according to Rumpf (left) and Weiler (right) (Weiler et al., 2010)

The dispersion strength σ_w is introduced as the force required for a total dispersion of the agglomerate F_{disp} on its total surface S_{agg} :

$$\sigma_w = \frac{F_{disp}}{S_{agg}} \qquad 2\text{-}10$$

Part of the assumptions of Rumpf's model are also made in this model: particles are considered spherical and of the same size, and the total breakage is instantaneous. Moreover, the agglomerates are also assumed spherical and only the forces in the direct neighboring of each particle are considered. The force required for the total dispersion of the agglomerate is then calculated as the product of the force required to break each contact F_{mean} by the number of contacts within the agglomerate n_{cont}:

$$\sigma_w = \frac{n_{cont}\, F_{mean}}{\pi\, {d_{agg}}^2} \qquad 2\text{-}11$$

Considering that the particles on the external layer possess less contacts than the particles within the agglomerate, equation 2-12 was proposed for a spherical agglomerate.

$$\sigma_w = \frac{(1-\varepsilon)F_{mean}}{2d_{agg}^2\varepsilon}.\left(\frac{{d_{agg}}^3}{{d_P}^3} - 4\frac{\left(1-\frac{\arccos\left(\frac{d_P}{d_{agg}-d_P}\right)}{180°}\right)}{\frac{d_P}{d_{agg}-d_P}}\right) \quad 2\text{-}12$$

The fragmentation of the agglomerate occurs when it is submitted to a stress higher than the cohesion strength. The dispersed agglomerates can then be disintegrated due to different stresses exerted by the fluid flow on the particles surface, such as the inertial stress, the rotary stress or the turbulent stress (Weiler et al., 2010).

The numerous original properties of nanoparticles imply a new behavior in terms of flammability and explosivity, which it is essential to properly determine to be able to prevent dust explosions and protect from it.

II.4. Nanoparticles explosions

Different studies were conducted to determine the ignition sensitivity and explosion severity of nanoparticles and, if observations vary with the physicochemical properties of the powder, a general tendency appears. Indeed, some authors noticed that the ignition sensitivity tend to increase when decreasing the particle size (Boilard et al., 2013; Bouillard et al., 2010; Mittal, 2014; Vignes et al., 2012, 2019) whereas explosion severity would tend to decrease for metallic dusts. In the case of some ignition parameters like LEL, some authors also highlighted the presence of a plateau below a critical size (Bouillard et al., 2010; Holbrow et al., 2010; Nazneen and Wang, 2019).

II.4.1. Reaction mechanisms

In addition to the evolution in the reactive surface area, decreasing the particle size also leads to the transition from a diffusional limitation for large particles to a reactional limitation for small particles (Bouillard et al., 2010; Huang et al., 2007). This transition was observed for different compounds: around 10 to 100 µm for carbonaceous materials, at 80 µm for polyethylene (Almerinda Di Benedetto et al., 2010), and around 30 µm for natural organic compounds like starch (Eckhoff, 2003). However, such a critical diameter depends on the operating conditions, and notably on the external temperature (Cuervo, 2015).

When regarding organic combustion, several steps are involved. First, the particles are heated, leading to a pyrolysis step during which char, tar and pyrolysis gases are produced. These two latter then undergo an homogeneous oxidation by reacting with the dioxygen from air (Di Benedetto and Russo, 2007). It also has been shown that combustion can be controlled by the gas phase oxidation or by the pyrolysis step depending on the particle size (Hertzberg et al., 1988). Then, from a certain size, the limiting phenomenon is no longer the dioxygen transfer to the particle surface nor the pyrolysis, but the combustion of the pyrolysis gases. However, in

practice, the pyrolysis and the oxidation step are not completely separated, leading to the simultaneous presence of pyrolysis gases and dispersed particles, which can be regarded as a hybrid mixture (Dufaud et al., 2012).

A critical diameter was also evidenced for metallic particles, notably around 10 µm for aluminum particles, although different mechanisms are involved during their combustion (Glorian et al., 2016; Lomba, 2016). Indeed, the combustion undergoes a surface oxidation, a melting or a vaporization of the particles depending on their size (Levitas, 2013; Mohan et al., 2009). The Damköhler number 2 is generally used to determine if the combustion process is controlled by the diffusion of dioxygen to the particles or by the surface reaction:

$$Da_{II} = \frac{\tau_{diff}}{\tau_{kin}} \qquad 2\text{-}13$$

In cases where $Da_{II} >> 1$, the combustion time of the diffusion-controlled process τ_{diff} is higher than the one controlled by the surface reaction τ_{kin}. The combustion is then limited by the diffusion of the dioxygen toward the particle surface. The metal below the oxide layer then melts, and the emitted gas moves away from the particle to meet the dioxygen. A detached flame is then obtained and nano-sized oxides are produced. On the contrary, if $Da_{II} << 1$, the surface reaction limits the combustion, which occurs directly on the surface of the particle, without vaporization of the metal. A combustion product with a size similar to the one of the initial particle is then obtained (Lomba, 2016). In practice, both processes operate during the combustion (Figure 2-10), and only the prevalence of one phenomenon to the other is distinguished.

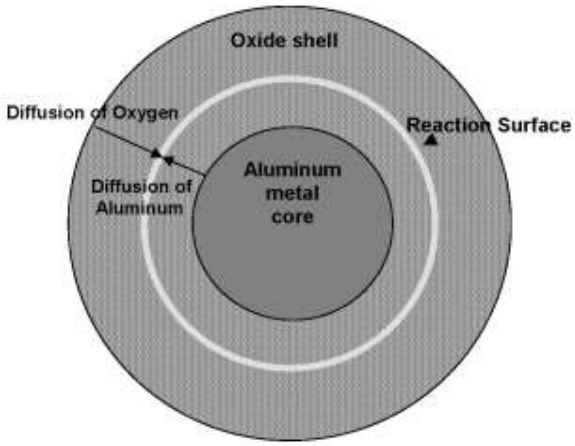

Figure 2-10 Scheme of an aluminum particle with the oxide layer, surface reaction and oxygen diffusion (Rai et al., 2006)

A third combustion way occurs when considering nanoparticles: due to the high curvature, Laplace pressure induces the fracture and spallation of the shell (Levitas, 2013) leading to the ejection of nanosized droplets which are then oxidized, leading to a final product which appears once again in the form of nanoparticles.

II.4.2. Ignition sensitivity

Generally, the ignition sensitivity tends to increase when decreasing the particle size, until a critical diameter from which it plateaus. However, the existence of such a critical diameter cannot be identified in the case of metallic particles: the minimum ignition energy sensitively decreases when decreasing the particle size, as shown in Table 2-5. It appears that some metallic powders, such as aluminum, exhibits MIE lower than 1 mJ, and can even ignite spontaneously when exposed to oxygen (Krietsch et al., 2015). This latter phenomenon, known as pyrophoricity, is obviously an issue when it comes to powder generation, handling, transport and storage, and it becomes necessary to evaluate a critical size below which particles can self-ignite (Sundaram et al., 2013).

Table 2-5 MIE of aluminum particles (Dufaud et al., 2011)

Particles	Al (42 µm)	Al (3 µm)	Al (200 nm)	Al (100 nm)	Zn (38 µm)	Zn (120 nm)
MIE (mJ)	440	14	7	< 1	> 1000	19

The MIE of carbonaceous powders being in the order of 250 to 2500 J (Turkevich et al., 2015), the influence of the particle size on this parameter cannot be evaluated with the modified Hartmann tube, which can only generate a maximum energy of 1 J. However, Bouillard et al. (2010) evidenced that the LEL of carbon black decreases when decreasing the particle size, until reaching a plateau at 60 $g.m^{-3}$ from BET diameter of 25 nm. These authors also highlighted that the MIT decreases when moving from the microscale to the nanoscale, but then could increase for small particles. The existence of this minimum probably comes from the fact that, for small particles, cohesion forces are stronger than for bigger ones, thus causing agglomeration (Eckhoff, 2012). A higher energy amount is then needed to ignite the powder, explaining the increasing in the MIT. This tendency is also visible when regarding the explosion severity parameters (Vignes et al., 2019).

II.4.3. Explosion severity

In a similar way than for ignition sensitivity, an increase in the explosion severity is observed when decreasing the particle size until a critical value. For carbonaceous powders, Eckhoff (2003) reported this value to be around 50 µm, which is confirmed by Bouillard et al. (2010), Holbrow et al. (2010) and Turkevich et al. (2016) who obtained an explosion severity similar to microparticles when testing nanoparticles.

When it comes to the most reactive metallic powders, such as aluminum or magnesium, no limit value could be found in the literature. However, Dufaud et al. (2011) and Vignes et al. (2019) evidenced that the explosion severity increases before decreasing when reducing the particle size by measuring the maximum overpressure and maximum rate of pressure rise of aluminum and zinc powders with different primary particle diameters, from 40 µm to 20 nm (Table 2-6).

Table 2-6 Explosion severity of different aluminum powders (Dufaud et al., 2011; Vignes et al., 2019)

Powder	P_{max} (bar)	$(dP/dt)_{max}$ (bar.s^{-1})	K_{St} (bar.m.s^{-1})	St class
Aluminum 18 nm	7.3	564	153	St 1
Aluminum 40-60 nm	8.9	2251	611	St 3
Aluminum 50-70 nm	8.3	1573	427	St 3
Aluminum 90-110 nm	7.9	1102	300	St 3
Aluminum 100 nm	8.2	1340	362	St 3
Aluminum 130 nm	7.8	1030	280	St 2
Aluminum 150 nm	10.2	2486	675	St 3
Aluminum 200 nm	9.5	2420	673	St 3
Aluminum 3 µm	9.8	2090	567	St 3
Aluminum 7 µm	9.1	1460	396	St 3
Aluminum 27 µm	7.5	400	106	St 1
Aluminum 42 µm	7.2	360	98	St 1

The explosivity difference between aluminum particles of 130 nm and 150 nm may come from different passivation degree and from agglomeration phenomenon which is probably more important for smaller particles. A high explosivity difference appears also between aluminum of 27 µm and 7 µm, increasing the maximum rate of pressure rise by 1000 bar.s^{-1} when decreasing the particle size of 20 µm and moving from class St 1 to St 3, which is the most violent class. This radical change can be due to a modification in the combustion mechanisms as previously mentioned, or to a flame propagation mechanism variation (Vignes et al., 2019).

II.4.4. Radiative heat transfer

When examining gas explosions, the radiative heat transfer is commonly neglected as the gases are generally transparent. However, Torrado (2017) evidenced that adding a small amount of nanoparticles in a gas considerably increases the radiation emitted during an explosion, as presented in Figure 2-11. Further investigations (Ben Moussa, 2017; Julien et al., 2017a; Proust et al., 2017) highlighted the influence of the radiative heat transfer on the flame propagation and the explosion severity, according to two possible effects. In the first case, the radiative heat transfer tends to heat the fresh unburnt mixture, which can speed up the flame propagation and increase the explosion severity (Haghiri and Bidabadi, 2010). On the contrary, in the second case, the heat losses on the walls tend to decrease the flame temperature, and thus the explosion overpressure (Bidabadi and Azad, 2015). In both cases, it is admitted that, although a dust

explosion flame propagates essentially by conduction, like gases, radiation also plays an important role during the propagation.

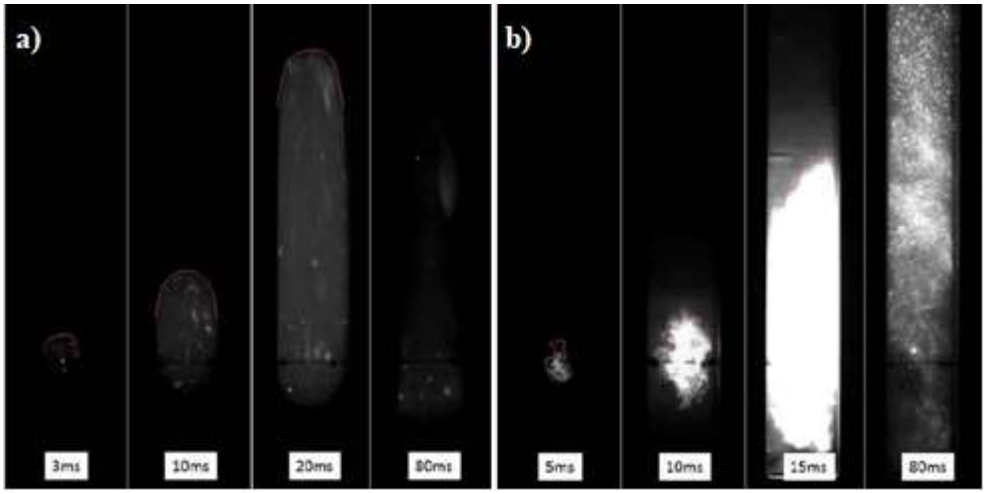

Figure 2-11 Flame propagation at an ignition delay time of 60 ms for a 12%v. methane/air mixture a) alone and b) containing 30 mg of carbon black nanoparticles (Torrado, 2017a)

Flame propagation mechanisms slightly differ depending if particles are micrometric or nanometric. Indeed, depending on the particle size, the scattering of incident light is modified, following Mie or Rayleigh theory, which is a limiting case of Mie theory for fine particles. Thus, for small particles whose diameter is smaller than the incident beam wavelength, i.e. nanoparticles, Rayleigh theory must be applied (Figure 2-12A). The light scattering then occur in every direction, inducing significant radiation which can increase the flame thickness. On the contrary, when examining larger particles, Mie theory is considered (Figure 2-12B and C), where the light scattering is mainly oriented toward the direction of incident light (Moosmüller and Arnott, 2009).

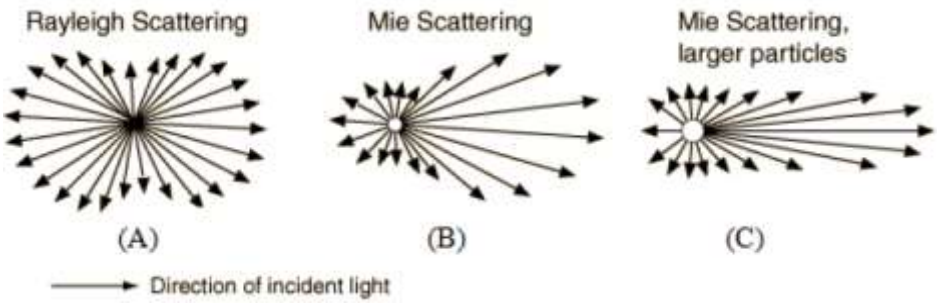

Figure 2-12 Spatial distribution of light scattering for particles of different sizes (Ben Moussa, 2017)

In view of these elements concerning nanoparticle explosions, it appears that standard procedures, initially conceived for microparticles, may not be adapted to nanoparticles explosions evaluation. Further considerations on this aspect are then developed in chapter 4.

Summary

This chapter presents the first step of the evaluation of the explosion risk related to the production, transport and handling of nanopowders, relying on a literature review divided into four parts.

First, an analysis of some past accidents involving different types of powders highlighted the reality and seriousness of the risk represented by dust explosions. Thus, the two European ATEX directives were introduced: the first one, 1999/99/CE directive (ATEX Workplace directive) classifies the workplace into zones depending on the formation probability of an explosive atmosphere. The equipment to use into such zones are then defined by the second one, i.e. 2014/34/UE directive. The implementation of safety measures to prevent and protect from dust explosions is then possible through the knowledge of the explosion characteristics of the dust involved in the process.

In a second part, the dust explosion phenomenology was explained. First, the distinction between ignition sensitivity, i.e. the probability that a dust ignites, and explosion severity, characterizing the effects of the explosion, was clarified. The standard parameters describing the ignition (minimum ignition energy, minimum ignition temperature, lower explosion limit) and the explosion (maximum overpressure, maximum rate of pressure rise, burning velocity) were then detailed, along with the main factors influencing them, such as the chemical composition, the dust concentration, the moisture content, the ignition energy, the initial turbulence and the particle size.

Since this work focuses on nanoparticles, the third part is dedicated to their specificities. More precisely, the agglomeration phenomenon inherent to nanomaterials was further investigated. Indeed, the main cohesion forces, such as van der Waals, electrostatic and capillary forces were detailed, along with the three main models describing agglomerates breakage established by Rumpf (1962), Kendall (1988) and Weiler et al. (2010).

Finally, the influence of nanoparticles specificities on their explosion behavior was discussed. Some authors then observed that the ignition sensitivity tends to increase when decreasing the particle size (Vignes et al., 2019) whereas the explosion severity shows a plateau (Bouillard et al., 2010). This plateau can be explained by the agglomeration of the nanoparticles, which then exhibit an explosion severity similar to microparticles. A transition from a diffusional limitation for large particles to a reactional limitation for small particles was also highlighted (Bouillard et al., 2010). This transition was found around 10 to 100 µm for carbonaceous compounds (Di Benedetto et al., 2010), around 30 µm for organic compounds (Eckhoff, 2003) and around 10 µm for metallic particles (Glorian et al., 2016). For such powders, a pyrophoric behavior was also mentioned, leading to a spontaneous ignition when exposed to air (Krietsch et al., 2015). Moreover, a transition from Mie scattering to Rayleigh scattering occurs when decreasing the particle size to the nano-range, thus inducing differences in the radiative heat transfer with regard to microparticles, possibly impacting the validity of the use of the cube-root law.

Résumé

Ce chapitre présente les premières étapes de l'évaluation des risques d'explosion liés à la production, au transport et à la manipulation de poudres nanométriques, et repose sur une revue bibliographique divisée en quatre parties.

Dans un premier temps, une analyse d'accidents impliquant différents types de poudres a souligné la réalité et la gravité du risque représenté par les explosions de poussières. Les deux directives européennes ATEX ont été introduites : la première, la directive 1999/99/CE classe les espaces de travail en zones selon la probabilité de formation d'une atmosphère explosive. Les équipements autorisés dans ces zones sont alors définis par la seconde directive, la directive 2014/34/UE. L'implémentation de mesures de sécurité pour prévenir et protéger contre les explosions de poussières est alors possible à partir de la connaissance des caractéristiques d'explosivité des poussières impliquées dans les procédés.

Dans une deuxième partie, la phénoménologie des explosions de poussières a été détaillée. D'abord, la distinction entre la sensibilité à l'inflammation, i.e. la probabilité qu'une poussière s'enflamme, et la sévérité d'explosion, qui concerne les effets de l'explosion, a été réalisée. Les paramètres décrivant l'inflammation (énergie minimale d'inflammation, température minimale d'inflammation, concentration minimale explosible) et l'explosion (surpression maximale d'explosion, vitesse maximale de montée en pression, vitesse de flamme) ont ensuite été détaillés, ainsi que les principaux facteurs influents, tels que la concentration en poussière, le taux d'humidité, l'énergie d'inflammation, la turbulence initiale et la taille de particules.

Ce travail se focalisant sur les nanoparticules, la troisième partie de ce chapitre a été dédiée à leurs spécificités. Plus précisément, le phénomène d'agglomération inhérent aux nanomatériaux a été analysé. En effet, les principales forces de cohésion, telles que les forces de van der Waals, électrostatiques et capillaires ont été détaillées, ainsi que les trois principaux modèles décrivant la fragmentation d'un agglomérat.

Enfin, l'influence des spécificités des nanoparticules sur le déroulement de leur combustion a été discutée. Certains auteurs ont observé que la sensibilité à l'inflammation tend à croître en diminuant la taille de particules tandis que la sévérité d'explosion se stabilise (Vignes et al., 2019). Ce plateau peut être expliqué par l'agglomération des nanoparticules, qui présentent alors une sévérité d'explosion similaires aux microparticules. La transition d'une limitation diffusionnelle pour de grosses particules vers une limitation réactionnelle pour de petites particules a également été démontrée (Bouillard et al., 2010). Cette transition a été obtenue vers 10 à 100 µm pour des composés carbonés (Di Benedetto et al., 2010), vers 30 µm pour des composés organiques (Eckhoff, 2003) et vers 10 µm pour des particules métalliques (Glorian et al., 2016). Pour ces dernières, un comportement pyrophorique a également été mentionné, donnant lieu à une inflammation spontanée lors d'une exposition à l'air (Krietsch et al., 2015). De plus, en diminuant la taille de particules jusqu'à l'échelle nanométrique, la transition d'une diffusion de Mie vers une diffusion de Rayleigh induit des différences dans le transfert radiatif par rapport aux microparticules, impactant probablement la validité de la loi cubique.

Chapter 3:
Powder and dust cloud characterization

To provide reliable explosion safety characteristics and have a better insight on the influential factors, the process safety engineer needs to assess properly the properties of the powders. However, a characterization before dispersion is not sufficient, notably due to the agglomeration phenomenon that can modify the particle size distribution (PSD) after dispersion. This chapter is dedicated to the powder and dust cloud characterization, and is divided into three parts: first, the powders are presented and classified according to the European Commission definition for nanomaterials. A characterization of the PSD of the powder before dispersion is also presented. In the second part, the dust cloud properties are investigated through dustiness and PSD measurements, performed according to three different methods. In addition, the turbulence level after the dust dispersion in the 20L sphere is evaluated through Particle Image Velocimetry measurements. Finally, a dimensional analysis describing the dust dispersion phenomenon is realized, and a correlation for the determination of the mean surface dimeter after dispersion in the 20L depending on the powder properties and operating conditions was proposed.

III.1. Powder properties

During this work, four different powders were chosen to highlight the specific behavior of each type of combustible powder, i.e. carbonaceous, organic or metallic: carbon black, nanocellulose, aluminum and carbon-coated silicon, as explained in chapter 1. Each powder is constituted of individual primary particles or crystallites of diameter lower than 100 nm. However, due to the tendency of nanoparticles to agglomerate and aggregate (Sokolov et al., 2015), the powders essentially contains agglomerates and aggregates of bigger size (Henry, 2013). It is therefore essential to qualify the exact 'nanometric' nature of the powders.

The different powders of interest are presented in this section, and a method proposed in the NanoDefine project (Rauscher et al., 2015; 2019) was applied to examine whether the powders can be considered as a nanomaterial according to the European Commission (2011/696/EU, 2011).

III.1.1. Powder description

As previously mentioned, the powders were selected depending on their chemical nature (carbonaceous, organic and metallic), but also as a function of their availability in the market and the level of knowledge on the materials. The chosen powders are presented in this section, along with Scanning Electron Microscopy (SEM) images.

Aluminum

With the aim of reducing fossil fuels consumption and carbon dioxide emissions, inorganic energy carriers are more and more investigated. Hydrogen has already been recognized as one of the future energy carriers. However, its storage and transportation can present some difficulties. In this context, some authors consider that aluminum could constitute an interesting alternative (Shkolnikov et al., 2011), since it can easily be stored and transported, contrary to

hydrogen. Furthermore, it mainly produces alumina during combustion and if the combustion process is combined with a reduction process, the aluminum can be retrieved and reused (Lomba, 2016).

Two aluminum nanopowders were studied during this work. The first sample was provided by QinetiQs Nanomaterials Limited, UK and studied in the framework of NANOSAFE 2 European Project (Vignes, 2008). It was then stored under ambient air 11 years. Since its primary particle diameter is of 100 nm, it will be referred to as "aluminum 100 nm". As shown in Figure 3-1, aluminum particles agglomerate form spherical clusters, which were already observed in 2008 and thus cannot be ascribed to the storage conditions. The second aluminum powder was supplied by Iolitec, Germany and presents a primary particle diameter around 40 to 60 nm and will be referred to as "aluminum 40-60 nm". This powder was stored under argon in plastic bags of 25g under vacuum to avoid a pre-oxidation of the powder. As presented in Figure 3-2, the aluminum of 40-60 nm is constituted of small agglomerates of around 10 µm, compared to several dozens of micrometers for the aluminum 100 nm.

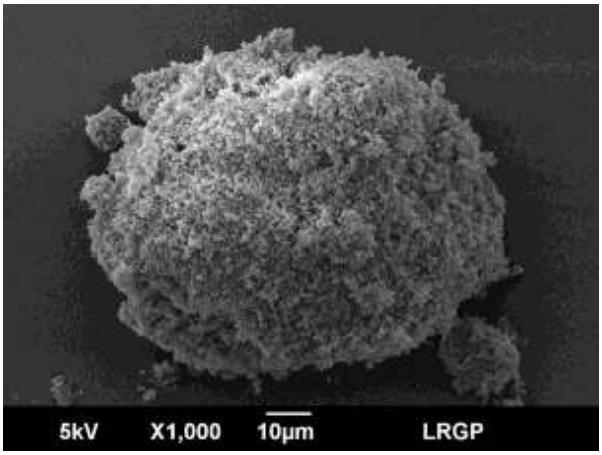

Figure 3-1 SEM image of aluminum 100 nm

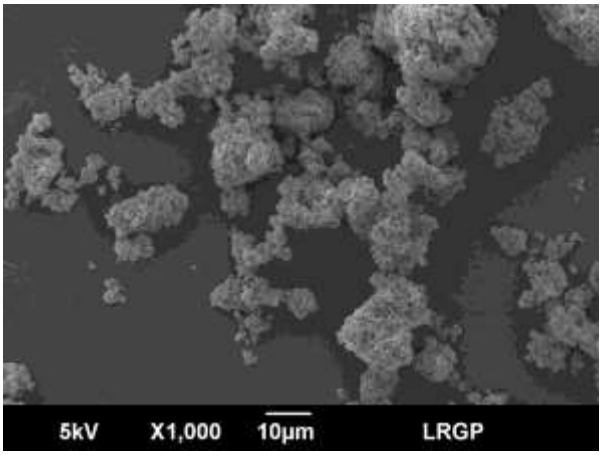

Figure 3-2 SEM image of aluminum 40-60 nm

Carbon blacks

Incomplete combustion, pyrolysis or thermal dissociation of oils can lead to the formation of carbon blacks. Due to its physical, electrical and optical properties, this powder is widely used in rubber industries, notably for tires (Fan et al., 2020) or as a pigment or ink (Ali et al., 2019; Li and Sun, 2007).

Reference product from Nanosafe 2 (Vignes, 2008), a long-term stored carbon black powder was also selected. The carbon black powder used was produced and referred to as Corax N550 by the society Degussa, a company acquired by Orion Engineered Carbon in 2015, and stored under ambient air for 11 years. The effects of this long storage are discussed in chapter 5. The primary particles, of diameter around 75 nm, form roughly spherical agglomerates of several dozens of nanometers as shown in Figure 3-3.

Carbon-coated silicon

A powder of carbon-coated silicon with a primary particle diameter around 40 nm (coating thickness of 2 nm) was supplied by Nanomakers, France and produced by laser pyrolysis. Its mechanical, chemical and thermal properties are of interest to increase the performances of materials used in different industrial sectors such as semiconductor industry, energy storage, aeronautics, space and automotive (Nanomakers, 2019). Once again, clusters of several micrometers are apparently form by agglomeration of the primary nanoparticles (Figure 3-4).

These particles are constituted of silicon and coated by a carbon layer, noted SiΩC, and cannot be assimilated to silicon carbide SiC. However, it should be noted that pure silicon carbide is stable up to 1570 K and is generally considered as a non-flammable material. Yet, when increasing its specific surface area, i.e. decreasing the particle size to the nano-range, and in presence of water, it can be oxidized (Boutonnet Kizling et al., 1992). This oxidation from the water can then release hydrogen and lead to an explosion if exposed to an ignition source. Indeed, explosion tests were performed at INERIS on a silicon carbide powder provided by Iolitec, with a primary diameter of 60 nm, which was classified as St 1 (P_{max} = 8.8 bar and $(dP/dt)_{max}$ = 260 bar.s^{-1}).

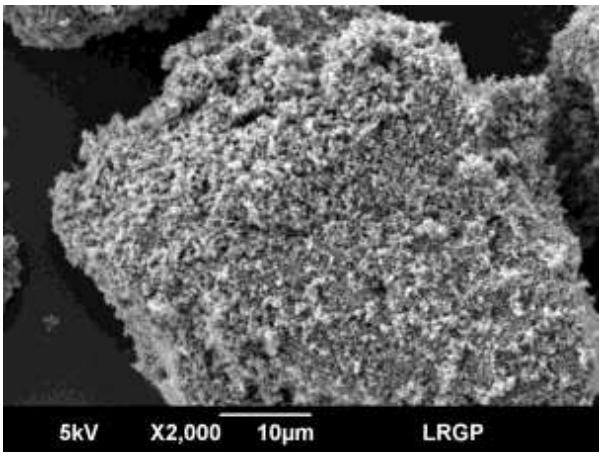

Figure 3-3 SEM image of carbon black

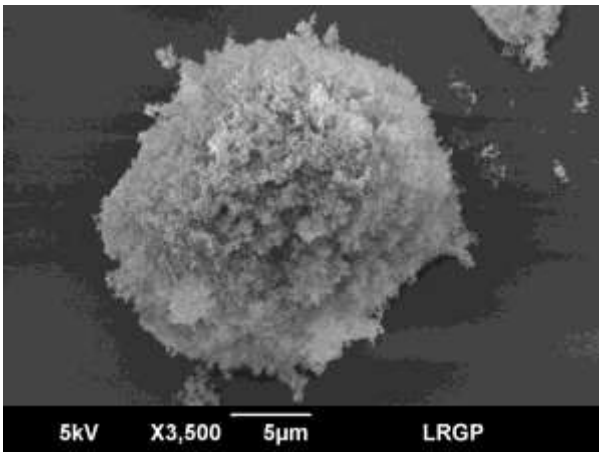

Figure 3-4 SEM image of silicon coated by carbon

Nanocellulose

Cellulose powder can be extracted from wood and plant fibers, and is then an abundant, renewable and biodegradable polymer. Due to its specific chemical and physical properties induced by the nanoscale and providing a wide variety of applications, the nanocellulose can be used is several different fields, such as in photonics, coating, 3D printing, plastics (Abitbol et al., 2016), biomedicine (Lin and Dufresne, 2014) or electronics (Shi et al., 2013).

The studied nanocrystalline cellulose, supplied by CelluForce, is constituted of crystallite fibers of average diameter and length of respectively 3 nm and 70 nm (CelluForce, 2016). Cellulose nanocrystals are generally obtained through the hydrolysis in sulfuric acid of different cellulose sources such as wood pulp, microcrystalline cellulose, cotton or other biopolymers. Since this acid hydrolysis occurs in a water suspension, the water must then be removed, for instance through freeze-drying (Börjesson and Westman, 2015). This drying step tends to cause the

agglomeration of the nanocrystals, which then combine to form particles from 1 to 50 µm, visible in the SEM image in Figure 3-5. However, when re-dispersed in water, individual nanocrystals can be retrieved. Due to this specificity, the classification of this powder as nanomaterial according to the European Commission can be questioned (see section III.1.2.).

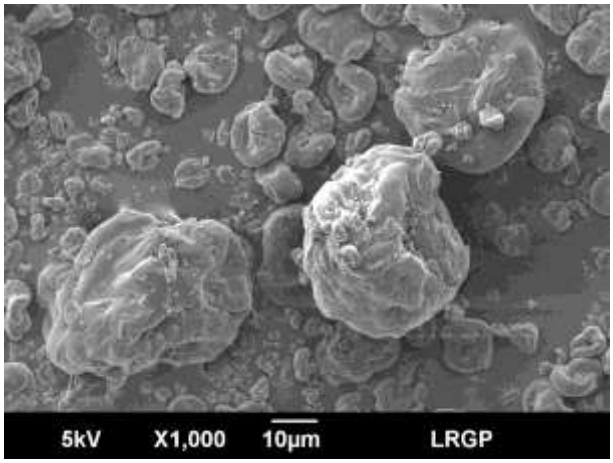

Figure 3-5 SEM image of nanocellulose

III.1.2. Nanomaterial classification and characterization

In addition to the definition of a nanomaterial describing a nanomaterial as a material containing 50% or more in the number size distribution with at least one external dimension in the range 1 nm – 100 nm, the European Commission published a recommendation specifying that a material can be classified as nanomaterial if its volume specific surface area (VSSA) is larger than 60 $m^2.cm^{-3}$ for spherical particles (2011/696/EU, 2011). However, a VSSA lower than this value does not necessary imply that the material should be classified as non-nanomaterial. Moreover, relying only on the knowledge of the specific surface area may lead to inappropriate classification, as, for instance, highly porous materials composed of particles smaller than 100 nm can develop a VSSA lower than 60 $m^2.cm^{-3}$ (Roebben et al., 2014). Thus, VSSA should not be regarded as an independent criterion to identify nanomaterials and should be coupled with image analysis to be adapted to non-spherical particles (Rauscher et al., 2019). For this reason, nanomaterial screening strategy based on the volume-specific surface area (VSSA) for the purpose of the European Commission recommendation was proposed by Rauscher et al. (2015) and is summarized in Figure 3-6. The calculation of the VSSA relies on the knowledge of the specific surface area and skeletal density ρ_{sk} of the powder. To determine the specific surface area, the BET adsorption method (from Brunauer, Emmett and Teller) is commonly used. It consists in the determination of the maximum gas volume adsorbed by a weighted sample at different pressures using Langmuir theory (Brunauer et al., 1938). The specific surface area is then deduced from physical properties of the adsorbed gas by considering physical adsorption.

The skeletal density of fine powders is usually measured using an helium pycnometer (Keng, 1969), which calculates the volume of solid excluding the pores to obtain the real (skeletal) density, by opposition to the bulk density which includes the volume of the pores.

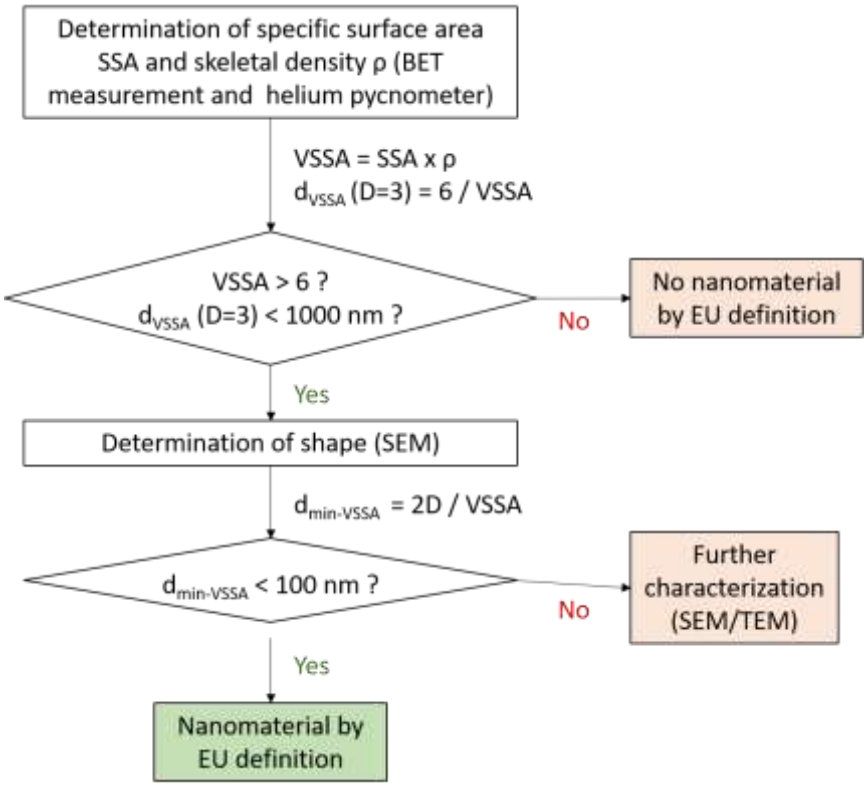

Figure 3-6 Simplified flow-chart of the method proposed in the NanoDefine project and explained by Wohlleben et al. (2017)

When applying the method described by Rauscher et al. (2015), the VSSA and the smallest particle dimension $d_{min-VSSA}$ are first calculated from the values of specific surface area and skeletal density ρ_{sk} using the following equations (Wohlleben et al., 2017):

$$VSSA = SSA * \rho_{sk} \quad 3\text{-}1$$

$$d_{min-VSSA} = \frac{2D}{VSSA} \quad 3\text{-}2$$

Since the determination of the dimension D requires knowledge on the particle shape, an assumption of D = 3, i.e. roughly spherical particles, is generally made for a first estimation of the parameters. If the VSSA is higher than 6 and the calculated value of d_{VSSA} with D = 3 is lower than 1 µm, a characterization of the particle shape is then recommended in the method to consider all types of particles and check for the presence of aggregation or multimodality (Wohlleben et al., 2017). The accurate value of D should then be used to calculate $d_{min-VSSA}$, which must be lower than 100 nm so that the powder is considered as a nanomaterial.

The studied powders were then characterized in terms of specific surface area and skeletal density using respectively the BET method (Tristar II Plus, Micromeritics) and a helium pycnometer (Accupyc 1330C, Micromeritics). The particle dimension was estimated through

SEM images (Figures 3-1 to 3-5 and Appendix 1), every powder being constituted of roughly spherical particles, which induces a dimension D = 3. The characteristics of the different powders are then presented in Table 3-1.

Table 3-1 Characteristics of the powders and application of the VSSA method

	Nanocellulose	**Carbon black**	**Aluminum 40-60 nm**	**Aluminum 100 nm**	**Carbon-coated silicon**
Primary diameter (nm)	3 nm width, 70 nm length	75	40-60	100	40
Specific surface area ($m^2.g^{-1}$)	N/A	40	24	23	55*
Skeletal density ($g.cm^{-3}$)	1.56	1.89	2.67	2.70	2.35
VSSA ($m^2.cm^{-3}$)	N/A	75.8	64.1	62.1	129
$d_{min\text{-}vssa}$ (nm)	N/A	79.2	93.5	96.7	46.5
Nanomaterial ?	?	✓	✓	✓	✓

(*Nanomakers, 2019)

From the available measurements and image characterization, both aluminum powders as well as carbon black and carbon-coated silicon present a minimum VSSA diameter $d_{min\text{-}VSSA}$ lower than 100 nm, which allows their classification as nanomaterial according to European Commission definition (Table 3-1). As previously mentioned, the nanocellulose is constituted of nanocrystals agglomerated to form microparticles. However, the estimation of the specific surface area by BET method relies on the adsorption of nitrogen on active sites, which are sparse on microparticles. Indeed, the experiments conducted on nanocellulose did not allow the validation of the five criterions required to validate the measurement of the specific surface area. It should be noticed that the specific surface area mentioned in the product specifications is of 400 $m^2.g^{-1}$ (CelluForce, 2016), which corresponds to the geometric surface area developed by the individual nanocrystals in water suspension, and was not experimentally validated. Due to the lack of a reliable VSSA value, this powder cannot accurately be classified strictly as a nanomaterial according to the EU definition using this method.

This work focuses on particles specificities after dispersion in air. Further characterization, notably concerning the particle size distribution (PSD) of the dust cloud, are then required, and will be developed in section III.2.

III.1.3. Particle size distribution (PSD) of the powders

European standards stipulate that the dust sample should be tested as received, and that the particle size distribution 'shall be determined for the sample as tested and given in the test report' (EN 14034-1, 2004; EN 14034-2, 2006). However, no instruction is provided on the method to apply for this characterization. Since industries mainly have access to the data provided by wet dispersion, this method is the most commonly used to perform such measurements. Thus, the particle size distribution of wet samples was measured in ethanol using the Mastersizer 2000 S (Malvern Instruments) and is presented in Table 3-2. Due to the high ratio surface/volume of nanoparticles and the combustion reaction occurring at the surface of the particles depending on the reaction regime and the chemical nature, the surface fraction was considered instead of the 'usual' volume fraction when analyzing the particle size distribution of nanoparticles. Moreover, when considering the volume fraction, the high volume of big agglomerates tends to occult the presence of smaller nano-agglomerates. Thus, the volume fraction measured by the apparatus was converted into a surface fraction using the equivalent volume diameter.

It appears that the mean surface diameter obtained after wet dispersion is significantly higher than the size of the agglomerates observed by SEM (Figure 3-1 to 3-5 and Appendix 1). Indeed, the particle-particle interactions are greatly influenced by the dispersion medium, as explained in chapter 2 (section II.3.2), which means that for the same material, the PSD in air will be different from the PSD in water or ethanol. This influence is mainly visible on the carbon black and aluminum 100 nm, for which a mean size of agglomerates respectively reaching 333 and 286 µm were measured, despite the fact that smaller agglomerates were identified by SEM. A mean diameter of 17 µm is observed for the nanocellulose, which is considerably smaller than for the other powders. Indeed, during the dispersion of the powder in ethanol, some bonds formed during the powder drying after the hydrolysis step can be broken, which then reduces the agglomerates size in the powder. Despite its convenience, this method is of limited interest to evaluate the PSD in explosion conditions as the dispersion is performed in air.

Table 3-2 Mean surface diameter of the powders measured by wet dispersion and dry sedimentation

	Nano-cellulose	**Carbon black**	**Aluminum 40-60 nm**	**Aluminum 100 nm**	**Carbon-coated silicon**
Wet dispersion in ethanol (µm)	16.8	333	48.8	286	68.5
Dry sedimentation (µm)	48	31	22	37	30

In addition to these measurements, the PSD of the powders was measured in air using a laser diffraction sensor HELOS/KR-Vario (Sympatec GmbH). The PSD was characterized by sedimentation of the powders in the measuring area of this apparatus which was set to identify particles from 0.5 to 175 µm. Although this process was realized manually and may therefore

be questioned in terms of repeatability, it gives a good order of magnitude of the PSD of the dust cloud subjected to very low shear rates. The mean surface diameters of the powders measured using this method are then presented in Table 3-2. Once again, the powders appear agglomerated, with mean surface diameters between 20 and 50 µm, which is consistent with the size of the agglomerates observed by SEM. However, the dispersion process can break the agglomerates and thus modify the PSD of the powder after dispersion. The dust cloud characteristics are then investigated in the next section.

III.2. Dust cloud properties

III.2.1. Powders dustiness

As explained in chapter 2 (section II.2), the combustible dust must be dispersed to generate an explosion. During handling operations, dust can be liberated from the bulk powdered material when the aerodynamic forces acting on individual dust particles are greater than the forces maintaining the cohesiveness of the bulk material. The ability of a powder to release dust during handling is generally termed as "dustiness" (Liden, 2006) and is recognized as one of the key parameter affecting the deflagration index (Klippel et al., 2013).

Dustiness measurements were performed on carbon black and nanocellulose powders by the French National Research and Safety Institute for the Prevention of Occupational Accidents and Diseases (INRS) according to the vortex shaker method defined by EN 17199-5 (2019). The mass-based and the number-based dustiness indices in the respirable fraction, respectively expressed in milligrams of aerosol per kilogram of powder and in particles per milligram of powder were then estimated using an Electrical Low Pressure Impactor (ELPI) (Table 3-3). According to the classification regions defined by EN 15051 (2006) and compared to the values obtained by Dazon et al. (2017) on carbon nanotubes, the characterized powders show a low to moderate respirable dustiness index.

Table 3-3 Number and mass-based dustiness in the respirable fraction of carbon black and nanocellulose (experiments performed by INRS)

Powder	Dustiness in number (#/mg)	Dustiness in mass (mg/kg)
Carbon black	$1.67 \times 10^5 \pm 3.38 \times 10^4$	$4.33 \times 10^1 \pm 3.48 \times 10^1$
Nanocellulose	$4.00 \times 10^4 \pm 1.25 \times 10^4$	$1.58 \times 10^3 \pm 4.31 \times 10^2$

In addition to these measurements, the particle size distribution of the airborne particles was also estimated in the vortex shaker for the two powders (Figure 3-7). The carbon black powder dispersion presents fine particles around 105 nm, whereas nanocellulose exhibits a bimodal distribution, with 67% of the particles in the micro-range, around the mean value of 2.15 µm, and 33% in the nano-range, around 20 nm. Both powders then possess the ability to emit fine

and ultrafine particles when dispersed, and the presence of nanoparticles along with the agglomerates after dispersion has been confirmed. In particular, through the example of the nanocellulose, this study evidences the risks concerning powders not classified as nanomaterials according to the EU definition that can release nanocrystals when dispersed.

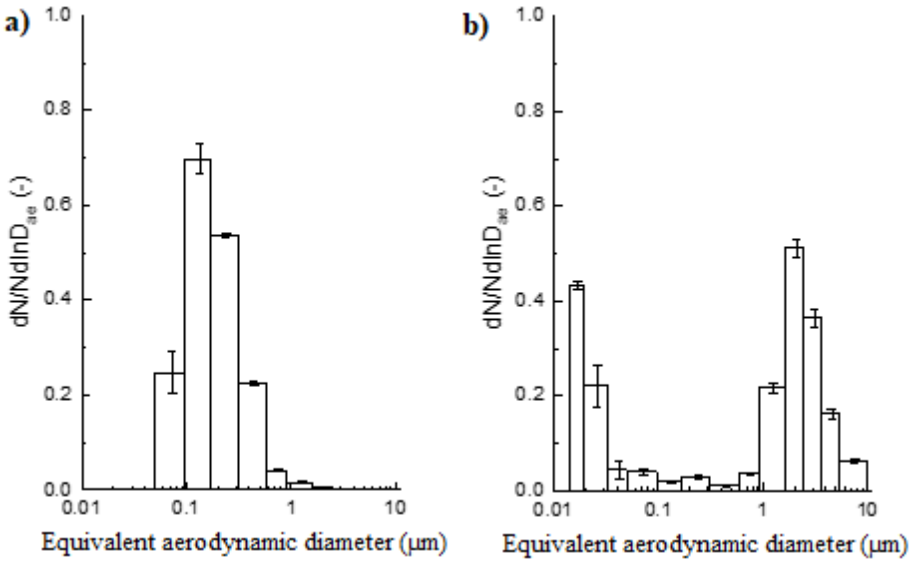

Figure 3-7 Histogram of the number granulometric distribution of aerosols emitted by the a) carbon black and b) nanocellulose by the vortex shaker method (experiments performed by INRS)

Another parameter, the dustability index, was introduced by Marmo et al. (2019) and considers the following properties: i) the dust tendency to disperse fine particles in air when handled, i.e. the dustiness ii) the dust tendency to settle in aggregates or fine particles iii) the dust behavior when lifted by an air blast. These authors then suggested that this dustability index is a key parameter affecting the dust explosivity by correlating it to the explosion index K_{St} (Di Benedetto et al., 2019). More specifically, preliminary results show that the K_{St} values increase with the dustability index (Marmo et al., 2019).

However, the dustiness and the PSD of the airborne particles are representative of the experimental conditions of the apparatus and cannot be scaled up directly to the flammability and explosivity test equipment which involves different level of mechanical stress energy. Thus, to accurately evaluate the influence of the characteristics of the dust cloud on its flammability and explosivity, measurements should be conducted in the same apparatuses.

III.2.2. Particle size distribution (PSD) of nanopowders clouds

To characterize the PSD of the dust during explosion tests, measurements were conducted after dispersion. However, no apparatus or technique currently allow the determination of particle size distributions over a range from 10 nm (primary particle) to 500 µm (agglomerates), at high frequency (each 1 millisecond or at least each 10 ms) and at high concentration (above the lower explosion limit). Thus, different techniques were combined.

III.2.2.1. Fast/Scanning Mobility Particle Sizer (FMPS/SMPS)

First, the presence of nanoparticles after dispersion of each powder in the 20L sphere, without ignition, was investigated using a Fast Mobility Particle Sizer (FMPS from INRS – S. Bau) measuring particles from 5.6 to 560 nm with 1 Hz time resolution and a Scanning Mobility Particle Sizer (SMPS– TSI) providing one measurement every two minutes. The dust dispersion follows the same procedure than during explosion tests, which is fully described in chapter 4, section IV.2: the weighted sample is placed in the dust container, and the sphere is evacuated at 0.4 bara. The container is then pressurized at 20 barg, and the electrovalve connecting the dust container and the 20L chamber opens, inducing the dispersion of the powder within the sphere. Despite the low frequency and mass concentration which prevent an accurate characterization, the presence of nanoparticles was observed even two minutes after dispersion, thus implying that nanoparticles were still present a few tens of milliseconds after dispersion (Figure 3-8) and confirming the results obtained by the Vortex Shaker method. However, the dispersion method, the observation time and physical principle of the measurement (electrical-mobility diameter) being different, the PSD cannot be quantitatively compared.

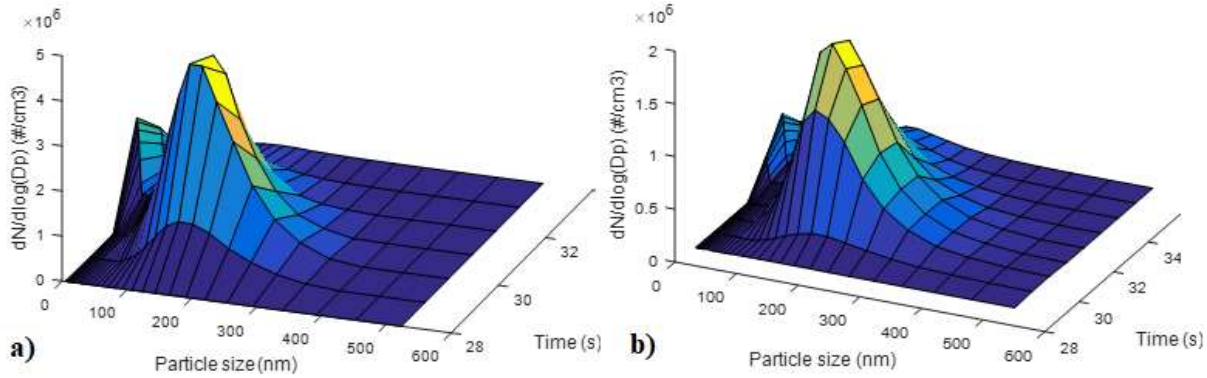

Figure 3-8 FMPS measurements of a) aluminum and b) nanocellulose powders

Although these apparatuses are commonly used to measure the particle size distribution of nanoparticles in air, the low measurement frequency compared to the ignition delay time, i.e. the delay between the dust dispersion and ignition, and the low mass concentration that can be tested make these equipment not adapted to the characterization of the PSD involved in explosion tests.

III.2.2.2. Dispersion in the Scirocco nozzle

Dry PSD measurements were also conducted using the Mastersizer 2000 particle size analyzer (Malvern Instruments) equipped with a dispersion system called Scirocco. The powder dispersion is ensured before the measurement by an air jet in a Venturi configuration (Ali et al., 2015; Bonakdar et al., 2016). Although this measurement is not conducted in the same conditions as the explosion tests, the evaluation of the particle size distribution after dispersion of the powder still provides information on the agglomerate breakage during the dispersion. Experiments were conducted on nanocellulose and carbon-coated silicon, and were previously

performed on the aluminum 40-60 nm and the aluminum 100 nm by Vignes et al. (2019) and Henry (2013) respectively. The mean surface and volume diameter of each powder measured using the Scirocco nozzle are presented in Table 3-4. This apparatus allows measurements of particles from 0.1 to 2000 µm, which implies that primary nanoparticles cannot be observed. Moreover, a clear difference appears between the mean volume diameter and the mean surface diameter, notably for the nanocellulose, which presents a mean surface diameter around 6 µm and a mean volume diameter of 20 µm, i.e. more than three times the mean surface diameter. This observation confirms that it is essential to consider the surface diameter instead of the volume diameter when characterizing nanoparticles, as the smallest particles are probably occulted by the high volume of the big agglomerates. However, these values are considerably lower than the values measured by dry sedimentation, proving that the nanoparticles are agglomerated. The partial breakage of the agglomerates then proves that the particle size distribution cannot be deduced only by the knowledge of the primary diameter, thus highlighting the importance of performing complementary characterization after dispersion.

Table 3-4 Mean surface and volume diameters after dry dispersion in the Scirocco nozzle

	Nanocellulose	**Aluminum 40-60 nm**	**Aluminum 100 nm**	**Carbon-coated silicon**
Dry sedimentation (µm)	48	22	37	30
Mean surface diameter (µm)	5.7	N/A	N/A	3.5
Mean volume diameter (µm)	20.1	6.2	4.9	7

III.2.2.3. Dispersion in the 20L sphere

An accurate characterization of the dust cloud requires a measurement in the explosion apparatus, at the moment and place of ignition. As explained in section III.2.2.1, the methods involving sampling are not adapted to such analysis due to a low frequency and a possible reagglomeration of the dust during the measurement. In situ high frequency measurements are accessible through the use of laser diffraction sensors, such as the particle size analyzer mentioned in section III.1.3 and used for the sedimentation measurements. However, such techniques require the visualization of the powder, and the standard 20L sphere used for explosion tests was initially conceived to remain rigid when undergoing explosion and is then not equipped with a visualization window big enough to allow optical measurements. This is the reason why Murillo (2016) developed a new dispersion vessel similar to the standard 20L sphere, which contains four lateral windows and another one on the top, made of borosilicate with a diameter of 9.7 cm (Figure 3-9).

Figure 3-9 Experimental set-up for the particle size distribution measurement in the visualization 20L sphere using the laser diffraction sensor (D'Amico, 2016)

The laser diffraction sensor HELOS/KR-Vario (Sympatec GmbH) previously used for sedimentation measurements, with 2000 Hz acquisition frequency and equipped with two lenses was used for in situ PSD determination. The first lens, called R1, allows measurements of particle sizes from 0.1 to 35 µm, but its low focal distance (2 cm) limits its use. Indeed, the particle size distribution must be determined at the center of the sphere, i.e. at the place of ignition, which is located around 8.5 cm away from the window. Thus, once again, this lens was mainly used to verify the presence of nanoparticles after dispersion.

The particle size distributions of the studied powders were estimated with the R1 lens at the moment of ignition, i.e. 60 ms after the beginning of the dispersion. For more reliability, the values obtained at 60 ± 5 ms were integrated, and the average values are presented in Figure 3-10. It then appears that the aluminum and carbon-coated silicon mainly exhibit fine particles smaller than 500 nm. The bimodal distribution of the nanocellulose previously identified in the vortex shaker appears one more time, centered on 900 nm and 5 µm. This shift with regard to the vortex shaker experiments can be explained by different dispersion conditions as well as different measuring devices, using different techniques and providing different size ranges. Furthermore, the ELPI system measures the aerodynamic diameter whereas the laser sensor gives access to optical diameters, which implies different physical principles. The carbon black powder, which shows agglomerates around 3 µm, seems more agglomerated than the other powders.

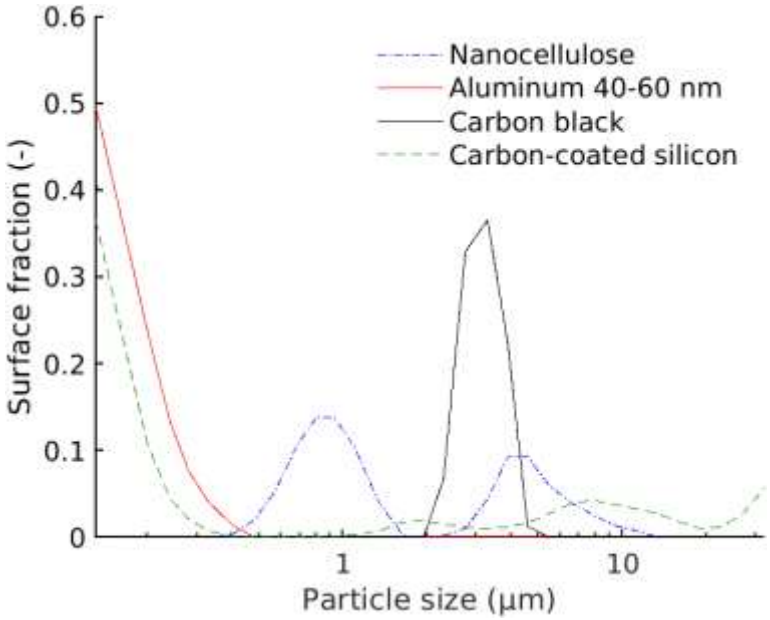

Figure 3-10 Particle size distribution of the powders measured by laser diffraction at the moment of ignition (R1 lens)

Another lens of the laser diffraction sensor was mainly used for particle size distribution measurements, as its focal distance is 10 cm. This 'R3 lens' allows the measurement of particles ranging from 0.5 to 175 µm, but it does not provide information on the presence of nanoparticles. However, the measured values correspond to the ignition location, which gives valuable information on the effect of the PSD on the explosion severity. Moreover, the fragmentation of the agglomerates can be estimated measuring the PSD before and after dispersion. The particle size distributions measured with the R3 lens at the time of ignition, with the same integration method (± 5 ms) than with the R1 lens, are presented in Figure 3-11.

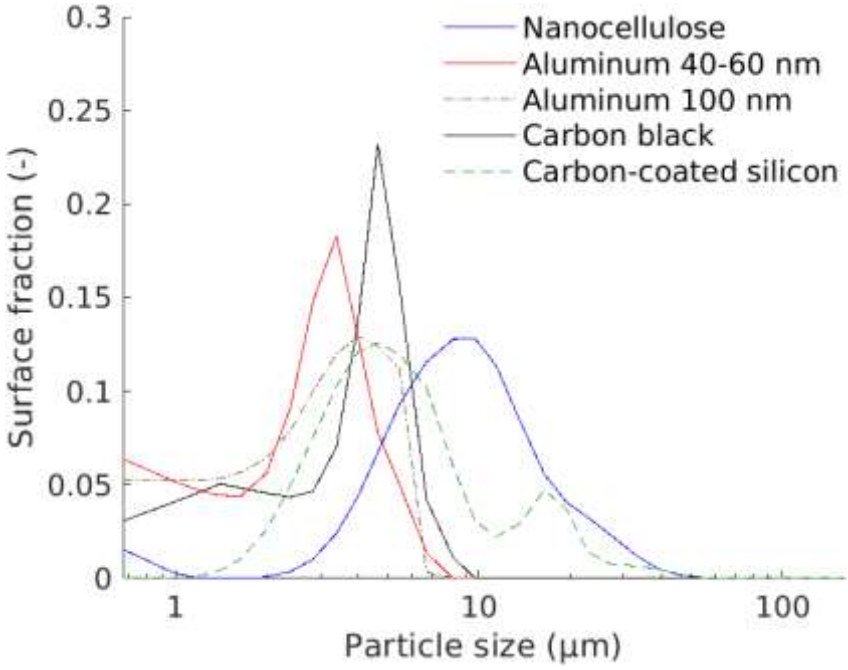

Figure 3-11 Particle size distribution of the studied powders measured by R3 lens

The carbon black still presents the agglomerates around 4 µm as well as smaller agglomerates not visible with the R1 lens. Both aluminum powders contain agglomerates ranging from 6 µm to less than 1 µm, which tends to suggest that they are the less cohesive powders. Finally, the carbon-coated silicon shows the bimodal distribution already slightly visible in Figure 3-10 centered around 4 and 11 µm. The second peak of nanocellulose now appears around 9 µm instead of 5 µm, due to the variation of measurement location. Indeed, this value was estimated at the center of the sphere whereas it was determined close to the window with the R1 lens. Moreover, the inherent heterogeneities due to the dust dispersion within the sphere and the initial turbulence also impact the PSD and the dust cloud behavior.

III.2.3. Initial turbulence

The initial turbulence, i.e. the turbulence level in the equipment before the ignition, was evaluated by Particle Image Velocimetry (PIV) according to the method and setup described by Vizcaya et al. (2018) and presented in Figure 3-12. A laser sheet (RayPower 2000 CW Dantex Dynamics) that illuminates the region of interest was coupled with a high-speed video camera (Phantom V91) that records the particle flow. The laser was set at 1.5W while the camera was configured with a resolution of 480 x 480 pixels, 6400 fps and a time-lapse of 150 µs. Video analyses were then realized with PIVLAB 1.35, an open source code working as a Matlab toolbox.

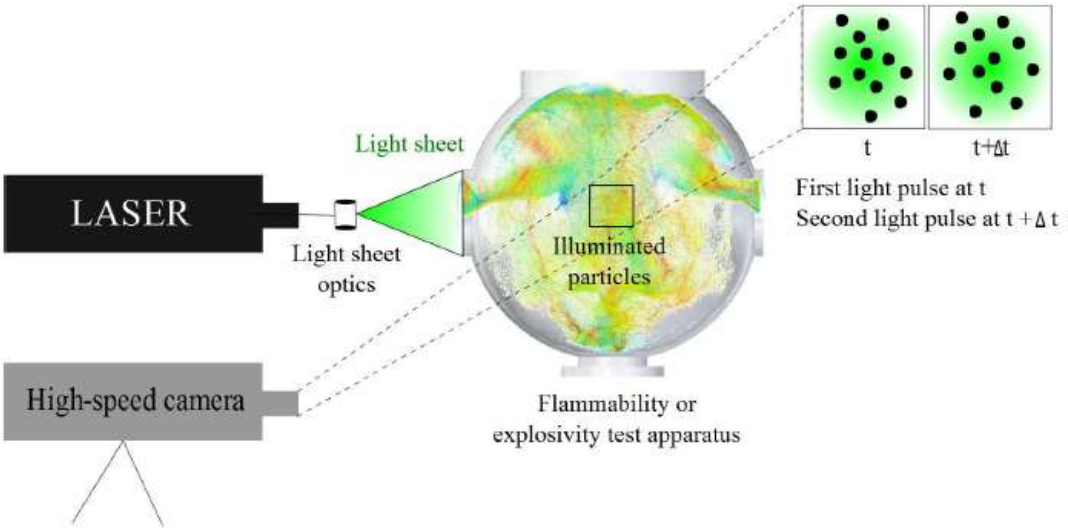

Figure 3-12 Experimental arrangement for Particle Image Velocimetry analyses - from Vizcaya et al. (2018)

Due to the high cost and multimodal particle size distribution of nanoparticles, starch particles of diameter around 10 µm were used as they are big enough to be observed, and small enough to not disturb the turbulent flow. Indeed, a relaxation time can be calculated from Stoke's drag law, as follows:

$$\tau_s = {d_p}^2 \frac{(\rho_p - \rho_{air})}{18\,\mu} \qquad 3\text{-}3$$

A value of 0.2 ms was determined for the starch powder, meaning that 0.2 ms after the dispersion, the starch dust follows the turbulent flow. Since the aim of the experiments is to evaluate the turbulence several dozens of milliseconds after the dispersion, this dust can be considered as a tracer of the flow. Moreover, after dispersion, all the studied nanopowders exhibit mean diameters lower or equal to 10 µm, inducing their relaxation time is lower than 0.2 ms and confirming that they follow the flow without influencing it.

By analyzing the movement of the particles between two images, a root-mean square velocity was then estimated for each couple of images. To improve the visibility of the results, the values were integrated every 5 ms, and the average values are presented in Figure 3-13. With regard to the time evolution of the flow turbulence, three stages can be identified: from 0 to 40 ms, the bulk of the dust cloud is characterized by a high turbulence; from 40 to 120 ms: a 'transition' stage characterized by a decrease of the fluctuations; 120 ms or more: a 'stability stage (Murillo et al., 2018). Then, it appears that the fixed ignition delay time of 60 ms is located in the transition stage, meaning a small variation in the ignition delay time can greatly impact the turbulence level, and thus the explosion severity. This influence will be further discussed in chapter 5, section V.6.

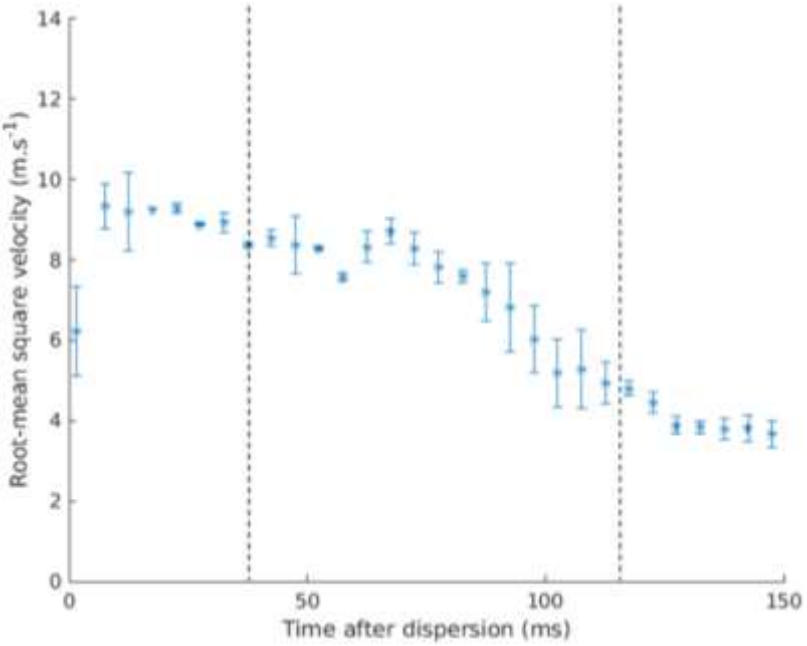

Figure 3-13 Evolution of the root-mean square velocity with time after dispersion

The breakage of the agglomerates constituting the powders during the dispersion in the 20L was then investigated through the measurements of the PSD before and after dispersion. However, as previously mentioned, no apparatus currently allows the measurement in the nanorange at high frequency and high concentration. An experimental evaluation of the PSD as a function of the dispersion conditions is then difficult. To overcome this issue, a semi-empiric correlation relating a fragmentation efficiency coefficient, i.e. the ratio between the mean surface diameter before and after dispersion, to the operating parameters and powders characteristics was developed in section III.3. through a dimensional analysis.

III.3. Dimensional analysis of dust dispersion

The dispersion in air (ρ_{air}, μ_{air}) of a powder whose characteristics are its density ρ_p, its initial mean surface diameter d_{agg} and the surface energy of its agglomerates ϕ, in a vessel in specific conditions (L_{car}, V_{ej}, u_{rms}) was considered, with the aim of estimating the mean surface diameter of the dust cloud after dispersion in the vessel (d_{50}). The parameters considered for the dimensional analysis are indexed in Table 3-5. Thus, 9 parameters are identified, implying 3 different dimensions. According to Vaschy-Buckingham theorem (Buckingham, 1914), the dust dispersion phenomenon can be described by 9 - 3 = 6 independent dimensionless numbers that can be related through a single correlation.

Table 3-5 Parameters considered for the dimensional analysis of dust dispersion

Notation	Definition	SI units	Dimension
L_{car}	Characteristic length of the dispersion vessel	m	L
V_{ej}	Ejection velocity of the powder	$m.s^{-1}$	$L.T^{-1}$
μ_{air}	Dynamic viscosity of air	Pa.s	$M.L^{-1}.T^{-1}$
ρ_{air}	Air density	$kg.m^{-3}$	$M.L^{-3}$
ρ_P	Bulk density	$kg.m^{-3}$	$M.L^{-3}$
u_{rms}	Turbulence level in the vessel	$m.s^{-1}$	$L.T^{-1}$
ϕ	Surface energy of agglomerates	$N.m^{-1}$	$M.T^{-2}$
d_{agg}	Mean surface diameter of agglomerates before dispersion	m	L
d_{50}	Mean surface diameter of agglomerates after dispersion	m	L

III.3.1. Determination of the dimensionless numbers

Three basic parameters which contain the three units, d_{50}, V_{ej} and μ_{air}, were chosen, and the remaining six parameters were then coupled to these basic parameters to define the dimensionless numbers, according to the following relation:

$$\pi_1 = \frac{\rho_{air}}{{d_{50}}^a {V_{ej}}^b {\mu_{air}}^c} \qquad 3\text{-}4$$

To obtain a dimensionless number π_1, conditions on the coefficients a, b and c must be verified:

For dimension M: 1 = c

For dimension L: -3 = a + b – c

For dimension T: 0 = - b – c

The dimensionless number π_1 can then be expressed as follows:

$$\pi_1 = \frac{\rho_{air}\, d_{50}\, V_{ej}}{\mu_{air}} \quad 3\text{-}5$$

A similar analysis led to the determination of the following dimensionless numbers:

$$\pi_2 = \frac{L_{car}}{d_{50}} \quad 3\text{-}6$$

$$\pi_3 = \frac{\rho_p\, d_{50}\, V_{ej}}{\mu_{air}} \quad 3\text{-}7$$

$$\pi_4 = \frac{u_{rms}}{V_{ej}} \quad 3\text{-}8$$

$$\pi_5 = \frac{d_{agg}}{d_{50}} \quad 3\text{-}9$$

$$\pi_6 = \frac{\phi}{V_{ej}\, \mu_{air}} \quad 3\text{-}10$$

To evaluate the physical meaning of those numbers, a comparison with existing dimensionless numbers was realized. The particle Reynolds number Re_p, represented by the ratio of agglomerate inertial forces and viscous forces, can then be recognized in π_1:

$$Re_p = \frac{\rho_{air}\, d_{50}\, V_{ej}}{\mu_{air}} = \pi_1 \quad 3\text{-}11$$

On a similar way, a combination between π_1 and π_2 leads to a Reynolds number of the flow:

$$Re = \frac{\rho_{air}\, L_{car}\, V_{ej}}{\mu_{air}} = \pi_1\, \pi_2 \quad 3\text{-}12$$

The Stokes number, which compares the inertial forces to the fluid driving forces, can also be identified through a combination between π_2, π_3 and π_4, and represents:

$$St = \frac{\rho_p\, {d_{50}}^2\, u_{rms}}{18\, \mu_{air}\, L_c} = \frac{\pi_3\, \pi_4}{\pi_2} \quad 3\text{-}13$$

Finally, the Weber number We is generally used to compare the inertial forces to the surface tension of droplets. However, different definitions of this number for agglomerates can be found in the literature (Bonakdar and Ghadiri, 2017; Calvert et al., 2013) based on the extension of classic We number taking into account a surface energy of the agglomerates based on the cohesive forces. In this work, the Weber number is defined as follows:

$$We = \frac{\rho_p\, d_{agg}\, {V_{ej}}^2}{\phi} = \frac{\pi_3 \pi_5}{\pi_6} \quad 3\text{-}14$$

The surface energy of an agglomerate ϕ can be experimentally evaluated by Atomic Force Microscopy (AFM). In this study, a virtual surface tension was considered and calculated according to the following relation (Wengeler and Nirschl, 2007):

$$\phi = \sigma_{agg}\, d_{agg} \quad 3\text{-}15$$

The cohesion strength of the agglomerate was calculated based on the model established by Weiler et al. (2010) previously explained in chapter 2, section II.3.3.3, and by considering that the main cohesion forces can be represented by van der Waals interactions. The following equation was then used to estimate the cohesion strength:

$$\sigma_{agg} = \frac{(1-\varepsilon)}{2\, d_{agg}\, \varepsilon} . \frac{A\, d_P}{24\, {h_p}^2} . \left(\frac{{d_{agg}}^3}{{d_P}^3} - 4\, \frac{\left(1 - \frac{\arccos\left(\frac{d_P}{d_{agg}-d_P}\right)}{180^\circ}\right)}{\frac{d_P}{d_{agg}-d_P}} \right) \qquad 3\text{-}16$$

The final dimensionless numbers chosen to characterize the dust dispersion are presented in Table 3-6. A correlation relating the different parameters using coefficients α_0 to α_5 to determine can then be developed:

$$Re_p = \alpha_0\, Re^{\alpha_1}\, St^{\alpha_2}\, We^{\alpha_3}\, {\pi_4}^{\alpha_4}\, {\pi_5}^{\alpha_5} \qquad 3\text{-}17$$

Table 3-6 Expression and physical meaning of the dimensionless number characterizing the dust dispersion phenomenon

Dimensionless number	Expression	Physical meaning
Re	$\frac{\rho_{air}\, L_{car}\, V_{ej}}{\mu_{air}}$	Ratio of fluid inertial forces and viscous forces
Re_p	$\frac{\rho_{air}\, d_{50}\, V_{ej}}{\mu_{air}}$	Ratio of agglomerate inertial forces and viscous forces
St	$\frac{\rho_p\, {d_{50}}^2\, u_{rms}}{18\, \mu_{air}\, L_c}$	Ratio of agglomerate inertial forces and fluid driving forces
We	$\frac{\rho_p\, {V_{ej}}^2\, d_{agg}}{\phi}$	Ratio of the dynamic forces and the surface energy of the agglomerate
π_4	$\frac{u_{rms}}{V_{ej}}$	Ejection shear stress coefficient
π_5	$\frac{d_{agg}}{d_{50}}$	Agglomerate fragmentation efficiency

III.3.2. Proposal of a correlation describing the dispersion of an agglomerated powder

To estimate the coefficient α_0 to α_5, each dimensionless number was evaluated through the determination of each considered parameter for each powder. The mean surface diameter before dispersion was estimated by sedimentation of the powder and the mean surface diameter after dispersion was determined in the 20L sphere using the Sympatec laser diffraction sensor. All the considered parameters for the determination of the dimensionless numbers are presented in Table 3-7.

Since the validity of the correlation will afterwards be verified on three mechanically agglomerated samples of carbon-coated silicon (SiΩC) supplied by Nanomakers, their properties are then also presented in Table 3-7. These samples are constituted of the same powder than that previously presented, with different densities, agglomerates sizes and cohesion strength. Two powders were agglomerated according to a process noted 'process A' with densities of 260 $g.L^{-1}$ and 400 $g.L^{-1}$, and will be noted respectively A1 and A2, and a powder was agglomerated according to a 'process B' with a density of 400 $g.L^{-1}$ and will be simply noted B. The experiments conducted on these samples to evaluate the influence of the agglomeration of the explosion severity are fully detailed in chapter 5, section V.1.

Table 3-7 Operating conditions and powder characteristics for the determination of the dimensionless numbers defining the dust dispersion

Operating conditions during the dispersion in the 20L sphere

ρ_{air} ($kg.m^{-3}$)	μ_{air} (Pa.s)	L_{car} (m)	V_{ej} ($m.s^{-1}$)	u_{rms} ($m.s^{-1}$)
1.2	1.85×10^{-5}	0.010	200	10

Characteristics of the powders before and after dispersion

	$\rho_{p,app}$ ($kg.m^{-3}$)	d_{agg} (µm)	d_{50} (µm)	d_p (nm)	F_{VdW} (N)	σ_{agg} (Pa)	ϕ ($N.m^{-1}$)
Nanocellulose	700	48	10	7.2	4.3×10^{-12}	2.3×10^{8}	1.1×10^{4}
Carbon black	380	31	4.7	75	2.0×10^{-10}	1.8×10^{6}	5.6×10^{1}
Aluminum (100 nm)	190	37	3.0	100	2.7×10^{-10}	3.6×10^{5}	1.3×10^{1}
Aluminum (40-60 nm)	190	22	2.7	50	1.3×10^{-10}	8.9×10^{5}	1.9×10^{1}
SiΩC – Raw powder	40	30	7.0	40	1.0×10^{-10}	4.2×10^{5}	1.3×10^{1}
SiΩC – Sample B	400	20	1.8	40	1.0×10^{-10}	3.5×10^{6}	6.9×10^{1}
SiΩC – Sample A1	260	26	1.9	40	1.0×10^{-10}	2.6×10^{6}	6.8×10^{1}
SiΩC – Sample A2	400	32	0.7	40	1.0×10^{-10}	4.9×10^{6}	1.6×10^{1}

The standard dispersion in the 20L sphere was considered, i.e. at atmospheric pressure and ambient temperature. Moreover, the ejection speed, the root-mean square velocity and the integral length scale were respectively taken from Murillo (2016), Dahoe et al. (2001) and Pu

et al. (1991). Similar mean surface diameters were measured, from 20 to 48 µm before dispersion, and from 1 to 10 µm after dispersion in the 20L sphere. To calculate the van der Waals forces acting on each powder, the Hamaker constant presented in chapter 2 (Table 2-4) were used, and an interparticle distance of 2 nm was considered. Since nanocellulose is constituted of fibers, an equivalent surface diameter was calculated. It then appears that the van der Waals forces are of the same order of magnitude for all the samples except for nanocellulose, due to its lower primary diameter. However, this was compensated by the high mean surface diameter measured by sedimentation, leading to a strong cohesion of the agglomerates, reaching $2.3x10^8$ Pa while the other powders exhibit cohesion strength between $3x10^5$ and $5x10^6$ Pa, which is consistent with the values mentioned by Weiler et al. (2010).

The values of the dimensionless numbers can be estimated from the operating conditions and characteristics of the different powders (Table 3-8). Among the chosen numbers, two numbers only depend on the operating conditions and are thus constant for each powder: Re and π_4. The Reynolds number, in particular, is equal to 10^5, which confirms the turbulent condition in the 20L sphere at the moment of dispersion. Since the mean volume diameters before dispersion were rather similar, the particle Reynolds numbers are also similar, with a variation from 9 to 61, except for the nanocellulose and the raw carbon-coated silicon due to their higher means surface diameter after dispersion.

More differences are observed when calculating the Stokes number, as it includes the powder density in addition to the mean diameter after dispersion. Indeed, the highest value is obtained for the nanocellulose, which is the densest powder, while the lowest value is observed for the raw carbon-coated silicon, which exhibits a very low density with regard to the other powders. However, it should be noted that all the values are lower than 1, implying that all the particles follow the flow in the 20L sphere. The Weber numbers are generally ranging from 3 to 8, except for the nanocellulose and the aluminum 100 nm. Indeed, the nanocellulose exhibits very high surface energy compared to the other powder, which explains the low value of the Weber number. On the contrary, the aluminum 100 nm presents a high mean surface diameter before dispersion and the lowest value of surface energy, inducing an easiest fragmentation of agglomerates.

The number π_5, characterizing the agglomerates fragmentation, lies between 4 and 14. Such values traduce a strong fragmentation during the dispersion in the 20L sphere, which can be due to the shear stress occurring during the pressurization in the dust canister, to the passage through the nozzle and to the wall impacts. However, the laser diffraction sensor only measures particles ranging from 0.5 to 175 µm, implying that the fragmentation can be even stronger, as highlighted by the sample A2 of carbon-coated silicon.

Table 3-8 Dimensionless number calculated for each powder during the dispersion in the 20L sphere

	Re	Re_p	St	We	π_4	π_5	ΔD (%)
Nanocellulose	1.3×10^5	135	2.3×10^{-1}	0.12	0.05	4.6	78
Carbon black	1.3×10^5	61	2.5×10^{-2}	8.3	0.05	6.60	85
Aluminum (100 nm)	1.3×10^5	39	5.1×10^{-3}	21.0	0.05	12.3	92
Aluminum (40-60 nm)	1.3×10^5	17.5	4.2×10^{-3}	8.5	0.05	8.06	88
SiΩC – Raw powder	1.3×10^5	91	5.9×10^{-3}	3.8	0.05	4.3	77
SiΩC – Sample B	1.3×10^5	23	3.9×10^{-3}	4.6	0.05	11.1	91
SiΩC – Sample A1	1.3×10^5	25	2.8×10^{-3}	4.0	0.05	13.7	93
SiΩC –Sample A2	1.3×10^5	9	5.9×10^{-4}	3.2	0.05	45.7	98

A mechanistic model of impact attrition notably highlighted the influence of the particle density, the impact velocity and the particle size, but also of the agglomerate hardness and the fracture toughness on the extent of breakage (Ghadiri and Zhang, 2002; Zhang and Ghadiri, 2002). Moreover, a mode diameter variation defined by $\Delta D = 100\ (d_{agg} - d_{50})/d_{agg}$ was calculated by Sanchirico et al. (2015), who classified the powders in two classes: class 1 containing the hardest dusts ($\Delta D < 50\%$) and class 2 for the ones that undergo a higher breakage ($\Delta D > 50\%$). Values between 77% and 98% were obtained in this work, implying that all the powders are in class 2. Furthermore, those values are slightly higher than the ones presented by Sanchirico et al. (2015). First, it should be noted that the diameter after dispersion was measured by Sanchirico et al. (2015) by collecting the settled dust several minutes after the dispersion, which allows the re-agglomeration of the powder, whereas the measurements in this work were conducted directly within the sphere and correspond to the moment and place of ignition. Then, these higher values can be attributed to weak bonding implied in the agglomeration phenomenon which leads to the formation of relatively easily breakable agglomerates.

Using the calculated dimensionless numbers presented in Table 3-8, the coefficients α_0 to α_5 of the relation 3-17 were estimated and are presented in Table 3-9. First, the coefficient α_0 appears to be close to unity, inducing a nearly proportional relation between the dimensionless numbers elevated at the right power. Then, from the expression of the agglomerate fragmentation efficiency π_5, it can be deduced that positive coefficients imply that high values of the affected

dimensionless numbers tend to increase the agglomerate breakage, i.e. decrease the particle size after dispersion. Nevertheless, since the Reynolds number and π_4 are constant for all the powders, their influence on the fragmentation cannot be analyzed by this dimensional analysis. The coefficient α_2 and α_3 are significantly lower than unity, inducing that the influence of the Stokes and Weber numbers on the dust dispersion can be neglected. More specifically, the extreme values of the Weber number obtained for the nanocellulose and the aluminum 100 nm induced a very small coefficient attributed to this number to stabilize the system. Finally, since the particle Reynolds number increases with the size of the agglomerates, a high value traduces a weak fragmentation of the agglomerates, which is represented by the negative sign of its coefficient. The correlation was then validated by calculating the mean diameter after dispersion for each considered powder and for the agglomerated SiΩC powders.

Table 3-9 Correlation coefficients related to the dust dispersion in the 20L sphere

$$\pi_5 = \alpha_0 \, Re^{\alpha_1} \, St^{\alpha_2} \, We^{\alpha_3} \, {\pi_4}^{\alpha_4} \, {Re_p}^{\alpha_5}$$

α_0	α_1	α_2	α_3	α_4	α_5
0.91	0.47	0.12	0.04	0.19	-0.62

III.3.3. Validation of the correlation

The mean volume diameter of each powder was calculated using the equation 3-17 with the coefficients presented in Table 3-9 and compared to the measured mean diameter. A good agreement between the correlation and the experiments appears in Figure 3-14, as the correlation always provides a mean volume diameter of the same order of magnitude than the measured one. Moreover, most of the values are included in the space defined by the red spotted lines, representing an uncertainty of 15%, except for the sample A1 of carbon-coated silicon and aluminum 100 nm for which errors of 49% and 52% are respectively observed, and for the sample A2 of carbon-coated silicon. In this case, a mean surface diameter of 0.7 µm was measured using the laser diffraction sensor whereas a diameter of 4.8 µm was calculated with the correlation. Since these three powders exhibit the highest values of π_5, the differences between the correlation and the experiments may come from a strong fragmentation not accurately represented by the model. To overcome this issue and accurately estimate the fragmentation in the 20L sphere, dispersion tests should be conducted with more powders of different nature and the measurements should be performed with an apparatus capable of measuring the nanoparticles dispersed at high concentration and frequency. Moreover, it would be interesting to consider not only the mean surface diameter, but the whole PSD after choosing the right metrics.

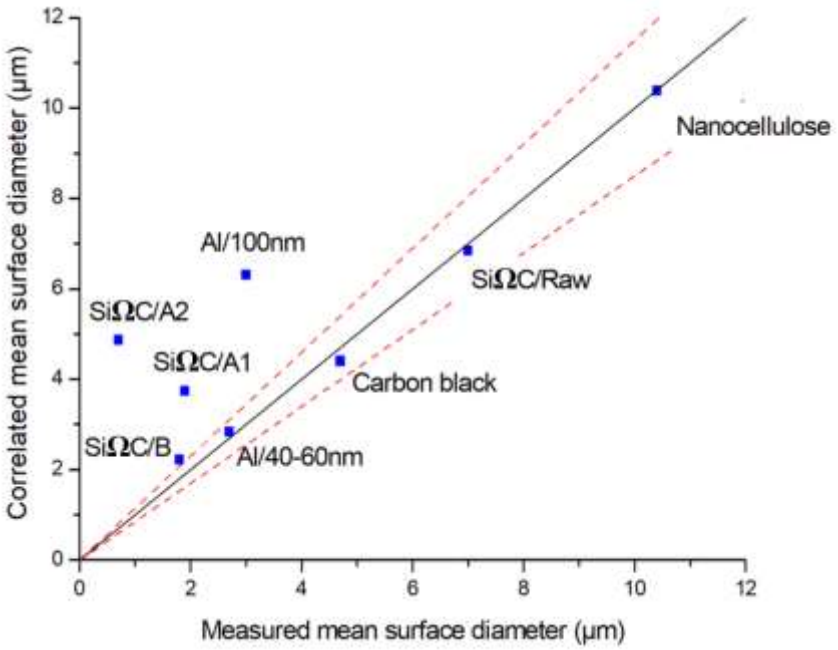

Figure 3-14 Comparison between the measured and correlated mean surface diameters after dispersion in the 20L sphere

Since this correlation is based on measurements conducted during the dispersion in the 20L sphere using the R3 lens of the laser diffraction sensor, its application is limited to these conditions. Thus, applying this correlation to the results obtained using the Scirocco would be inaccurate, due to a different dispersion process and a different measuring range. Considering the high values of fragmentation efficiency measured, it appears that the dispersion in the 20L sphere leads to significant changes in the particle size distribution, notably due to the agglomeration phenomenon.

Thus, care must be taken when analyzing the experiments conducted in the 20L sphere. Indeed, if the aim is to consider the worst-case scenario, which probably corresponds to the strongest fragmentation, the dispersion procedure of the 20L sphere is adapted. However, the process safety engineer, when extrapolating the results to industrial conditions, must imperatively keep the PSD difference in mind.

Summary

This chapter was dedicated to the characterization of powders and related dust clouds. It was divided into three main parts.

First, a presentation of the powders considered in this work was realized: nanocellulose, carbon black, carbon-coated silicon and two aluminum powders. A classification method based on the calculation of the volume-specific surface area and on image analysis was applied to verify that the powders can be considered as nanomaterials according to the European Commission definition. Except for the nanocellulose, for which further tests were performed thereafter, all powders are classified as nanomaterials. Particle size distribution (PSD) tests were performed in wet dispersion, which is convenient but of limited interest when testing dust dispersed in air, and by dry sedimentation, to estimate the PSD of agglomerates submitted to low shear stress. The presence of micro-agglomerates constituted of the individual nanoparticles was then evidenced.

Since dust explosions require the dispersion of the powder, PSD measurements were also conducted after dispersion. First, the dustiness, i.e. the ability of a powder to release fine particles, was measured for carbon black and nanocellulose, showing that both powders can release nanoparticles. PSD measurements were conducted using a Fast Mobility Particle Sizer (FMPS) and a Scanning Mobility Particle Sizer (SMPS) and highlighted the presence of nanoparticles even two minutes after dispersion. Dispersion tests were also performed using a Scirocco device, showing the partial breakage of the agglomerates after dispersion of the dust. Finally, an in-situ laser diffraction sensor was coupled to a visualization 20L sphere to estimate the PSD within the combustion chamber, at the moment and place of ignition. A clear difference then appeared between the mean diameters measured by sedimentation and the diameters measured after dispersion, due to the high shear stress occurring during the dispersion process. The dust cloud is then constituted of micro- and nano-agglomerates. Therefore, the consideration of the PSD not only before dispersion, but also after injection in the apparatus is essential when testing nanoparticles explosion severity in order to know exactly what explodes. In addition to these tests, the evolution turbulence level with time after the dispersion of the dust in the 20L sphere was evaluated through Particle Image Velocimetry and highlighted that the standard ignition delay time is located in a transient zone. This implies that a small variation of ignition delay time can significantly modify the turbulence level, and thus the explosion severity.

However, such measurements can hardly be conducted due to the opacity of the original 20L sphere and to a technique limitation: currently, no apparatus allows the measurements of nanoparticles at high frequency and high concentration. Thus, a semi-empiric correlation relating the operating parameters and powders characteristics to a fragmentation efficiency coefficient, defined as the ratio between the mean surface diameter before and after dispersion, was proposed and showed encouraging results.

Résumé

Ce chapitre est dédié à la caractérisation des poudres et des nuages associés et divisé en trois parties.

D'abord, une présentation des poudres considérées dans ce travail a été réalisée : nanocellulose, noirs de carbone, silicium enrobé de carbone et deux poudres d'aluminium. Une méthode de classification basée sur le calcul d'une surface spécifique volumique couplée à une analyse d'image a été appliquée pour vérifier que les poudres peuvent être considérées comme des nanomatériaux selon la définition de la Commission Européenne. A l'exception de la nanocellulose, pour laquelle des tests complémentaires ont été réalisés par la suite, toutes les poudres étudiées sont classifiées en tant que nanomatériaux. Des mesures de distribution de tailles de particules (DTP) ont été réalisées en voie liquide, ce qui est pratique mais d'un intérêt limité quand il s'agit de tester des poudres dispersées dans l'air, ainsi que par sédimentation en voie sèche afin d'estimer la DTP des agglomérats soumis à un faible cisaillement. La présence de micro-agglomérats constitués de nanoparticules a alors été mise en avant.

Puisqu'une explosion de poussière nécessite la dispersion de la poudre, des mesures de DTP ont également été conduites après dispersion. D'abord, la pulvérulence du noir de carbone et de la nanocellulose a été mesurée, démontrant la capacité des deux poudres à émettre des nanoparticules. Des mesures de DTP ont été réalisées à l'aide d'un Fast Mobility Particle Sizer (FMPS) et d'un Scanning Mobility Particle Sizer (SMPS) et ont démontré la présence de nanoparticules jusqu'à deux minutes après dispersion. Des essais de dispersion ont aussi été conduits à l'aide d'un disperseur Scirocco et ont montré la fragmentation des agglomérats lors de la dispersion. Enfin, un granulomètre à diffraction laser couplé à une sphère de visualisation de 20L ont permis une estimation in situ de la DTP dans la chambre de combustion, au moment et à l'endroit de l'inflammation. Une différence nette est alors apparue entre les diamètres moyens mesurés par sédimentation et les diamètres mesurés après dispersion, à cause du fort cisaillement induit par le processus de dispersion. Le nuage est ainsi constitué de nano- et de micro-agglomérats. Ainsi, la considération de la DTP avant dispersion, mais aussi après injection dans l'enceinte est essentielle lors de l'évaluation de la sévérité d'explosion des nanoparticules afin de savoir exactement ce qui explose. L'évolution du niveau de turbulence avec le temps après dispersion de la poudre dans la sphère de 20L a également été évaluée par Particle Image Velocimetry (PIV). Le délai d'inflammation préconisé par les standards internationaux se situant dans une zone de transition, une faible variation dans ce délai peut fortement modifier le niveau de turbulence, et ainsi la sévérité d'explosion de la poudre.

Cependant, la caractérisation visuelle du nuage de poussières ne peut être systématiquement effectuée à cause de l'opacité de la sphère standard et d'une limitation technique : actuellement, aucun appareil ne permet la mesure de nanoparticules à haute fréquence et forte concentration. Ainsi, une corrélation semi-empirique reliant les conditions opératoires et les caractéristiques de la poudre à un coefficient d'efficacité de fragmentation, défini par le ratio entre le diamètre moyen en surface avant et après dispersion, a été proposée et a montré des résultats encourageants.

Chapter 4:
Standard evaluation of flammability and explosivity

Now that the particle size distribution of each powder was measured before and after dispersion, the process safety engineer is interested in the evaluation of the standard safety parameters. Thus, this chapter, dedicated to their determination, is divided into three parts. First, the standard methods to measure the ignition sensitivity parameters, i.e. the minimum ignition energy, the minimum ignition temperature and the lower explosion limit, are detailed, and the values obtained for each powder are presented and discussed. This part also contains a dimensional analysis describing the dust ignition phenomenon, which is useful to identify the most influential parameters on ignition sensitivity. The second part focuses on the explosion severity of the powders, through a presentation of the standard methods for the evaluation of the maximum overpressure and the maximum rate of pressure rise and a discussion about the values obtained for the chosen powders. The last part of this chapter is dedicated to the observations realized during the tests and to a questioning of the validity of the international standards, originally designed for micropowders, when it comes to the evaluation of the flammability and explosivity of nanopowders.

IV.1. Ignition sensitivity

The ignition sensitivity of the powders was evaluated through the determination of the minimum ignition energy, minimum ignition temperature and the lower explosion limit. Since only dust clouds are considered in this thesis, the minimum ignition temperature of the layer was not measured. Moreover, all the experiments being performed in atmospheric conditions, the limiting oxygen concentration was not investigated in this work either. First, each measurement method is detailed, and the standard values obtained for each powder are then presented in section IV.1.4.

IV.1.1. Minimum Ignition Energy

As mentioned in chapter 2, the Minimum Ignition Energy (MIE) of a dust cloud is the lowest energy that can ignite the dust-air mixture under specific test conditions. It is generally measured in a modified Hartmann tube, also called Mike 3, according to international standards (ASTM E2019-03, 2007; ISO/IEC 80079-20-2, 2016). This apparatus, produced by TÜV SÜD Schweiz AG and Cesana-AG and presented in Figure 4-1, is constituted of a 1.2 liters vertical tube coupled to an ignition system. The ignition source consists of two electrodes separated by 6 to 8 mm, connected to a discharge circuit constituted of an adaptable inductance from 1 to 2 mH and several capacitors able to provide different amounts of energy. Thus, the electrodes can deliver energies from 1 mJ to 1000 mJ, with discrete values of 1, 3, 10, 30, 100, 300 and 1000 mJ.

The test procedure consists in placing a weighted dust sample at the bottom of the tube and to disperse it within the tube using a pulse of compressed air at 7 barg. The ignition sources are then activated after a delay, called ignition delay time, set before the beginning of the test. If a flame propagation is observed within the dust cloud, the ignition test is considered positive. Otherwise, tests must be performed 10 times in the same conditions to ensure that no ignition was observed in those conditions.

In addition to the previously described elements constituting the setup, a mushroom-shaped nozzle is used to control the distribution of both the air and the dust in the vertical tube. It is thus assumed that the dust cloud is homogeneous during the ignition. However, since this hypothesis may not be valid due to segregation phenomenon (in case of agglomeration or for samples with large PSD) or depending on the dispersibility of the dust, experiments must be conducted in different conditions. Therefore, in addition to the variation of the ignition energy and the dust concentration, the ignition delay time, i.e. the delay between the dust dispersion and the ignition, must also be modified in order to consider the influence of the turbulence on the properties of the dust cloud.

The concentration is then modified to guarantee that the minimum ignition energy will be measured at the most ignition sensitive concentration, usually corresponding to a concentration slightly greater than the theoretical stoichiometric concentration.

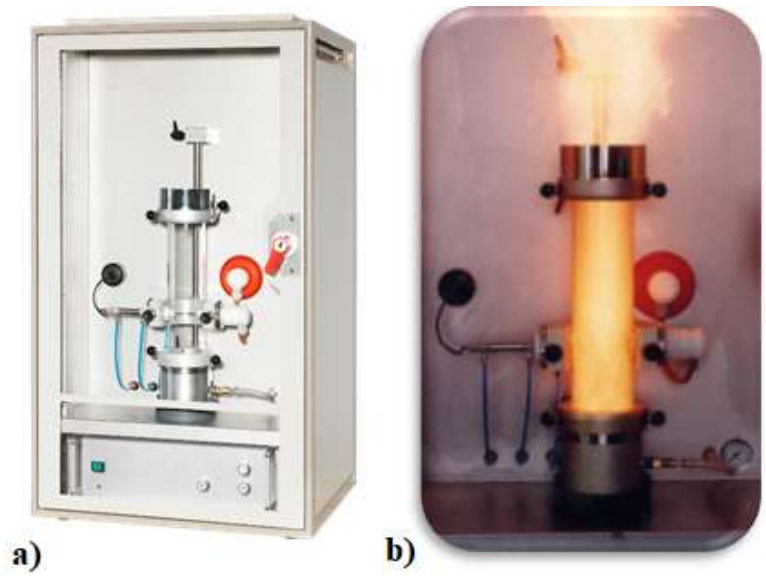

Figure 4-1 a) Modified Hartmann tube (TÜV SÜD Schweiz AG, 2020) b) Modified Hartmann tube during an ignition

After varying the different parameters, the value of the minimum ignition energy can be estimated through a statistic relation (Cesana and Siwek, 2001a). The following equation then links the highest energy inducing no inflammation E_1, the lowest energy generating an ignition E_2, the number of tests during which an ignition occurred at E_2, noted $I_{[E2]}$, and the total number of tests performed at E_2 $(NI + I)_{[E2]}$:

$$MIE = 10^{\left(\log E_2 - I_{[E2]}\frac{\log E_2 - \log E_1}{1+(NI+I)_{[E2]}}\right)} \qquad 4\text{-}1$$

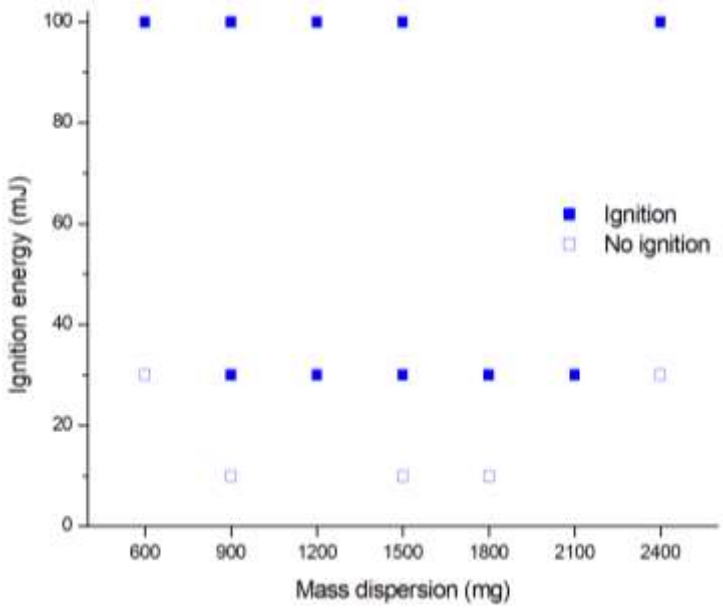

Figure 4-2 Results of MIE test for nanocellulose at tv = 120 ms

For instance, results of minimum ignition energy tests performed on the nanocellulose are presented in Figure 4-2. The lowest energy leading to an ignition was found at 30 mJ, and no ignition was observed at 10 mJ, leading to a MIE of 16 mJ. Additional tests were performed at 90 and 150 ms and confirmed these results.

IV.1.2. Minimum Ignition Temperature

Similarly to the minimum ignition energy, the Minimum Ignition Temperature (MIT) is the lowest temperature able to ignite a dust cloud under specific test conditions. According to international standards (ASTM E1491-06, 2012; EN 50281-2-1, 2000; IEC 1241-2-1, 1994), it can either be measured in a vertical Godbert-Greenwald furnace (Eckhoff, 2019) or in an horizontal oven, called "BAM oven", designed at the Bundesanstalt für Materialforschung und-prüfung (BAM) in Berlin, Germany. Siwek (1996) highlighted that MIT measured in the Godbert-Greenwald oven was generally higher than the one measured in the BAM oven and proposed the following correlation to link both temperatures :

$$MIT_{GG} = 1.1\ MIT_{BAM} - 10°C \qquad 4\text{-}2$$

In this work, the Godbert-Greenwald oven was used for MIT tests (Figure 4-3). This furnace is constituted of a vertical silica tube electrically heated and open at its bottom. The upper part of the tube is connected through a Pyrex tube to a dust container, itself related to a compressed air reservoir. The temperature of the furnace is controlled using two thermocouples calibrated for temperatures ranging from 20°C to 1000°C. An experiment consists in injecting a weighted dust sample in the oven through an air pulse of variable pressure. For a given mass and injection pressure, the oven temperature is raised from stages of 50°C until an ignition occurs, i.e. until a flame is visible under the bottom of the tube. A temperature reduction is then realized by stages of 10°C, until no ignition is observed for 10 consecutive trials. As for the determination

of the minimum ignition energy, the dust concentration and the injection pressure, therefore turbulence, are varied to ensure the determination of the lowest minimum ignition temperature.

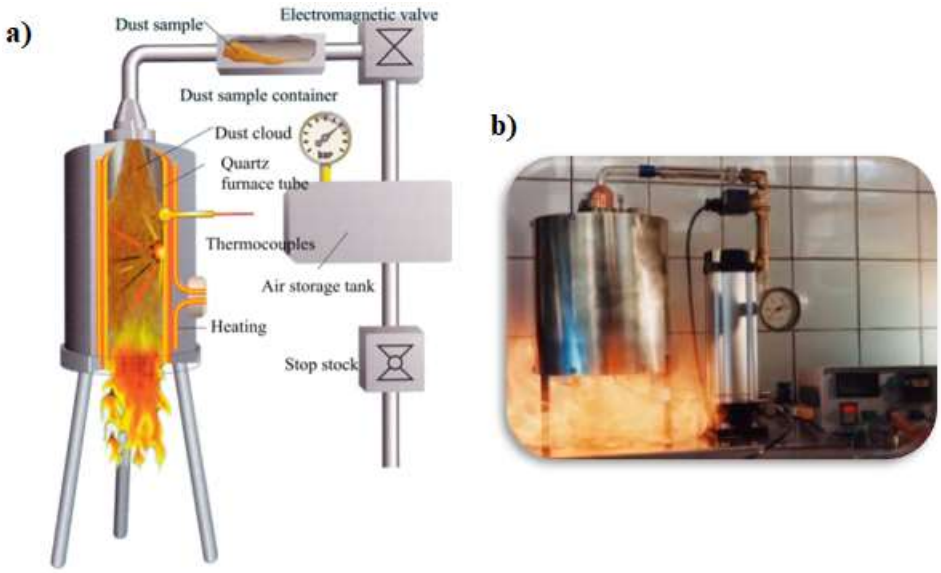

Figure 4-3 a) Schema of the Godbert-Greenwald oven (Xu et al., 2017) and b) Godbert-Greenwald oven during an ignition

IV.1.3. Lower Explosion Limit

The Lower Explosion Limit (LEL) is the lowest amount of dust capable of propagating a deflagration through a well dispersed dust cloud under specific conditions (ASTM E1515-14, 2014; EN 14034-3, 2006). It is generally measured in a 1 m^3 vessel or a 20L sphere, although it can also be estimated in the modified Hartmann tube presented previously in section IV.1.1. In this work, the determination of the LEL was realized in the 20L sphere and conducted according to the same procedure than the determination of the explosion severity parameters. Although the determination of the LEL should be performed with an ignition energy of 2 kJ according to international standards (EN 14034-3, 2006), it was estimated in this work using the same ignition energy than when evaluating the explosion severity, i.e. 10 kJ. This approximation may then lead to a value slightly lower compared to the standards, which also provides more conservative results. Since the experimental procedure to perform explosion tests in the 20L sphere is explained in section IV.2, it will not be detailed in this section. The LEL is then defined as the first concentration for which an explosion is observed in the 20L sphere. Contrary to the measurements of MIE and MIT, no variation of ignition delay time or ignition energy is recommended for the determination of the LEL.

IV.1.4. Ignition sensitivity of the powders

The ignition sensitivity of each considered powder was evaluated through the determination of the minimum ignition energy, minimum ignition temperature and lower explosion limit (Table 4-1). To highlight the modifications in the ignition sensitivity when decreasing the particle size

from the micro-range to the nano-range, the ignition parameters of micropowders of the same nature available on the GESTIS-DUST-EX database are presented alongside.

It is generally admitted (Wu et al., 2010a) that metallic powders are easily ignited and are even able to exhibit a pyrophoric behavior, i.e. ignite spontaneously in contact with oxygen, as pointed out by Krietsch et al. (2015), Mohan et al. (2012) and Sundaram et al. (2013). This high sensitivity is reflected in the results concerning both aluminum and carbon-coated silicon powders, mainly regarding their minimum ignition energies lower than 1 mJ and 4 mJ respectively. Dufaud et al. (2011), Sundaram et al. (2016) and Vignes et al. (2019) also highlighted that aluminum nanoparticles are more easily ignited than microparticles, notably due to higher reactive surface area and different oxidation mechanisms (reaction limitation rather than diffusional limitation). This tendency was observed for other metallic powders, such as magnesium (Mittal, 2014; Nifuku et al., 2007) and titanium (Boilard et al., 2013), but also for organic powders. Indeed, the studied nanocellulose exhibits a MIE of 16 mJ whereas microcrystalline cellulose presents a much higher MIE, reaching 590 mJ (Santandrea et al., 2019c).

Table 4-1 Ignition sensitivity parameters of the studied nanopowders compared to micropowders of the same nature

Powder	MIE (mJ)	MIT (°C)	LEL ($g.m^{-3}$)
Nanocellulose	**16**	**420**	**250**
"Cellulose" (< 70 µm)	*> 100*	*500*	*60*
Carbon black	**> 1000**	**> 900**	**60**
"Carbon" (< 250 µm)	*N/A*	*N/A*	*60*
Carbon-coated silicon	**4**	**560**	**125**
"Silicon" (< 70 µm)	*> 100*	*> 850*	*125*
Aluminum 40-60 nm	**< 1**	**550**	**60**
Aluminum 100 nm	**< 1** [1]	**550** [1]	**125**
"Aluminum" (< 70 µm)	*440* [2]	*590*	*60*

[1] (Vignes, 2008), [2] (Dufaud et al., 2011)

However, the ignition sensitivity of some powders does not seem to be affected by a transition to the nanoscale. For instance, Turkevich et al. (2016, 2015) found that the ignition sensitivity of carbonaceous nanoparticles is similar to the one of coals and usual carbon blacks. More precisely, Bouillard et al. (2010) evidenced that the MIT of carbon blacks decreases when decreasing the particle size, but increases when the primary diameter reaches the nano-size range. This observation can be explained by strong cohesion forces causing the particles to agglomerate (Eckhoff, 2012). The studied carbon black could not be ignited by an electrical spark or a hot surface in the limitation of the equipment, although its LEL was easily reached.

From the knowledge of the ignition sensitivity parameters of the powders, some recommendations can then be prescribed. The powders can notably be classified depending on their MIE (Janes et al., 2008). It appears on Table 4-1 that both aluminum powders very low MIE and are therefore considered as extremely sensitive to electrostatic ignition. Therefore, their ignition by a brush, a cone or a propagating discharge, even a corona discharge in the case of aluminum, is not negligible. The nanocellulose and carbon-coated silicon powders are also very sensitive to electrostatic ignition, with MIE of respectively 16 mJ and 4 mJ, and can be easily ignited by an electrical spark or a propagating brush or cone discharge (Lüttgens et al., 2017). These ignitions sources must then be considered when applying the ATEX directives. However, it has to be noticed that corona and brush discharge, capable of igniting gas clouds, are unlikely to ignite dust clouds. Specific handling conditions depending on the MIE value are recommended by the standard IEC TS 60079-32-1:2013+A1:2017, such as grounding plant or personnel, to avoid electrostatic discharges to ignite the product. Low level of electrification must also be maintained, and charges capable of igniting the clouds must be neutralized. The carbon black powder could not be ignited by an electrical spark, meaning it is not ignition sensitive for energies lower than 1 J, according to ISO/IEC 80079-20-2 (2016). Thus, in accordance with the ATEX directives, the ignition probability of this powder by an electrical discharge is considered as extremely low. However, this powder can be ignited by energies higher than 1 J, as proven by tests in the 20L sphere with an energy of 10 kJ and must not be considered as non-explosible.

Concerning the MIT of the dust clouds, the same conclusions than for the MIE can be drawn, i.e. the presence of hot surfaces capable of igniting the dust clouds must be avoided or limited. Table 4-1 also shows that the LEL of aluminum and carbon black is of 60 $g.m^{-3}$, which can easily be reached during an accidental dispersion. Specific prevention measures to suppress or limit dust accumulation must then be applied to avoid an accident. Moreover, even though the LEL of carbon-coated silicon and nanocellulose are higher, reaching 125 $g.m^{-3}$ and 250 $g.m^{-3}$ respectively, both compounds exhibit low MIE and MIT, which still makes their ignition very likely.

Thus, although each parameter is generally considered independently from the others, a reliable prevention of the dust ignition relies on a consideration of the three parameters simultaneously. The dependence of the ignition sensitivity factors on the dust characteristics and operating conditions was notably investigated in the next section through a dimensional analysis.

IV.1.5. Dimensional analysis: dust cloud ignition

A dimensional analysis similar to the one conducted in chapter 3 for the dust dispersion was realized to characterize ignition of a dust cloud. The considered characteristics of the dust cloud are its concentration C, minimum ignition energy MIE, thermal conductivity λ, enthalpies of combustion and vaporization ΔH_{comb} and ΔH_{vap}, critical ignition diameter dc, which is the smallest flame volume allowing the flame propagation (van der Wel, 1993), and characteristic reaction time τ_c. This dust cloud is dispersed in air (ρ_{air}, μ_{air}) with a velocity u, and the dust-air mixture exhibits an average heat capacity C_p. The dust cloud is ignited by an ignition energy

IE, and only the convective heat transfer is considered, characterized by the convection heat transfer coefficient h (no radiative heat transfer). The parameters considered for the dimensional analysis are indexed in Table 4-2. 13 parameters were identified, involving 4 different dimensions. Thus, according to Vaschy-Buckingham theorem (Buckingham, 1914), the dust ignition phenomenon can be described by 9 independent dimensionless numbers.

Table 4-2 Parameters considered for the dimensional analysis of dust ignition

Notation	Definition	SI units	Dimension
ρ_{air}	Air density	$kg.m^{-3}$	$M.L^{-3}$
h	Convection heat transfer coefficient	$W.m^{-2}.K^{-1}$	$M.T^{-3}.\theta^{-1}$
u	Fluid velocity	$m.s^{-1}$	$L.T^{-1}$
μ_{air}	Dynamic viscosity of air	$kg.m^{-1}.s^{-1}$	$M.L^{-1}.T^{-1}$
C_P	Average heat capacity of the dust and fluid	$J.kg^{-1}.K^{-1}$	$L^2.T^{-2}.\theta^{-1}$
C	Dust concentration	$kg.m^{-3}$	$M.L^{-3}$
d_c	Critical diameter of the dust cloud	m	L
λ	Thermal conductivity	$W.m^{-1}.K^{-1}$	$M.L.T^{-3}.\theta^{-1}$
ΔH_{comb}	Enthalpy of combustion of the dust cloud	$J.mol^{-1}$	$L^2.T^{-2}$
ΔH_{vap}	Enthalpy of vaporization of the dust cloud	$J.mol^{-1}$	$L^2.T^{-2}$
τ_c	Characteristic chemical time	s	T^{-1}
MIE	Minimum Ignition Energy of the powder	J	$M.L^2.T^{-2}$
IE	Effective ignition energy	J	$M.L^2.T^{-2}$

The same method than the one presented in chapter 3 was applied to determine the dimensionless numbers. The comparison to existing numbers then led to the numbers presented in Table 4-3. Among them, the Spalding number B_T, comparing the available energy to the energy required for the evaporation, is generally written as follows:

$$B_T = \frac{C_p \, \Delta T}{\Delta H_{vap}} \qquad 4\text{-}3$$

where ΔT is the difference of the temperature of the ignition source and the ambient temperature. However, this parameter is not considered in this dimensional analysis as an energy balance can relate it to the ignition energy and the mass of the dust cloud. This latter can be expressed as a function of the dust cloud concentration and volume, leading to the following relation:

$$\frac{\pi}{6} C \, {d_c}^3 \, C_p \, \Delta T = EI \qquad 4\text{-}4$$

It should be noted that the Biot number, defined by the same expression than the Nusselt number, could be used to compare the heat transfer resistance inside and at the surface of a body. However, since this analysis focuses on the dust cloud ignition, only the Nusselt number was considered.

Table 4-3 Expression and physical meaning of the dimensionless numbers characterizing the dust ignition phenomenon

Dimensionless number	Expression	Physical meaning
Nusselt number Nu	$Nu = \frac{h\, d_c}{\lambda}$	Characterization of the convective heat transfer in a fluid
Stanton number Sta	$Sta = \frac{h}{\rho_{air}\, u\, C_p}$	Ratio of heat transferred into a fluid to the thermal capacity of the fluid
Reynolds number Re	$Re = \frac{\rho_{air}\, u\, d_c}{\mu_{air}}$	Ratio of fluid inertial forces and viscous forces
Spalding number B_T	$B_T = \frac{EI}{\Delta H_{vap}\, C\, {d_c}^3}$	Ratio of available energy to energy required for the evaporation
Damköhler number Da_{II}	$Da_{II} = \frac{d_c\, \rho_{air}\, C_p}{h\, \tau_c}$	Ratio of characteristic diffusion time to characteristic chemical time
Lewis number Le	$Le = \frac{\lambda}{\rho_{air}\, C_p\, d_c\, u}$	Ratio of mass diffusivity to thermal diffusivity
π_1	$\pi_1 = \frac{EMI}{EI}$	Overdriving coefficient
π_2	$\pi_2 = \frac{C}{\rho_{air}}$	Ratio of dust concentration to fluid density
π_3	$\pi_3 = \frac{\Delta H_{comb}\, C\, {d_c}^3}{EI}$	Ratio of energy generated by the reaction to energy provided by the ignition source

A correlation relating the different dimensionless numbers can then be written. To be able to determine the ignition energy to apply when performing explosion tests depending on the minimum ignition energy of the dust, this correlation was written as a function of the number π_1:

$$\pi_1 = f(Nu, Sta, Re, B_T, Da_{II}, Le, \pi_2, \pi_3) \qquad 4\text{-}5$$

Since all the parameters involved in this dimensional analysis, such as the combustion and vaporization enthalpies, the critical diameter or the characteristic reaction time, could not be easily estimated for the considered powders, an analysis similar to the one realized in chapter 3 could not be conducted in this part. However, the main difference between the dust ignition of microparticles and nanoparticles lies in the critical diameter, minimum ignition energy and

characteristic reaction time. These differences are then represented by the number π_1 and the Damköhler number Da_{II}, which represents the ratio of the diffusion time over the reaction time. Thus, $Da_{II} << 1$ implies that the combustion is limited by the surface reaction, while $Da_{II} >> 1$ means that the diffusion of the dioxygen toward the particle surface limits the combustion (Di Benedetto et al., 2010).

Previous works providing values of characteristic chemical times for organic powders, it is then possible to approximate the Damköhler number 2 for one particle of nanocellulose. The critical diameter d_c was then substituted by the particle size after dispersion, the air density ρ_{air} is equal to 1.2 $kg.m^{-3}$ at ambient temperature and the convection heat transfer coefficient h of air was taken around 10 $W.m^{-2}.K^{-1}$. Due to the density difference between the fluid and the powder, the average heat capacity of the air/fuel mixture was considered equal to the heat capacity of the powder, i.e. around 1230 $J.kg.K^{-1}$ for the cellulose (Hatakeyama et al., 1982). The characteristic chemical time was estimated using Figure 4-4, which represents the pyrolysis limiting regimes dependence on the particle size and external temperature, based on kinetics established by Di Blasi and Branca (2001). The external temperature was considered equal to the adiabatic flame temperature at equilibrium conditions, which was determined around 2000K by the CEA software (McBride and Gordon, 1996).

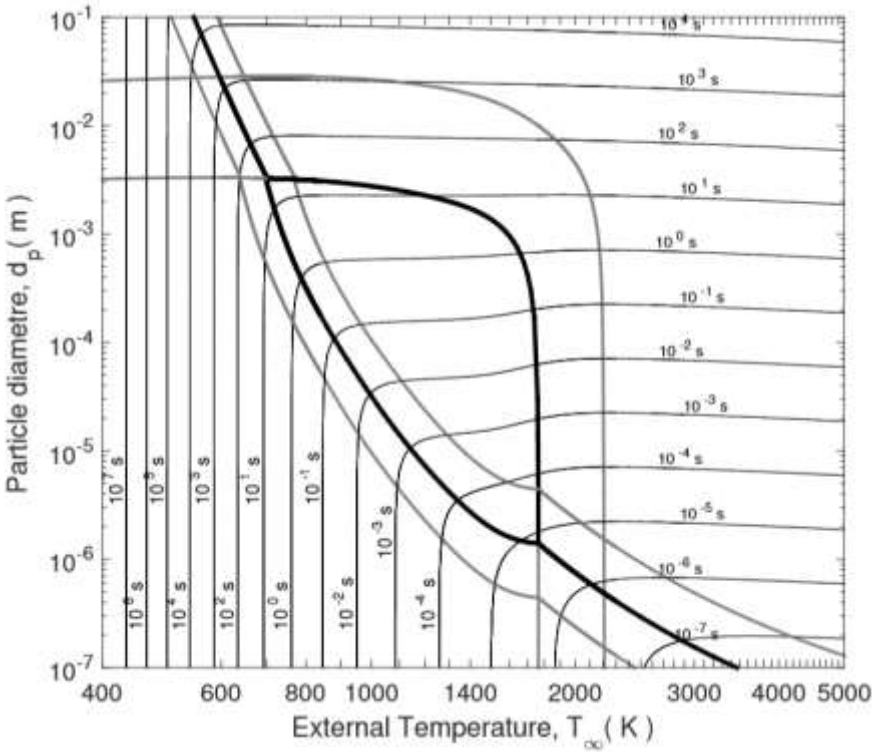

Figure 4-4 Pyrolysis limiting regimes according to the particle size, the external temperature and the kinetic model of Di Blasi and Branca (2001) (from Cuervo (2015))

The mean surface diameter measured after dispersion of nanocellulose in the 20L sphere being around 10 µm, a characteristic chemical time around 10^{-3} s is obtained, leading to a Damköhler number of 1.5. This value traduces a fast pyrolysis of the particle with a combustion mainly

occurring in gaseous phase. The transition from a reaction to a diffusion limitation was estimated around 30 µm for organic powders (Dufaud et al., 2012), which is confirmed by a Damköhler number of 0.9, implying a combustion limited by the dust pyrolysis. It should be noted that, for individual nanoparticles of 100 nm diameter, a characteristic chemical time of 10^{-6} s is obtained at 2000K, inducing a Damköhler number of 14.8, characterizing a very fast pyrolysis step.

However, these values are calculated for an individual particle. To reach the lower explosion limit, the number of nanoparticles in the dust cloud is considerably higher than that of microparticles. This number can be notably calculated as follows:

$$n_p = \frac{C\ {d_c}^3}{\rho_p\ {d_p}^3} \qquad 4\text{-}6$$

For instance, considering an organic dust cloud at a concentration of 60 $g.m^{-3}$, a critical diameter of 7 mm (Khalili et al., 2012) and a dust density of 700 $kg.m^{-3}$ (e.g. nanocellulose), the number of microparticles of 100 µm diameter is of the order of 10^3 while the number of nanoparticles of 100 nm reaches 10^{10}. This high number implies a very small distance between the particles, which can induce a group combustion, i.e. the individual particle does not react independently but is influenced by the combustion of the whole dust cloud. The characterization of such combustion behavior would then require the knowledge of the distance between the particles and the flame thickness, or, even better, a minimum distance allowing the heat transfer between the particles to take the radiation into account.

Although the influence of the Damköhler number on the number π_1 and, this way, on the minimum ignition energy cannot be quantified, such modifications in the combustion behavior can then explain the different ignition sensitivity when moving from the micro-scale to the nano-scale. Such analysis could then be used as a base for future parametric analysis, such as the development of a safety by design method for nanopowders.

IV.2. Explosion severity

After the determination of the ignition sensitivity of the powders, which allows to develop prevention methods to reduce explosion likelihood, the explosion severity must be evaluated to design protection equipment. The next section then defines the maximum overpressure and maximum rate of pressure rise, characterizing the explosion severity, along with their measurement method. The results obtained with each powder are also presented and discussed.

IV.2.1. Definition and measurement

The explosion severity is represented by the maximum overpressure (P_{max}) and the maximum rate of pressure rise $(dP/dt)_{max}$. Those parameters can be evaluated in a $1m^3$ vessel or in a 20L sphere, more generally used in laboratories because of its dimensions, according to EN 14034-1 (2004), EN 14034-2 (2006) and ISO 6184/1 (1985). All the explosions tests performed in this work were conducted in the 20L sphere, following the experimental procedure described in

detail by Cesana and Siwek (2001). The apparatus is constituted of a stainless-steel spherical chamber of 20L capable of resisting static pressures up to 40 bars, equipped with a cooling jacket that dissipates the heat generated during the explosion (Figure 4-5a). A dust canister of 0.6L is connected to the combustion chamber through a pneumatic electro-valve which opens in less than 10 ms, and an injection nozzle is present at the bottom of the chamber (Figure 4-5b).

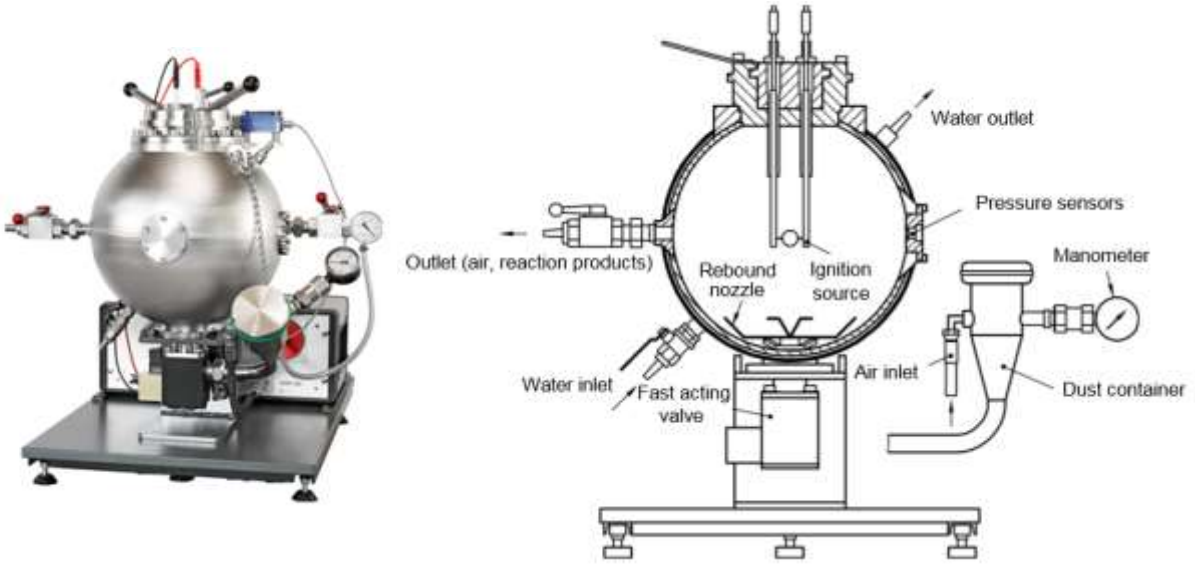

Figure 4-5 Siwek 20L sphere from a) TÜV SÜD Schweiz AG (2020) and b) EN 14034-1-2 (2004; 2006)

The experiment starts by evacuating the sphere at 0.4 bara in order to reach the atmospheric pressure within the chamber after the dust dispersion. Then, the canister, filled with the weighted dust sample, is pressurized at 20 barg, with compressed synthetic air (80% N_2/20% O_2). It should be noted that its composition can be modified to evaluate the limiting oxygen concentration. Afterwards, the electrovalve opens, inducing the dispersion of the dust by the pressure gradient between the chamber and the dust container. When entering the 20L sphere, the dust goes through a rebound nozzle to be distributed within the vessel (EN 14034-1-2, 2004; 2006). Chemical ignitors (Fr. Sobbe GmbH) are composed of 40%m. of zirconium, 30%m. of barium nitrate and 30%m. of barium peroxide. This delay, called ignition delay time t_v, can be modified in the KSEP 7 software but remains set at 60 ms for standard tests. Two piezoelectric sensors (Kistler Type 701A) connected to a data acquisition system then record the pressure-time evolution during the explosion (Figure 4-6).

Right after the injection, the pressure increases from 0.4 bar to reach the atmospheric pressure. The ignition delay time t_v, i.e. the delay between the beginning of the injection and the activation of the ignition source, is fixed to 60 ms in the 20L sphere (EN 14034-1, 2004; EN 14034-2, 2006). This delay controls the degree of turbulence of the dust cloud, but also the local concentration of the dust (Dahoe, 2000; Murillo, 2016). After the ignition of the dust, the pressure increases until it reaches a maximum value noted Pm, coupled with the maximum value of the slope of the pressure profile, $(dP/dt)_m$. Finally, the remaining suspended dust and gas are evacuated using an outlet valve, and the combustion products are extracted from the

apparatus. The 20L sphere is then cleaned between each test and disassembled and washed after each test series.

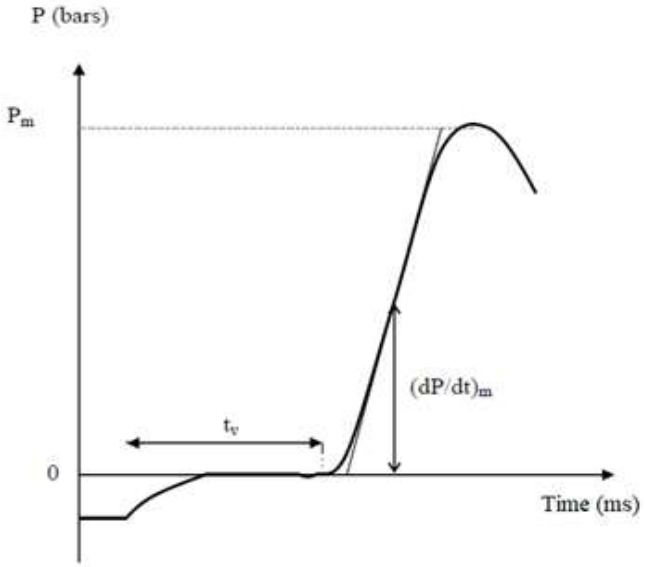

Figure 4-6 Pressure-time evolution during an explosion in the 20L sphere

Tests must be performed at different concentrations to find the maximum value of P_m and $(dP/dt)_m$. Those maximum values are then defined as the maximum overpressure P_{max} and the maximum rate of pressure rise $(dP/dt)_{max}$, which are the parameters defining the explosion severity of the dust. As explained in chapter 2, the value of $(dP/dt)_{max}$, which depends on the vessel volume, can be normalized using the deflagration index K_{St} calculated from the following relation (Bartknecht, 1989):

$$K_{St} = \left(\frac{dP}{dt}\right)_{max} V^{\frac{1}{3}} \qquad 4\text{-}7$$

Equation 4-7 aims at proposing a volume-independent parameter, the K_{st}, in order to extrapolate the experimental results obtained in a 20L sphere to larger vessels. However, it should be noted that only the dust concentration is varied during the tests, neglecting the influence of the ignition energy and ignition delay time on the explosion severity parameters, contrary to MIE and MIT tests. Moreover, although tests are conducted for several concentrations and reproduced around the P_{max} and $(dP/dt)_{max}$ values, only the most severe explosion is considered for the determination of P_{max} and K_{St} values.

IV.2.2. Explosion severity of the considered powders

In order to take advantage of all the experiments conducted on the powders, the evolution of the explosion overpressure and rate of pressure rise with the concentration are presented respectively in Figure 4-7 and Figure 4-8, and the explosion severity parameters are summarized in Table 4-4. It should be noted that this part does not aim to better understand the explosion mechanisms of nanopowders or to take a critical look at the tests performed under standard conditions, but simply to follow the classic path imposed by compliance with standards. Nevertheless, such investigations will be realized and detailed in chapter 5.

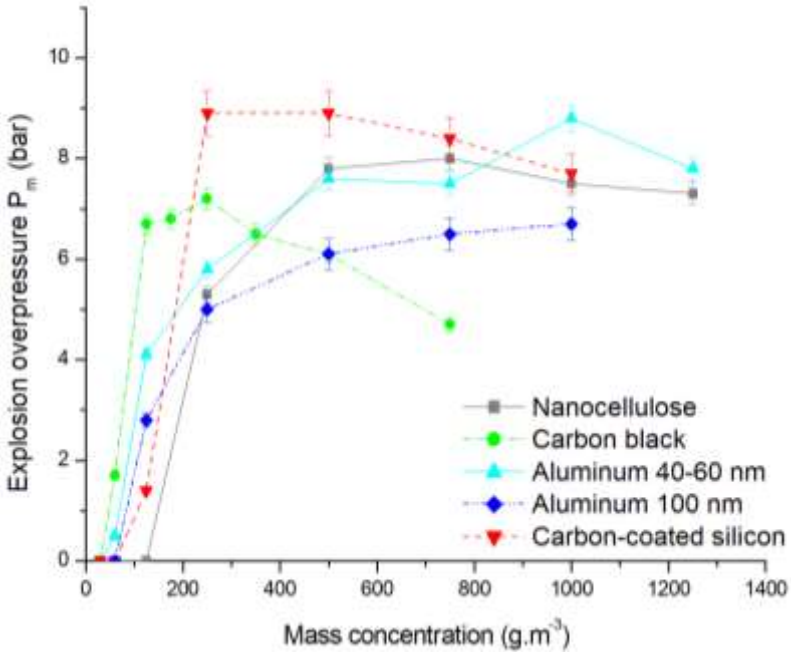

Figure 4-7 Evolution of the explosion overpressure with the concentration for the raw powders in standard conditions

First, the LEL values mentioned in Table 4-1 can be retrieved in Figure 4-7. In addition, it can be observed that, for all the powders, the explosion overpressure first increases with the concentration, as the limiting reagent is the combustible. It then reaches a maximum, corresponding to the experimental optimal concentration, and starts decreasing due to a lack of oxygen (Eckhoff, 2003). Each powder being of different nature, their optimal concentrations are different. It then appears that the maximum overpressure of carbon black was reached at 250 g.m^{-3}, whereas it was obtained only at 1000 g.m^{-3} for the aluminum 40-60 nm. Moreover, similar overpressures were measured for aluminum 40-60 nm (8.8 bar) and the carbon-coated silicon (8.9 bar), but the optimal concentration, defined as the concentration leading to the maximum value of P_m and $(dP/dt)_m$, of the carbon-coated silicon is obtained long before the aluminum, i.e. around 250 g.m^{-3}. It should be noted that the maximum overpressure and maximum rate of pressure rise of the aluminum 100 nm were not reached due to a lack of powder. However, the measured overpressures are slightly lower than that measured on the exact same powder by Vignes (2008), probably due to a decreased reactivity caused by a passivation of the powder during the long storage.

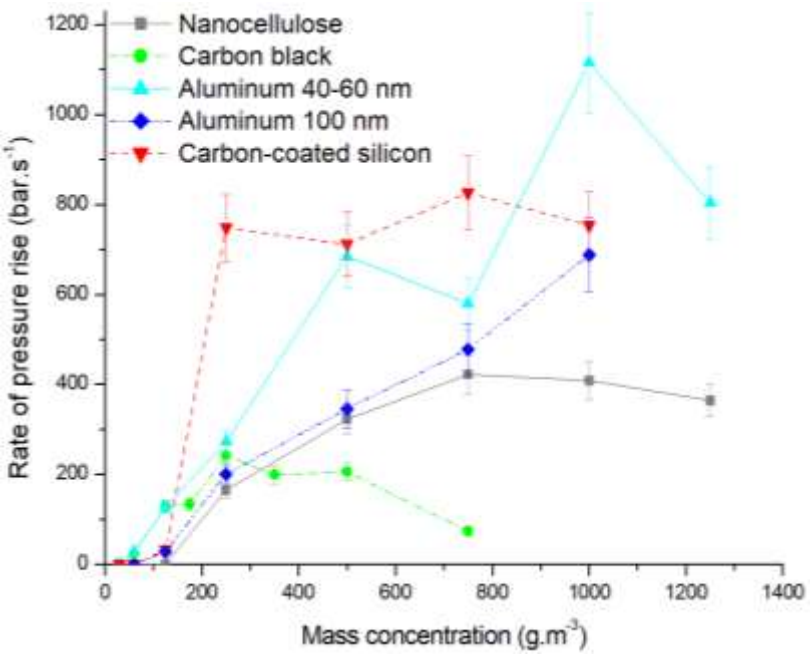

Figure 4-8 Evolution of the rate of pressure rise with the concentration for the studied powders in standard conditions

If similar maximum overpressures were obtained for the four powders, from 7 bars to 9 bars, larger variations can be observed in terms of rate of pressure rise (Figure 4-8). Indeed, concerning the carbon black, this parameter only reached 242 bar.s^{-1} at the maximum, whereas it was of 750 bar.s^{-1} for the carbon-coated silicon at the same concentration. The highest value was attained by the aluminum 40-60 nm and reaches 1115 bar.s^{-1} at a concentration of 1000 g.m^{-3}. The standard explosion severity parameters presented in Table 4-4 show that carbonaceous and organic powders present a medium explosion severity classified in St class 1, whereas metallic based powders lead to a much higher explosion severity, ranked in St class 2 or 3. These observations are in agreement with Bouillard et al. (2010), Dufaud et al., (2011) and Holbrow et al. (2010). However, it should be noted that, when testing the explosion severity of aluminum powders, some alumina was observed in the dust container for concentrations from 500 g.m^{-3} to 1000 g.m^{-3}, meaning that part of the explosion occurred in the dust canister. Besides the fact that this phenomenon can be harmful to the handler, it also leads to a misestimation of the pressure evolution within the 20L chamber. Therefore, even though the maximum overpressure and the maximum rate of pressure rise for the aluminum 40-60 nm were determined to be equal to respectively 8.8 bars and 1115 bar.s^{-1}, the real values are most probably actually higher, which is currently not considered for the design of protective equipment. It should also be reminded that, because of the lack of powder, testing was only possible up to a concentration of 1000 g/m³, which implies that the maximum values may be higher than the ones presented in Table 4-4.

Table 4-4 Explosion severity parameters for the studied powders compared to micropowders of the same nature

Powder	P_{max} (bar)	$(dP/dt)_{max}$ (bar.s^{-1})	K_{St} (bar.m.s^{-1})	St class
Nanocellulose	**8.1**	**435**	**118**	**1**
Microcrystalline cellulose [1]	*7.1*	*317*	*86*	*1*
Carbon black	**7.2**	**242**	**66**	**1**
"Carbon" (< 250 µm)	*8*	*556*	*151*	*1*
Carbon-coated silicon	**8.9**	**944**	**256**	**2**
"Silicon" (< 70 µm)	*10.8*	*497*	*135*	*1*
Aluminum 40-60 nm	**8.8**	**1115**	**303**	**3**
Aluminum 100 nm	**6.7***	**688***	**187***	**1**
Aluminum 3 µm [2]	*9.8*	*2090*	*567*	*3*
Aluminum 42 µm [2]	*7.2*	*360*	*98*	*1*

[1] (Santandrea et al., 2020a), [2] (Dufaud et al., 2011), * P_m and $(dP/dt)_m$

In a similar way to the analysis of the ignition sensitivity of the studied powders, the explosion parameters of some micropowders, found on the GESTIS-DUST-EX database or mentioned by Dufaud et al. (2011) and Santandrea et al. (2020a), are presented in Table 4-4. First, it appears that the nanocellulose and carbon black leads to the less severe explosions and are classified as St 1. Nevertheless, a decrease of 27% in the value of $(dP/dt)_{max}$ of the cellulose appears when moving to the nanocrystals to microcrystals, along with a decrease of 12% in the value of P_{max}, traducing a higher explosion severity of nanoparticles. Although the values of P_{max} and $(dP/dt)_{max}$ reported for the carbon micropowder are slighty higher than the measured ones for the carbon black, the class St remains unchanged. This observation can be explained by the long storage (more than 10 years) of the powder, which will be discussed in section V.2.1.

In risk management, three different types of measures are applied: inherent, engineered and procedural (Khan and Amyotte, 2003). In the first place, it is necessary to prevent the dust ignition through the application of inherent safety measures, which must be given priority over the other two prevention and protection means, and consists in four key principles (Bollinger and Crowl, 1997; Yuan et al., 2013). First, the minimization principle relies on the use of small quantities of combustible dust and on the low frequency of the performing of the hazardous procedure. Then, the substitution consists in replacing the hazardous material or procedure by a less hazardous one (Amyotte et al., 2003). Another way, called moderation, is to use the material in a less dangerous form or to modify the process conditions to limit the probability of dust dispersion or ignition. Finally, the simplification principle is applied by designing a process in order to eliminate opportunities for errors by avoiding the excessive use of add-on safety devices (Amyotte et al., 2009).

Without knowledge on the process involving the powder, only inherent safety measures, and more specifically the moderation principle, can be discussed. In the case of dust explosion, this method can be applied by passivating metallic particles or increasing the particle size. Indeed, Sundaram et al. (2013) stated that aluminum nanoparticles presenting an oxide layer thicker than 0.5 nm can be considered non-pyrophoric, thus limiting the probability of ignition, but also the explosion severity. Although the oxide layer of the aluminum 100 nm was not estimated, its long storage under ambient air probably induced the passivation of the powder, which is illustrated by the low explosion severity compared to the values initially obtained by Vignes (2008), which reached around 8 bars and 1000 $bar.s^{-1}$. Moreover, as evidenced by the example of aluminum 42 µm in Table 4-4 and highlighted by Boilard et al. (2013), Dufaud et al. (2011) and Wu et al. (2009), increasing the particle size from the nano-range to the micro-range can reduce the ignition sensitivity of metallic powders. However, as mentioned in chapter 2, they also highlighted that particles between 150 nm and 3 µm lead to the most severe explosions. A compromise must then be found to limit both ignition sensitivity and explosion severity. To increase the 'particle' size and still conserve the properties of the dust, controlled agglomeration may also be considered to reduce the explosion risk (Wu et al., 2010c), as it can also facilitate the powder transport, handling and storage for instance.

IV.3. Questioning the standards…

This chapter, dealing with normative aspects, showed what a study of flammability and explosivity of a powder conducted under the strict conditions of standards could bring as raw results and conclusions. The powders considered in this work were then characterized in terms of ignition sensitivity and explosion severity according to standards methods and some recommendations were established to avoid ignition or explosion when handling these powders. However, there are still significant issues concerning those tests.

Indeed, the high ignition sensitivity of certain nanopowders, highlighted in section IV.1.4 (carbon-coated silicon, nanocellulose, aluminum 40-60 nm), may result in an enhanced overdriving phenomenon with regard to micropowders due to the use of an ignition energy of 10 kJ in the 20L sphere. This excessive amount of energy then impacts the flame propagation in the combustion chamber and leads to an overestimation of the explosion overpressure (Going et al., 2000; Zhen and Leuckel, 1997). In addition, it should be noticed that a so-called 'under-driving' phenomenon can also be observed in the 20L sphere due to walls effects, which tends to decrease the flame temperature, and thus the overpressure and rate of pressure rise values (Dastidar, 2019; Kuai et al., 2012).

The high sensitivity of nanopowders can also induce a pre-ignition during the pressurization of the dust container before the injection (Dufaud et al., 2011; Krietsch et al., 2015; Wu et al., 2010). In a first instance, the observation of alumina in the dust container when testing the aluminum nanopowders was attributed to this phenomenon. Nevertheless, further investigations on this point are detailed in section V.4. Anyway, the presence of alumina in the dust container traduces that at least a part of the explosion occurred in the canister, thus leading to a

misestimation of the pressure-time evolution measured within the 20L sphere. Currently, the international standards do not propose any solution to overcome this issue.

Moreover, although the explosion tests are conducted for different concentrations and reproduced around P_{max} and $(dP/dt)_{max}$, only the maximum value of P_m and $(dP/dt)_m$ is taken into account, without considering the whole evolution with the concentration nor the optimal concentration leading to this maximum explosion severity. However, the complete evolution of P_m and $(dP/dt)_m$ with the concentration provides relevant information. Indeed, explosion severity can increase very fast with the dust concentration, as shown in Figure 4-8 regarding the carbon-coated silicon, for which a rate of pressure rise of 30 $bar.s^{-1}$ is obtained at 125 $g.m^{-3}$, i.e. the LEL, and reaches 750 $bar.s^{-1}$ at 250 $g.m^{-3}$, i.e. at the next testing concentration.

Furthermore, European standard (EN 14034-1, 2004; EN 14034-2, 2006) stipulate that both the moisture content and the particle size distribution 'shall be determined for the sample as tested and given in the test report'. No instruction is given on the method to apply for their determination, inducing the particle size distribution may be estimated by wet dispersion, which is convenient but of limited interest when testing the explosivity of a dust cloud in air. Moreover, when it comes to nanoparticles, the particle size distribution can be different before and after dispersion due to the fragmentation of the agglomerates. A note in international standards specifies that, if the size of the particles can be reduced by the dispersion process and if 'this effect may be important', the particle size distribution after dispersion (without ignition) should be evaluated. However, no critical particle size is given to indicate when this additional characterization is required and no method is recommended to perform it, whereas each measuring procedure (wet or dry measurement, dispersing system, solvent…) leads to a specific fragmentation efficiency and thus explosivity. frequency.

So, the process safety engineer now has access to the standard parameters characterizing the flammability and explosivity of his powders. But what should he do with these values ? He now knows that the nanoparticles naturally tend to agglomerate, notably for concentrations higher than the LEL, and that the agglomerates can be broken if submitted to a high shear stress (see chapter 3). Thus, except if his process induces the same shear stress than the 20L sphere, the measured values does not correspond to the same powder characteristics than the ones involved in his process. He has standard values that can be compared to the values measured for micropowders and/or databases, but this is not satisfying to provide a reliable and accurate risk analysis.

Nevertheless, recent provisions for protocols concerning explosivity and flammability assessment for powders containing nano-objects were released in the Technical Specification CEN/TS 17274 (2018) developed by CEN TC 352/WG3/PG3. However, although these guidelines recommend special care when testing nanomaterials due to their high sensitivity, no apparatus or procedure modification is proposed. For instance, very reactive samples should be stored and transported 'under partial vacuum conditions or under argon or any inert preferably nontoxic fluid' and the type of package should be reported (CEN/TS 17274, 2018), but the concern of potential pre-ignition when testing those very reactive materials is not addressed. On a similar way, the guidelines specify that the particle size distribution of powders containing

nanoparticles should be characterized ‘(d10%, d50%, d90%) by any suitable method in terms of volume, number’. Once again, no specific method is recommended and no mention of a characterization of the dust cloud, i.e. after dispersion, can be found. Thus, to provide more relevant, reliable and reproducible data, the standards conditions will be modified in the next chapter, and alternative procedures will be proposed.

Summary

This chapter is dedicated to the determination of the standard safety parameters of the powders and to the establishment of recommendations related to these parameters.

First, the ignition sensitivity of the powders was investigated through the measurement of the minimum ignition energy, the minimum ignition temperature and the lower explosion limit. After a presentation of the standard methods and apparatus to measure these elements, the values obtained for each powder were discussed. It then appears that the considered powders, except for the carbon black, are particularly sensitive with regard to micropowders, especially in terms of minimum ignition energy. Indeed, the nanocellulose and carbon-coated silicon exhibit minimum ignition energies of 16 mJ and 4 mJ respectively, while both aluminum were ignited by an electrical spark of 1 mJ. Specific measures to avoid electrostatic discharges, such as grounding plant or personnel, must then be implemented when handling such nanopowders. The parameters influencing the ignition sensitivity were discussed through a dimensional analysis describing the ignition of a dust cloud, notably highlighting the different kinetic limitations during the combustion of micro- and nanoparticles.

In a second part, the protocol for the measurement of the explosion severity characteristics, i.e. the maximum overpressure and the maximum rate of pressure rise, was detailed for the 20L sphere, and the determined values were presented. Organic and carbonaceous powders were then classified as St 1, showing a medium explosivity, while the metal-based powders, i.e. carbon-coated silicon and aluminum 40-60 nm, lead to much more severe explosions and were respectively classified as St 2 and St 3.

The last part of this chapter focused on the observations related to the experiments conducted and on a questioning of the validity of the international standards for the evaluation of the ignition sensitivity and explosion severity of nanopowders. Indeed, due to their high ignition sensitivity, the pressurization of the dust container before the injection of the powder in the 20L sphere can be sufficient to ignite the powder before the activation of the chemical igniters. This results in a misestimation of the pressure-time evolution measured in the combustion chamber and can also damage the apparatus. Moreover, the amount of energy required to ignite such powders is quite low (a few millijoules), while the standard ignition energy in the 20L is of 10 kJ, which can give rise to an overdriving phenomenon, disturbing the flame propagation and leading once again to misestimated values. Finally, the high shear stress induced by the dispersion in the 20L sphere can break the agglomerates, implying that the particle size distribution can be different before and after dispersion, which is not specifically considered in the international standards.

Résumé

Ce chapitre est dédié à la détermination des paramètres standard de sécurité des poudres et à l'établissement de recommandations concernant ces paramètres.

D'abord, la sensibilité à l'inflammation des poudres a été évaluée par la mesure de l'énergie minimale d'inflammation, la température minimale d'inflammation et la concentration minimale explosible. Après une présentation des méthodes et appareils standards pour la mesure de ces éléments, les valeurs obtenues pour chaque poudre ont été discutées. Il apparait alors que les poudres considérées, à l'exception du noir de carbone, sont particulièrement sensibles comparées aux microparticules, notamment au niveau de l'énergie minimale d'inflammation. En effet, la nanocellulose et le silicium enrobé de carbone montrent des énergies minimales d'inflammation de 16 mJ et 4 mJ respectivement, alors que les deux poudres d'aluminium ont été enflammées par une étincelle de 1 mJ. Des mesures spécifiques pour éviter les décharges électrostatiques, telles qu'une mise à la terre des installations ou du personnel, doit alors être implémentée lors de la manipulation de ces nanopoudres. Les paramètres influençant la sensibilité à l'inflammation d'une poudre ont été détaillés à travers une analyse dimensionnelle décrivant la combustion d'un nuage de particules, mettant notamment en lumière les différentes limitations cinétiques lors de la combustion de micro- et de nanoparticules.

Dans une seconde partie, le protocole pour la mesure des caractéristiques de sévérité d'explosion, i.e. la surpression maximale d'explosion et la vitesse maximale de montée en pression, a été détaillé pour la sphère de 20L, et les valeurs déterminées ont été présentées. Les poudres organiques et carbonées ont alors été classées St1, ce qui traduit une explosivité modérée, tandis que les poudres métalliques, i.e. l'aluminium et le silicium enrobé de carbone, ont mené à des explosions bien plus sévères et ont été classées respectivement St3 et St2.

La dernière partie de ce chapitre se focalise sur les observations liées aux essais expérimentaux et à un questionnement concernant la validité des standards internationaux pour l'évaluation de la sensibilité à l'inflammation et la sévérité d'explosion des nanopoudres. En effet, à cause de leur forte sensibilité à l'inflammation, la pressurisation du réservoir avant l'injection de la poudre dans la sphère de 20L peut être suffisante pour enflammer la poudre avant l'activation des inflammateurs pyrotechniques. En résulte alors une mauvaise estimation de l'évolution de la pression en fonction du temps mesurée dans la chambre de combustion, et peut également endommager le matériel. De plus, la quantité d'énergie nécessaire pour enflammer ces poussières est assez faible (quelques millijoules), tandis que l'énergie d'inflammation standard dans la sphère de 20L est de 10 kJ, ce qui peut mener à un phénomène d'overdriving et influer sur la propagation de la flamme, menant une fois encore à des résultats erronés. Enfin, le fort cisaillement induit par la dispersion dans la sphère de 20L peut fragmenter les agglomérats, impliquant que la distribution de tailles de particules peut être différente avant et après la dispersion, ce qui n'est pas spécifiquement considéré dans les standards internationaux.

Chapter 5:
Standards versus reality

The process safety engineer now has access to the standard values of ignition sensitivity and explosion severity of his powders, thanks to ignition and explosion tests conducted in chapter 4, in the standard equipment and conditions. However, during the tests, some observations led to questioning the validity of the standard procedure to evaluate the explosivity of nanopowders, and thus that of the measured values. Indeed, although the standard conditions and apparatuses are fixed, each powder is different, and its properties can impact the three main phenomena of a dust explosion: the dust dispersion, the ignition, and the flame propagation, i.e. the explosion itself, as presented in Figure 5-1. The main influences of the powder properties and of the process on each phenomenon are represented, knowing that some properties are interdependent. It should be noted that a similar summary of main influences was proposed by Skjold (2003).

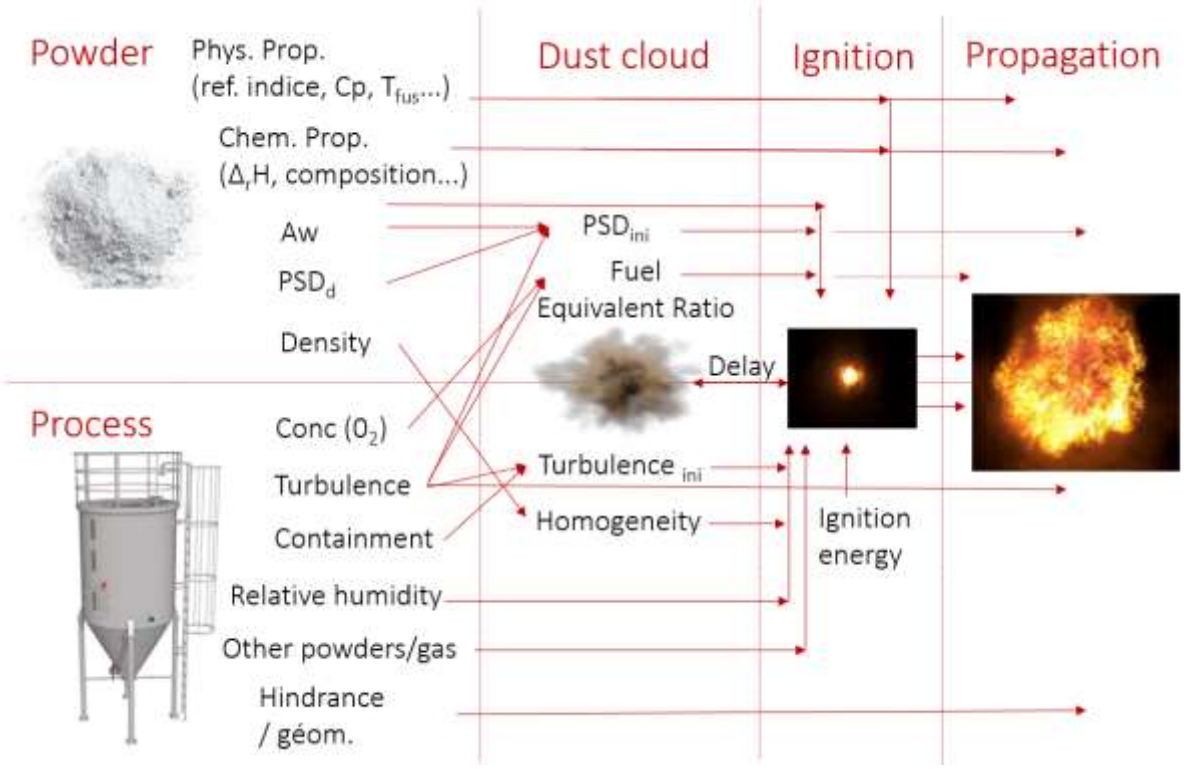

Figure 5-1 Main influences of the powder and process properties on the dust cloud (dispersion), the ignition and the flame propagation

In order to accurately assess the explosion risk of his powders, the process safety engineer would like further information on such influences concerning his samples. The dispersion properties of these powder were already characterized in chapter 3, and the standard explosion parameters were determined in chapter 4. This chapter is then dedicated to the evaluation of the influence of different parameters on the ignition sensitivity and mainly on the explosion severity: the particle size distribution, the water activity, the initial turbulence and the ignition energy. Since these parameters can affect the dust explosion depending on the powder nature and properties, several examples involving powders of different natures are presented in this chapter, and in terms of standard explosion parameter are presented to highlight some testing issues and propose adequate solutions.

In a first time, a focus will be realized on the sample preparation and formatting: how to modify them to make the influence of the agglomeration more visible ? Does the presence of water affect the ignition sensitivity and explosion severity ? In a second time, the influence of several parameters, in addition to the dust sample, mentioned by the international standards EN 14034 will be investigated: ignition energy and source, dispersion procedure, nozzle, ignition delay time. By systematically detailing, step by step, the standards, the existence of alternative solutions can be envisaged for nanoparticles.

V.1. Stronger together? Influence of the agglomeration on nanopowders explosion

'The size of the dust particles can be reduced by the dispersion process. In cases where this effect may be important, its magnitude can be evaluated by determining the particle size distribution once more after dispersion (without ignition)
(EN 14034-1-2, 2004; 2006)

The small size of nanoparticles implies that they tend to agglomerate through weak bonding such as van der Waals, electrostatic, capillary or magnetic forces (see chapter 2, section II.3.2). Dispersion tests performed in the 20L sphere, presented in chapter 3, evidenced that the agglomerates are partially broken by the injection procedure, thus modifying the particle size distribution (PSD) of the cloud (Sanchirico et al., 2015). The impact of the agglomeration on the explosion severity was estimated by a modification of the agglomerates size and cohesion strength. Since the addition of a cohesion agent would modify the reactions involved in the explosion, three ways can be envisaged: grinding, sieving, and mechanical agglomeration (e.g. wet or dry granulation, compaction).

The dispersion procedure in the 20L sphere already inducing a high shear stress, it would be difficult to further reduce the size of the agglomerates after dispersion. Indeed, the cohesion strengths proposed by Rumpf (1962) and Weiler et al. (2010) evolve with the reverse of the squared particle diameter (see section II.3.3). This implies that the smallest the particle (or agglomerate), the harder it is to be broken (Deng et al., 2016). Moreover, dry powder grinding would not allow the obtention of agglomerates smaller than around 1 µm, and the process would produce heat and possibly electrostatic discharges that could be sufficient to ignite the most sensitive powders. Therefore, powder grinding was not considered as a suitable solution. This section is then divided in two parts, which respectively focus on nanocellulose sieving and mechanical agglomeration of nanocellulose and carbon-coated silicon.

V.1.1. Effects of PSD selection

In an attempt to obtain different agglomerate sizes, the nanocellulose was dried under vacuum at 90°C and sieved using a 40 µm mesh strainer submitted to low amplitude vibrations, to avoid the breakage of the bigger agglomerates. Indeed, the mean surface diameter measured by

sedimentation was around 48 µm. This procedure then allows the separation of the bigger agglomerates to the finer particles. The particle size distribution of each fraction was measured using the laser diffraction sensor by sedimentation. The upper fraction was constituted of agglomerates of sizes between 40 and 100 µm, whereas the lower fraction exhibited a surface diameter around 10 µm. The agglomerates sizes of each sample are summarized in Table 5-1. It should be noted that the sieving process does not modify the size of the agglomerates and only aims at separating the agglomerates according to their size. However, the biggest agglomerates, i.e. the less cohesive, may be broken during the sieving process (Deng et al., 2016).

Table 5-1 Characteristics of the raw and sieved nanocellulose

Powder	Raw powder	Fine fraction	Large fraction
Sieving size (µm)	N/A	< 40	> 40
Mean surface diameter by sedimentation (µm)	48	10	54
Mean surface diameter after dispersion in the 20L sphere (µm)	10.4	8.2	12.3

The dust clouds emitted after dispersion in the 20L sphere were also characterized at the center of the sphere and at the moment of ignition (Figure 5-2).

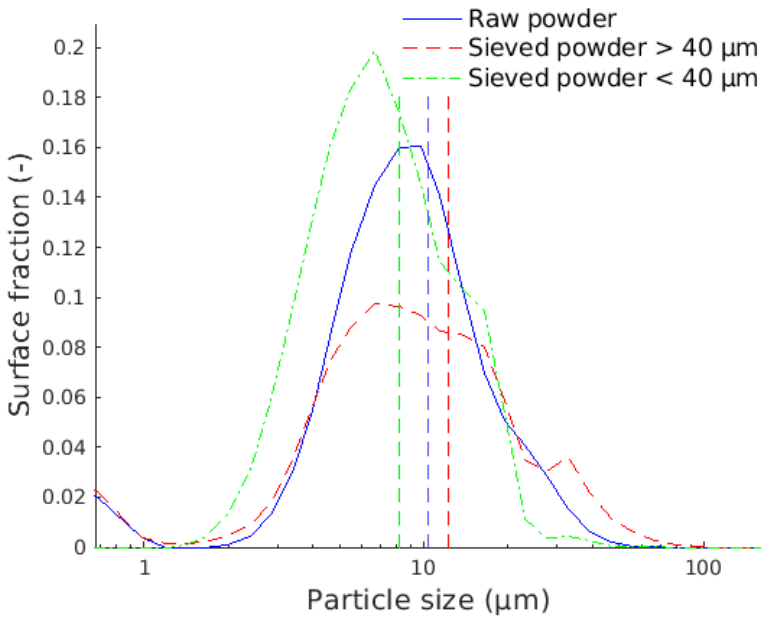

Figure 5-2 Particle size distribution of raw and sieved nanocellulose after injection in the 20L at the moment of ignition (at 60 ms)

Despite the high shear stress induced by the dispersion system of the 20L sphere, a slight difference in the particle size distributions of the samples can be observed. Indeed, the mean surface diameter obtained by dispersion of the powder sieved below 40 µm is 8.2 µm whereas the dispersion of the bigger agglomerates (> 40 µm) led to a mean surface diameter of 12.3 µm. As a comparison, the mean surface diameter by dispersion of the raw powder is 10.4 µm. In addition to these slight differences, the presence of particles smaller than 1 µm was evidenced for the raw and sieved powder (< 40µm), whereas these particles are not observed for the sieved powder (> 40µm), which confirms the efficiency of the sieving procedure.

However, probably due to the small differences in the PSD after dispersion, the explosion tests performed on the different samples conduced to rather similar explosion severities (Figure 5-3). Indeed, a maximum overpressure of 8.9 ± 0.4 bar and a maximum rate of pressure rise of 555 ± 66 bar.s^{-1} were obtained for the bigger agglomerates (> 40 µm), whereas these parameters respectively reached 8.7 ± 0.4 bar and 473 ± 56 bar.s^{-1} for the finest powder. Nevertheless, the lowest concentration inducing an explosion was obtained at 125 g.m^{-3} with the raw powder and the smallest agglomerates and only at 250 g.m^{-3} with the sample of agglomerates bigger than 40 µm. Thus, despite the breakage of the majority of the agglomerates observed in Figure 5-2, the sample constituted of agglomerates bigger than 40 µm, which contains fewer fine particles or agglomerates than the initial powder, appears to be less ignition sensitive than the two other samples. This observation tends to corroborate the theory stipulating that the ignition sensitivity of a powder is mainly affected by the presence of fine particles (Saeed et al., 2019).

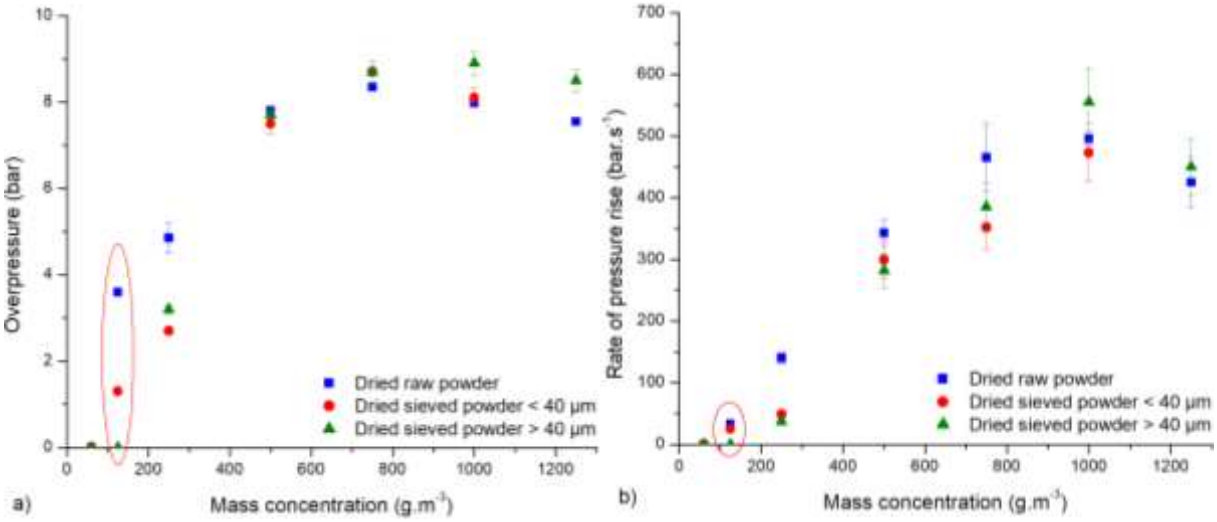

Figure 5-3 Effects of nanocellulose sieving on a) the maximum overpressure and b) the maximum rate of pressure rise

To further investigate on the influence of fine particles on the ignition sensitivity, ignition energy tests were conducted in the modified Hartmann tube. As previously mentioned, the minimum ignition energy of the raw dried powder was evaluated at 5 mJ. After drying and sieving at 40 µm, both obtained fractions also presented minimum ignition energies of 5 mJ. However, when drying the nanocellulose and selecting only a PSD greater than 70 µm by the

same previously described sieving protocol, the bigger fraction exhibited a minimum ignition energy of 14 mJ. The effects of the presence of fine particles on the ignition sensitivity were then also observed concerning the minimum ignition energy, despite the shift of the critical agglomerate size. This latter may be explained by the different dispersion procedure (lifting by an air pulse of 7 barg), and testing conditions, in terms of volume, concentration and homogeneity, that directly impact the measurements. Moreover, sieving is not an accurate separation method, as small agglomerates can also be physically coated to bigger ones and be present in the samples of larger PSD. Furthermore, only one dimension smaller than the mesh is sufficient for an agglomerate to be retrieved in the low fraction, independently from its volume. It also has to be underlined that a hand sieving was performed to avoid the breakage of the agglomerates, which decreases the reproducibility of the process.

V.1.2. Effects of mechanical agglomeration

Since the agglomerates that naturally exist in the raw powder are too easily breakable to evaluate the influence of the particle size distribution on the explosion severity, artificial agglomeration was realized. The effects of a mechanical agglomeration were investigated on nanocellulose and starch, which were dried, compressed, ground and sieved, and on different agglomerated samples of carbon-coated silicon directly supplied by Nanomakers (Rambouillet, France).

V.1.2.1. Organic powders

Product characterization

To avoid the influence of humidity of the powder, the nanocellulose was dried under vacuum at 90°C. It was then compressed without additive using a press (Instron 5569) to form tablets, with a maximum force applied of 40 kN. The tablets were then ground and sieved between 32 and 180 µm. Indeed, this range is higher than the size range of the natural agglomerates (mean surface diameter 48 µm), and the agglomerates are still small enough to lead to an explosion when dispersed in adequate conditions (concentration, ignition source…). Scanning Electron Microscopy was performed on the raw and agglomerated samples to visualize the difference of structure of the two samples (Figure 5-4). It should be noted that all the SEM experiments were conducted in dry conditions.

In Figure 5-4a, different agglomeration levels within the raw powder are visible, from small agglomerates of less than 1 µm to big agglomerates of a few dozens of micrometers. Figure 5-4b then shows an agglomerate obtained after the compaction process, reaching around 100 µm diameter, which is consistent with the sieving range and confirms the efficiency of the agglomeration process of the powder.

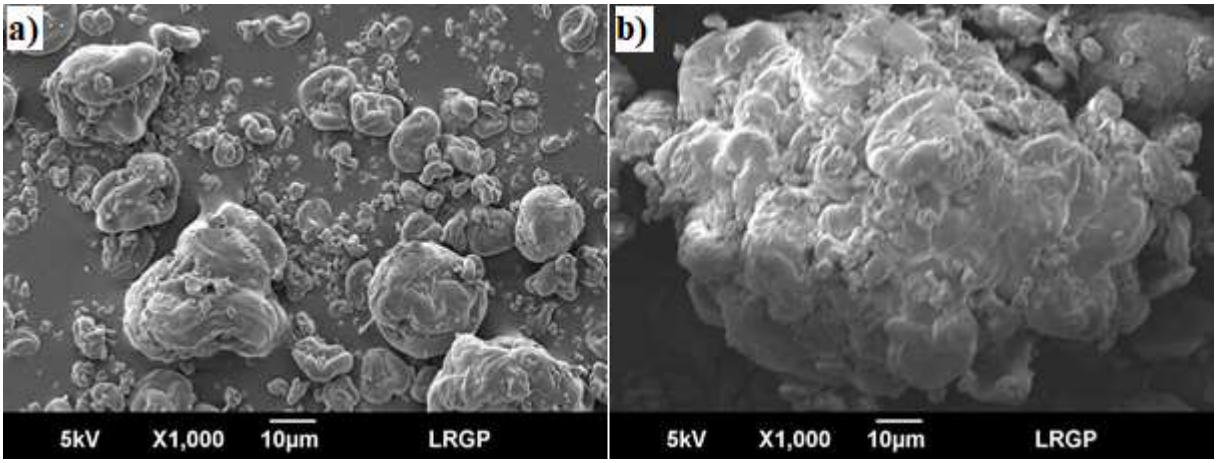

Figure 5-4 Nanocellulose observed by Scanning Electron Microscopy a) Raw powder b) Agglomerated powder

Dispersion tests were performed in the 20L sphere in standard conditions to evaluate the particle size distribution of the dust cloud, evidencing a slight shift toward bigger agglomerates (Figure 5-5). The mean surface diameter after dispersion of the raw and agglomerated dispersed samples are then respectively 10.4 µm and 15.8 µm (shown by the dotted lines). More specifically, no agglomerate higher than 60 µm can be observed, traducing the fact that the agglomerates are fragmented by the high shear stress induced by the dispersion in the 20L sphere. This trend confirms that the injection procedure breaks the agglomerates until recovering primary aggregates, i.e. clusters of particles irreversibly bounded, or strongly bounded agglomerates. Nevertheless, fine particles smaller than 1 µm were observed with the raw powder, whereas no particle smaller than 3 µm was identified in the agglomerated powder, traducing a different fragmentation efficiency of the agglomerates.

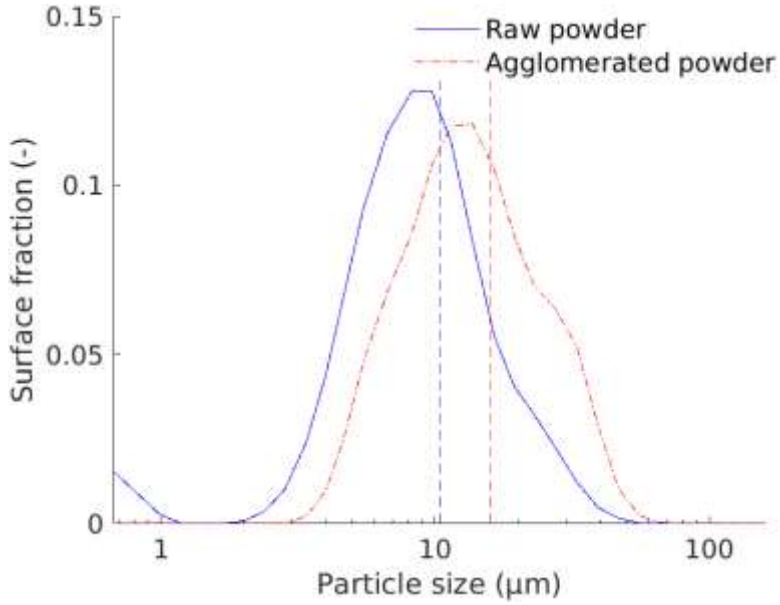

Figure 5-5 Particle size distribution of the raw and agglomerated nanocellulose after dispersion in the 20L sphere (mean surface diameter represented by the dotted line)
[106]

The production of the agglomerates was very time-consuming and technical issues occurred on the press, preventing further investigations on nanocellulose during this work. Nevertheless, agglomeration experiments were previously carried out on a micron starch powder (Santandrea et al., 2019a). Even if these tests do not concern nanopowders, they are presented as they demonstrate the major influence of the reactive surface developed by a dust cloud on the explosion severity, which is obviously also the case for nanoparticles.

The starch powder was therefore compressed and ground, as previously described, and sieved between 224 µm and 450 µm to form bigger agglomerates and see a modification in the PSD after dispersion (Figure 5-6). However, mean surface diameters of 12 µm and 14 µm were respectively observed after dispersion of the raw and agglomerated powders, evidencing once again the strong fragmentation during the dust injection process.

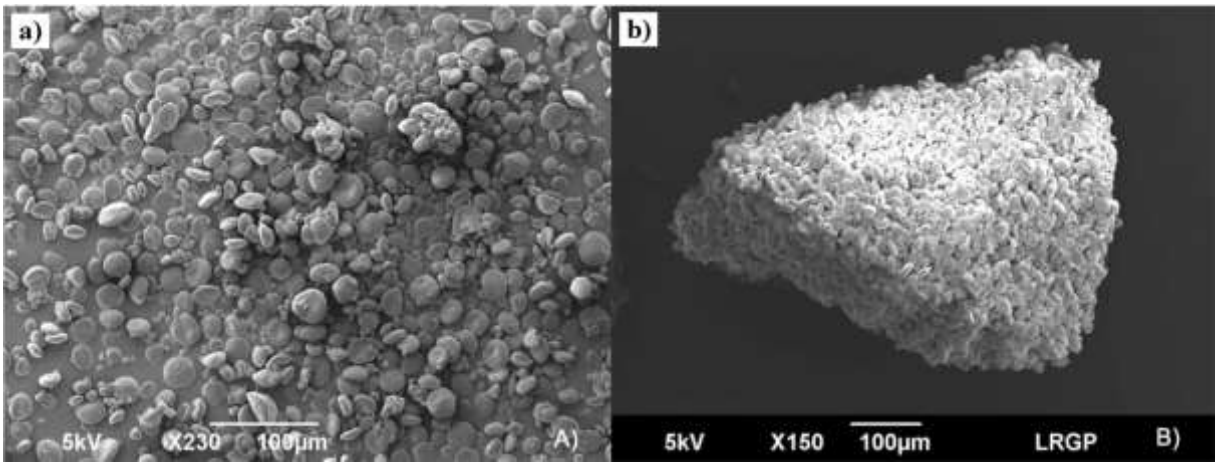

Figure 5-6 SEM images of a) raw starch powder and b) a starch agglomerate generated by dry granulation

Explosion severity measurements

Explosion tests were performed in standard conditions on both starch samples. If similar evolutions of the explosion overpressure with the mass concentration were obtained, a shift was observed concerning the evolution of the rate of pressure rise with the mass concentration (Figure 5-7a). Indeed, the same values of $(dP/dt)_{max}$ were measured for both samples, but at different mass concentrations. Although the mass concentration is useful for the transposition of experimental data on an industrial scale, this representation gives very little information about the mechanisms involved in the dust explosion. Various limitations are encountered during the explosion of an organic powder. The devolatilization step of the particle can be controlled by internal or external heat transfer. In the case of starch particles or agglomerates, as in the case of many organic particles smaller than approximately 300 µm, both Biot and Damköhler numbers, defined in section IV.1.5, are lower than unity, which excludes the possibility of a heat transfer limitation (Di Benedetto et al., 2010). The explosion can also be controlled by the reactions occurring in heterogeneous phase or between the pyrolysis gases and oxygen. By considering the formalism of the shrinking core model, the rate-controlling step

will depend on one of the following three phenomena: diffusion through the gas film, diffusion through the ashes/porous shell, surface reaction. By considering the specific surface area of the powder, and more exactly, the total reactive surface of the fuel exposed to the oxidizing agent, a first selection of the rate-limiting steps can be made.

Considering spherical particles and a particle density of 615 $g.m^{-3}$ (Murillo, 2016), specific surface area after dispersion of 0.81 $g.m^{-2}$ and 0.68 $g.m^{-2}$ were respectively calculated for the raw and agglomerated powders. When analyzing the evolution of the rate of pressure rise with the surface concentration (Figure 5-7b), it appears that the offset between the raw starch and its agglomerates disappears or, at least, is less perceptible. A maximum rate of pressure rise of 355 ± 40 $bar.s^{-1}$ was then measured for a surface concentration of 810 $m^2.m^{-3}$. The consumption rate being considered as proportional to the particle/agglomerate surface, a limitation due to the diffusion through the ashes or porous shell can be excluded.

As a conclusion, the combustion is certainly controlled by the surface reaction or diffusion of oxygen onto the surface. Although the powder was not constituted of nanoparticles, this finding clearly highlights the influence of the reactive surface on the combustion reaction. Due to the small size and high specific surface area of nanoparticles, this effect will then be even more heightened for nanopowders. In such cases, the reactive surface should be considered instead of the mass concentration for a better representation of the combustion phenomenon.

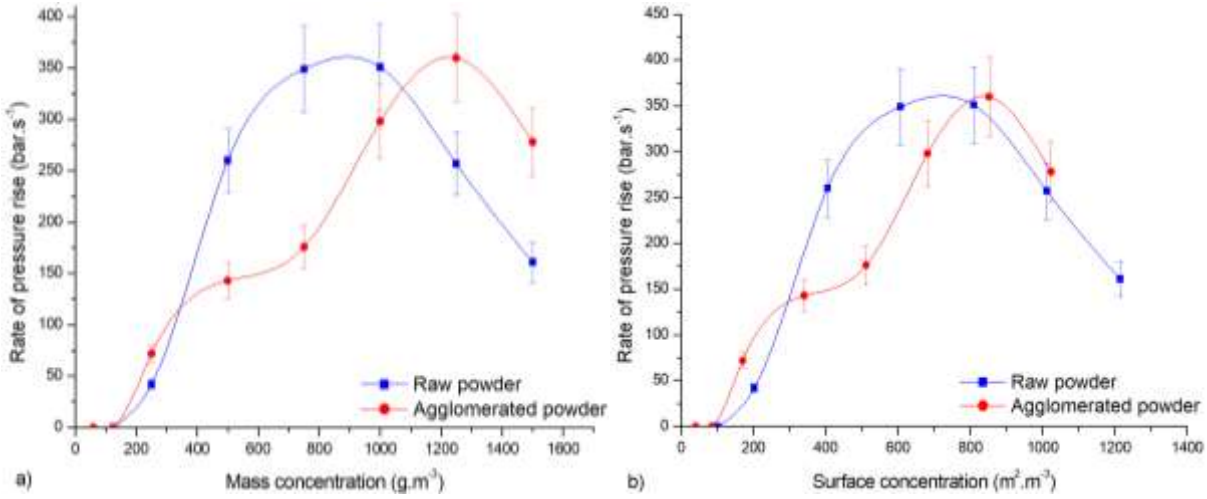

Figure 5-7 Evolution of the rate of pressure rise with a) the mass concentration and b) the overall surface concentration

V.1.2.2. Carbon-coated silicon

Product characterization

The effects of a mechanical agglomeration were also investigated on carbon-coated silicon, noted "SiΩC", through different agglomerated samples directly supplied by Nanomakers. Due to the low density of the nanoparticles, such modification notably facilitates the transportation of the powder, increases the powder flowability, and can also decrease the ignition sensitivity

and explosion severity, which will be investigated in this section. In this sense, this type of modification could be considered as a direct application of the moderation principle of inherent safety (Amyotte et al., 2007; Dufaud, 2011).

Four samples constituted of the same powder with different densities, agglomerates sizes and cohesion strengths were then studied in this work: the raw powder of primary diameter of 40 nm and density of 40 $g.L^{-1}$, two samples agglomerated according to a process noted 'process A' with densities of respectively 260 $g.L^{-1}$ and 400 $g.L^{-1}$, which will be noted powders A1 and A2, and a sample agglomerated according to a 'process B' with a density of 400 $g.L^{-1}$, noted sample B. The specific processes of agglomeration are confidential and unfortunately cannot be described here (Nanomakers). Experiments performed with a helium pycnometer led to skeletal densities around 2.3 ± 0.05 $g.cm^{-3}$ for all the powders, except for the powder A2 which exhibited a skeletal density of 2.5 ± 0.05 $g.cm^{-3}$ was obtained. Scanning Electron Microscopy analyses were performed on each sample in dry conditions to visualize the shape modifications due to the agglomeration (Figure 5-8).

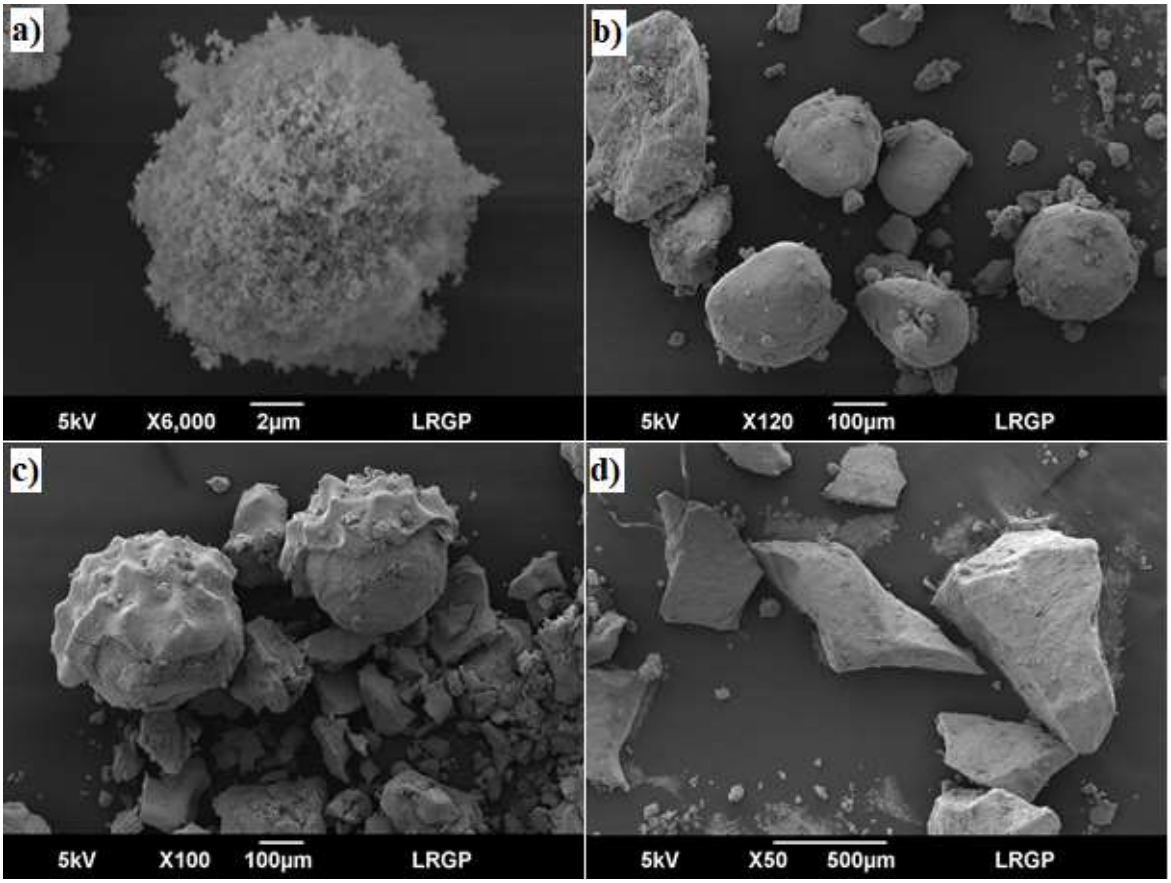

Figure 5-8 Carbon-coated silicon observed by Scanning Electron Microscopy a) Raw powder b) Sample A1 (260 $g.L^{-1}$) c) Sample A2 (400 $g.L^{-1}$) d) Sample B (400 $g.L^{-1}$)

The raw powder appears to be constituted of small spherical agglomerates of apparent diameters lower than 10 µm, as shown in Figure 5-8a. The modified powders also present the same kind of agglomerated structures, but also bigger agglomerates. Indeed, the powder A1 seems

essentially composed of big 'roughly spherical' agglomerates with a diameter around 100 to 200 µm (Figure 5-8b). Similar agglomerates can be found in the sample A2, but with agglomerates size around 300 µm (Figure 5-8c). Finally, when using the process B to agglomerate the powder, non-spherical agglomerates with an average size reaching 500 µm were formed (Figure 5-8d).

The mean diameter of the different samples was also measured by wet dispersion in ethanol using a Mastersizer 2000 S (Malvern Instruments). Analyzing the wet dispersion measurements presented in Table 5-2, it appears that all the agglomerated samples present a mean diameter much higher than that of the raw powder, i.e. 68 µm, and that the powder B exhibits the highest diameter, reaching 442 µm, which is consistent with the SEM observations. However, when regarding the powders agglomerated by process A, it seems that the powder A1 is more agglomerated that the powder A2, which is inconsistent with SEM measurements. Once again, it should be kept in mind that the wet dispersion in ethanol modifies the interactions between particles (variation of zeta potential) and does not provide accurate information concerning the particle size distribution of a powder in air.

Table 5-2 Mean diameter of the different samples of carbon-coated silicon measured by sedimentation and wet and dry dispersion

	Raw powder	Sample A1	Sample A2	Sample B
Mean diameter by wet dispersion in ethanol (µm)	68	352	261	442
Mean surface diameter by sedimentation – R5 lens (µm)	207	249	132	297
Mean surface diameter by sedimentation – R3 lens (µm)	30	26	32	20
Mean surface diameter after dispersion in the 20L sphere (µm) – R1+R3+R5 Helos diffraction sensor	9	4	3.5	12
Mean surface diameter after dispersion (Scirocco) (µm)	3.5	5.3	5	20

The surface diameter was then also measured by sedimentation of the powder using two lenses of the laser diffraction sensor: R3 and R5 (Table 5-2). Unfortunately, the R5 lens was calibrated at the end of this thesis work, and only experiments on the carbon-coated silicon could be performed. This lens allows the measurement of particles from 4.5 to 875 µm, inducing that the agglomerates observed by SEM can be observed. First, the powder B is then confirmed to be the most agglomerated ($d_{50,R5}$ = 297 µm), although this was not visible using the R3 lens. Then, the sample A2 presents a lower mean diameter than the sample A1, which is conversely

proportional to the particle density and confirms the measurements performed by wet dispersion. Finally, the raw powder presents a mean surface diameter of 207 µm, which is considerably higher than the size of the agglomerates observed by SEM. It should be reminded that this lens does not allow the measurement of particles smaller than 4.5 µm, implying that the small agglomerates may not have been measured by the apparatus.

To estimate the PSD during the combustion and specifically at the moment of ignition, dispersion tests were performed with the laser diffraction sensor coupled with the visualization 20L sphere. Nevertheless, as seen in Table 2, each lens give a peculiar and useful information on the PSD, but in the case of a nanopowder, a more global view is necessary. Unfortunately, as previously said, no apparatus currently allow such a measurement (from nm to hundreds of micrometers) at high frequency and concentration. An alternative solution could consist in using the same in-situ laser sensor and repeating three times (at least) the same dust dispersion experiment with the three lenses (R1, R3 and R5). In order to normalize the intensities of the peaks, it may be useful to insert an internal reference (nearly monomodal powder of low and fixed concentration, with a narrow PSD which does not interfere with the studied powder). An instance of such application for carbon-coated silicon is given in Figure 5-9.

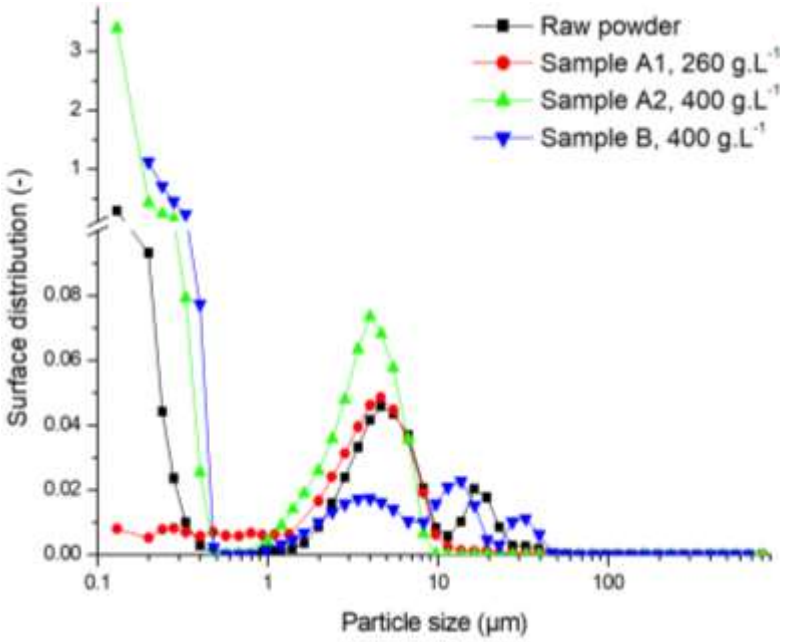

Figure 5-9 Particle size distribution of the four samples of carbon-coated silicon after dispersion in the 20L at the moment of explosion (R1-R3-R5 lenses)

Figure 5-9 allows the visualization of the PSD of the nanopowders over a wide range of size (from 0.1 µm to 875 µm). It appears that sample B (400 g.L-1) presents the biggest agglomerates after dispersion in the sphere, with modes at 4, 15 and 35 µm (omitting the primary particles and nanometric agglomerates). The powders A1 and A2 show the smallest agglomerates after dispersion, with mean surface diameters of 4 and 3.5 µm, respectively (Table 2). The raw SiΩC powder, in addition to the common agglomeration mode at

approximately 4 µm, also presents larger structures around 20 µm (Figure 5). It should be noticed that, unlike the other samples, no significant peak is obtained for the powder A1 at particle size lower than 0.5 µm which may seem surprising and requires additional tests with R1 lens.

These observations can lead to several comments:

i) The measuring range being limited at 0.1/0.2 µm, the particle size distributions may be different below this value, and the presence of individualized nanoparticles is certainly more marked for the raw powder.

ii) During the agglomeration process, especially with process A, the structure of the initial agglomerates could have been weakened, reducing the cohesion strength of these initial agglomerates. During particle size measurements by wet dispersion or by sedimentation in air, their structure is not significantly modified. On the contrary, the very high shear rate induced by the dispersion in the 20L (pressurization at 20 bar) can break these agglomerates, demonstrating the existence of a threshold stress.

Finally, the PSD after dry dispersion using the Scirocco device, described in section III.2.2.2 was also measured with the Mastersizer 2000 particle size analyzer (Malvern Instruments). The results, presented in Table 5-2, are consistent with the SEM images, as the powder B seems the more agglomerated, with a mean surface diameter of 20 µm, and the raw powder presents the smallest particles and a mean surface of 3.5 µm. It should be noted that the shear stress induced by the dispersion in the Scirocco device is much lower than that induced during the injection in the 20L sphere, notably due to a lower dispersion pressure (2 barg). Such values then tend to show that the initial agglomerates are broken during the dispersion in the 20L sphere, but not in the Scirocco device, which corroborates the assumption considering that the initial agglomerates were weakened during the mechanical agglomeration of the powder. However, a whole characterization of the particle size distribution, from the nanometer to several hundred of micrometers, is necessary to conclude on this phenomenon. Unfortunately, as previously said, no apparatus currently allow such a measurement at high frequency and concentration.

Explosion severity measurements

Explosion tests were then performed on each sample in the standard 20L sphere (Figure 5-10). First, it should be noticed that the increase of overpressure and rate of pressure rise with the dust concentration is very fast, which tends to decrease the accuracy at the ‘transition’ concentration, i.e. 125 $g.m^{-3}$. Indeed, in this transition zone, a small variation in the dust concentration can greatly impact the pressure-time evolution. The maximum overpressures obtained are similar independently from the agglomeration state of the sample, reaching around 8.8 bar (Figure 5-10a), which implies that the same amount of powder seems to react according to the same reaction mechanisms. From the observation of the overpressure evolution with the concentration, agglomeration seems to have a limited effect on the thermodynamics development of the explosion. On the other hand, significant differences appear when regarding

the maximum rate of pressure rise obtained for each powder (Figure 5-10b). The raw powder leads to the most severe explosion, with a maximum rate of pressure of 944 ± 118 bar.s^{-1}. The theoretically less agglomerated powder, i.e. powder A1, is slightly less severe and reaches 822 ± 98 bar.s^{-1}. Both powders are then classified in the St2 class, with explosivity index K_{St} of respectively 256 ± 32 bar.m.s^{-1} and 223 ± 27 bar.m.s^{-1}. The explosions induced by the powders agglomerated with a density of 400 g.L^{-1} are less severe, reaching 713 ± 85 bar.s^{-1} for the sample A2 and only 556 ± 60 bar.s^{-1} for the sample B, which ranks both powders as St1.

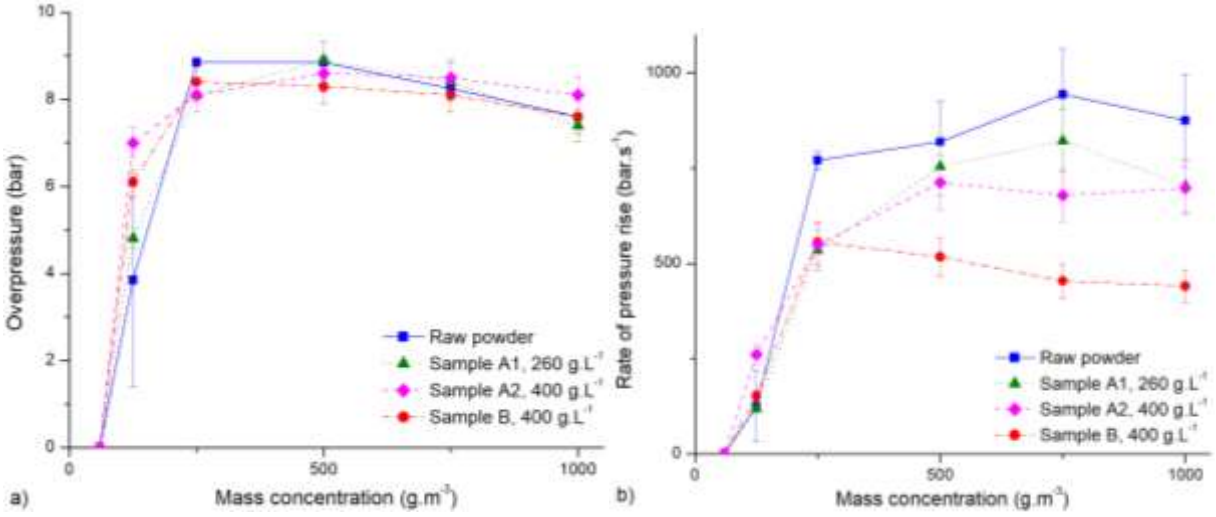

Figure 5-10 Evolution of the a) maximum overpressure and b) maximum rate of pressure rise with the mass concentration of the four samples of carbon-coated silicon

The explosion severity results performed in standard conditions then showed that the same maximum overpressure is obtained while the maximum rate of pressure is affected by the agglomeration state of the powder. Since the mechanical agglomeration does not modify the specific surface area (Nanomakers, 2019), such modification cannot be attributed to this parameter. On a similar way than for the starch powder, a total reactive surface area developed after dispersion was approximated considering spherical agglomerates, the density of each powder and the mean surface diameter measured after dispersion in the 20L sphere. The evolution of the overpressure and rate of pressure rise with the surface concentration are then presented in Figure 5-11.

Contrary to the deviation observed for the starch powder, the correlation of the explosion severity with the total surface of the agglomerates does not seem adequate for the carbon-coated silicon. Indeed, the combustion of organic powder is limited by the pyrolysis step or by the surface reaction of the particles (Di Benedetto et al., 2010), whereas the carbon-coated silicon does not undergo the pyrolysis step. Since the combustion does not occur in gaseous phase, the distance between the particles is of great importance. Indeed, increasing the concentration reduces this distance, leading to a transition between the combustion of the individual particle (small concentration) to a group combustion at higher concentrations. This can notably explain the strong difference of explosion severity observed between 125 g.m^{-3} and 250 g.m^{-3} for the

four samples. Thus, no direct relation exists between the explosion severity parameters and the total surface developed by the agglomerates, as the mechanisms change with the distance between the particles.

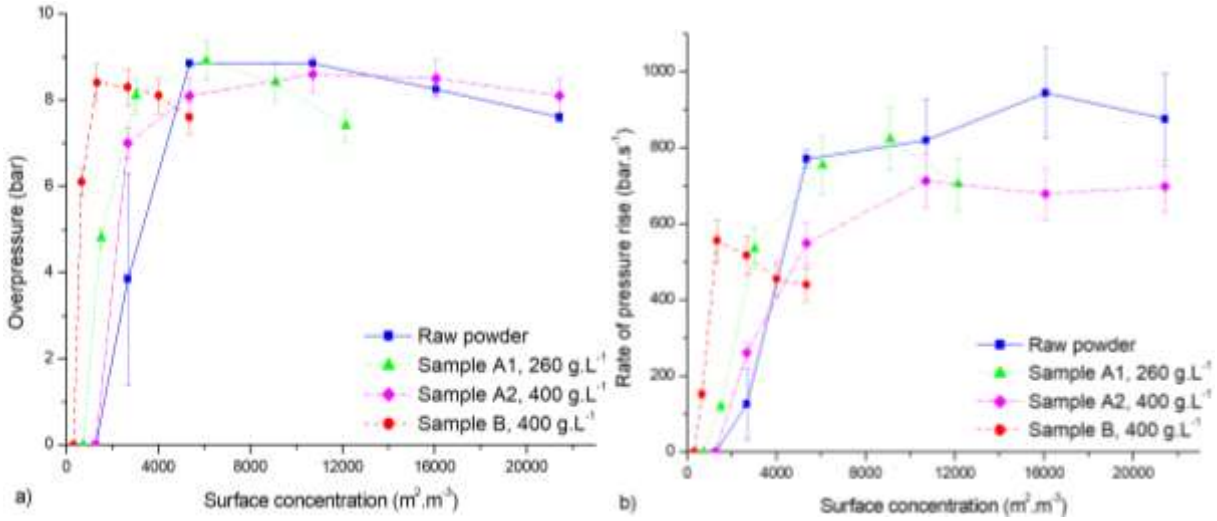

Figure 5-11 Evolution of the a) maximum overpressure and b) maximum rate of pressure rise with the surface concentration of the four samples of carbon-coated silicon

Since the combustion of silicon consumes oxygen and produces silica, the final pressure in the sphere is lower than the atmospheric pressure, inducing that no combustion gases can be collected nor analyzed. However, the stabilized pressure after explosion can provide information on the combustion gases production and oxygen consumption. Since the combustion of the carbon leads to the production of, among others, carbon monoxide and dioxide, the amount of oxygen consumed cannot be precisely quantified due to the unknown production of combustion gases. Nevertheless, in light of the similar measured overpressures, it was previously established that the reaction mechanisms and products were not affected by the agglomeration state. The same amount of combustion gases is then assumed to be produced during the combustion of carbon for each sample. Thus, the analysis of the pressure after explosion can allow a comparison of the amount of oxygen consumed during the explosion of each sample (Figure 5-12a).

To evaluate the combustion mechanisms, two hypotheses were investigated. First, successive reactions were considered: the carbon reacts first, followed by the silicon. The second hypotheses consists in simultaneous reactions of the carbon and the silicon. The considered reactions are the formation of carbon dioxide from the carbon and oxygen, and the reaction of silicon with oxygen to form silica. Knowing that the particle diameter is 40 nm with 2 nm of coating, a molar proportion of 38% of carbon and 62% of silicon was considered. For each concentration, the remaining oxygen after the combustion of the raw powder was estimated in both cases, and, considering that the nitrogen does not react, the final pressure after explosion was estimated. It then appears in Figure 5-12b that the experimental final pressure seems to follow the same evolution than in the case of simultaneous reactions of carbon and silicon.

However, the value experimentally measured at 125 $g.m^{-3}$, around 0.97 bara, corresponds to the value calculated at 60 $g.m^{-3}$. This shift may be due, as previously explained, to a variation from an individual contribution of the particle to a group contribution of the agglomerates. The powders agglomerated by the process A, i.e. powders A1 and A2, follows the same evolution of the raw powder with a final pressure stabilized around 0.87 bara. On the contrary, the final pressure obtained after combustion of powder B stabilized around 0.89 bara, which can traduce a different combustion mechanism. This difference can come from the agglomeration process, which may have induced a decrease in the specific surface area, or at least in the surface available for the combustion after dispersion, which would explain the lowest explosion severity.

However, when the combustion is limited by the diffusion of oxygen toward the particle surface, the fractal dimension, i.e. the shape of the agglomerate, can impact the accessibility of oxygen to this surface. A simulation based on Monte Carlo methods is presented in Appendix 2 to evaluate the influence of the fractal dimension of an agglomerate on the accessibility of oxygen to its surface. It was notably shown that an accessibility difference of 20% can appear between a linear agglomerate (fractal dimension equal to 1) and a spherical agglomerate (fractal dimension equal to 3), which can also explain the differences in the explosion severity observed between the sample B and the other samples.

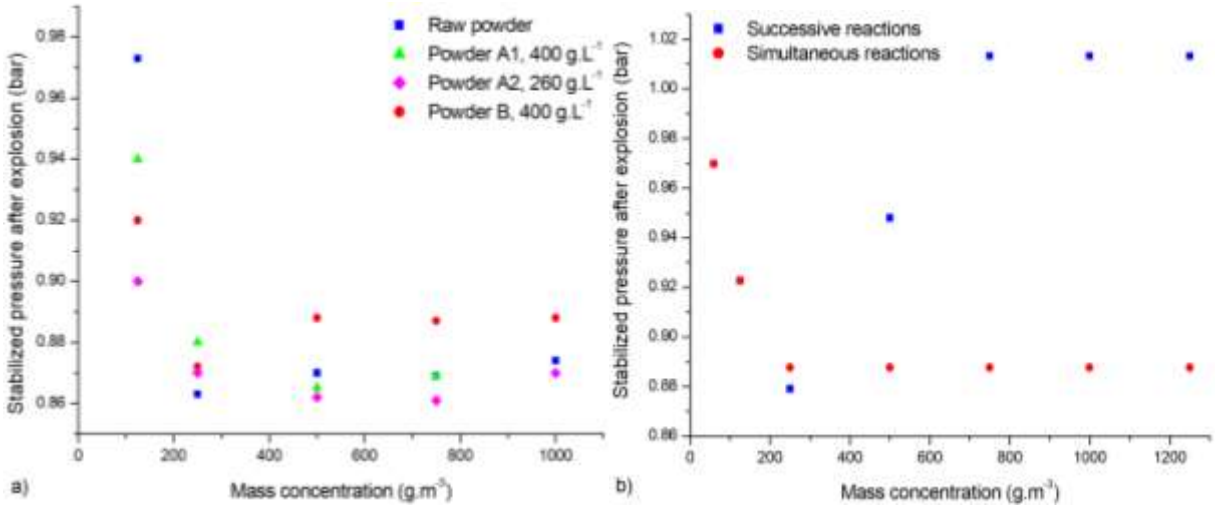

Figure 5-12 Evolution of the stabilized pressure after explosion in the 20L sphere with the mass concentration a) experimentally measured for the different samples of carbon-coated silicon b) calculated for the raw powder

As a conclusion, the agglomeration of the carbon-coated silicon significantly decreased the explosion severity, which can be due to a combination between the modification in the available reactive surface area after dispersion and to a modification of the combustion behavior, from an individual to a group contribution. Such effects will now be investigated on the ignition sensitivity of the powder.

Ignition sensitivity measurements

In addition to the experiments conducted in the 20L sphere, the minimum ignition energy of the different powders was determined in the modified Hartmann tube. While the minimum ignition energy of the raw powder was evaluated at 5 mJ, no ignition was observed at 1J for the three other samples when varying the dust quantity from 0.6 to 1.8 g and the ignition delay time from 90 ms to 150 ms. Although some glowing particles were observed when testing the sample agglomerated at 260 $g.L^{-1}$ by process A, no flame was obtained. The agglomeration then appears to significantly reduce the ignition sensitivity of this dust concerning the energy to provide to obtain an explosion. As shown in Figure 5-10, the lowest concentration for which an explosion was obtained at 10 kJ is the same for all the samples, i.e. 125 $g.m^{-3}$. Since these tests were performed at 10 kJ, additional tests should be conducted with the standard ignition energy to apply to determine the LEL, i.e. 2 kJ (EN 14034-3, 2006). Still, the LEL does not seem modified with the agglomeration state of the powder, which can notably be explained by the strong fragmentation of the agglomerates during the dispersion in the 20L sphere. Indeed, the agglomerates submitted to the high shear stress of the injection device in the 20L sphere tend to break more easily than the agglomerates lifted by the air pulse in the modified Hartmann tube, which give them ignition properties similar than the raw powder.

V.2. To the last drop: influence of humidity

‘ The maximum explosion pressure increases with decreasing moisture content. Therefore the moisture content shall be determined for the sample as tested and given in the test report.’
(EN 14034-1-2, 2004; 2006)

Humidity can greatly influence the explosion behavior of micropowders (Traoré et al., 2009; Yuan et al., 2014). It should be reminded that, when dealing with metal powders, the explosion severity can be increased by the dust moisture because of water reduction onto the particle surface and hydrogen generation occurring at high temperatures. For organic nanoparticles, such phenomenon will not take place, but other effects of the presence of water have to be considered. In this part, a focus is realized on the sample preparation through an aging phenomenon and the moisture content of the powder, and their influence on the explosion severity was then highlighted.

V.2.1. Powder aging

Powder characterization

Two of the studied powders, the carbon black and the aluminum 100 nm were stored for 11 years under ambient air. The aging effects on the explosion severity were notably discussed by Santandrea et al. (2019b). Since the aluminum 100 nm does not show significant size variation on Scanning Electron Microscopy images, and that the effects of the probable passivation of

the powder during the storage on the explosion severity were already discussed in section IV.2.2., focus is realized on the carbon black powder. SEM images of carbon black reveal that the size of the agglomerates varied along the time It can be outlined from Figure 5-13 that 11 years of storage promoted the enlargement of the agglomerates of carbon black (from 100 µm to 1 mm), which is also visually perceptible. Such phenomenon leads to a modification of the surface area-to-volume ratio of the agglomerates and then changes their properties (Yeap, 2018).

The water activity Aw, which is the partial vapor pressure of water divided by the standard state partial vapor pressure of water, was measured on the raw carbon black powder, and after vacuum drying at 90°C. When drying the powder, the Aw decreases from 0.4 to 0.03. However, by waiting 1 or 15 minutes before measuring the water activity, the Aw increases and reaches respectively 0.11 and 0.22. Because of the high specific surface area, nanoparticles are prone to adsorb vapors and especially water, as a function of their chemical nature. SEM images also showed that the drying step leads to a partial breakage of the agglomerates (Figure 5-13c), which confirms that the aging is mainly due to humidity.

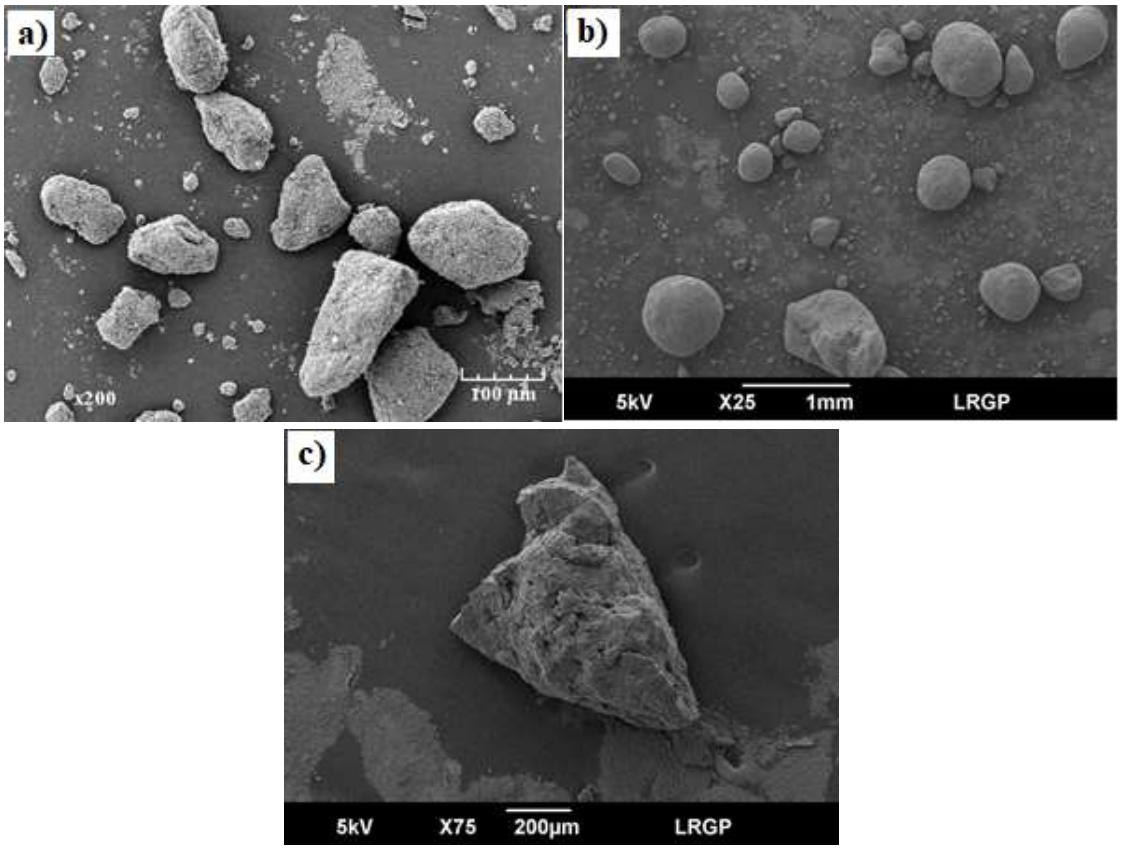

Figure 5-13 SEM image of carbon black agglomerates in a) 2006, b) 2017 (raw powder) and c) 2017 (dry powder)

Explosion severity measurements

To evaluate the impact of aging on the explosion severity, explosion tests were conducted on the carbon black under standard conditions on the raw and dried powders, and the results were

compared to the ones obtained in 2006 (Figure 5-14). The maximum explosion overpressure of carbon black is not significantly modified by aging (Figure 5-14a). However, the maximum rate of pressure rise greatly decreases with the aging of the particles (Figure 5-14b): it drops from 503 bar.s^{-1} (Bouillard et al., 2010) to 242 bar.s^{-1}, which is probably due to a change in the PSD and to the water adsorbed. Despite the partial breakage of the agglomerates when drying the powder, similar rates of pressure rise were measured for the raw and dried powders in 2017. Unfortunately, no in situ measurements were performed in 2006, making impossible a comparison of the PSD of the dust cloud at 60 ms, before and after aging. Nevertheless, as demonstrated in chapter 3, the agglomerates do not fragment completely during their injection (Yeap, 2018), and the presence of bigger agglomerates can impact the final PSD of the carbon nanoparticles in the sphere, thus reducing the overall surface/volume ratio of the powder and its reactivity. Indeed, since the evolution of the P_m with the concentration is similar in 2006 and 2017 (either dried or not) (Figure 5-14a), the same thermodynamics are applied during the explosion, meaning that the same amount of powder reacted. On the contrary, the rate of pressure rise, describing the kinetics, is greatly affected. Specific attention must therefore be paid when storing nanoparticles before testing them, as the moisture content can greatly influence both the particle size and the combustion reaction and can increase rapidly in the powder when exposed to air.

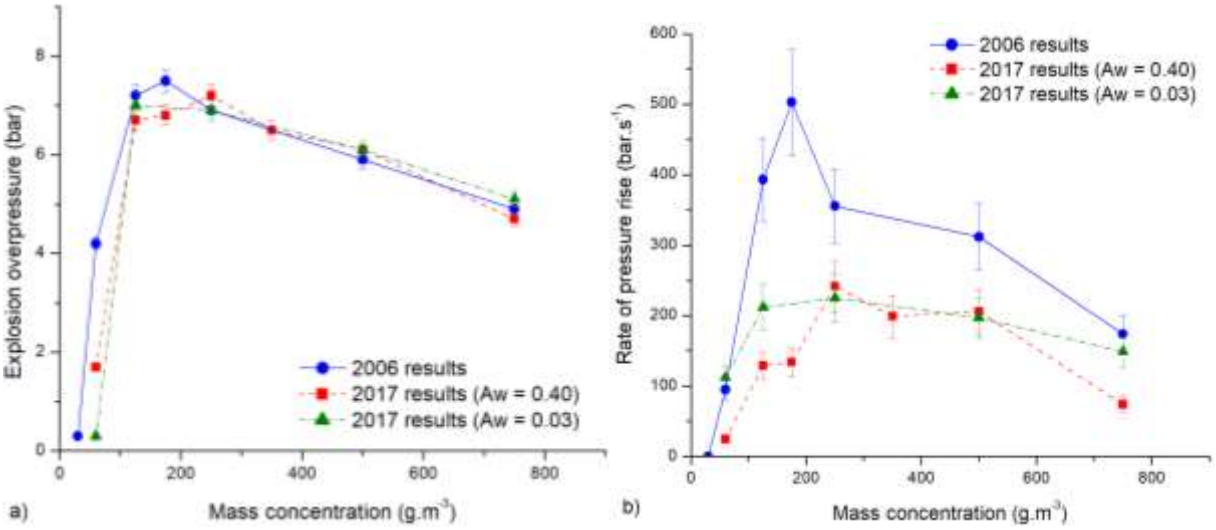

Figure 5-14 Evolution of the explosion a) overpressure and b) rate of pressure rise with the concentration for carbon black powder in 2006 and 2017 (raw and dry)

V.2.2. Influence of water activity on dust explosions

The tendency of nanoparticles to adsorb water, highlighted in section V.2.1, raises some questions concerning the dust preparation before the tests. Indeed, as an example, the process safety engineer uses nanopowders in a dry form in his processes. However, in the absence of special precaution during the transport and storage before performing ignition and explosion tests, the powders can absorb water from ambient atmosphere. The influence of water on dust

explosions, although often not well developed by current standards, was then investigated on nanocellulose and carbon black powders (Santandrea et al., 2019c, 2020c).

European standards EN 14034 stipulate that the moisture content 'shall be determined for the sample as tested and given in the test report'. The presence of water can either come from the moisture content of the powders or the water vapour present in the explosive atmosphere. Indeed, combustion gases collected after explosions of dried carbon black nanopowder and analysed by gas chromatography revealed the formation of hydrogen during the combustion. This may may seem surprising when it comes to the oxidation of pure carbon. It should not be forgotten that, during the injection procedure, the 20L is initially vacuumed at 0.4 bar absolute. Hence, for a relative humidity of 0.4, the initial molar percentage of water in the sphere is 0.36%. At high temperature, the water can react with carbon monoxide to generate carbon dioxide and hydrogen (Wagman et al., 1945). Therefore, even when performing the powder injection with synthetic air, the water contained in the residual air of the sphere can impact the chemical reactions occurring during the explosion. This statement is especially true if the particles react directly with water (for instance, hydrogen generation with metals by water reduction) and if their specific surface area is large, which is the case of nanopowders.

In order to highlight the potential influence of the relative humidity of the air remaining in the sphere after vacuuming it at 0.4 bara, experiments were performed by flushing it several times with synthetic air before starting the test procedure. By adopting this procedure, the water content in the sphere before dust injection theoretically decreases from $0.4\%_{mol}$ to $0.1\%_{mol}$.

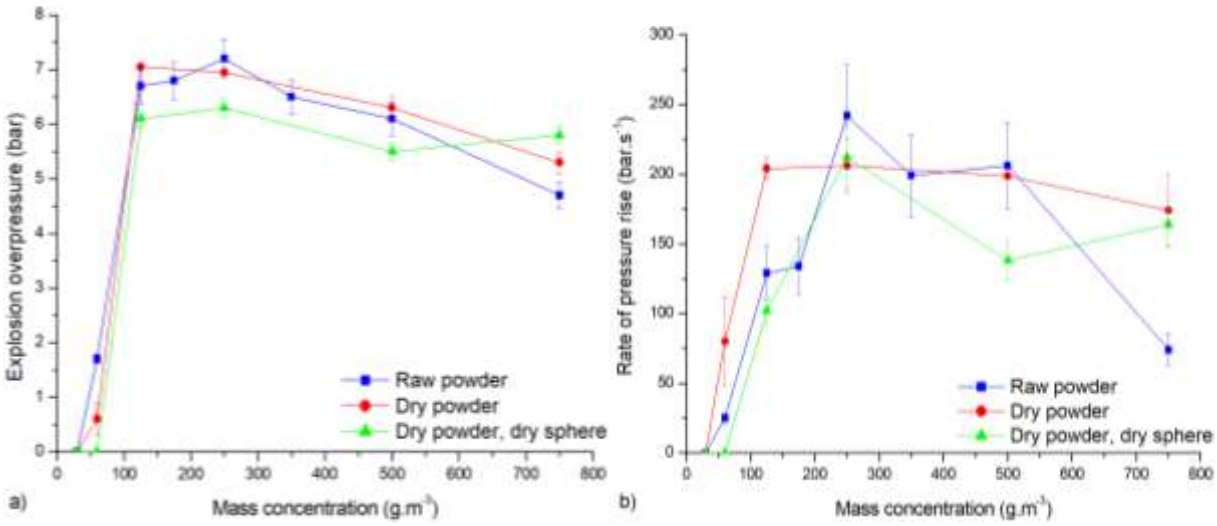

Figure 5-15 a) Overpressure and b) rate of pressure rise of raw or dried carbon black as a function of the relative humidity in the 20L sphere

Figure 5-15a shows that similar overpressure evolutions are obtained whatever the powder treatment or the test procedure. Nevertheless, a maximum overpressure of 7.2 bar was obtained with the raw powder and a standard injection whereas it only reached 6.3 bar when drying both the powder and the sphere. In addition, the maximum rate of pressure rise (Figure 5-15b)

obtained with the raw powder is, as expected, significantly greater than with the dried powder. These differences can be due to a contribution of the formed hydrogen to the explosion.

After the explosion of dried powder in the dried sphere, the combustion gases were once again collected and analyzed (Figure 5-16).The hydrogen content appears always greater when using the standard procedure, which highlights the influence of the relative humidity of the air on the combustion mechanisms taking place during an explosion. These examples show that variations (in storage time, relative humidity, water activity) that may seem insignificant have a significant impact when it comes to the explosion severity of nanoparticles.

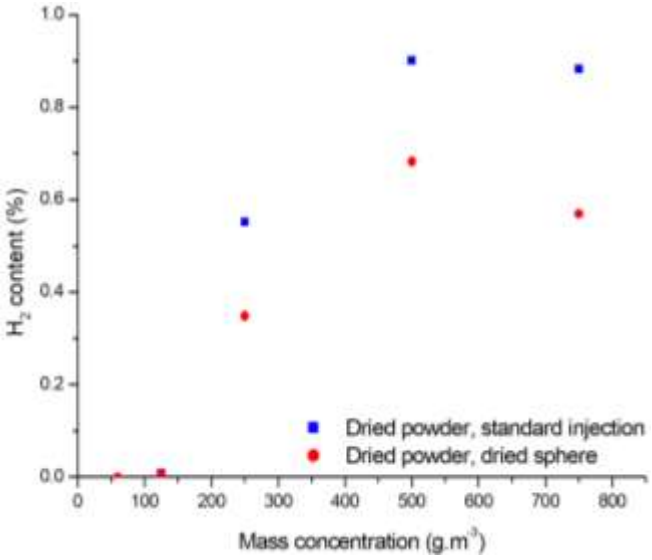

Figure 5-16 Hydrogen content in the burnt gases after dried carbon nanopowder explosion in the 20L sphere using standard or modified injection procedure

Ignition and explosion tests were also carried out on raw (Aw = 0.23) and dried nanocellulose (Aw = 0.03 after drying under vacuum at 90°C) (Santandrea et al., 2020c). The water activity, the PSD obtained by sedimentation and after dispersion in the 20L sphere, the minimum ignition energy as well as the explosion parameters are presented in Table 5-3. The PSD of the raw and dry samples of nanocellulose was measured before and after dispersion and remains unchanged, which shows that the agglomeration state of the powder was not affected by the drying process. Thus, the influence of water activity can be specifically assessed for the ignition and explosion severity.

Similar maximum overpressures were measured for the dried and raw nanocellulose, reaching respectively 8.3 bar and 8.1 bar at 750 $g.m^{-3}$, meaning that the thermodynamics are barely affected by the humidity of the powder. The maximum rate of pressure rise increased from 435 $bar.s^{-1}$ from the raw sample to 500 $bar.s^{-1}$ for the dry sample, i.e. an increase of 14%. This value is close to the experimental error related to the evaluation of the maximum rate of pressure rise in the 20L sphere, which is around 10% (Proust et al., 2007). Although small variations in the combustion kinetics of nanocellulose appears when drying the powder, such modifications can be attributed to a modification of the exchanges due to the presence of water. The combustion

gases were once again collected and analyzed, highlighting the formation of hydrogen during the combustion, around 12%m. However, this molar percentage was obtained when testing both (raw and dried) powders, implying that the presence of water does not influence the production of hydrogen.

Moreover, the minimum ignition energy (MIE) of the raw powder was evaluated to 16 mJ whereas a MIE of 5 mJ was measured for nanocellulose dried at 90°C under vacuum, implying that the dried powder is considered as particularly sensitive instead of normally sensitive. Furthermore, the LEL (measured at 10 kJ) was obtained at 125 $g.m^{-3}$ when drying the powder, whereas it was obtained only at 250 $g.m^{-3}$ with the raw powder. These modifications show the influence of the water activity of the powder on the ignition sensitivity.

Table 5-3 Characteristics of the raw and dry nanocellulose

Powder	Raw	Dry
Water activity (Aw)	0.23	0.03
Mean surface diameter by sedimentation (µm)	48	45
Mean surface diameter d_{50} after dispersion in the 20L sphere (µm)	9	10
Maximum overpressure (bar)	8.1	8.3
Maximum rate of pressure rise ($bar.s^{-1}$)	435	496
Minimum Ignition Energy (mJ)	16	5
Minimum Explosive Concentration ($g.m^{-3}$)	250	125

In this part, the influence of the powder humidity was highlighted through two examples: carbon black and nanocellulose. In the case of carbon black, the presence of humidity led to the agglomeration of the powder. But, instead of decreasing the reactivity of the powder because of PSD modifications and heat sink effects, the presence of adsorbed humidity led to a slight increase of the explosion severity because of the production of hydrogen, which then participates to the explosion. On the contrary, the presence of water in the nanocellulose powder did not lead to PSD modifications, but slightly decreases the explosion severity and the ignition sensitivity.

The true influence of the water activity on the flammability and explosivity of a nanopowder appears then to be strongly powder dependent even for organic materials, for which water adsorption is often considered to have a positive impact on safety, i.e. by promoting agglomeration and limiting the dispersion of the powder. In order to avoid any misestimation of safety parameters, the influence of water activity especially for nanopowders, should be further discussed in the standards.

V.3. Too much is a waste: role of the ignition energy

'The ignition source comprises two chemical igniters each having an energy of 5 kJ.'
(EN 14034-1-2, 2004; 2006)

As evidenced in chapter 4, section IV.1.4, some nanoparticles exhibit very low ignition energy, sometimes even lower than 1 mJ (Wu et al., 2010b). However, even for such powders, the standard ignition energy needed to perform explosion tests in the 20L sphere is 10 kJ (EN 14034-1, 2004; EN 14034-2, 2006). This large difference of energy can lead to an overdriving phenomenon, which is already known to occur for microparticles and artificially increases the explosion severity (Going et al., 2000; Zhen and Leuckel, 1997). Since nanoparticles are generally more ignition sensitive than microparticles (Bouillard et al., 2010; Holbrow et al., 2010), this phenomenon can be enhanced when evaluating nanoparticles explosion severity.

In order to estimate which ignition energy would be suitable to avoid overdriving, experiments were conducted with nanocellulose using different ignition energies (Santandrea et al., 2020c). Two pyrotechnical igniters of 5 kJ were selected, according to international standards, as well as one igniter of 100J, which is the lowest energy proposed by Fr. Sobbe GmbH for chemical igniters. The ignition energy was further reduced by using an ignition source composed of two tungsten electrodes connected to a KSEP 320 system (Kühner AG - 15 kV / 15 mA, i.e. 225 W) which generates a permanent spark whose energy can be varied through spark duration. An alternative solution to Kühner software (KSEP7) has been developed in this work in order to accurately control the ignition delay time when using the permanent spark. Since a huge amount of powder on the electrodes would inhibit the spark, explosion tests were performed at 500 $g.m^{-3}$, which is much greater than the minimum explosive concentration LEL (125 $g.m^{-3}$) and just below the optimal concentration (750 $g.m^{-3}$).

Table 5-4 shows the maximum overpressure and rate of pressure rise obtained at this concentration for each ignition energy. It should be noted that the KSEP software automatically modifies the values in order to consider the overdriving. However, as shown in Table 5-4, this correction is not sufficient. Indeed, it appears that, with regard to the experimental reproducibility, similar values were reached when using an electrical spark delivering 10J and chemical igniters of 100 J, meaning that no overdriving phenomenon occurred at these low energies. However, when compared to the values obtained with lowest energies, the use of 10 kJ chemical igniters increases the overpressure of around 20% and the rate of pressure rise of 40%. The contribution of ignition energy to the explosion severity through the modification of the flame propagation can thus lead to a misestimation of the explosion severity, since the flame kernel growth is directly affected by the ignition source. A solution may be to set a maximum difference between the minimum ignition energy of the powder and the actual ignition energy used in explosion tests to limit this phenomenon. An alternative solution would be to better assess the explosion severity increase, especially the maximum explosion pressure, due to overdriving in order to withdraw it more accurately from the experimental results.

Table 5-4 Explosion characteristics of 500 g.m^{-3} of nanocellulose as a function of ignition energy (corrected values from KSEP 7.1)

Ignition energy	10 J (electrical spark)	100 J (chemical igniter)	10 kJ (chemical igniters)
Overpressure P_m (bar)	6.5 ± 0.3	6.1 ± 0.3	7.8 ± 0.4
Rate of pressure rise $(dP/dt)_m$ (bar.s^{-1})	210 ± 25	200 ± 24	345 ± 41

V.4. Too sensitive or too violent: some considerations on pre-ignition

'If other dust dispersing systems than those described are used, a propagation of the explosion from the explosion vessel into the dust container cannot be excluded'.
(EN 14034-1-2, 2004; 2006)

Metallic nanoparticles are generally recognized to be very ignition sensitive (Martin et al., 2018; Wu et al., 2010b) and can spontaneously ignite when exposed to air (Krietsch et al., 2015; Mohan et al., 2012; Wu et al., 2014) or when injected in an experimental setup. When a powder ignites before the ignition source has been triggered, this phenomenon is called 'pre-ignition'. Various authors have already encountered it when testing titanium (Boilard et al., 2013) and aluminum (Dufaud et al., 2011; Santandrea et al., 2019b). Thus, some modifications in the 20L sphere were proposed in order to avoid this drawback (Krietsch et al., 2013; Santandrea et al., 2019b; 2019c). However, such changes require an accurate understanding of the pre-ignition phenomenon and further investigations were especially performed on the aluminum 40-60 nm (Santandrea et al., 2020c). This powder was stored under argon and exposed to ambient air only a few minutes before performing the experiments, during the sample preparation. Tests were carried out according to EN 14034 standards, and led to the observation of alumina in the dust container for concentrations of 500, 750 and 1000 g.m^{-3} (Figure 5-17), which, in a first sight, seems to testify of the so-called famous pre-ignition phenomenon.

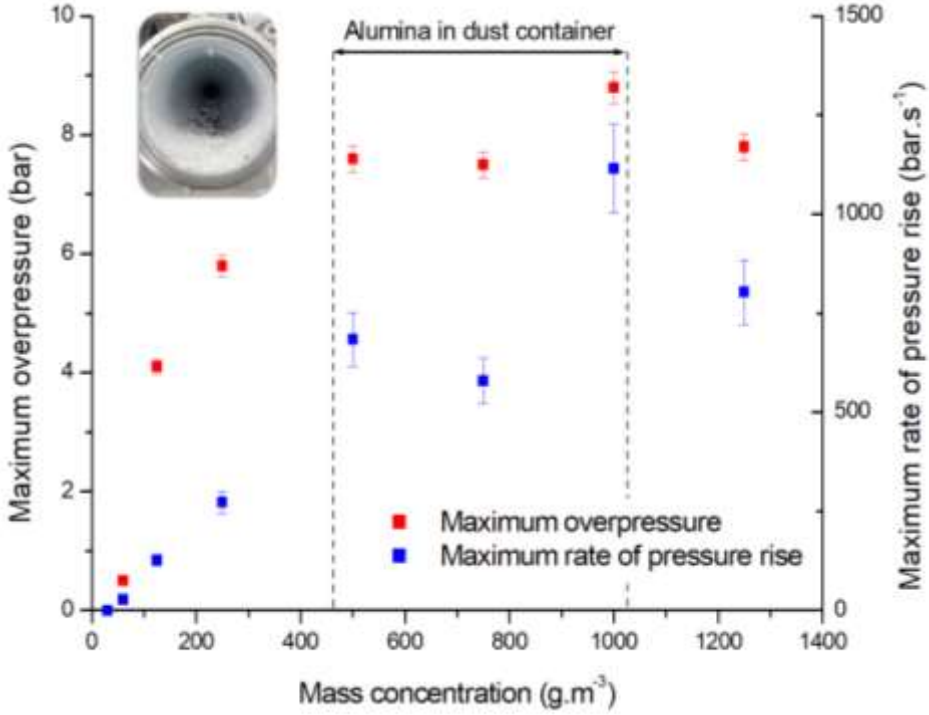

Figure 5-17 Evolution of explosion characteristics of aluminum nanopowder in standard conditions (10 kJ - 60 ms)

One possible adjustment of the operating conditions consists in removing the oxygen from the dust container and injecting the powder with pure nitrogen. The sphere was then enriched with oxygen after vacuuming to obtain atmospheric composition after powder injection, at the time of the explosion. However, for concentrations greater than 250 $g.m^{-3}$, explosion started long before the activation of the igniters, about 15 ms after the beginning of the dust injection, meaning the aluminum spontaneously ignited when in contact with the oxygen enriched atmosphere. The final pressure, obtained after total cooling of the sphere using the double jacket, was recorded when stabilized. It appears that the final pressure is always lower than the atmospheric pressure (Figure 5-18). Indeed, the combustion of aluminum mainly consists in the production of solid alumina generated from the reaction between solid aluminum and gaseous oxygen, thus decreasing the global pressure in the vessel due to oxygen consumption. Therefore, by assuming that nitrogen is inert and that all the oxygen from air was consumed, a final pressure of around 0.8 bara should be obtained in the case of a total reaction. However, when using nitrogen injection, it appears that the final pressure is below this value for concentrations of 500 and 750 $g.m^{-3}$, reaching respectively 0.73 and 0.74 bara. This observation implies that a nitridation reaction, possible at high pressure and temperature (2800K) (Kwon et al., 2003; Loryan and Borovinskaya, 2003), certainly occurred, possibly during the pressurization, and generates aluminum nitrides. AlN cannot be oxidized due to the lack of oxygen, already partially consumed, and to kinetic limitation caused by rapid condensation and encapsulation of gaseous AlN (Kwon et al., 2003). Such phenomenon is certainly also observable for Al microparticles, but is promoted for nanopowders due to their high specific surface area and increased reactivity.

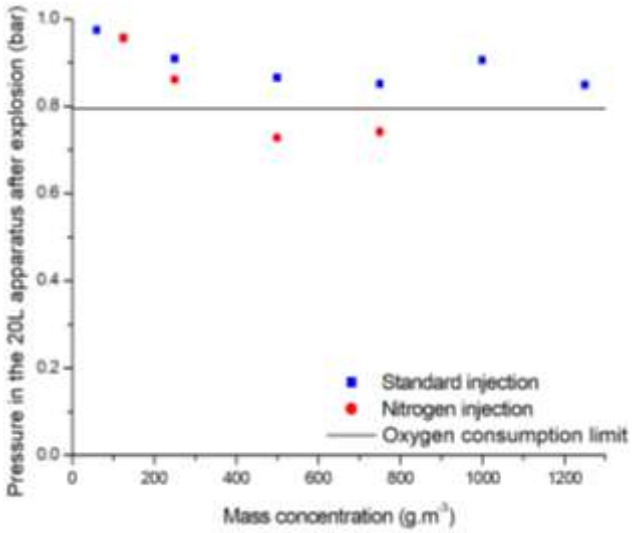

Figure 5-18 Pressure after explosion and cooling of the sphere at different aluminum nanopowder concentrations for standard injection and nitrogen injection.

So, for concentrations corresponding to the maximum explosion severity, for instance at 750 $g.m^{-3}$, alumina was observed in the dust container both for air and pure nitrogen injection. However, when analyzing the pressure-time evolution for both injection types, it appears that different pressure profiles are observable (Figure 5-19). During a standard air injection, a 'normal' pressure-time graph was obtained (Figure 5-19a); whereas an early explosion clearly occured a few milliseconds after the beginning of the dust injection when using nitrogen injection. In the latter case, the explosion took place as soon as the aluminum was in contact with the oxygen enriched atmosphere and long before the activation of the igniters (Figure 5-19b). A rather similar trace was obtained by Boilard et al. (2013) with nano-Ti injected under air. It then appears that, in our case, the presence of alumina in the dust container during standard injection cannot be explained by a 'pre-ignition' phenomenon since the explosion occurred only after the activation of the igniters. To confirm this interpretation, standard injections of 750 $g.m^{-3}$ of aluminum nanopowders were performed without activating the chemical igniters in the sphere and, as expected, no explosion occurred.

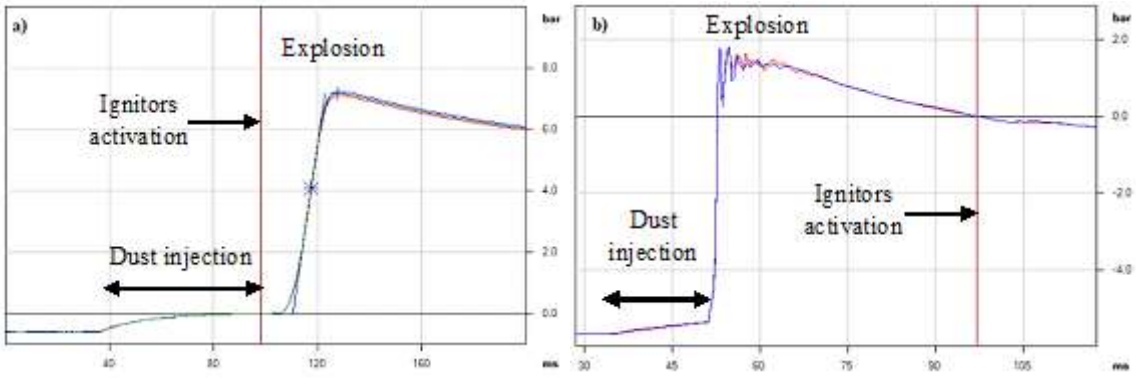

Figure 5-19 Pressure-time evolution of an aluminum explosion at 750 g.m-3 with a) air injection b) nitrogen injection.

[125]

To clarify what happened in the dust container and explain the presence of alumina with air injection, measurements were performed using an oscilloscope to estimate the closing delay of the electrovalve, for ignition delays of 60 ms and 120 ms. It appears in Figure 5-20a that, for an ignition delay of 60 ms, the ignition starts before the electrovalve begins to close, enabling the flame to possibly go back to the dust container. Figure 5-20b shows that the opening delay of the electrovalve is independent of the ignition delay. At this point, it should be underlined that EN 14034-2 (2006) standard specifies that the electrovalve should open in less than 10 ms but no clear instructions on the closing time are provided. Nevertheless, this work notably proposes an alternative to the fast-acting valve, provided that its opening time is lower than 100 ms, which is significantly greater than 60 ms.

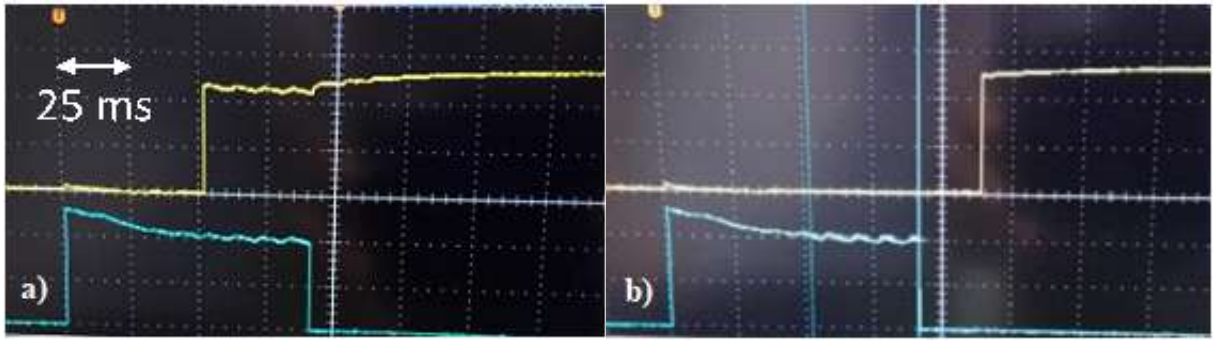

Figure 5-20 Electrical signal of the electrovalve (blue lower curve) and of the ignition (yellow upper curve) for ignition delay times of a) 60 ms and b) 120 ms

From this knowledge, since explosions involving metallic nanoparticles demonstrate a high severity and a fast flame propagation, the assumption of an explosion occurring in the sphere and reaching back the dust container seems more likely than that of a pre-ignition during the powder injection. To confirm this hypothesis, standard experiments with an ignition delay time of 70 ms instead of 60 ms were performed, which allows the electrovalve to close before the flame reaches the bottom of the sphere. It should be added that such tv variation has only a small influence on the turbulence and will not sensitively impacts the flame propagation speed.

After the tests, no alumina was observed in the dust container, consolidating the hypothesis of the flame coming back to the dust container. Thus, to accurately evaluate the explosion severity of very explosive powders, especially metal nanopowders, it appears essential that the electrovalve closes well before the activation of the igniters, by modifying its actuation parameters or by increasing the ignition delay time of several milliseconds. Nevertheless, a too large increase of t_v may change the dust cloud turbulence and may probably reduce the explosion severity. Finally, it should be noted that the existence of this phenomenon does not question the existence of a ‘real’ pre-ignition, i.e. ignition during the pressurization, which was frequently reported (Wu et al., 2010b).

V.5. Scattering little things: nanopowders dispersion in the 20L sphere

'For testing, the dust is dispersed into the sphere from a pressurized dust container via the fast-acting valve and a rebound nozzle'
(EN 14034-1-2, 2004; 2006)

V.5.1. Nozzle modification

Symmetric nozzle

The influence of the dispersion system, including the outlet valve, on the PSD and homogeneity of the dust cloud greatly depends on the nature of the powders (Bagaria et al., 2016; Sanchirico et al., 2015). If this statement is true for microparticles, it is probably even more significant for nanoparticles. Indeed, due to their strong Van der Waals interactions, nanopowders exhibit agglomeration phenomenon and these structures tend to break during their dispersion, widening the particle size distribution (Bagaria et al., 2016). The inertial effects are obviously weaker on a nanoparticle than on a microparticle or an agglomerate which leads to a segregation phenomenon and modifies the dispersion dynamics. Wengeler and Nirschl (2007) showed that nanoparticles and microparticles exhibit different dispersion properties and that no complete dispersion of primary particles can be achieved.

When performing explosion tests in the 20L sphere, EN 14034 standards recommend the use of the rebound nozzle to disperse the powder (Figure 5-21a). Nevertheless, several alternatives were proposed by other authors to disperse the powder adequately and reduce the heterogeneity of the dust cloud (Dahoe, 2000; Krietsch et al., 2015). More recently, a new symmetric nozzle was proposed to improve the experimental reproducibility by increasing the temporal stability of the nominal dust concentration (Murillo et al., 2018). This new nozzle is based on the geometry of the standard rebound nozzle for which an axial symmetry has been applied (Figure 5-21b).

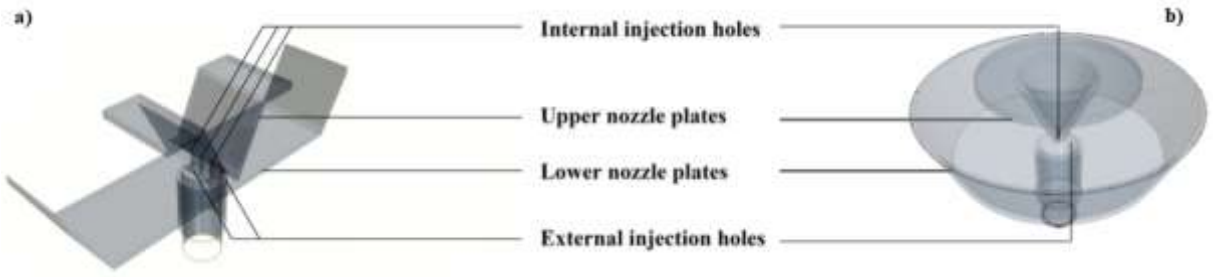

Figure 5-21 Schemas of the a) rebound nozzle and b) symmetric nozzle – from Murillo et al. (2018)

Dispersion and explosion tests were carried out in the 20L using the rebound nozzle and the symmetric nozzle with various nanopowders, notably on carbon black (Santandrea et al., 2019b, 2019c). In situ particle size distribution measurements using the laser diffraction sensor (Helos, Sympatec) showed that similar breakage of the agglomerates occurred when performing tests with the rebound or the symmetric nozzle. Indeed, mean surface diameters of 4.7µm and 3.5µm were respectively measured. Since both nozzles led to similar PSD after dispersion of carbon black, the potential differences in the explosion severity can be attributed to different turbulence level and homogeneity in the 20L sphere.

Figure 5-22 shows that the maximum explosion pressure is not modified by changing the dispersion nozzle, and thus is not affected by the dust cloud turbulence. However, the rate of pressure rise of carbon nanoparticles greatly varies as a function of the nozzle. Indeed, the maximum rate of pressure rise reaches 250 bar.s^{-1} with the rebound nozzle, which generates a greater level of turbulence than the symmetric nozzle, for which a maximum rate of pressure rise of 173 bar.s^{-1} was obtained. Consequently, the rebound nozzle seems to deliver most conservative results though results can be quite poorly reproductible. Dispersing the powder through a symmetric nozzle delivers lower values of explosion severity parameters and then does not correspond to the worst-case scenario, but allows a better experimental reproducibility (Murillo et al., 2018).

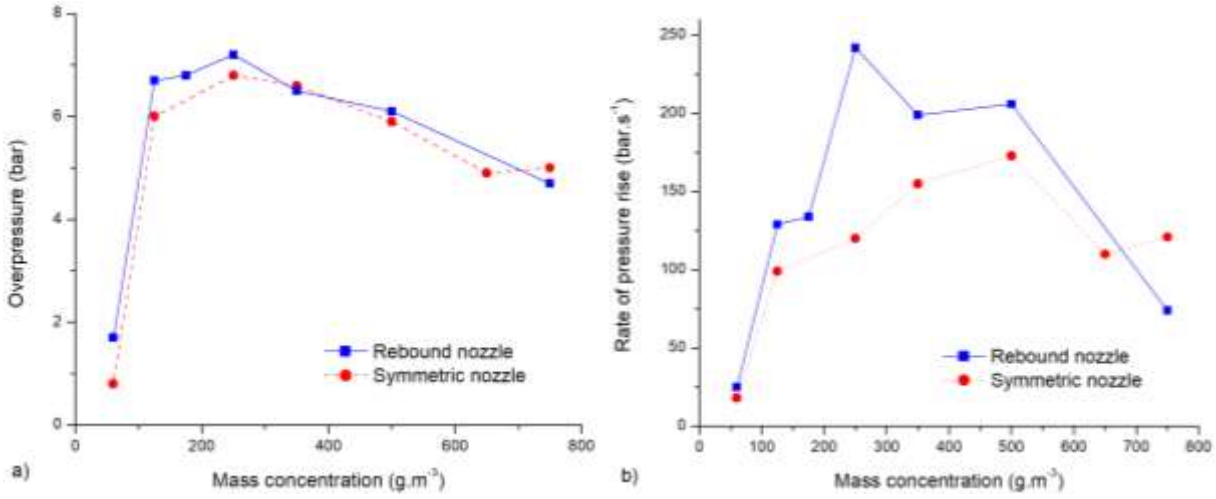

Figure 5-22 Evolution of the a) overpressure and b) rate of pressure rise with the concentration of carbon black using the rebound and symmetric nozzles

Slotted and perforated cylindrical nozzles

Although the rebound nozzle provides the most critical values of explosion severity parameters, the dispersion induced by this nozzle is not able to represent the diversity of the dispersion scenarios during an accident. Several scenarios could then be considered, such as the dispersion of powder layers by a turbulent flow or dust lifting in an enclosed conveyor, for instance. In this case, the most representative procedure would be to place the powder directly in the explosion chamber, which will be discussed in section V.5.2. Although dust lifting corresponds

to representative conditions in industries, other dispersion ways can be considered. In particular, a crack can appear on a pressurized pipe, thus inducing a very high shear stress which may break agglomerates. To assess the PSD modification and the explosion severity under such conditions, a new nozzle presented in Figure 5-23a was designed. It is constituted of a cylinder of 40 mm high and 26.7 mm diameter, that ends by a half-sphered shape equipped with a linear slot of 3 mm on 17 mm. Obviously, trying to get a homogeneous cloud in the sphere with this type of nozzle is illusory. Subsequently, a second nozzle was designed to evaluate the fragmentation of agglomerates passing through a similar nozzle with the same ejection surface more uniformly distributed. This second nozzle, represented in Figure 5-23b, is equipped with two series of eight circular holes of 2 mm diameter, can be compared to that developed by Zhang and Zhang (2015), which leads to homogeneous dispersion in the explosion vessel.

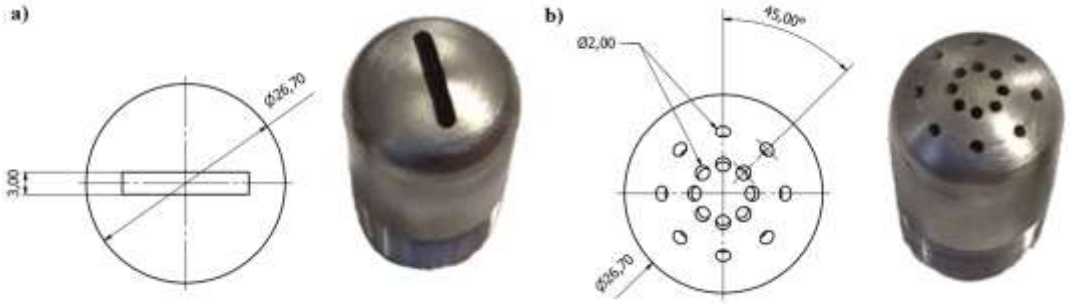

Figure 5-23 Representation of the a) slotted cylindrical nozzle and b) perforated cylindrical nozzle (dimensions in mm)

In situ PSD measurements were performed with the different nozzles and compared to the measurements obtained with the rebound nozzle (Figure 5-24). Despite a different signal intensity, the two new nozzles lead apparently to a similar particle size distribution, with a slight shift toward small particles when compared to the standard rebound nozzle.

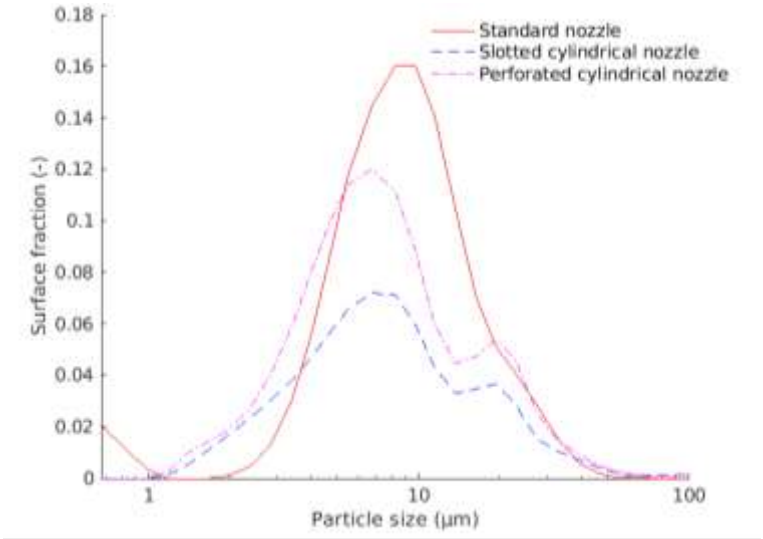

Figure 5-24 Effect of the nozzle on the particle size distribution of nanocellulose particles 60 ms after dispersion

[129]

Even if it is difficult to fully investigate this aspect without knowing the whole PSD, the fragmentation induced by the two new nozzles seems stronger than with the rebound nozzle, although the dust cloud is less homogeneous due to the vertical shape of the new nozzles. Indeed, whereas the mean diameter d_{50} obtained with the rebound nozzle is stable a few milliseconds after dispersion, it stabilized only 80 ms after dispersion with the two other nozzles. The high turbulent kinetic energy generated by such nozzles can also be responsible of re-agglomeration after a few milliseconds as shown by the apparition of a second peak around 20 µm.

Explosions tests were also performed in standard conditions, apart from the nozzle variation. The different turbulence conditions along with the different homogeneity and PSD impact the explosion severity, as presented in Table 5-5. Although the number of tests performed is too small to obtain a reliable margin of error for the new nozzles, it appears that similar maximum overpressures were obtained in each case, implying that equivalent amounts of dust reacted during the explosion. However, the maximum rate of pressure rise increases of about 37% when using these new nozzles (perforated and slotted), which traduces an impact on the reaction kinetics and flame propagation dynamics. As the impact of the new nozzles on the PSD of the dust cloud exists, but does not apparently seem to be significant, such rise of explosion severity may be attributed to an increase of the turbulence at 60 ms. Finally, the standardized procedure applied for dispersing nanopowders in the 20L sphere does not automatically lead to the most conservative results, notably in terms of maximum rate of pressure rise. Other injection methods may then be considered for nanopowders. More specifically, a dispersion by dust lifting, i.e. by placing the dust directly on the nozzle within the sphere, was investigated in the next section.

Table 5-5 Influence of the nozzle on the maximum overpressure and maximum rate of pressure rise of nanocellulose (tv = 60 ms)

Ignition energy	Rebound nozzle	Perforated cylindrical nozzle	Slotted cylindrical nozzle
Maximum overpressure P_{max} (bar)	8.35 ± 0.05	8.0	7.9
Maximum rate of pressure rise $(dP/dt)_{max}$ ($bar.s^{-1}$)	496 ± 12	792	786

V.5.2. Injection procedure

First of all, dispersion tests were performed on carbon black to highlight the influence of both the injection procedure and the outlet valve on the PSD. Measurements were then performed under different conditions: a standard injection with the rebound nozzle, a standard injection without nozzle, and a ‘dust lifting’ without nozzle. In this latter configuration, the dust is placed directly at the bottom of the sphere and does not undergo the pressurization step in the 0.6L

chamber nor the injection through the electrovalve. It appears in Figure 5-25 that the dispersion by dust lifting without nozzle presents fewer fine particles (< 3 µm) than the dispersion by standard injection through the electrovalve, with or without nozzle. Then, it seems that an important part of the fragmentation of the agglomerates is not related to the presence of the rebound nozzle but occurs during the injection within the sphere, which was already confirmed by Kalejaiye et al. (2010) and to a lesser extent Bagaria et al. (2016). However, the latter authors also stressed that the cloud turbulence and dispersion nozzle play a major role in particle breakage, in particular in their 36-L explosion apparatus, which may be due to a weaker shear stress during the dust injection. To sum up, it seems that the high shear stress induced by the pressure difference between the combustion chamber and the pressurized dust container is the main cause of the agglomerate breakage and that the 'standard' rebound nozzle does not appear to play a main role in this phenomenon.

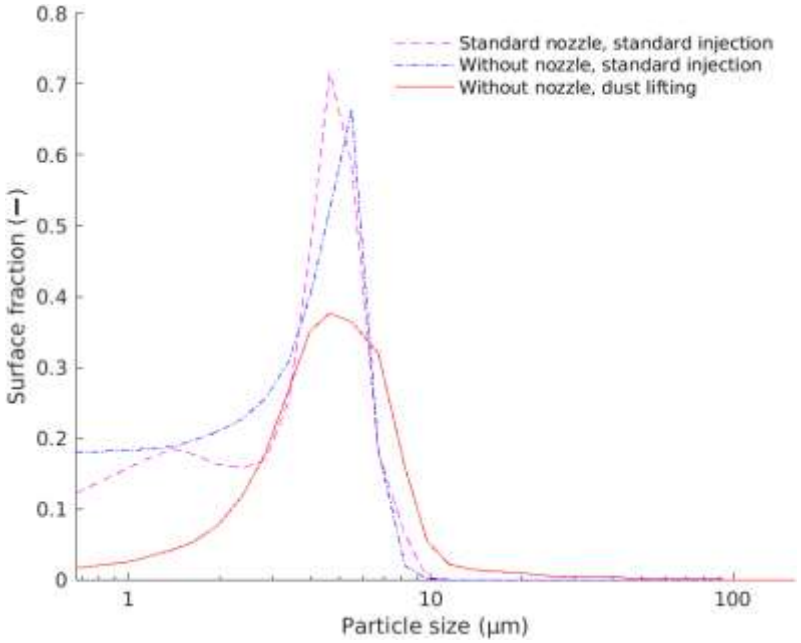

Figure 5-25 Effect of the injection procedure on the particle size distribution of carbon black nanoparticles at the moment of ignition (tv = 60 ms)

Particle Image Velocimetry (PIV) measurements (see section III.2.3) were conducted in the 20L sphere to determine the evolution of the turbulence level with time within the apparatus in four different configurations: standard injection with the rebound and symmetric nozzles, and dust lifting also with both nozzles. It appears in Figure 5-26 that the four configurations led to rather similar values of root-mean square velocities, decreasing from around 10 $m.s^{-1}$, measured 10 ms after dust dispersion, to 3.5 $m.s^{-1}$, obtained after 140 ms. Nevertheless, in the transition zone, from 60 ms to 120 ms, the injection of the dust through the container and the rebound nozzle seems to induce a higher turbulence than the other dispersion procedures, notably the dust lifting on the symmetric nozzle. Moreover, in this last case, the root-mean square velocity stabilizes 80 ms after the dust dispersion, which can be due to a better homogeneity within the sphere.

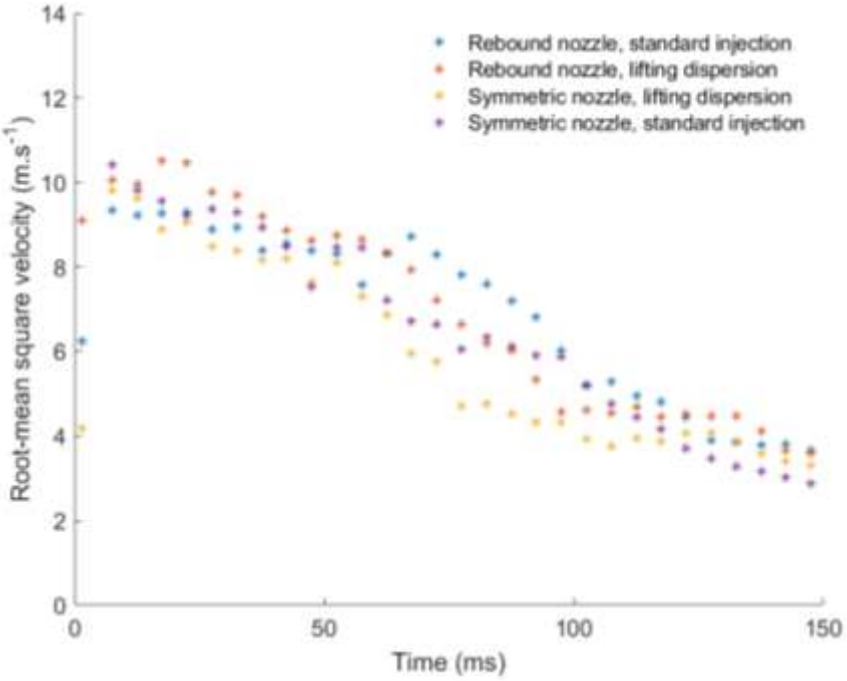

Figure 5-26 Evolution of the root-mean square velocity with time after dispersion for different dispersion procedures

Explosion tests were performed on the aluminum powder with a primary diameter of 100 nm, using the four different configurations of powder injection (Santandrea et al., 2019b). In Figure 5-27, it is clearly visible that, whatever the configuration tested and the concentration, the standard procedure (rebound nozzle and standard injection) always leads to the most severe explosion characteristics. It should be noted that dispersion tests on aluminium using the four dispersion procedures led to similar mean surface diameter, around 3 µm.

The maximum overpressure of the aluminium nanoparticles varies as a function of the injection mode (Figure 5-27a), which raises the question of the full conversion of the powder. Especially in the case of dust lifting with the symmetric nozzle, P_m decreases at 5.4 bars whereas it reaches 6.5 bars at 750 $g.m^{-3}$ when the standard procedure is applied. This assertion is confirmed by collecting the dust after combustion at the bottom of the 20 L sphere, where grey crusts composed of both alumina and aluminum can be observed after dispersion by dust lifting. However, the same tests carried out on the carbon black nanopowder led to similar overpressure values whatever the dispersion procedure. Indeed, the efficiency of the dust dispersion varies with the dust density and agglomeration level, which limits the reliability of this lifting procedure. It is worth noting that the LEL is not significantly modified by the various procedures.

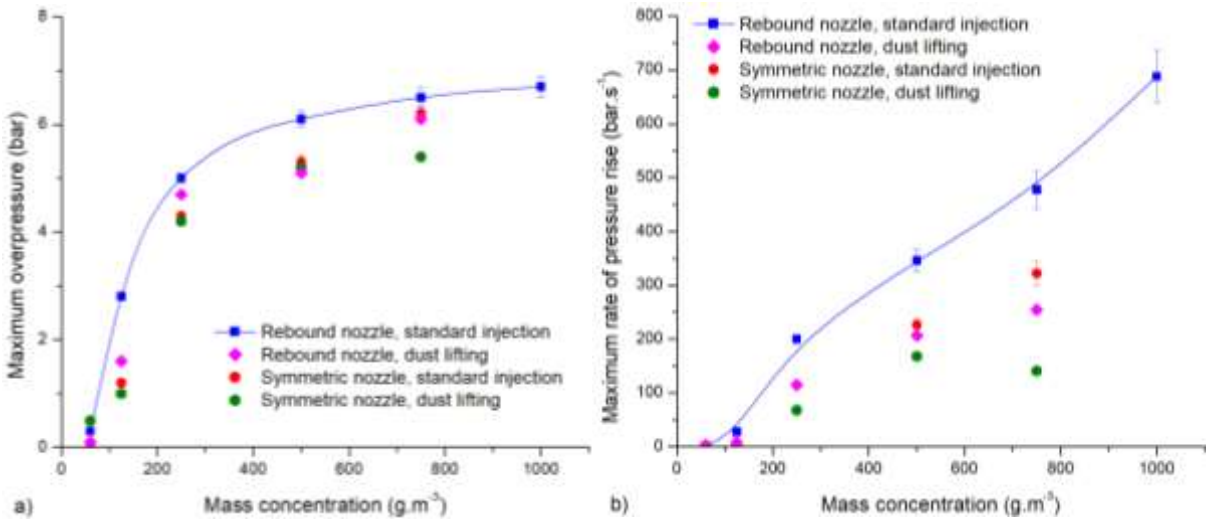

Figure 5-27 Evolution of the a) overpressure and b) rate of pressure rise of aluminum 100 nm for various injection procedures

Concerning the maximum rate of pressure rise (Figure 5-27b), the difference between the standard procedures and the other injection modes seems to increase as the dust concentration increases. It should be underlined that the $(dP/dt)_{max}$ was not identified over the chosen concentration range, whereas the theoretical stoichiometry (by considering only the oxidation of aluminum in alumina) is reached at 315 $g.m^{-3}$. Other reactions should then be considered such as the nitridation of aluminum at high temperature, which is confirmed by measuring the pressure drop in the 20L sphere after explosion and cooling. Thus, at high dust concentrations, the final pressure is lower than the one obtained by only removing the oxygen, which is due to nitrogen consumption and the generation of aluminum nitride (Loryan and Borovinskaya, 2003). SEM observations combined with EDX (energy dispersive X-ray spectrometry) performed on the oxidation residues confirm these results.

Moreover, dust lifting leads to lower explosivity than with the standard injection procedure. It should be highlighted that, when the concentration exceeds 750 $g.m^{-3}$, the standard procedure systematically led to the presence of alumina within the dust container, which is due to a propagation of the flame back to the canister, as explained in section V.4. This phenomenon did not occur with the symmetric nozzle, nor with the dispersion by dust lifting. Indeed, the maximum rate of pressure rise, and, consequently, the flame velocity, greatly decreases when using the symmetric nozzle or dispersing the powder by dust lifting. This induces that the electrovalve may have enough time to close before the flame can go to the container. Moreover, the shape of the symmetric nozzle can hinder the flame propagation toward the dust container.

Finally, even if only slight PSD changes were observed using various nozzles and injection procedures with the aluminum powders, significant variations of the dust explosivity are observed. This is consistent with the results obtained by Wu et al. (2010a), who found that if the particle sizes of 35 nm and 100 nm of aluminum powders were comparable after

agglomeration, yet their explosive parameters were different. The following assumptions can be proposed:

i) The slight PSD modifications and notably the presence of fine particles with diameters lower than 1 μm, which cannot be seen by the laser diffraction sensor, have a noticeable impact on the evolution of the reactive specific surface area,

ii) The same modification have also an effect on the particles optic emissivity, which decreases as the size of the observed particles decreases towards nanosized particles (Sundaram et al., 2013, 2016),

iii) The injection procedure changes the dust cloud homogeneity within the sphere, which can influence the flame propagation and the radiative transfer (Cassel et al., 1957),

iv) The use of different nozzles implies changes in the initial turbulence level (Figure 5-26), parameter impacting the flame kernel growth and flame front propagation (Proust, 2006).

To sum up, dispersing the powder by dust lifting impacts both the PSD (Figure 5-25) and the initial turbulence (Figure 5-26). Modifications on the overpressure and rate of pressure rise of aluminum were also observed. Although not leading to the most conservative results, this method seems more representative of an accidental dispersion than the injection through the electrovalve and the rebound nozzle. Moreover, this dispersion method can be used to evaluate the explosion severity of very sensitive metallic nanopowders in the most critical conditions, i.e. minimizing the oxidation of the powder before the explosion tests, and to avoid pre-ignition phenomenon (Krietsch et al., 2013). However, as shown on aluminum, this procedure does not allow a complete dispersion of very dense powders, such as metallic ones. Therefore, a new 'mushroom nozzle' was designed by Krietsch et al. (2013) to adequately disperse the powder within the sphere. This nozzle could then be considered as a potential alternative to the standard rebound nozzle, which does not provide results representative of industrial conditions nor the most conservative ones (see section V.5.1).

V.6. Punctuality is the politeness of kings: influence of the ignition delay time

'Ignition delay t_v: time between the initiation of the dust dispersion and activation of the ignition source. […] In the 20L sphere, ignition delay time t_v = 60 ms'
(EN 14034-1-2, 2004; 2006)

It is common knowledge that the initial turbulence within the sphere varies as a function of time (Amyotte et al., 1988; Dahoe et al., 2001; Zhen and Leuckel, 1997). Indeed, as explained in chapter 3 (section III.2.3), right after the injection, the turbulence level is high and decreases with time through three stages: high turbulence and heterogeneity of the cloud (from 0 to 40

ms), transient stage (from 40 to 120 ms) and a stability stage from 120 ms (Murillo et al., 2018; Santandrea et al., 2019b). This tendency is represented in Figure 5-28a by the red points. According to ASTM E1226-19 (2019) and EN 14034-1-2 (2004; 2006), the standard ignition delay time t_v is 60 ms, which means that the igniters activation occurs 60 ms after the beginning of the injection. This standard value is then located in the second phase, which is the transient phase characterized by a significant decrease of the velocity fluctuations.

The parameter t_v, set in the KSEP software, can be modified, but it also changes the injection dynamic, as shown in Figure 5-28b, which presents the pressure increase in the 20L sphere during the dust injection (from 0.4 bara to atmosphere pressure). If the ignition delay time is below 60 ms, the injection is faster, which leads to greater heterogeneities within the cloud and a lower stability. For t_v above this value, the injection is still made in 60 ms. However, the red points in Figure 5-28a were obtained by studying the evolution of the root-mean square velocity with time after dust dispersion for an ignition delay time set to 60 ms. Particle Size Velocimetry (PIV) measurements were then conducted by modifying this value and evaluating the turbulence level of the cloud at the moment of the ignition for different t_v (blue points in Figure 5-28a). Therefore, the blue point at 20 ms corresponds to the root-mean square velocity measured 20 ms after dispersion with an ignition delay time set to 20 ms. It then appears that, during the transition stage, for ignition delay times close to 60 ms, there is no significant difference in the turbulence level compared to the standard (60, 90 and 120 ms). However, for the two other stages, there is a slight difference both in the turbulence and heterogeneity of the dust cloud.

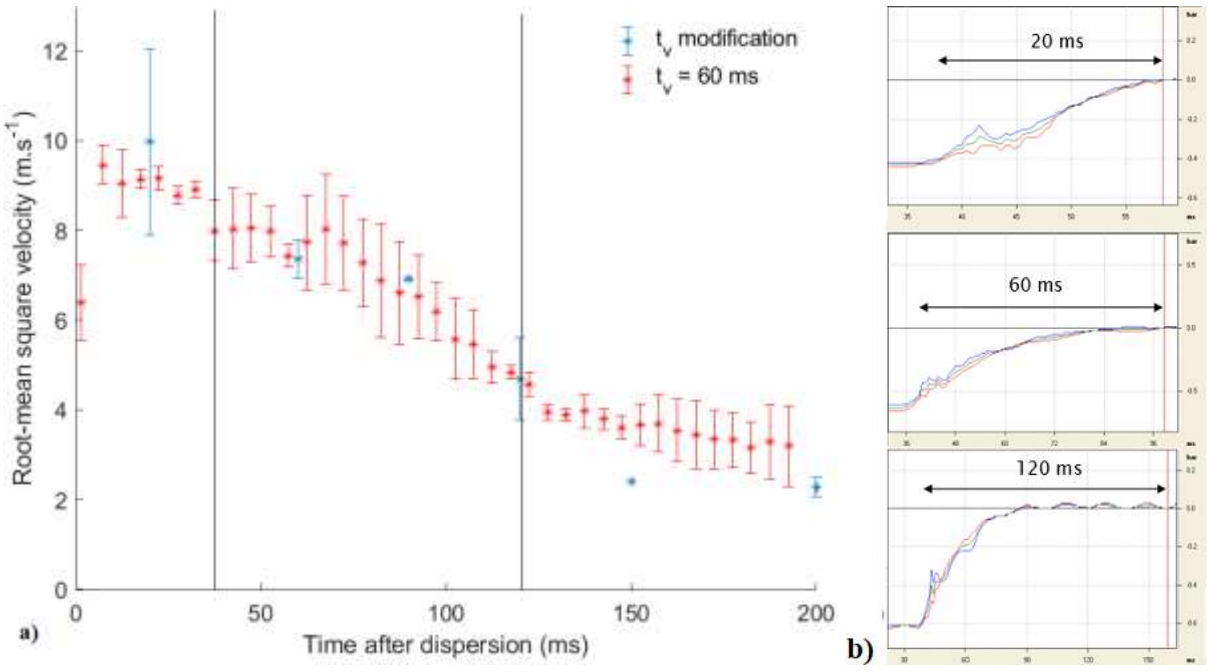

Figure 5-28 a) Time evolution of the root-mean-square velocity within the 20L sphere during a standard injection for various ignition delay times b) Modifications of the injection dynamic for various ignition delay times

If the dependency of turbulence on the ignition delay time is long proven and admitted, its impact on the PSD is still to evaluate quantitatively, especially for nanopowders (Santandrea et al., 2020c). Indeed, as a function of the particle nature and size, a high turbulence level can either induce a shear stress causing deagglomeration in the dust cloud or increase the number of contacts between particles, thus causing agglomeration. Moreover, when performing experiments with long ignition delay time, the influence of agglomerates settling can modify significantly the amount of dust that reacts during the explosion. Furthermore, as previously showed in Figure 5-28b, decreasing the ignition delay time below 60 ms also modifies the injection dynamic to reach the atmospheric pressure before ignition. Thus, varying the ignition delay time can modify both the PSD and the initial turbulence.

Figure 5-29 presents PSD measurements conducted for the dispersion of dried nanocellulose at different ignition delay times and plotted at the moment of ignition for each. Then, it appears that variations in the ignition delay time between 20 and 120 ms do not significantly impact the PSD of nanocellulose after dispersion, in the measuring range of the apparatus. Though the whole range of particle size should be measured to draw an accurate conclusion, it seems that variations of ignition delay times will impact mainly turbulence and only slightly the PSD, at least in the case of the nanocellulose.

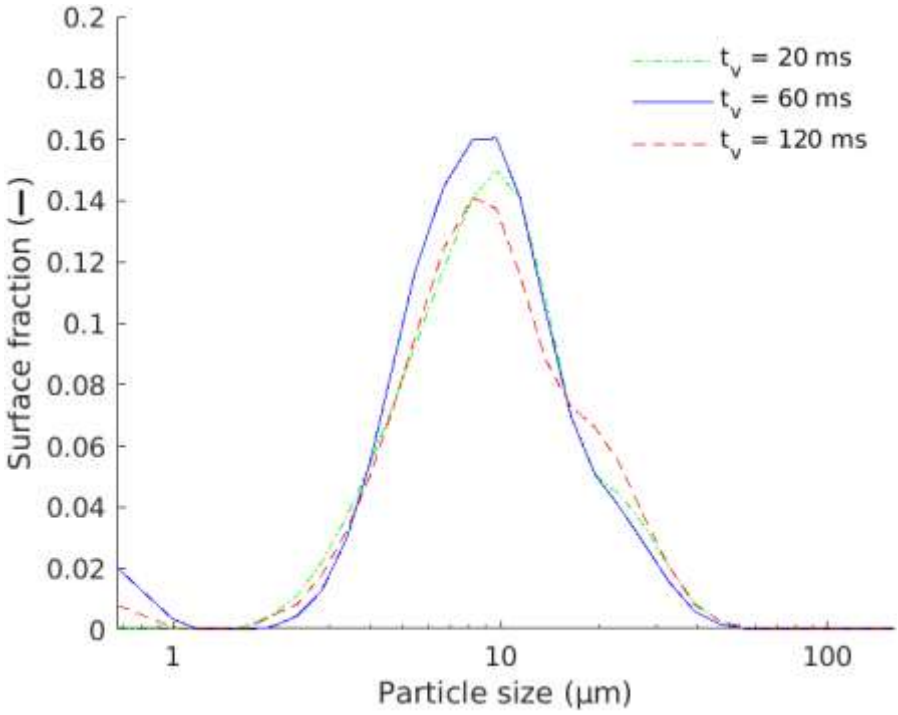

Figure 5-29 Particle size distribution of nanocellulose at the moment and place of ignition for different ignition delay times (R3 lens)

Explosion tests with ignition delay time variation were performed on nanocellulose and carbon black, with concentrations of 750 $g.m^{-3}$ and 250 $g.m^{-3}$ respectively, which are the concentrations leading to the most severe explosions in standard conditions. To evaluate directly the influence of the turbulence level on explosion severity characteristics, the values of maximum

overpressure and maximum rate of pressure rise presented in Figure 5-30 are plotted against the root-mean square velocity for ignition delay times from 20 ms to 200 ms. Since the PIV measurements were only conducted until 150 ms, the relation between ignition delay time and root-mean square velocity proposed by Dahoe et al. (2001) was used.

In Figure 5-30a, it appears that the maximum overpressure increases for both powders when slightly increasing the initial turbulence level in the combustion chamber, until reaching maximum values of 7.0 ± 0.2 bar at 3.5 $m.s^{-1}$ i.e. 60 ms, for the carbon black and of 8.4 ± 0.3 bar at 1.5 $m.s^{-1}$ i.e. 100 ms, for the nanocellulose. This increase is due to the promoting effect of a moderate turbulence, which tends to improve the mass transfer by increasing the flame stretching and thus enhancing the flame propagation. It should be added that, at very low turbulence levels, the influence of the sedimentation of bigger particles or agglomerates should be taken into account as it can induce a more heterogeneous distribution of powders in the sphere. Conversely, at high turbulence (> 6 $m.s^{-1}$), an intense flame stretching occurs. It improves the mass transfer and has a positive impact on the combustion kinetics, which is clearly visible in Figure 5-30b. Indeed, although diffusional limitation is unlikely to be observed when testing nanoparticles, such limitation is expected for organic micro-agglomerates (Dufaud et al., 2012). Finally, it should be kept in mind that a too high turbulence level can also lead to micro-scale flame quenching.

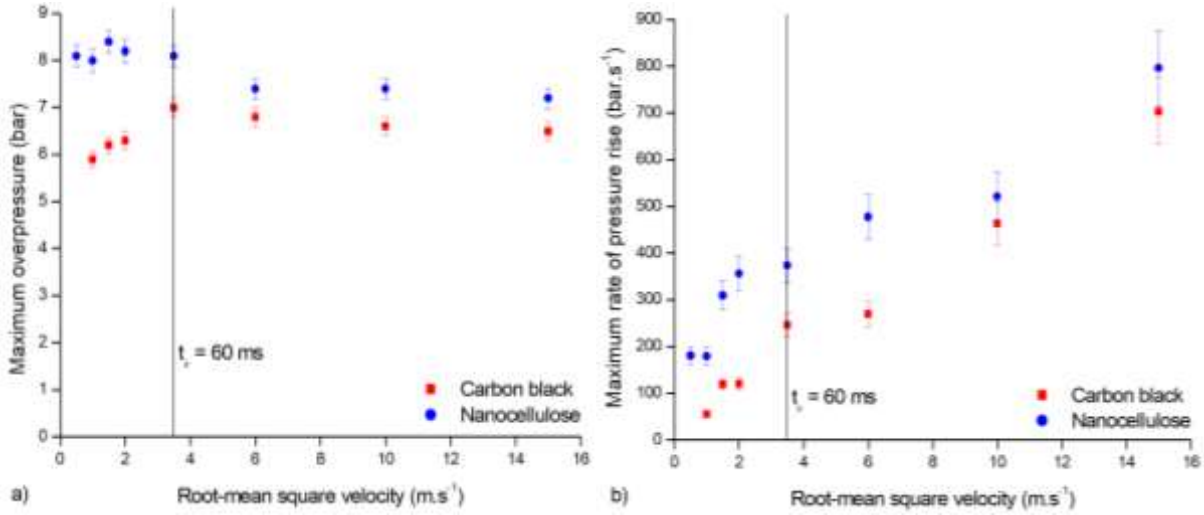

Figure 5-30 Evolution of a) the maximum overpressure and b) the maximum rate of pressure rise with the root-mean square velocity in the 20L sphere

Combustion gases were collected and analyzed by gas chromatography, studying specifically the ratio CO/CO_2 (Figure 5-31). This ratio is higher than unity for ignition delay times lower than 100 ms, i.e. root-mean square velocities higher than 1.5 $m.s^{-1}$, and decreases for higher ignition delay times for both powders. Although this ratio does not significantly vary for nanocellulose, a significant decrease is observed for carbon black, from 5.7 at 15 $m.s^{-1}$ to 0.6 at 1 $m.s^{-1}$. This evolution notably reflects the quenching occurring at high turbulence identified when studying the maximum overpressure (Figure 5-30a). Furthermore, it shows that,

nanoparticles being tracers of the gas flow, the turbulence level of the dust cloud can impact the maximum overpressure through a modification of oxidation products and mechanisms by quenching effects. Torrado (2017) notably noticed a premature extinction of the flame when studying hybrid mixtures from around 6 $m.s^{-1}$. The initial turbulence level also influences the maximum rate of pressure rise through turbulence/combustion interactions.

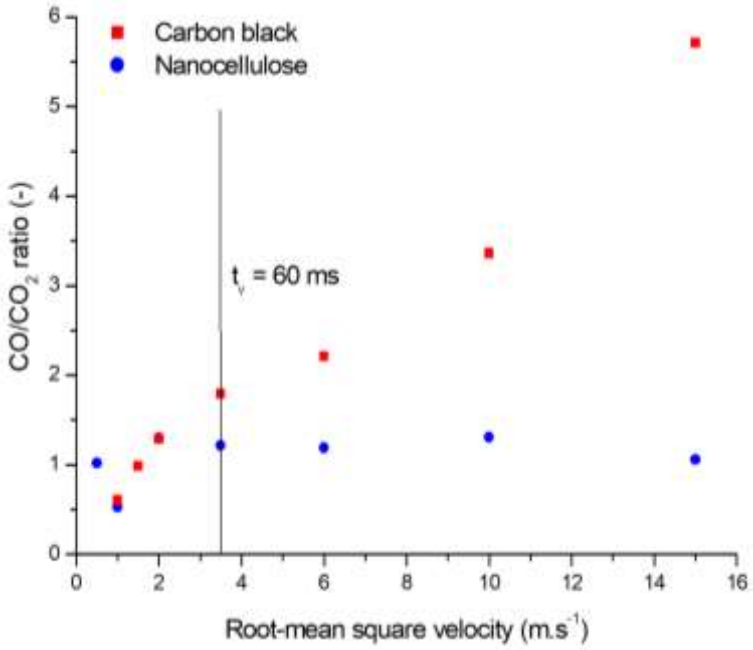

Figure 5-31 Evolution of the CO/CO2 ratio of the combustion gases of nanocellulose and carbon black with the root-mean square velocities

Summary

Nanopowders specificities (e.g. low sedimentation rate, agglomeration, high surface area, etc.) induce explosive behaviors that are sometimes different from that observed for micropowders or, more generally, lead to exacerbated trends. As a consequence, in addition to safety issues inherent in handling nanopowders, standards could be refined so that cautious approaches are considered when performing the tests. For instance, the following improvements or advices can be suggested:

i) It should be kept in mind that the PSD of nanopowders will be modified by deagglomeration during their dispersion, even if existing PSD measurement methods cannot identify such a shift. Surface PSD will be preferred to volume-based distribution.

ii) Alternative nozzles allow to reach higher explosion severities. Since standards objective is not to reproduce the exact industrial conditions, and that the standard nozzle does not always lead to the most conservative results, priority should focus on the reliability of the results by choosing nozzles providing a better cloud homogeneity.

iii) The ignition source should be adapted to the low minimum ignition energy of the nanopowders in order to avoid overdriving or, at least, this phenomenon should be better considered by assessing the additional energy given to the dust cloud.

iv) Pre-ignition of very sensitive nanopowders in the dust container can be avoided by injecting them under nitrogen (but spontaneous ignition still can occur in the sphere) or by using dust lifting as for MIE determination. However, as a result of their high flame speed propagation, the opening time of the electrovalve should be reduced to avoid a ‘backfire’ in the container or the delay tv should be adapted.

v) Variations of the ignition delay time can be helpful to obtain the most conservative results. However, a too low turbulence level (e.g. < 2 m.s^{-1}) can lead to agglomerate sedimentation, whereas a too high turbulence level (e.g. > 6 m.s^{-1}) can induce alternative combustion mechanisms.

vi) Special attention must be paid to the nanopowders storage conditions and to the humidity of the ambient and injection air. Indeed, the presence of water can modify the flammability and explosivity of the powder depending on its nature and its ability either to react with the water.

Finally, the results obtained must be transposed on an industrial scale, with the same limitations inherent to the cube-root law as those encountered for micropowders. An alternative approach would be to use the advantages of nanopowders, in particular their low sedimentation rate, to determine their laminar flame velocity, which is an intrinsic parameter that can be used as an input for CFD simulations. The next chapter is then dedicated to the evaluation of this parameter, notably on nanocellulose.

Résumé

Les spécificités des nanopoudres (agglomération, propriétés d'adsorption, grande surface spécifique, etc.) induisent un comportement explosif parfois différent de celui observé pour les poudres micrométriques, ou, plus généralement, conduit à des tendances exacerbées. Ce chapitre est donc dédié à mettre en lumière ce genre de tendances à travers six parties et l'exemple de quatre poudres de différentes natures. Par exemple, les améliorations suivantes peuvent être suggérées :

i) Il est important de garder en mémoire que la distribution de tailles de particules (DTP) des poudres nanométriques est modifiée par désagglomération durant la dispersion, même si les techniques de mesures de DTP actuelles ne permettent pas de quantifier ce décalage. La DTP sera préférentiellement exprimée en surface à la place de la distribution volumique.

ii) Des disperseurs alternatifs permettent d'atteindre des valeurs plus élevées de sévérité d'explosion. Puisque l'objectif des standards n'est pas de reproduire les conditions industrielles, et que le disperseur standard ne mène pas systématiquement aux résultats les plus conservatifs, la priorité devrait être donnée à la fiabilité des résultats, notamment en choisissant des disperseurs permettant une meilleure homogénéité du nuage.

iii) La source d'inflammation devrait être adaptée à la faible énergie minimale d'inflammation des poudres nanométriques afin d'éviter un phénomène dit 'd'overdriving', ou, tout du moins, ce phénomène devrait être mieux caractérisé afin d'estimer l'énergie supplémentaire fournie au nuage pour la combustion.

iv) La pré-inflammation des nanopoudres particulièrement sensibles dans le réservoir à poussière peut être évitée par une injection sous azote (mais une inflammation spontanée peut se produire dans la sphère), ou par simple soulèvement de la poudre, comme pour la détermination de l'énergie minimale d'inflammation. Cependant, du fait de leur vitesse de propagation rapide, le temps d'ouverture de l'électrovanne devrait être réduit afin d'éviter un retour de flamme dans le réservoir à poudres, ou le délai d'inflammation devrait être adapté.

v) Des modifications dans le délai d'inflammation peuvent être utiles afin d'obtenir les résultats les plus conservatifs possibles. Cependant, un niveau de turbulence trop faible (e.g. < 2 m.s^{-1}) peut conduire à la ségrégation des agglomérats, tandis qu'un niveau de turbulence trop élevé (e.g. > 6 m.s^{-1}) peut mener à des mécanismes de combustion alternatifs.

vi) Une attention particulière doit être porté aux conditions de stockage des nanopoudres et à l'humidité de l'air ambiant et de l'air d'injection. En effet, la présence d'eau peut modifier l'inflammabilité et l'explosivité des poudres en fonction de leur nature et de leur capacité à réagir avec l'eau.

Finalement, les résultats obtenus doivent être extrapolés à l'échelle industrielle, avec les mêmes limitations inhérentes à la loi cubique que celles rencontrées pour les poudres micrométriques. Une approche alternative serait d'utiliser les avantages des nanopoudres, en particulier leur faible vitesse de sédimentation, afin de déterminer leur vitesse laminaire de flamme, qui est un paramètre intrinsèque au mélange poussière/air qui peut être utilisé comme donnée d'entrée pour des codes CFD. Le chapitre suivant est ainsi dédié à l'évaluation de ce paramètre, notamment pour la nanocellulose.

Chapter 6:
Flame propagation study

In the previous chapter, the influence of the operating conditions on the explosion severity parameters, i.e. the maximum overpressure and maximum rate of pressure rise, was highlighted, evidencing that the international standards may not be fully adapted, or at least could be greatly improved to assess the risk of nanoparticles explosion. However, since the process safety engineer wants to extrapolate the results to his industry and processes, he needs to apply 'scale-up' relationships such as the cube-root law – with all the limitations already described in chapter 2.

Another possibility is to directly determine a parameter depending only on the considered dust/air mixture. For instance, the laminar burning velocity is an intrinsic property of the fuel-air mixture, that can be used in advanced simulations (CFD or phenomenological approach) to evaluate the consequences of an explosion scenario in specific conditions (Figure 6-1). If the determination of this parameter is possible but difficult for gas/air mixtures (Halter, 2005), it is far from being obvious for dust/air mixtures. Indeed, the compulsory dust dispersion step is, in practice, in total contradiction with the term 'laminar'. Moreover, such determination should be done with conventional test apparatuses and 'easy-to-perform' procedures for standardization purposes. However, this alternative wat of assessing the explosion risk is promising, especially with nanopowders, whose specific behavior can be, in this case, a strength.

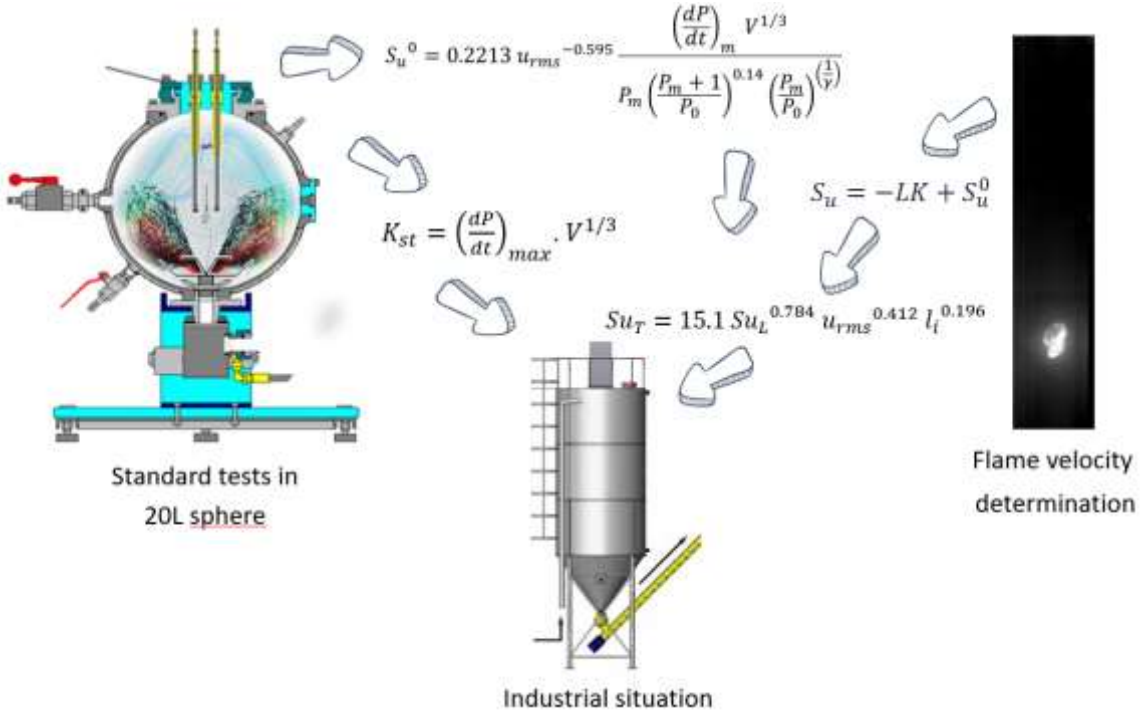

Figure 6-1 Representation of the existing methods to assess the explosion risk in an industrial situation

This chapter is dedicated to the determination of the laminar burning velocity of nanopowders and is divided into three main parts. Due to the high minimum ignition energy (> 1 J) of the carbon black (see section IV.1.4) and to the important radiative heat transfer and high explosion

severity of aluminum (see section IV.2.2) that could respectively disturb the flame visualization and damage the equipment, focus was realized on the estimation of the laminar burning velocity of nanocellulose.

First, the burning velocity will be estimated by visualization of the flame propagation in two apparatuses: a vertical 1 m long tube with a square cross-section and a 20L sphere equipped with visualization windows and a vent (section VI.1.1). In the section VI.1.2, a semi-empiric correlation based the pressure-time evolution recorded during standard explosion tests in the 20L vessel is detailed, and the values obtained by the three methods are discussed in section VI.1.3. The section VI.2 presents a numerical one-dimensional model, initially developed for hybrid mixtures and adapted to the flame propagation of nanocellulose. The influence of the radiative heat transfer on the flame propagation will also be discussed. Finally, turbulent velocity models estimating the burning velocity in specific conditions, as shown in Figure 6-1, will be applied on the experimental values.

VI.1. Experimental determination

Not trivial for pure gases, the estimation of the laminar burning velocity of dust-air mixtures is much more difficult to perform than for gases due to the inherent turbulence related to the powder dispersion. Nevertheless, as mentioned in chapter 2, section II.2.3, experiments were already conducted using the burner method (Dahoe et al., 2002; Julien et al., 2017; Lomba et al., 2019; van der Wel, 1993), the contained explosions method (Silvestrini et al., 2008; Skjold, 2003; van der Wel, 1993) and the tube method (Andrews and Bradley, 1972; Cuervo et al., 2017; Di Benedetto et al., 2011; Proust, 2006). Since those tests were conducted in turbulent conditions, a numerical extrapolation to a zero degree of turbulence, or a least to a laminar flow, was required (Bradley et al., 1989).

Despite the great accessibility of these methods, experimental issues remain and usually limit the reproducibility and accuracy of the results. In addition to be related to the stochastic nature of turbulence, issues can also come from particle agglomeration, instabilities of the biphasic flow, set-up fouling or flame front visualization difficulties. However, for specific reactive mixtures such inconveniences may be limited: for instance, testing gas-dust mixtures with a low dust concentration, called gas-driven hybrid mixtures (Di Benedetto and Russo, 2007), in a semi-open tube allowed the determination of their laminar flame velocity and highlighted the influence of turbulence/combustion interactions on the flame propagation (Cuervo, 2015; Torrado et al., 2017).

The low inertia of nanoparticles allows tests with very long ignition delay time. Consequently, experiments can be performed at low turbulence with nanoparticles, while sedimentation would occur for micropowders under the same experimental conditions. Decreasing the turbulence level of the initial dust cloud can help approaching the laminar flame velocity of dust-air mixtures, which is then expected to be independent from turbulence. This concept was developed through the characterization of the burning velocity of the dried nanocellulose

powder using three different procedures and set-up (Santandrea et al., 2020a). The first two procedures consist in a flame propagation visualization in a semi-open tube and a vented vessel and are presented in section VI.1.1. Then, the laminar burning velocity was calculated using a correlation based on the pressure-time evolution during an explosion in the 20L sphere, which is developed in section VI.1.2.

VI.1.1. Flame propagation visualization

The laminar burning velocity was evaluated through the visualization of the flame propagation in a flame propagation tube and in the modified 20L sphere presented in section III.2.2.3. The experimental method along with the video analysis and the calculation of the laminar burning velocity are presented in this section. It should be noted that the term 'laminar burning velocity' is employed based on several assumptions, such as a laminar flow in the equipment and the application of methods designed for gases, implying that the final value is mainly an estimation of this parameter. This term will be further discussed in section VI.1.1.2.

VI.1.1.1. Experimental method

The first apparatus is a flame propagation tube of 7 x 7 x 100 cm^3 open at its upper end and implementing the ignition system of the modified Hartmann tube, presented in section IV.1.1, which was coupled with a high-speed video camera at 4000 fps with 240 µs of exposure time (Phantom V9.1). The equipment and procedure are fully described by Cuervo et al. (2017) and Torrado et al. (2017) who validated the set-up and procedure with methane and obtained encouraging results for hybrid mixtures of starch and methane and of carbon black and methane. However, the small volume, especially around the ignition zone, implies that the flame is influenced by the walls quite soon after the ignition, which impacts its propagation. Therefore, the analysis is limited to the first moments of the flame kernel growth (from 5 to 20 ms), between ignition and the flame spatial acceleration (or sometimes quenching) due to the presence of the wall. Consequently, in order to increase the volume dedicated to the spherical flame propagation, a second method was developed to study flame propagation within a modified 20L sphere.

The 20L sphere developed by Murillo (2016) equipped with four visualization windows was adapted by Torrado (2017) to perform hybrid mixtures explosion tests and to study the flame propagation of such mixtures. Therefore, a lateral window was removed to integrate an ignition source composed of two tungsten electrodes connected to a KSEP 320 system (Kühner AG - 15 kV / 15 mA, i.e. 225 W) generating a permanent spark whose duration, and thus energy, can be varied. A modification of the Kühner software was necessary to control accurately the ignition delay time, called 't_v', when using the permanent spark. A pressure relief valve, opening at 1.15 atm, was added on the top of the sphere to protect the windows during the explosion. This notably allows performing tests at constant and not too high pressure, and thus to neglect the pressure evolution during the analysis. The flame front and shape are imaged

using a Schlieren system, combined with the high-speed camera. The Schlieren setup consists in a 150 W xenon lamp (66475-150XV-R22 Xenon Light Source) equipped with a lens, a pinhole with a diameter of 1 mm to obtain a single-point light source, and a spherical mirror reflecting the punctual light toward a filter placed in front of the camera (Figure 6-2). This technique, notably described by Mazumdar (2013), allows the observation of density variations, which provides a better visualization of the front flame. The tests were performed at 300 mJ in the tube and at 10 J in the vented 20L sphere, which is the lowest deliverable energy using the permanent spark controlled by the new software. Using the KSEP 320 system, the ignition energy of 10 J is delivered by an electrical spark of 225 W during 44 ms. It should be noticed that, although the minimum ignition energy of nanocellulose was determined at 5 mJ, no overdriving phenomenon was evidenced using an ignition energy of 10 J (see section V.3), implying that the influence of the ignition energies used in the experiments on the flame propagation can be neglected.

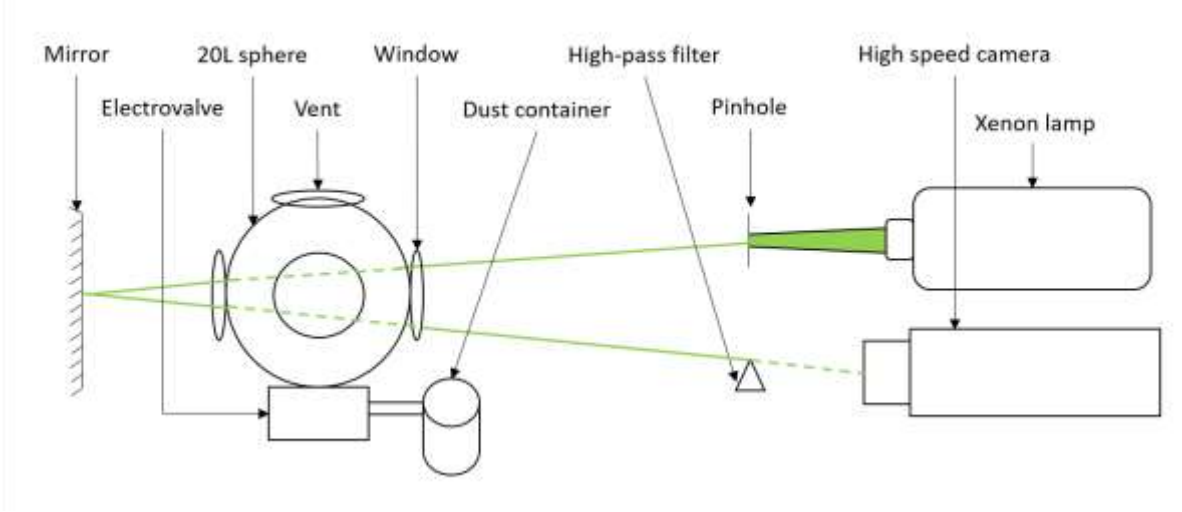

Figure 6-2 Schematic of the Schlieren setup and the modified 20L sphere

The turbulence level of the dust cloud estimated by Dahoe et al. (2001) using a laser Doppler anemometer was considered in the 20L, and the measurements performed by Particle Image Velocimetry (PIV) by Cuervo (2015) were used to estimate a root-mean square velocity u_{rms} of the dust cloud in the flame propagation tube. Regarding the values presented in Table 6-1, it appears that the turbulence level is always higher in the 20L sphere than in the propagation tube, which is due to the high pressure applied during the injection in the sphere and to the use of a dust canister. However, for both equipment, the turbulence level decreases rapidly for low ignition delay time (from 60 to 120 ms, decrease by 71% in the 20L sphere and 39% in the tube) and seems to stabilize for high ignition delay times (> 200 ms), as discussed by Murillo et al. (2018) and Santandrea et al. (2019b). Indeed, between 100 ms and 200 ms, the root-mean square velocity decreases of 67% in the 20L sphere and 60% in the tube, and only of 14% in the 20L and 25% in the tube between 300 ms and 400 ms. This “more stable stage” allows to reach pseudo-laminar conditions and to approach a laminar burning velocity when increasing

sufficiently the ignition delay time. More specifically, for an ignition delay time of 400 ms, Reynolds numbers of 3280 and 680 were respectively calculated in the 20L sphere and in the propagation tube. Such values induce that the flow in the 20L sphere is still turbulent even 400 ms after the dust dispersion (Re > 3000), although close to the limit of the turbulent flow, whereas a laminar flow is obtained in the tube after the same ignition delay time (Re < 2000) (Upp and LaNasa, 2002).

Table 6-1 Root mean square velocities measured in the 20L sphere and in the propagation tube (Cuervo, 2015; Dahoe et al., 2001)

Ignition delay time (ms)	u_{rms} in the 20L sphere ($m.s^{-1}$) **(Dahoe et al., 2001)**	u_{rms} in the propagation tube ($m.s^{-1}$) **(Cuervo, 2015)**
60	3.5	1.4
100	1.5	1.0
200	0.5	0.4
300	0.35	0.2
400	0.3	0.15

VI.1.1.2. Flame propagation and stretching observation

The propagation speed can be estimated using existing mathematical models based on several hypothesis (Chen and Ju, 2007; Frankel and Sivashinsky, 1984; Joulin and Clavin, 1979). The flame is then assumed to be spherically expanding and governed by an overall one-step exothermic reaction, and the thermodynamic properties of the mixture such as the molecular weight, the specific heat and the thermal conductivity are considered constant. The potential heat losses at the vessel walls are neglected and the combustion process is assumed to be isobaric, which seems reasonable before the flame is affected by the vessel walls and is ensured by the presence of calibrated vents. With all these hypotheses, the laminar burning velocity can be estimated using a linear or a non-linear methodology, from the knowledge of the turbulent burning velocity and flame stretching (Andrews and Bradley, 1972; Clavin, 1985; Markstein, 1964).

To evaluate those parameters, flame propagation videos were analyzed by a model developed by Cuervo (2015) in MatLab's Simulink using the Vision toolbox (Cuervo et al., 2017; Torrado et al., 2017). This model isolates the flame profile for each frame of the video as shown in Figure 6-3 and calculates the position of the flame front z, the estimated cross-section area A_S and the estimated flame surface A_f. In the case of flame kernels growing spherically, the flame radius is generally considered to estimate the spatial velocity (Law, 2006; Varea, 2013). However, it will not be the case as the flame kernel appears to grow as an ellipsoid at low turbulence levels. The spatial velocity is calculated by deriving the position of the front flame.

Since the laminar flame velocity is independent of the vessel geometry and size, only the phase of 'free' flame kernel propagation is considered, i.e. when the flame is not significantly affected by the vessel walls, i.e. by the compression of the gases between the kernel and the walls or by the gas-wall heat transfers. It should be noted that, due to the contribution of the ignition source and the small size of the initial flame kernel, which can be located -with respect to the camera- behind unburnt particles, the very first milliseconds of the videos are also often delicate to analyze. The position of the flame z being known for different times, the spatial velocity of the flame S_S can be deduced.

Figure 6-3 Time evolution of the flame profile in the semi-open tube for a dispersion of 500 g.m^{-3} of nanocellulose at 340 ms ignition delay time

For a spherical flame propagating in a tube, a mass balance on the unburnt gases can be written:

$$\frac{\partial m_u}{\partial t} = \frac{\partial \rho_u . V_u}{\partial t} = -\rho_u . A_f . S_u \qquad 6\text{-}1$$

with m_u the mass of the unburnt gases, which decreases with time, ρ_u the density of the unburnt gases, V_u the volume of the unburnt gases, A_f the flame surface and S_u the combustion speed, i.e. the local flame speed, considered constant. Since the density of the unburnt gases is constant, one can write:

$$\frac{\partial V_u}{\partial t} = -A_f . S_u \qquad 6\text{-}2$$

For a spherical flame, the spatial velocity S_s, considered uniform over the whole surface, according to an axe x can be expressed:

$$\frac{\partial x}{\partial t} = S_s \qquad 6\text{-}3$$

Considering a flame kernel growth from the center, the flame section A_S that grows on dx can be introduced as:

$$\frac{\partial V_u}{\partial x} = -A_s \qquad 6\text{-}4$$

The relation 6-3 then becomes:

$$\frac{\partial V_u}{\partial t} = \frac{\partial V_u}{\partial x} . \frac{\partial x}{\partial t} = \frac{\partial V_u}{\partial x} . S_S \qquad 6\text{-}5$$

Injecting equation 6-5 into equation 6-2 then leads to equation 6-6:

$$S_u = \frac{A_f}{A_s} . S_s \qquad 6\text{-}6$$

Andrews and Bradley (1972) notably determined this formula relying on similar hypotheses: the flame burning velocity S_u remains constant (which essentially means that the local fuel equivalent ratio does not change during the flame propagation), the flame thickness is small in comparison to the flame curvature and if the spatial velocity S_S is uniform over the whole surface of the flame. A thermal expansion factor χ, represented by the ratio between the densities of the hot burnt gases and the initial cold gases, is generally added to this relation to convert the 'unstretched burning velocity' into a 'laminar burning velocity' (Halter, 2005). However, this factor represents the volume increase of the flame kernel, which is already considered by the flame section, as just demonstrated. For this reason, this factor was not considered in this work.

Moreover, as previously explained, only the 'free' flame kernel growth is considered, meaning the analysis is stopped when the flame is close to the walls but is still unaffected by their presence. This induces that, at this early stage, the flame kernel growth is unaffected by the thrust of the gases against the bottom of the tube and by the associated pressure increase, which has been verified by observing the negligible displacement of the flame kernel geometric center during the analysis. It should be underlined that the burning velocity of a fuel-air mixture depends on the initial dust concentration, the pressure and the temperature, but also the turbulence. More than any other parameter, this point is very important and specific to dust explosion due to the inherent turbulence developed when generating the dust cloud. This effect can be estimated using the flame's stretching factor K, called Karlovitz factor (Karlovitz et al., 1951), defined as:

$$K = \frac{1}{A_f}\frac{dA_f}{dt} \qquad 6\text{-}7$$

The sign of the Karlovitz factor indicates the expansion (K positive) or compression (K negative) of the flame surface. Since the stretching can be due to the curvature of the flame or to the strain rate of the flow, the stretching factor can be decoupled in two different variables K_c and K_s (Bradley, 2000). However, in this work, the flame stretching will be considered as a single phenomenon combining both effects.

In the literature, two relations to link the Karlovitz factor to the burning velocity are mainly used by considering the assumptions previously mentioned: a linear relation and a non-linear one. Although those relations were initially established for gases, Cuervo et al. (2017) and Torrado et al. (2017) obtained encouraging results by applying them to starch/methane as well as carbon nanoparticles/methane hybrid mixtures. In this work, the same relations are applied to pure dust explosion. Indeed, the low inertia of nanocellulose nanoparticles allows measurement at very low turbulence, leading to a spherical/ellipsoidal flame kernel growth. Moreover, the organic nature of the chosen powder induces a fast devolatilization which implies that, under usual concentration and turbulence conditions, the dust combustion would be controlled by gas combustion (Di Benedetto and Russo, 2007).

Linear relation

Most of the authors studying the flame propagation and laminar burning velocity of dusts using the tube method (Cuervo et al., 2017; Dahoe et al., 2002; Di Benedetto et al., 2011) use a linear relation established for pure gases and stating that, in a first approach, Karlovitz factor can be linked to the flame burning velocity by the following relationship (Clavin, 1985; Markstein, 1964):

$$S_u = -\delta_M K + {S_u}^0 \quad 6\text{-}8$$

where $S_u°$ is the laminar burning velocity and δ_M, the Markstein length, whose sign provides an indication on the stability of the flame (Clavin, 1985). This linear relation is valid if the flame stretching is weak, i.e if the Karlovitz number is low, and if the ratio of thermal diffusivity to mass diffusivity, called the Lewis number, is equal to unity.

Non-linear relation

Even if the linear relation has been extensively adopted in various studies concerning flame propagation (Beeckmann et al., 2019; Bradley et al., 2019; Ichikawa et al., 2019; Torrado et al., 2017), it has some limitations (Petersen and Emmons, 1961). Indeed, this relation is less accurate for Lewis numbers different from unity (Tien and Matalon, 1991) and if the flame stretching level is high, which corresponds to great values of Karlovitz factor (Vagelopoulos et al., 1994). As a consequence, some authors developed and applied a nonlinear relation to link the laminar flame velocity to the flame stretching of gaseous mixtures (Buckmaster, 1977; Halter et al., 2010; Kelley and Law, 2009; Sivashinsky, 1975):

$$\left(\frac{S_u}{{S_u}^0}\right)^2 . ln\left(\frac{S_u}{{S_u}^0}\right)^2 = -\frac{2\delta_M K}{{S_u}^0} \quad 6\text{-}9$$

The previous analysis was applied along with relations 6-4 and 6-5 to the experimental data recorded during flame propagation in the semi-open tube and in the vented 20L sphere.

VI.1.1.3. Estimation of the laminar burning velocity

An illustration of the evolution of the burning velocity with the Karlovitz factor is presented in Figure 6-4 for a concentration of 500 $g.m^{-3}$ of nanocellulose. It appears that both relations seem in satisfactory agreement with the experimental data. In this example, the unstretched flame velocity obtained using the linear relation is of 20.5 ± 0.6 $cm.s^{-1}$ and of 21.3 ± 0.6 $cm.s^{-1}$ using the nonlinear relation proving a good consistency between both methods.

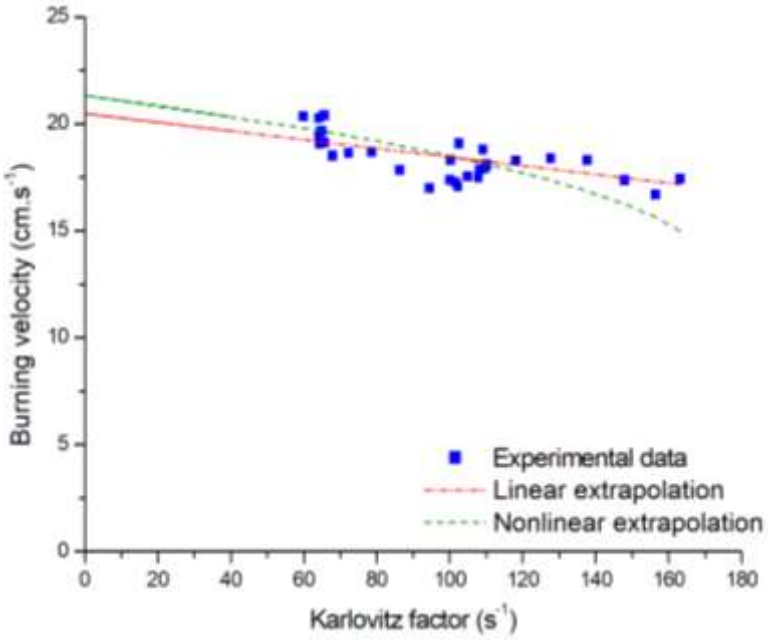

Figure 6-4 Illustration of the burning velocity – stretching factor relation for a 500 g.m^{-3} nanocellulose-air mixture for tv = 340 ms

Since the derivation process used to determine the Karlovitz factor and the spatial velocity can induce some uncertainties, the time evolution of the position of the flame front, the flame area and cross-section was systematically smoothed based on a second order polynomial as shown in Figure 6-5 to obtain a general trend and avoid local discontinuities. The coefficient of determination is systematically greater than 0.99, showing a good agreement with the experimental results.

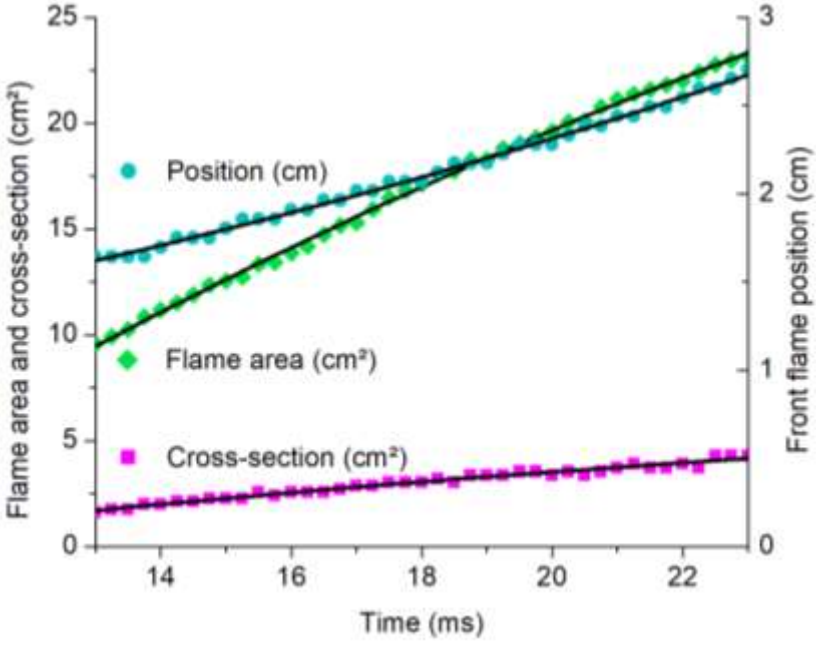

Figure 6-5 Evolution of the front flame position, flame area and cross-section with time for a 500 g.m^{-3} nanocellulose-air mixture for tv = 340 ms

[151]

Figure 6-6 represents the evolution of the burning velocity with the stretching factor after data smoothing, showing a better agreement with the different theoretical relationships than the initial raw experimental data. Indeed, the laminar burning velocity now reaches 23.1 ± 0.3 $cm.s^{-1}$ with a coefficient of determination of 0.95 instead of 0.36 in the previous case with the linear fitting, and it reaches 21.8 ± 0.4 $cm.s^{-1}$ using the nonlinear fitting. Since the mathematical treatment provides results with a better accuracy without modifying significantly the velocity values, it was systematically realized during the videos analysis phase. Videos of explosion occurring in the flame propagation tube and in the vented 20L sphere were then analyzed according to previously described method and the laminar burning velocity was estimated using both linear and nonlinear relations.

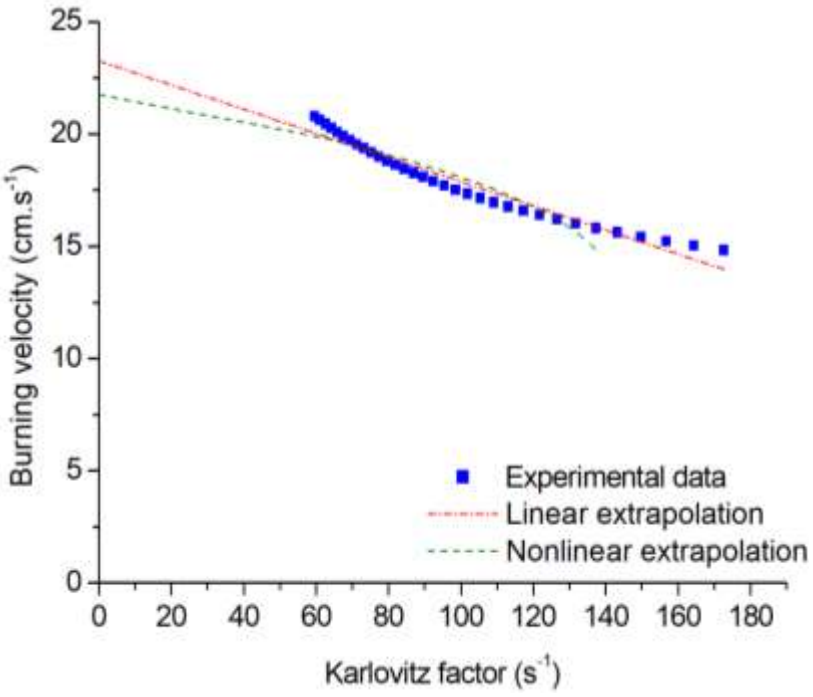

Figure 6-6 Illustration of the burning velocity – stretching factor relation after smoothing for a 500 $g.m^{-3}$ nanocellulose-air mixture for tv = 340 ms

VI.1.1.4. Determination of the optimal operating conditions

Explosion tests were performed at different ignition delay times and at a concentration of 500 $g.m^{-3}$, estimated in the tube by considering the dust weight and an average dispersion height of 0.35 cm. This concentration is close to the experimental optimal concentration (around 750 $g.m^{-3}$) and ensures a visualization of the flame kernel without interference coming from the particles, which occurs with larger concentrations. At high turbulence, i.e. at ignition delay time lower than 200 ms, the flame kernel grows up rapidly with important stretching and is rapidly influenced by the walls (Figure 6-7a). As a consequence, only a few milliseconds of the video are suitable for the analysis, and the flame profile is difficult to identify due to the important turbulence. When slightly reducing the turbulence, the flame kernel growth is slower, but the

turbulence level remains too important (u_{rms} > 1 m.s^{-1}) to precisely define the flame profile (Figure 6-7b). At very low turbulence, the flame kernel growth is still slow and nearly spherical, showing a behavior similar to gases, i.e. a rather smooth flame surface and a flame front with a paraboloidal shape (Figure 6-7c). It is then possible to correctly identify the flame profile, with 10 to 20 ms of video which can be confidently analyzed. Moreover, it can be noticed that the flame kernel does not move when growing, which shows that it is barely affected by the dust cloud inertia or by the burnt gases thrust. As a result of these observations, experiments were conducted in the tube and in the vented 20L sphere with ignition delay times from 300 ms to 450 ms, due to a limitation of the modified Hartmann tube.

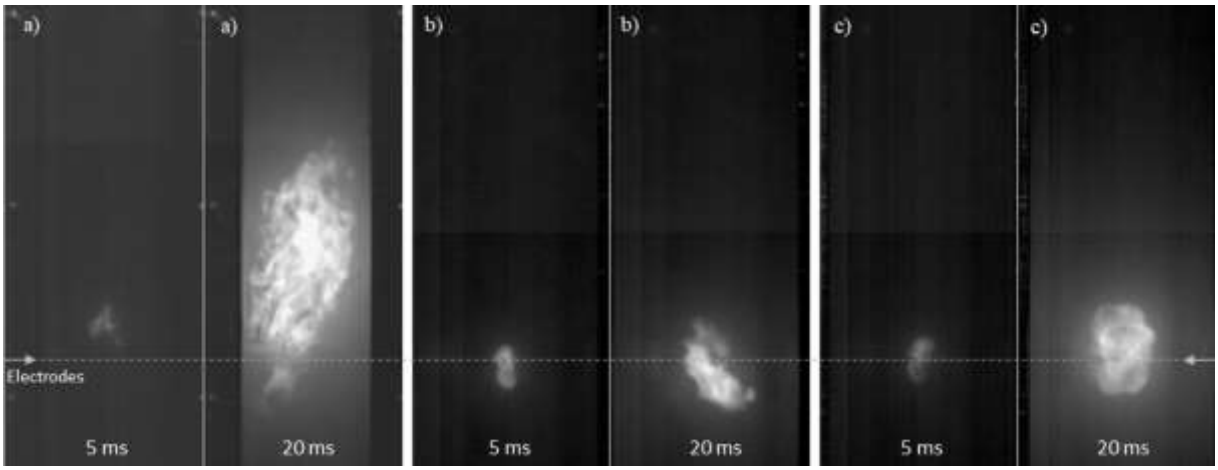

Figure 6-7 Flame propagation of 500 g.m^{-3} of nanocellulose in the tube 5 ms and 20 ms after ignition for different ignition delay times a) 125 ms b) 235 ms c) 450 ms

Figure 6-8 presents the results obtained in the flame propagation tube and in the vented 20L sphere at different ignition delay times, calculated by linear and nonlinear relations. It appears in Figure 6-8a that laminar burning velocities between 18 and 23 cm.s^{-1} are obtained using the linear equation and that velocities ranging between 17.5 and 26 cm.s^{-1} are obtained with the nonlinear relation (Figure 6-8b), which remains in the same order of magnitude. This confirms the relevance of the applied method, as using these relations allows to significantly reduce the influence of the turbulence. Indeed, the measured values seem independent from the ignition delay time. Both methods then lead to similar values in the flame propagation tube, even if the dispersion of the experimental data seems to be more significant when applying the nonlinear equation. Figure 6-8b shows that the analytical uncertainties are much higher when applying the nonlinear relationship to the experimental data measured in the vented 20L sphere.

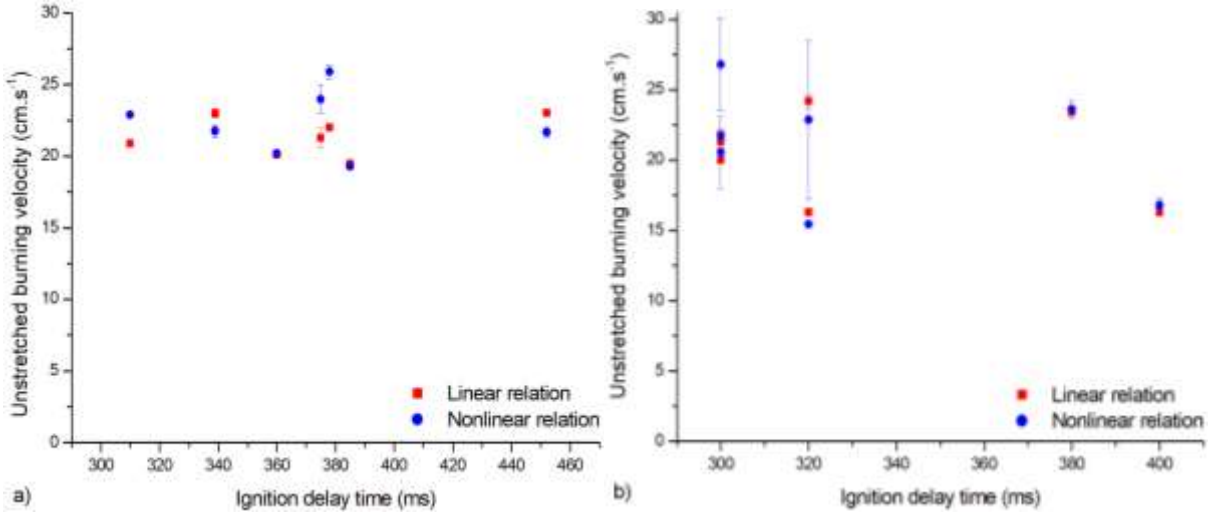

Figure 6-8 Evolution of the laminar burning velocity of 500 g.m^{-3} of nanocellulose with ignition delay time calculated by the linear and nonlinear relations in a) the propagation tube b) the vented 20L sphere

Figure 6-9 shows that the application of the nonlinear relationship is more relevant for the experimental data corresponding to a high-stretch region (Karlovitz factor from 270 to 400 s^{-1}) of the flame propagation in the tube. However, this zone corresponds to a period of time during which the flame propagation may still be affected by the ignition (near 400 s^{-1}). In most cases, as for instance for the other experimental set of data presented in Figure 6-9 (380 ms in the vented sphere), the linear fit will be preferred to the nonlinear model, especially at low stretching rates. It can also be observed in Figure 6-9 that the number of experimental points selected for the analysis is often reduced in the case of the vented sphere. Indeed, with regard to the tube, the larger volume of the 20L vented sphere is both an advantage and a drawback: an advantage because it reduces the wall effects and a drawback because, during the very first moments of the flame kernel growth, the thickness of the unburnt cloud located between the ignition zone and the window is great, which hinders the flame visualization and sometimes reduces the 'analyzable duration' of the video down to 5 ms. This limitation can be partially overcome by using a Schlieren system, as presented in section VI.1.1.1.

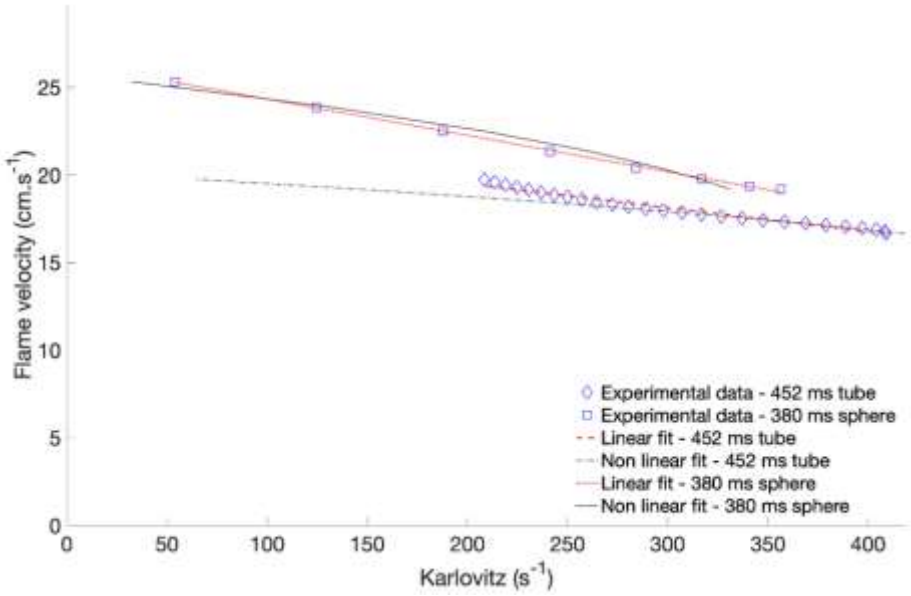

Figure 6-9 Comparison of linear and nonlinear methods applied to a nanocellulose explosion: 500 g.m^{-3}concentration, tv = 452 ms – tube and tv = 380 ms – vented sphere

An explosion in the 20L sphere and the dust kernel 5 ms and 10 ms after ignition of 500 g.m^{-3} of nanocellulose are presented in Figure 6-10a and Figure 6-10b respectively. In view of the experimental uncertainties and the slight discrepancies between the non-linear and linear relationship, only the results obtained by the latter method will be considered now.

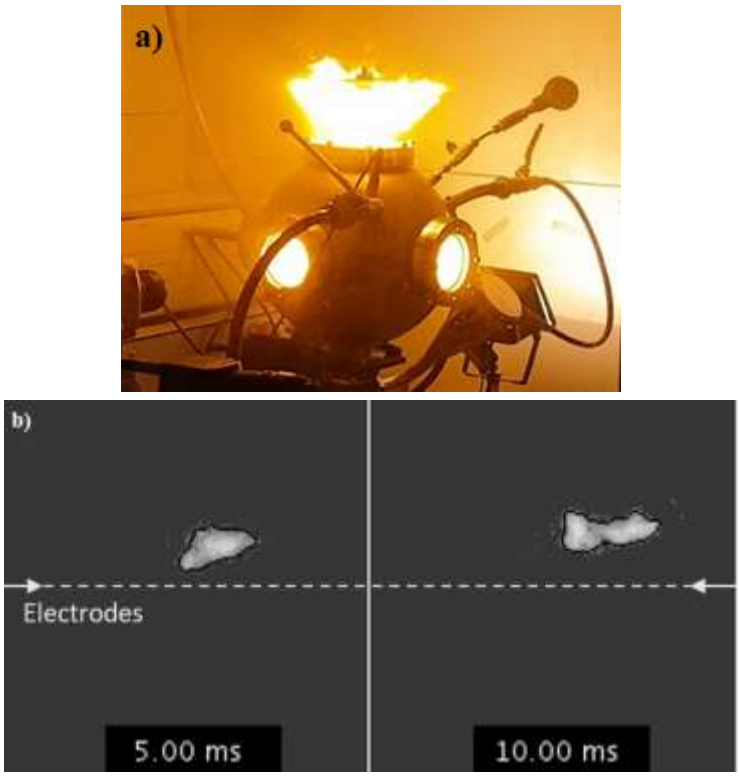

Figure 6-10 Explosion in the vented 20L sphere and b) visualization of the flame kernel 5 ms and 10 ms after ignition of 500 g.m^{-3} of nanocellulose and ignition delay time of 300 ms

[155]

VI.1.2. Pressure-time evolution interpretation

An alternative way to estimate the laminar burning velocity is provided through the recording of the pressure evolution during an explosion in the 20L sphere. Indeed, some authors such as Silvestrini et al. (2008) developed some correlations between the laminar burning velocity and the parameters K_{St} and P_{max} obtained in the 20L sphere. The results obtained by analyzing the flame propagation will be compared to the ones calculated from the following semi-empiric correlation defined by Silvestrini et al. (2008):

$$S_u{}^0 = 0.11 \frac{K_{St}}{P_{max}\left(\frac{P_{max}+1}{P_0}\right)^{0.14}\left(\frac{P_{max}}{P_0}\right)^{\left(\frac{1}{\gamma}\right)}} \qquad 6\text{-}10$$

where P_0 is the atmospheric pressure and γ the ratio of specific heats. As the previously defined relations, this correlation is based on several assumptions, such as the spherical expansion of the flame and the neglecting of the turbulent length scales. Moreover, the establishment of this correlation lies on other existing relations also relying on strong hypotheses, like a laminar flow or the fact that the burnt gases are 'trapped' behind the expanding flame front, meaning the thermal expansion factor is considered (see section VI.1.1.2) (Harris, 1983).

Furthermore, the explosivity index K_{St} is mentioned in the correlation, meaning that the "cube-root" law and its related hypotheses were used. For instance, the flame front is considered to be a thin reaction zone as defined by Dahoe et al. (1996), and Silvestrini et al. (2008) considered that P_{max} was defined as the maximum overpressure for a single explosion experiment and that a K_{St} parameter can be defined from a test performed at a single dust concentration and not from tests performed over a wide range of concentration. Thus, equation 6-10 was corrected and the following relation was applied during this work:

$$S_u{}^0 = 0.11 \frac{\left(\frac{dP}{dt}\right)_m V^{1/3}}{P_m\left(\frac{P_m+1}{P_0}\right)^{0.14}\left(\frac{P_m}{P_0}\right)^{\left(\frac{1}{\gamma}\right)}} \qquad 6\text{-}11$$

To ensure the comparison with the experiments relying on the flame propagation visualization, the explosions tests were performed in the standard 20L sphere with a permanent spark of 10 J to avoid an overdriving phenomenon and a dependence of the results on the ignition source. The laminar burning velocity of nanocellulose was then estimated using those three methods (tube, open-sphere and standard tests coupled with the previous correlation) to test the strengths and weaknesses of each method and ensure the consistency of the methods by identifying a reliable value of laminar burning velocity for nanocellulose.

VI.1.3. Comparison of the laminar burning velocities

Since the turbulence intensity is different in the tube and in the sphere, results were plotted as a function of the root mean square velocity measured in both equipment by Particle Image Velocimetry. Figure 6-11 then shows that very low turbulence level, from 0.21 to 0.13 $m.s^{-1}$ is

reached using the tube, whereas u_{rms} reaches a minimum of 0.3 $m.s^{-1}$ in the 20L sphere. However, similar values of laminar burning velocity are obtained, from 19 to 23 $cm.s^{-1}$ in the tube and from 16 to 24 $cm.s^{-1}$ in the sphere. This is due to the fact that, when increasing the ignition delay time, the turbulence level decreases in both equipment until it reaches a plateau, as mentioned in section VI.1.1.1. This latter is observed from 200 ms in both equipment, corresponding to a root-mean square velocity of 0.4 $m.s^{-1}$ in the propagation tube and 0.5 $m.s^{-1}$ in the 20L sphere. The flame propagation tube seems to produce more clustered values, which can be explained by the better visualization of the flame kernel providing a longer analyzable video than in the vented 20L sphere, thus a more accurate analysis of the flame propagation, and by a lower turbulence level. Indeed, the red spotted lines in Figure 6-11 evidences the great repeatability of the measurements when approaching a zero turbulence.

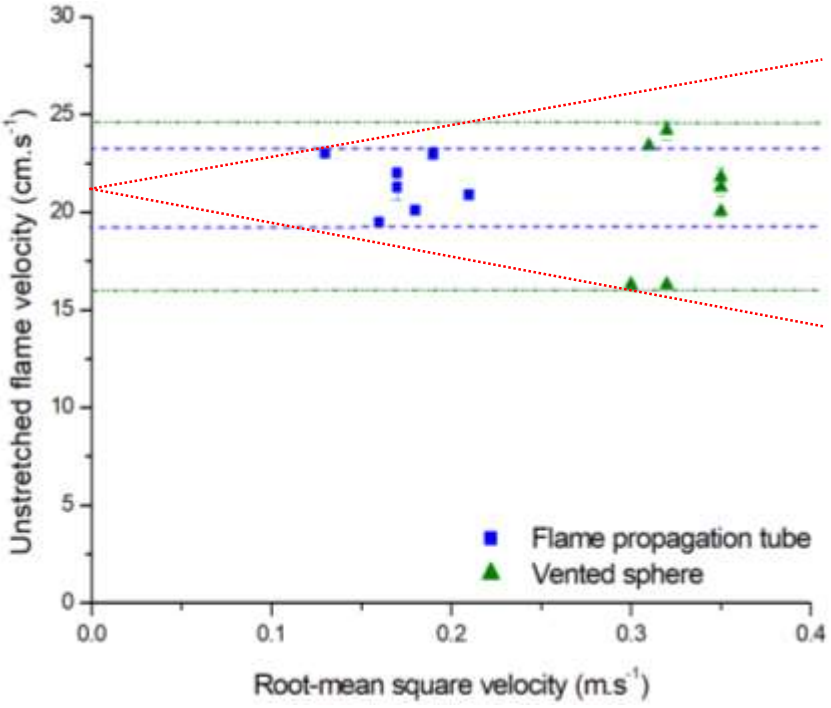

Figure 6-11 Evolution of the laminar burning velocity with the root mean square velocity in the flame propagation tube and in the vented 20L sphere

The values of the laminar burning velocities obtained through visualization of the flame propagation were then compared to the value acquired by pressure-time recording in the standard 20L apparatus (Figure 6-12).

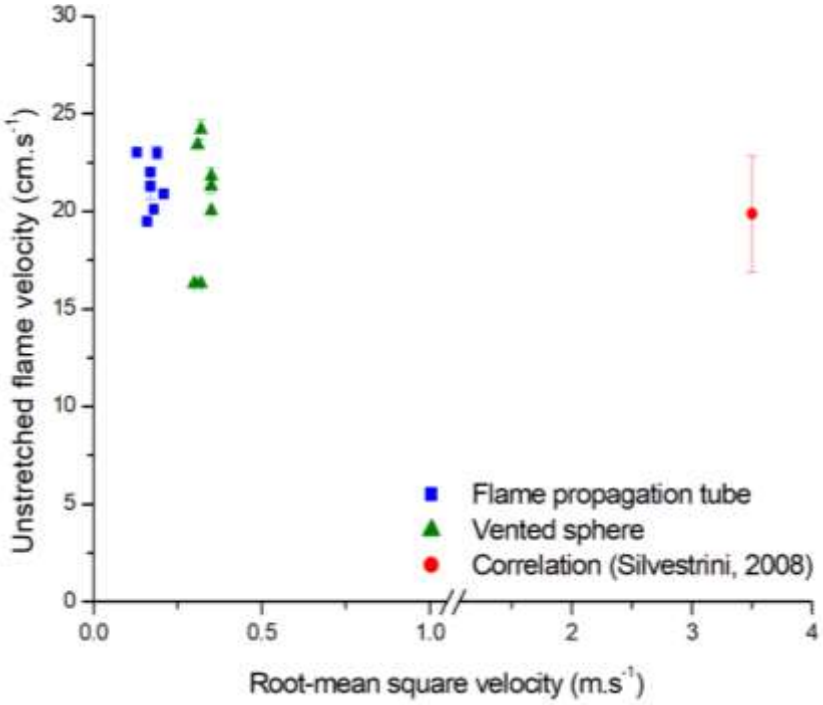

Figure 6-12 Evolution of the laminar burning velocity with the root-mean square velocity in the flame propagation tube, the vented 20L sphere and the standard 20L sphere

Using the semi-empirical correlation previously detailed (Equation 3-7), an laminar burning velocity of 19.9 $cm.s^{-1}$ is obtained for an explosion of 500 $g.m^{-3}$ of nanocellulose at a root mean square velocity of 3.5 $m.s^{-1}$ while the same value was reached in the flame propagation tube and vented 20L sphere for root-mean square velocities of 0.2 $m.s^{-1}$ and 0.3 $m.s^{-1}$ respectively. This is due to the fact that the empirical coefficient of the correlation was established by considering explosion tests performed in standard conditions in the 20L sphere. The equation was applied with a coefficient 0.11 as proposed by the authors, but it makes it valid only for $(dP/dt)_m$ and P_m obtained with an ignition delay time of 60 ms, i.e. a root-mean square velocity of 3.5 $m.s^{-1}$, as previously presented in Table 6-2.

The laminar burning velocity was then calculated by application of the correlation 3-7 to the parameters P_m and $(dP/dt)_m$ obtained with a standard explosion in the 20L sphere, with an ignition energy of 10J and ignition delay time of 60 ms. Moreover, since Cuervo (2015) and Dahoe et al. (2001) showed that the vertical velocity of the particles is close to zero for ignition delay times greater than 300 ms in the propagation tube and in the 20L sphere, and since the flame kernel stays put when growing (see section VI.1.1.4), the flame propagation visualized in both equipment is considered to be independent of the turbulence level. However, in addition to the difficulties to identify the flame kernel in the vented sphere, significant fluctuations in the velocity in the sphere can explain the more important scattering of the values of the laminar burning velocities obtained compared to the ones obtained in the tube. The values of laminar burning velocity of the nanocellulose determined for each method are presented in Table 6-2.

Table 6-2 Laminar burning velocity of the nanocellulose estimated by the three different methods

Method	Flame propagation tube (flame visualization)	Vented 20L sphere (flame visualization)	Standard 20L sphere (pressure evolution)
Laminar burning velocity ($cm.s^{-1}$)	21.4 ± 1.4	20.5 ± 3.2	19.9 ± 3.0

It first appears that the three methods lead to similar results, around 21 $cm.s^{-1}$. As a comparison, Krause and Kasch (2000) reported laminar burning velocities presented in the literature for different concentrations of two organic powders: lypocodium and cornstarch. Values from 17 $cm.s^{-1}$ to 69 $cm.s^{-1}$ were then obtained for lycopodium, and velocities between 13 $cm.s^{-1}$ and 59 $cm.s^{-1}$ were acquired for cornstarch. More specifically, van der Wel (1993) reported a laminar flame velocity for cornstarch of 13 $cm.s^{-1}$ at 400 $g.m^{-3}$ using the 20L sphere coupled with a correlation based on Mallard and Le Chatelier thermal theory, and 13 to 20 $cm.s^{-1}$ using the burner method for concentrations from 400 $g.m^{-3}$ to 600 $g.m^{-3}$. Haghiri and Bidabadi (2010) also calculated laminar burning velocities for organic powders from 15 $cm.s^{-1}$ to 45 $cm.s^{-1}$ for concentrations from 30 $g.m^{-3}$ to 100 $g.m^{-3}$ using a model considering the thermal radiation effect. Moreover, Cuervo et al. (2017) also measured a laminar burning velocity for 915 $g.m^{-3}$ of starch around 19.9 $cm.s^{-1}$. Since starch and nanocellulose have similar structures and composition, these values are in good agreement with the value of 21.4 $cm.s^{-1}$ obtained in the tube for the nanocellulose, despite the different concentrations.

The Markstein length was also calculated from video analysis of the flame propagations in the tube and the vented sphere. Similar values were obtained in both equipment, with a mean value of -0.25 mm in the propagation tube and of -0.19 mm in the vented sphere. A negative value of the Markstein length means that the flame speed increases with the stretch rate, implying that the flame is unstable. However, the obtained values are very low (absolute values usually lower than 1 mm), and some positive values up to 0.3 mm were also obtained when analyzing the flame propagation videos under certain conditions, which makes it difficult to draw an accurate conclusion on the Markstein length of nanocellulose flames. Nevertheless, it should be stressed that these values are much lower than that obtained by Dahoe et al. (2002) for cornstarch-air mixtures, i.e. 11.0 mm, but are a bit higher than those encountered for methane-air mixtures, i.e. from 0.1 to 0.2 mm. This can be related to the fact that nanocellulose is prone to devolatilization when exposed to high temperatures. However, complementary tests with different concentrations are necessary to conclude on this point.

VI.1.4. On the application of the correlation

Although the values obtained with the three methods are in good agreement, the propagation tube provides the less scattered values of laminar burning velocity, notably due to a lowest turbulence level. The calculation performed using Silvestrini et al. (2008) correlation also

provides a value in good agreement with the values measured by flame propagation analysis, but with a higher uncertainty than in the propagation tube. It is mainly due to the lack of reproducibility of the experiments in the standard 20L sphere at 60 ms (Proust et al., 2007). Indeed, at an ignition delay time of 60 ms, the turbulence level is in the "transition stage" identified by Murillo et al. (2018), and turbulence variations have a strong impact on the maximum rate of pressure rise. Adapting the correlation with a coefficient estimated from experiments performed in pseudo-laminar conditions, i.e. higher ignition delay time, would then improve the accuracy of the estimation of the laminar burning velocity. It would then be interesting to use flame propagation analysis on different powders to determine such a coefficient and to apply it to the correlation established by Silvestrini et al. (2008). However, this adapted correlation would have to be used with P_m and $(dP/dt)_m$ measured in the same turbulent conditions than the coefficient, which can limit the application of such a relation. To apply this correlation (6-11) to different conditions and represent industrial situations, an evaluation of the evolution of the correlation coefficient (here 0.11) with the initial turbulence is then required.

Since the correlation has been validated for nanocellulose at 60 ms, an estimation of the coefficient dependency with the turbulence was realized by analyzing the explosion tests performed with 750 $g.m^{-3}$ of nanocellulose and 250 $g.m^{-3}$ of carbon black for ignition delay times from 20 ms to 200 ms and 120 ms respectively. By applying the correlation 6-11 and considering the value obtained at 60 ms as a reference, the corrected correlation coefficients were estimated for different root-mean square velocities, as presented in Figure 6-13. It appears that the coefficient value to consider in order to obtain the laminar burning velocities of 20.2 $cm.s^{-1}$ and 23.4 $cm.s^{-1}$ calculated for the carbon black and nanocellulose respectively increases when decreasing the root-mean square velocity. Indeed, the correlation coefficient can be correlated to the root-mean square velocity by a decay law similar to the one established by Dahoe et al. (2001) relating the root-mean square velocity and the time. By combining the values calculated from the tests performed on nanocellulose and carbon black, the relation 6-12 was deduced:

$$C = 0.2213\, {u_{rms}}^{-0.595} \qquad 6\text{-}12$$

This relation, represented by the dotted line in Figure 6-13, shows a good agreement with the experiments. Notably, a correlation coefficient of 0.105 is calculated for an ignition delay time of 60 ms, i.e. a root-mean square velocity of 3.5 $m.s^{-1}$, instead of the original coefficient of 0.11. This relation can be directly injected in the correlation initially established by Silvestrini et al. (2008), leading to equation 6-13.

$${S_u}^0 = 0.2213\, {u_{rms}}^{-0.595} \frac{\left(\frac{dP}{dt}\right)_m V^{1/3}}{P_m\left(\frac{P_m+1}{P_0}\right)^{0.14}\left(\frac{P_m}{P_0}\right)^{\left(\frac{1}{\gamma}\right)}} \qquad 6\text{-}13$$

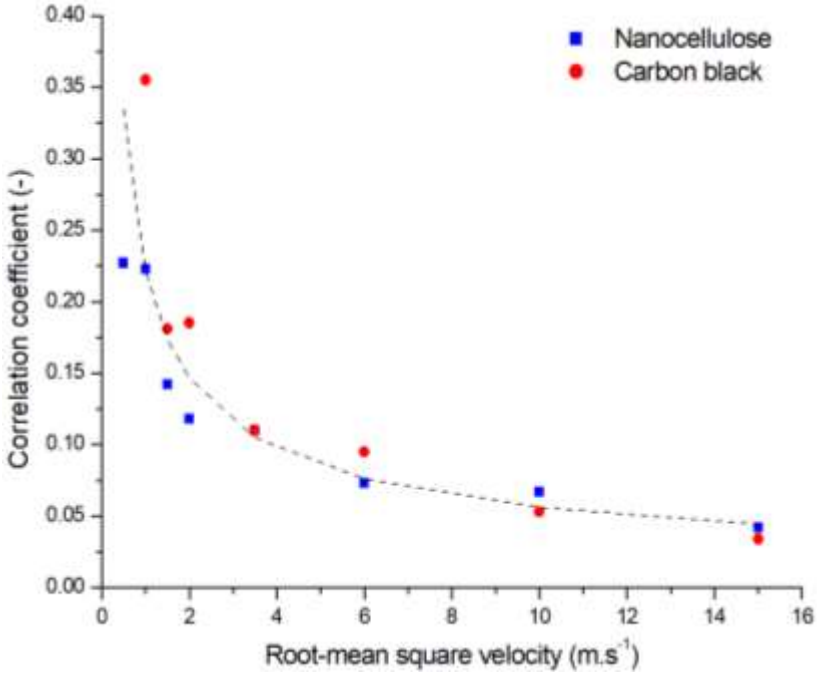

Figure 6-13 Evolution of the correlation coefficient to calculate the laminar burning velocity with the root-mean square velocity in the 20L sphere

This new relation was applied to the nanocellulose and carbon black powders for each ignition delay time. Average values of 24.6 ± 3.1 cm.s^{-1} and 18.4 ± 2.5 cm.s^{-1} were then respectively calculated for nanocellulose (750 g.m^{-3}) and carbon black (250 g.m^{-3}). Those values correspond to differences of respectively 5% and 9% compared to the values calculated with the original correlation, thus evidencing a good agreement. Although more tests performed on more powders and more concentrations would be required to reinforce its accuracy, such equation could then allow the assessment of the laminar burning velocity of a dust-air mixture in different operating conditions.

Then, this correlation was applied to all the powders studied in this work on the optimal concentration (see section IV.2.2, Table 4-4), and the maximum values are presented in Table 6-3. It appears that both aluminum powders exhibit laminar burning velocities around 58 cm.s^{-1}, which is considerably higher than the values presented in the literature, which are however quite scattered. One of the highest values was reported by Ballal (1983) who performed micro-gravity measurements on aluminum particles of 10 µm, and obtained a laminar burning velocity of 41 cm.s^{-1}. It should be noted that the mean surface diameter of both powders after dispersion was measured around 3 µm (see chapter 3, section III.2.2.3), which corresponds to the strongest contribution of the radiative heat transfer on the flame propagation. Such influence will notably be discussed in section VI.2.2 for the nanocellulose. However, this may explain the high velocity of the flame propagation of aluminum nanopowders, and the backfire to the dust container identified in section V.4 of chapter 5. The laminar burning velocity of the carbon-coated silicon is also quite high, although no comparative value can be found in the literature, notably due to the non-flammable nature of micro silicon carbide.

Nevertheless, the same tendency than observed on explosion severity experiments appears in Table 6-3, the raw powder presenting the highest explosion severity. Finally, the laminar burning velocity of the carbon black is rather similar to that of nanocellulose, which is consistent with their common St class.

Table 6-3 Laminar burning velocity of each powder calculated according to equation 3-9

Nanocellulose	Carbon black	Al / 40-60 nm	Al / 100 nm	SiΩC Raw powder	SiΩC A1	SiΩC A2	SiΩC B
23.4	20.2	57.3	58.3	48.0	41.4	38.2	31.1

VI.1.5. Influence of the dust concentration

Even though the theoretical stoichiometric concentration for the combustion of nanocellulose is of approximately 250 $g.m^{-3}$, the most severe explosions were obtained for concentrations of 750 $g.m^{-3}$ and 1000 $g.m^{-3}$ in terms of maximum overpressure and maximum rate of pressure rise (see section IV2.2). It is then legitimate to investigate on the influence of the dust concentration on the laminar burning velocity. However, its estimation through flame propagation at high concentration is difficult since the dust cloud can hinder the visualization of the flame kernel. A few tests were performed in the flame propagation tube at larger dust concentrations (i.e. 750 $g.m^{-3}$) and a slight increase of the flame velocity has been observed. However, since it is currently impossible to accurately estimate the laminar burning velocity at high concentration using the flame propagation visualization due to flame obscuring, it was calculated as previously, using the correlation established by Silvestrini et al. (2008) coupled with the standard results presented in section IV.2.2. It has to be noticed that those experiments were carried out with chemical ignitors of 10 kJ, contrary to the value presented in Figure 6-14 which was obtained using an electrical spark of 10 J.

Since the laminar burning velocity is calculated from the knowledge of the maximum overpressure and the maximum rate of pressure rise, it follows the same evolution than those parameters (Figure 6-14), i.e. it increases with the concentration until reaching a maximum value. Such value was obtained around 31 $cm.s^{-1}$ for a concentration of 1000 $g.m^{-3}$, and is rather close to the laminar burning velocity of methane in stoichiometric conditions generally reported to be around 35 $cm.s^{-1}$ (Bradley et al., 2017) for a maximum overpressure of 7.2 bars and a K_g of 395 $bar.m.s^{-1}$, measured in standard conditions by Torrado et al. (2017a). The value calculated for the nanocellulose with the correlation then seems higher than expected considering its medium explosion severity compared to pure methane, thus questioning the validity of the correlation for high concentrations. Indeed, Silvestrini et al. (2008) have chosen 24 dust-air mixtures to calculate the coefficient for the semi-empiric correlation. However, it should be stressed that, among these mixtures, only 3 dust concentrations were higher than 500 $g.m^{-3}$.

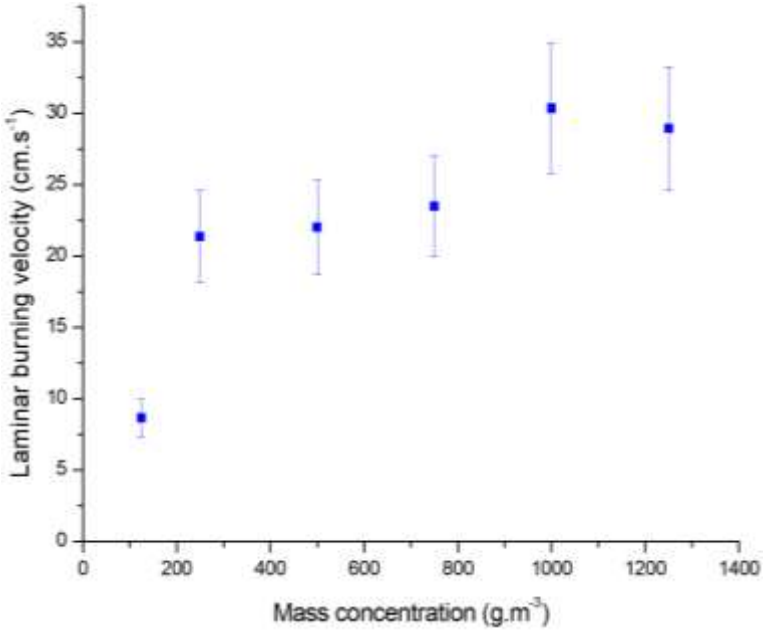

Figure 6-14 Evolution of the laminar burning velocity calculated by a semi-empiric correlation with the mass concentration

The same method considering mixtures with a larger range of concentrations may then extend the validity of the correlation to higher concentrations. Indeed, in order to realize an accurate evaluation of the explosion consequences, the influence of the dust concentration on the laminar burning velocity must be considered. Since flame propagation visualization is often more difficult at high concentrations, laminar burning velocity numerically obtained could be considered. Numerical models can also highlight the contribution of a phenomenon: in the next section, the influence of the radiative heat transfer on the flame propagation of nanocellulose will notably be discussed.

VI.2. One dimensional modelling of flame propagation

Complementary to experiments relying on the flame visualization and the pressure-time evolution, the laminar flame velocity was approached by adapting a one-dimension flame propagation model developed by Torrado et al. (2018) and initially designed to describe gas and hybrid mixtures explosions (Santandrea et al., 2020b). In a first approach, a comparison was realized between the laminar burning velocities obtained by considering, on the one hand, the combustion of the pyrolysis gases, and on the other hand, considering directly the combustion of the dust. Thus, the validity of the hypothesis of a dust combustion controlled by the gas combustion can be verified. In a second approach, the influence of the radiative heat transfer on the flame propagation is investigated.

VI.2.1. Model principle

The model developed by Torrado et al. (2018) was adapted to nanocellulose using the same initial hypotheses, i.e. considering a flame propagating without stretching and gravity, in quiescent conditions. Thus, the propagation was considered in a horizontal tube with a numerical length of 5 cm involving two parallels walls divided into three distinct zones: preheat, reaction and post-flame, knowing that the flame propagates from the post-flame zone to the preheat zone. In addition, the tube was split into 160 volumes in which the reactive mixture is considered homogeneous. Mass, species and energy balances, notably based on the properties of the considered chemical species, were expressed in the simulation domain.

The transitory flame properties are determined solving the mass and energy conservation equations, taking into account the mixture density, the mass fraction and reaction rate of the i component, the mass diffusion flux and velocity (Poinsot and Veynante, 2005). In particular, the mass reaction rate of a component depends on its molecular weight and the rate of the reactions in which it is involved. The rate of each reaction r_j is then expressed as:

$$r_j = k \prod \varphi^{n_i} \quad 6\text{-}14$$

where φ is the mole concentration and n_i the reaction order of the component i in the reaction j. The reaction constant is assumed to follow the Arrhenius law and is defined as:

$$k_j = A_i T^{\beta} \exp\left(\frac{-E_i}{RT}\right) \quad 6\text{-}15$$

Two methods were considered: first, as for the flame visualization experiments, a fast devolatilization of the dust and a flame propagation kinetically limited by the combustion of the pyrolysis gases. Indeed, a Damköhler number for the nanocellulose combustion was calculated in section IV.1.5 and reached 1.5, which traduces that the dust combustion is limited by the gas combustion. Since cellulose and starch are both polymers formed of glucose chains, both compounds are assumed to produce the same pyrolysis gases when tested in the same conditions. Thus, pyrolysis experiments were conducted on wheat starch in a Godbert-Greenwald oven modified according to Dufaud et al. (2012) to collect the post-pyrolysis gases, which were then analysed by gas chromatography. The composition obtained for a concentration of approximately 500 $g.m^{-3}$ and a temperature of 973K obtained by Pietraccini et al. (2020) was then used as the initial composition of the fuel in the model for a numerical determination of the laminar flame velocity of nanocellulose (Figure 6-15).

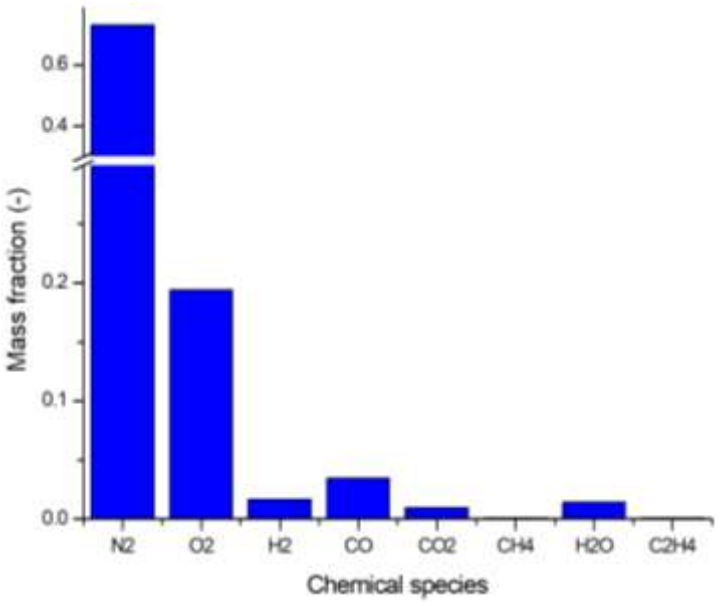

Figure 6-15 Initial composition of the nanocellulose pyrolysis gases/air mixture considered in the flame propagation model

The second method consists in considering simultaneously the pyrolysis of the dust and the combustion of the pyrolysis gases. The reactions mechanisms and kinetics estimated by Pietraccini et al. (2020) from the knowledge of the composition of the pyrolysis gases (Figure 6-15) was used, considering the following reactions:

$$C_6H_{10}O_5 \xrightarrow{k_1} 1.17\ H_2 + 3.4\ CO + 0.02\ CO_2 + 0.45\ CH_4 + 0.32\ C_2H_4 + 0.83\ H_2O + 0.72\ C_2H_4O$$

$$C_6H_{10}O_5 \xrightarrow{k_2} 0.8\ H_2 + 1.7\ CO + 0.55\ CO_2 + 0.04\ CH_4 + 0.05\ C_2H_4 + 0.4\ H_2O + 1.83\ C_2H_4O$$

$$C_6H_{10}O_5 \xrightarrow{k_3} 5\ H_2O + 6\ C$$

The activation energies E_i and pre-exponential factors A_i of the three reaction rate constants k_i are presented in Table 6-4.

Table 6-4 Parameters of the reaction rate constants considered for the pyrolysis of nanocellulose

Reaction rate constants	Pre-exponential factor (s^{-1})	Activation energy ($kJ.mol^{-1}$)
k_1	1.2×10^{17}	318.6
k_2	8.8×10^{17}	41
k_3	2.8×10^{5}	72.6

During the pyrolysis of organic powders, permanent gases, tar and char are generated (Nowakowska et al., 2018). The acetaldehyde C_2H_4O was not considered as a reactant for the combustion, nor the ethylene, due to the small amount generated during the pyrolysis.

For both methods, the combustion of the pyrolysis gases is then considered. In this work, it is assumed to follow a semi-global kinetic mechanism in order to describe the temperature and final fraction of the components in the burnt gases. A detailed combustion mechanism is not implemented due to the numerical complexity demand to solve the differential equations for all the involved species.

Table 6-5 Reaction mechanisms considered for the combustion of the pyrolysis gases (Units cal, mol, m, s)

#	Reaction	A_i	β	*Ei*	Reaction order	Reference
1	$CH_4 + 0.5O_2 \rightarrow CO + 2H_2$	2.45×10^9	0	3×10^4	$[CH_4]^{0.5} [O_2]^{1.25}$	(Jones and Lindstedt, 1988)
2	$CH_4 + H_2O \rightarrow CO + 3H_2$	3×10^5	0	3×10^4	$[CH_4] [H_2O]$	(Jones and Lindstedt, 1988)
3	$CO + H_2O \rightarrow CO_2 + H_2$	2.75×10^6	0	2×10^4	$[CO] [H_2O]$	(Jones and Lindstedt, 1988)
-3	$CO_2 + H_2 \rightarrow CO + H_2O$	9×10^7	0	2.8×10^4	$[CO_2] [H_2]$	(Torrado et al., 2018)
4	$H_2 + 0.5O_2 \rightarrow H_2O$	3.85×10^{13}	-1	4×10^4	$[H_2]^{0.25} [O_2]^{1.50}$	(Jones and Lindstedt, 1988)
-4	$H_2O \rightarrow H_2 + 0.5O_2$	9.27×10^{18}	0.88	9.8×10^4	$[H_2O] [H_2]^{-0.75} [O_2]$	(Andersen et al., 2009)
5	$O_2 \rightarrow 2O\cdot$	1.5×10^9	0	1.13×10^5	$[O_2]$	(Frassoldati et al., 2009)
6	$H_2O \rightarrow H\cdot + OH\cdot$	2.3×10^{22}	-3	1.2×10^5	$[H_2O]$	(Frassoldati et al., 2009)
7	$CO + 0.5O_2 \rightarrow CO_2$	1.26×10^4	0	10×10^3	$[CO] [O_2]^{0.25} [H_2O]^{0.5}$	(Andersen et al., 2009)
-7	$CO_2 \rightarrow CO + 0.5O_2$	1.95×10^{12}	-0.97	78.4×10^3	$[CO_2] [H_2O]^{0.5} [O_2]^{-0.25}$	(Andersen et al., 2009)
8	$C(s) + 0.5\ O_2 \rightarrow CO$	1.1×10^4	0	42.8×10^3	$[O_2]^{0.5}$	(Bews et al., 2001)

Since the main chemical species constituting the pyrolysis gases of nanocellulose are the same than the species initially taken into account in the model for the flame propagation of a methane/air flame (Torrado et al., 2018), the same reaction mechanisms were used. Reactions involving radicals H, OH and O are also considered to improve the prediction of the flame

temperature (Frassoldati et al., 2009). In addition, since the pyrolysis step mainly produced carbon monoxide, a reversible oxidation reaction of this gas to produce carbon dioxide was added (Table 6-5, reactions 7 and -7).

In each volume, the species and energy balances are then expressed. The species balance notably considers the mixture density and, for each component, the mass fraction, the diffusion fluxes and the mass reaction rate. In a first approach, the energy balance considers the temperature and, for each species, the specific heat, enthalpy of formation and heat conductivity. Both the convection and conduction are then taken into account, and the radiative heat transfer will be added to this balance in section VI.2.2. The calculation of the flame velocity relies on the numerical integration of the differential equations of mass, species and energy. The space derivatives were discretized using the finite volume method with 160 control volumes to obtain a system of ordinary differential equations, which was solved using the integration functions ODE in Matlab. The expression of the mass and species balance, the mass diffusion fluxes and the energy balance, along with the numerical resolution, are properly described by Torrado et al. (2018).

The resolution of the ordinary differential equations requires an initial value of the temperature and mass fractions of all the considered species in every numerical domain. The composition in the preheat zone, which represents 25% of the numerical domain, is defined by the mass fractions of the considered mixture in laboratory conditions. As a first approximation, the mass fractions and temperature are assumed to evolve linearly in the reaction zone, implying those values are known if the initial and final conditions are fixed. To estimate the conditions in the post-flame zone (70% of the considered distance), the adiabatic temperature and mass fraction of the burnt gases for a steady flame were calculated using PREMIX program (Kee et al., 1993). This approach, represented in Figure 6-16, allows reducing the calculation time and to improve the convergence of the program, by initializing all the conditions close to a stable solution.

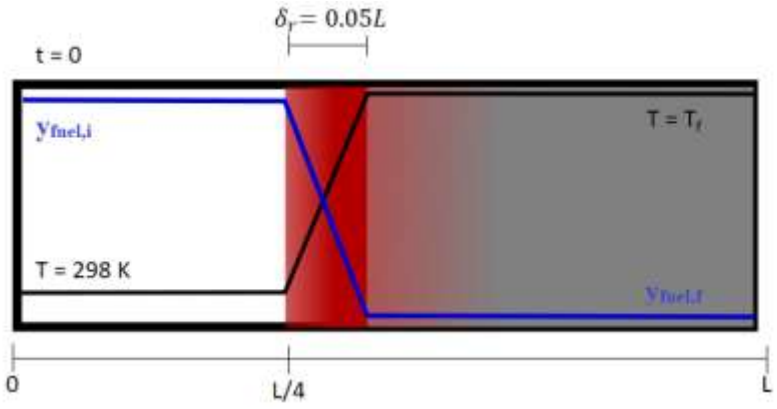

Figure 6-16 Schema of the initial conditions of the temperature and fuel fraction in each zone of the flame

The system previously defined was then analyzed considering a distance L of 5 cm and an integration time of 50 ms. The evolution of the temperature with time is presented in Figure

6-17 for 500 g.m^{-3} of nanocellulose considering only the combustion of the pyrolysis gases, at different positions to describe each zone, knowing that the preheat zone spreads up to 1.25 cm and that the post-flame zone starts at 1.5 cm. It appears that, in the post-flame zone (2.5 and 5 cm), the temperature is constant with time, since the reaction already occurred. Then, a fast increase of the temperature after a few milliseconds is visible in the reaction zone, and progressively shifts toward the preheat zone with time, describing the propagation of the flame.

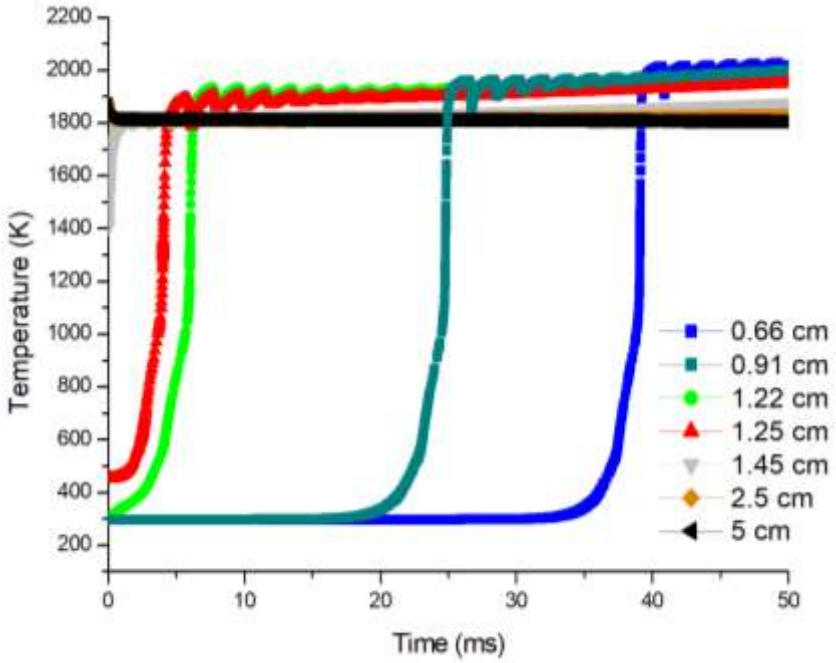

Figure 6-17 Evolution of the temperature with time for different control volumes when modelling the flame propagation of nanocellulose (quiescent conditions, 500 g.m^{-3})

VI.2.2. Influence of the pyrolysis step

The position of the flame front, assimilated to the highest temperature, was recorded for each integration time and is presented in Figure 6-18. It should be reminded that the reaction zone was initially located between 1.25 cm and 1.5 cm. However, before 1 ms, a very fast displacement of the flame is observed, preventing a clear determination of the flame front position between 1.4 and 1.5 cm. Nevertheless, a linear time-evolution of the flame position can be observed from 1 ms to 50 ms. A laminar flame velocity of 17.5 cm.s^{-1}, represented by the slope of the linear regression, was then obtained for the combustion of the pyrolysis gases of nanocellulose.

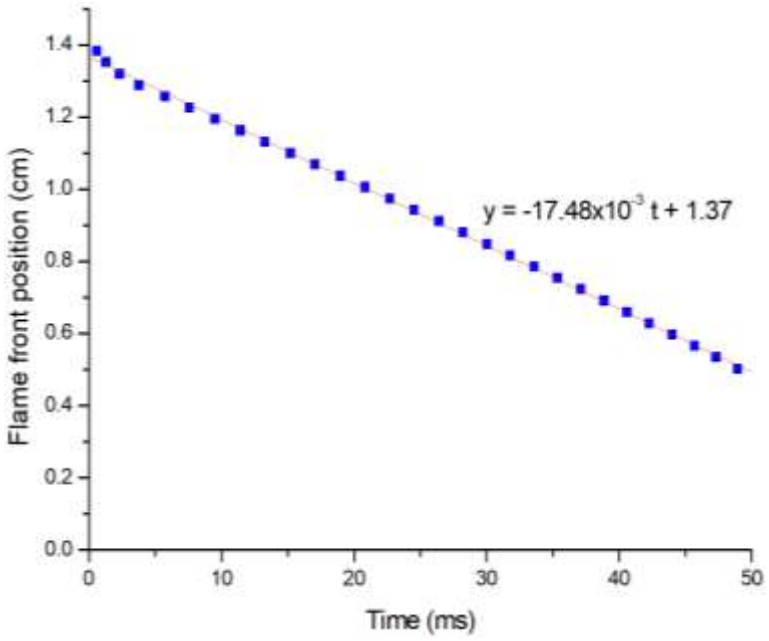

Figure 6-18 Evolution of the flame front position with time during the combustion of nanocellulose pyrolysis gases

The numerical and experimental values of laminar flame velocity obtained for 500 $g.m^{-3}$ of nanocellulose are summarized in Table 6-6. First, since the assumption of a fast devolatilization was realized in both cases, the value obtained by considering the combustion of the pyrolysis gases in the model is compared to the experimental values obtained by flame visualization. The value determined numerically appears to be of the same order of magnitude than the experimental ones, with a maximum difference of 22% with regard to the laminar flame velocity measured in the flame propagation tube. This value is also consistent with laminar flame velocity of "wood gas" at the stoichiometry mentioned in the literature by Mollenhauer and Tschöke (2010) and Przybyla et al. (2008), reaching around 14 $cm.s^{-1}$ and 20 $cm.s^{-1}$ respectively. Then, a decrease of 12% appears when considering the dust pyrolysis reactions in the model in addition to the combustion of these gases, thus validating the assumption of a fast pyrolysis.

Table 6-6 Numerical and experimental values of laminar flame velocity of nanocellulose

Determination method	Laminar flame velocity ($cm.s^{-1}$)
Propagation model (dust combustion)	15.3
Propagation model (combustion of pyrolysis gases)	17.5
Flame visualization: propagation tube	21.4
Flame visualization: vented sphere	20.5
Pressure-time evolution: application of Silvestrini et al. (2008) correlation	19.9

VI.2.3. Influence of the radiative heat transfer

Although the pyrolysis step is fast, the particles that did not react can also impact the flame propagation through a thermal energy transfer, which tends to increase the propagation velocity. To evaluate this influence, the radiative heat transfer, added to the flame propagation model by Torrado et al. (2018) and based on the work of Haghiri and Bidabadi (2010), is now considered during the combustion of the pyrolysis gases of nanocellulose. The radiation then occurs between the propagating flame and a gray-two-phase environment, including the absorption, emission and scattering of thermal radiation intensity (Torrado, 2017). However, since the model considers homogeneous zones, which is not the case in practice, all the dust reacts when considering the pyrolysis reactions, which prevents from evaluating the influence of some remaining particles. Only the combustion of the pyrolysis gases was then considered, and some nanoparticles of cellulose were added to the numerical system, without reaction.

Since it is difficult to evaluate the amount of remaining particles that did not react, several dust concentrations, assumed constant with time, were tested, and a cloud constituted of spherical particles of the same diameter homogeneously dispersed over the simulation domain was considered. Moreover, due to the agglomeration of the nanoparticles, the particle size after dispersion must be considered. Since particle size distribution measurements after dispersion of nanocellulose in the 20L sphere led to a mean value of 10 µm (see section III.2.2.3), this value was chosen as a reference for the calculation, along with 100 nm, to represent the primary particles, and 60 µm, to represent the agglomerates which are not broken by the dispersion process In this model, Mie scattering, valid for micron particles, was then considered to define the radiative heat transfer. It should be noted that Rayleigh scattering, encountered for particles smaller than 100 nm, do not contribute significantly to the flame expansion due to the emission in every direction (Dufaud et al., 2011; Hong and Winter, 2006). Thus, decreasing the particle size below this size would only decrease the radiative heat transfer contributing to the flame propagation, and so the flame velocity. The concentration of dust that did not react during the combustion of the 500 $g.m^{-3}$ of nanocellulose was varied from 2.5 $g.m^{-3}$ to 100 $g.m^{-3}$, to represent the radiative heat transfer at the beginning and at the end of the reaction. The radiative heat transfer was then added to the energy balance and the heat capacity of the dust was then taken into account during the calculation of the mean heat capacity of the mixture.

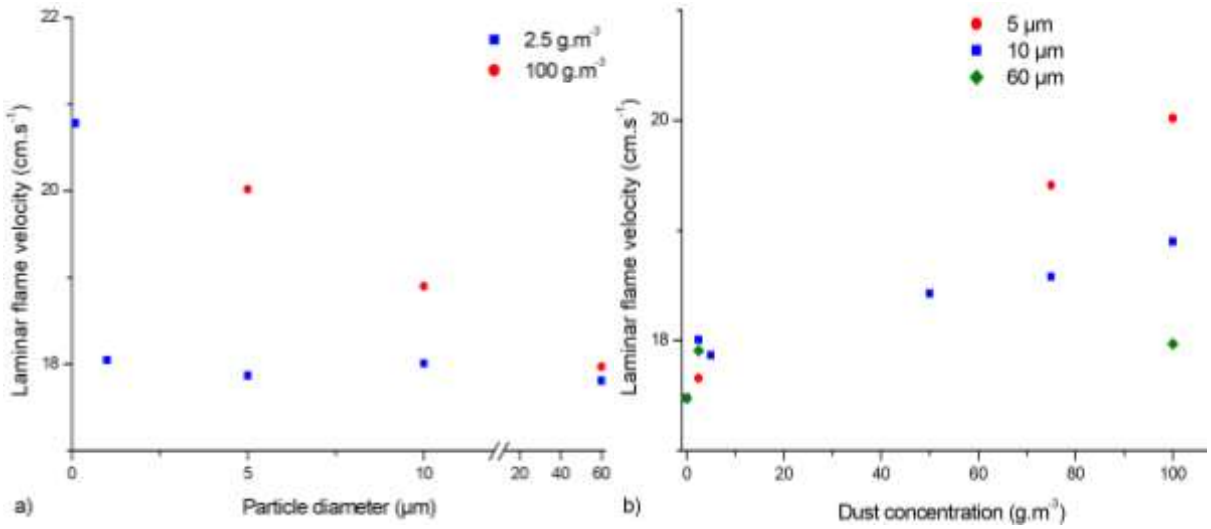

Figure 6-19 Influence of the a) primary diameter and b) dust concentration considered for the radiative heat transfer during the combustion of the pyrolysis gases of 500 g.m^{-3} of nanocellulose

In Figure 6-19a, it appears that small particles contribute more to the radiative heat transfer than bigger particles in the micro-range. Indeed, particles of 60 µm bring similar contribution to the flame acceleration, i.e. an increase of around 0.5 cm.s^{-1}, at 2.5 g.m^{-3} and 100 g.m^{-3}, which corresponds to an increase of 2% to 3% with regard to the value calculated without considering the radiation. In contrast, 100 g.m^{-3} of particles of 5 µm lead to a flame velocity of 20 cm.s^{-1}, i.e. 14% higher than the flame velocity of the pyrolysis gases. It should be underlined that the contribution of particles of 100 nm to the radiative heat transfer may be overestimated since Mie scattering was considered for the calculation whereas Rayleigh scattering is more representative of the heat transfer of nanoparticles. In Figure 6-19b, it appears that a dust concentration of 2.5 g.m^{-3} leads to a mean flame velocity of around 17.8 cm.s^{-1} for particles between 5 and 60 µm. As a consequence, increasing the dust concentration also increases the contribution of the radiative heat transfer to the flame propagation, leading to a burning velocity of 20.0 cm.s^{-1} when considering 100 g.m^{-3} of 5 µm particles.

Therefore, as expected, both the dust concentration and the particle size are of great importance when considering the radiative heat transfer. Indeed, the absorption coefficient K_a and the scattering coefficient K_s directly depend on the dust concentration, the dust density and the particle size, as follows (Haghiri and Bidabadi, 2010):

$$K_a = \frac{3}{2}\frac{C}{\rho_p\, d_p}\, Q_{abs} \qquad 6\text{-}16$$

$$K_s = \frac{3}{2}\frac{C}{\rho_p\, d_p}\, Q_{sca} \qquad 6\text{-}17$$

where C is the dust concentration, ρ_p the particle density, d_p the particle diameter and Q_{abs} and Q_{sca} respectively the absorption and scattering efficiency.

The absorption and scattering coefficients are then directly proportional to the total reactive surface area (TSA) developed by the particles in the cloud, which can be expressed as follows for spherical particles:

$$TSA = \frac{6\,C}{\rho_p\, d_p} \qquad 6\text{-}18$$

A linear evolution of the calculated flame velocity with the total surface area developed by the particles considered in the radiative heat transfer appears in Figure 6-20. Then, it can be observed that the radiative heat transfer generated by particles developing a total surface area lower than 10 $m^2.m^{-3}$ does not lead to a significant increase of the flame velocity, with values between 17.5 and 18 $cm.s^{-1}$. However, when considering a total surface area of 100 $m^2.m^{-3}$, a flame velocity of 20.8 $cm.s^{-1}$ is reached, which corresponds to an increase of 19% compared to the initial value of 17.5 $cm.s^{-1}$ (without radiation), thus proving again the importance of considering the surface area when analysing dust explosions, instead of focusing only on mass concentration. It should also be noted that increasing the concentration too much would lead to an important increase of absorption, which would limit the heat radiation in the preheat zone. It can be related to the inter-particle distance, which is also of great interest when dealing with the group combustion, discussed in chapters 4 and 5.

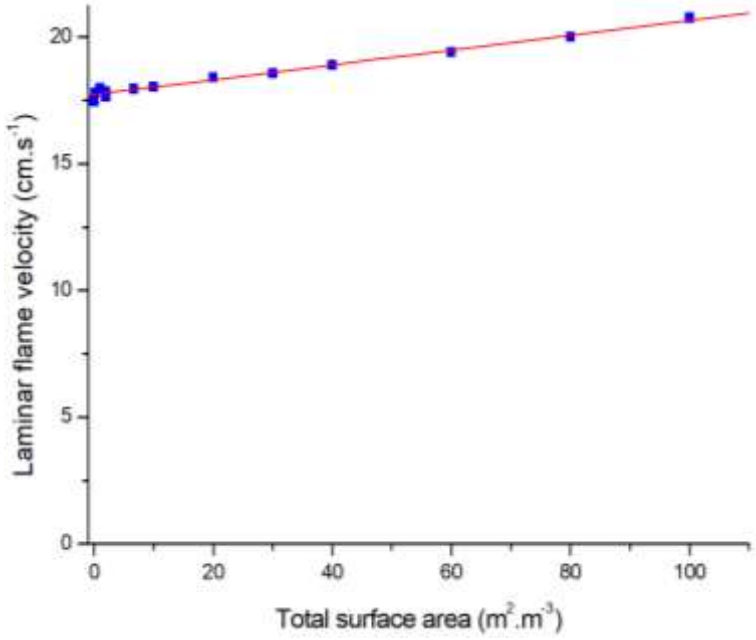

Figure 6-20 Influence of the total surface area of the particles implied in the radiative heat transfer on the flame velocity

The values experimentally and numerically determined could then be used as inputs in simulation and by adding the contribution of the turbulence of the dust cloud, the consequences of an explosion in specific conditions can be estimated. It implies that the turbulent burning velocity has to be deduced from the knowledge of the laminar burning velocity and the turbulence level.

VI.3. Application of turbulent velocity models

Several correlations relating the turbulent burning velocity to the laminar burning velocity and the turbulence intensity exist in the literature, and were notably summarized by Andrews et al. (1975), Dahoe et al. (2013) and Gülder (1991). Although these models were established for premixed flames, some of the correlations presented by Dahoe et al. (2013) were tested in this study to be compared, in a reverse approach, to the values of turbulent burning velocities obtained by analyzing the flame propagation in the tube (Table 6-7). In addition to those correlations, the relation (g) established by Popat et al. (1996) used in the FLACS-DustEx CFD code, i.e. the most commonly used to estimate burning velocities and other model parameters from experimental data, was applied to the experimental data produced in this work (Ghaffari et al., 2019; Skjold, 2007).

Table 6-7 Some turbulent burning velocity models for premixed flame propagation

Notation	Formula	Reference
(a)	$\frac{Su_T}{Su_L} = 1 + \frac{u_{rms}}{Su_L}$	(Damkoehler, 1947)
(b)	$\frac{Su_T}{Su_L} = \sqrt{1 + \left(\frac{u_{rms}}{Su_L}\right)^2}$	(Shelkin, 1947)
(c)	$\frac{Su_T}{Su_L} = 1 + \sqrt{\frac{5}{12}}\frac{u_{rms}}{Su_L}$	(Taylor, 1922)
(d)	$\frac{Su_T}{Su_L} = 1 + \sqrt{2}\left(\frac{u_{rms}}{Su_L}\right)^{1/2}$	(Taylor, 1922)
(e)	$\frac{Su_T}{Su_L} = \sqrt{1 + \left(\frac{2\,u_{rms}}{Su_L}\right)^2}$	(Leason, 1951)
(f)	$\frac{Su_T}{Su_L} = 1 + \left(\frac{u_{rms}}{Su_L}\right)^2$	(Clavin and Williams, 1979)
(g)	$Su_T = 15.1\, {Su_L}^{0.784}\, {u_{rms}}^{0.412}\, {l_i}^{0.196}$	(Popat et al., 1996)

Concerning the models mentioned by Dahoe et al. (2013), it appears in Figure 6-21 that an average difference of 55% is observed between the model providing the best fitting, i.e. model (d) from Taylor (1922), and experimental data, meaning none of the models actually fits the experimental data. Since the same statement was underlined for premixed flames of methane-

air and hydrogen-air mixtures by Dahoe et al. (2013), it cannot be only related to the fact that correlations established for premixed flame were applied to a diffusional flame.

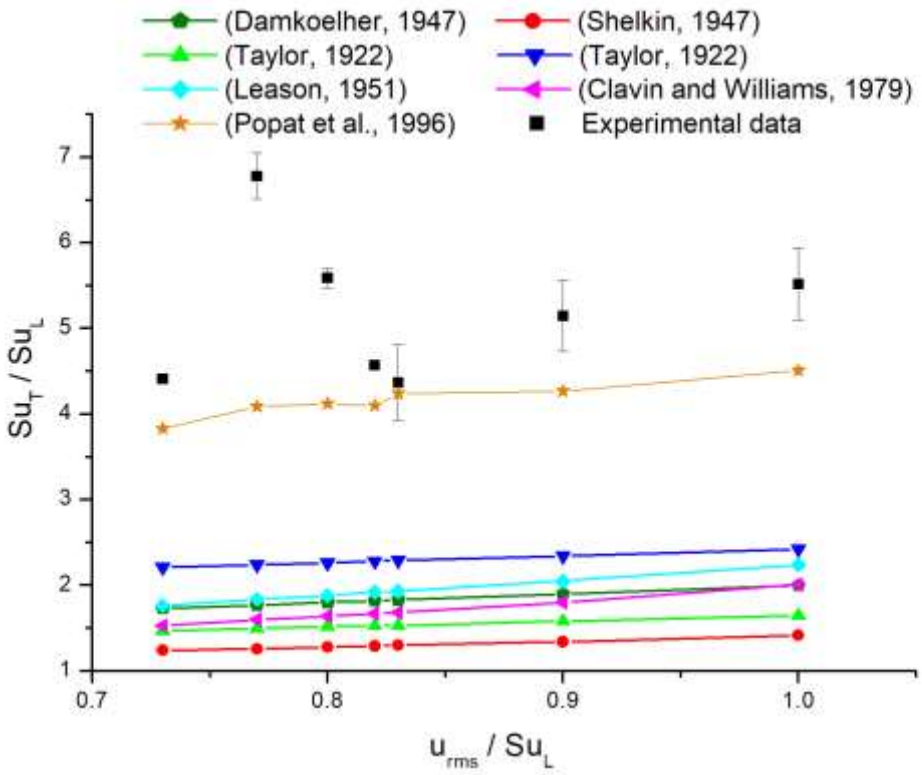

Figure 6-21 Comparison between models listed in Table 6-7 and experimental turbulent burning velocities measured in the flame propagation tube

Dahoe et al. (2013) then realized a dimensional analysis describing the flame propagation considering the laminar burning velocity, the laminar flame thickness, the root-mean square velocity, the turbulence macro length scale, the powder density, the dynamic viscosity, the diffusion coefficient, the thermal conductivity, the specific heat, the radiant flux at a reference temperature, the pressure, the reference temperature and the gravitational acceleration. They proposed a semi-empiric correlation of the following form:

$$\frac{Su_T}{Su_L} = 1 + a_1 {Da_{II}}^{a_2} \left(\frac{u_{rms}}{Su_L}\right)^{a_3} \qquad 6\text{-}19$$

a_1, a_2 and a_3 being three coefficients to determine experimentally and Da_{II}, the Damköhler number 2. They observed that two distinct sets of coefficients exist in their operating conditions, revealing that the establishment of a unique correlation allowing the calculation of the turbulent burning velocity from the knowledge of the laminar burning velocity and the turbulence intensity is not trivial, even for gases.

A dimensional analysis was proposed in chapter 3 concerning the dispersion phenomenon and in chapter 4 concerning the dust ignition. Since the dimensional analysis realized by Dahoe et al. (2013) describing the flame propagation already considers the main parameters affecting the

dust propagation, it will not be conducted in this work. However, as highlighted in chapter 4, the Damköhler number is affected by the size decrease from the micro-range to the nano-range, notably through the characteristic chemical time. Moreover, as a function of the concentration and interparticle distance, a group contribution can occur instead of an individual contribution of each particle. Thus, the coefficients a_1, a_2 and a_3 should be evaluated separately for microparticles and nanoparticles in order to consider such modifications.

The model established by Popat et al. (1996) and considered in the CFD code used by Skjold (2007) clearly provides the best fitting with the experimental data from this work, with an average difference of 20%. The difference can be due to experimental uncertainties, notably concerning the point at Su_T/Su_L = 6.8, but also to the different assumptions concerning the correlation, such as a constant kinematic viscosity and the integral length scale l_i equal to 1 cm (Skjold, 2003). A proper estimation of the turbulent velocity being essential to provide an accurate risk assessment concerning the consequences of an explosion, further investigations on such models are required.

Summary

To overcome the influence of the operating conditions on the explosion severity parameters, efforts focused on the determination of the laminar burning velocity, an intrinsic property of the fuel-air mixture. This chapter was divided into three parts, respectively dedicated to an experimental and numerical determination of the laminar burning velocity of nanocellulose, and to the application of turbulent flame velocity models.

In the first part, the laminar burning velocity of nanocellulose has been assessed by three different methods. The first two methods consists in the direct visualization of the flame propagation at low turbulence in a vertical 1 m long tube or in a vented 20L sphere coupled with the application of relationships relating the flame speed and its stretching, while the third relies on the use of correlations based on the pressure time evolution during a standard explosion test. All three methods lead to similar values of nanocellulose-air laminar burning velocity, i.e. approximately 21 $cm.s^{-1}$. It was notably underlined that using such flame propagation analyses at low turbulence can support the development of interesting semi-empiric correlations allowing the estimation of the laminar burning velocity from the knowledge of the pressure-time evolution in the standard 20L sphere.

The laminar burning velocity of nanocellulose was also determined using a one-dimensional flame propagation model already validated for hybrid mixtures. The numerical system, composed of mass and energy balances equations and of mass reaction rates adapted to the combustion reactions, was solved by the finite volume method, considering in a first approach a propagation by conduction and convection. Two cases were compared: the simultaneous pyrolysis of the dust and combustion of the pyrosis gases on the one hand, and only the combustion of the pyrolysis gases, considering a fast devolatilization of organic powders (notably highlighted in chapter 4) on the other hand. Both methods led to similar values, with a decrease of only 12% in the laminar flame velocity when considering the pyrolysis reaction, which validates the hypothesis of a fast pyrolysis step not limiting the combustion. Since, in practice, the devolatilization is not instantaneous, the particles that did not react yet can contribute to the radiative heat transfer, which was then added to the energy balance. The existence of a linear relation between the laminar flame velocity and the total surface area developed by the particles implied in the radiative heat transfer was highlighted, proving once again the importance of the reactive surface area. An increase up to 19% in the laminar burning velocity was observed when considering the contribution of the radiative heat transfer to the flame propagation. Indeed, although the heat transfer of nanoparticles tends to be neglected due to Rayleigh scattering, which does not contribute to the flame propagation, the contribution of the remaining micro-agglomerates (Mie scattering) after dispersion must be considered.

In the last part, the laminar burning velocity was converted in a turbulent burning velocity using existing models. However, the calculations did not show a good consistency with the values obtained experimentally, showing that the conversion from the laminar burning velocity to a turbulent burning velocity knowing the turbulent conditions is far from being trivial for dusts.

Résumé

Afin de maîtriser l'influence des conditions opératoires sur les paramètres de sévérité d'explosion, les efforts se sont focalisés sur la détermination de la vitesse laminaire de flamme, un paramètre intrinsèque au mélange poussière-air. Ce chapitre est divisé en trois parties, respectivement dédiées à la détermination expérimentale et numérique de la vitesse laminaire de flamme de la nanocellulose, et à l'application des modèles de vitesses de flamme turbulentes.

Dans la première partie, la vitesse laminaire de flamme de la nanocellulose a été estimée par trois différentes méthodes. Les deux premières consistent en une visualisation directe de la propagation de flamme à faible turbulence dans un tube vertical de 1 m de long et dans une sphère de 20L éventée, couplée à l'application de relations liant la vitesse de la flamme et son étirement, tandis que la troisième méthode repose sur l'utilisation d'une corrélation basée sur l'évolution de la pression en fonction du temps durant un essai standard d'explosion. Ces trois méthodes ont mené à des valeurs similaires de vitesses laminaires de flamme pour la nanocellulose, d'environ 21 $cm.s^{-1}$. Il a notamment été souligné que ces analyses de propagation de flamme à faible turbulence peuvent aider au développement de corrélations semi-empiriques permettant une estimation de la vitesse laminaire de flamme à partir de la connaissance de l'évolution de la pression avec le temps dans la sphère de 20L.

La vitesse laminaire de flamme de la nanocellulose a également été déterminée à l'aide d'un modèle numérique de propagation de flamme en une dimension, déjà validé pour des mélanges hybrides. Le système numérique, composé d'équations de bilans de masse et d'énergie et de vitesses de réactions massiques adaptées aux réactions de combustion, a été résolu par la méthode des volumes finis, en considérant dans un premier temps une propagation par convection et conduction. Deux approches ont été comparées : une réaction simultanée de pyrolyse de la poudre et de combustion des gaz de pyrolyses d'un côté, et la combustion des gaz de pyrolyse, considérant une dévolatilisation rapide des poudres organiques (notamment discuté dans le chapitre 4) de l'autre. Les deux méthodes ont conduit à des valeurs similaires, avec une diminution de 19% dans la valeur de vitesse laminaire de flamme en considérant la réaction de pyrolyse, ce qui valide l'hypothèse d'une pyrolyse rapide ne limitant pas la combustion. Puisqu'en pratique, la dévolatilisation n'est pas instantanée, les particules qui n'ont pas encore réagi peuvent contribuer au transfert radiatif, qui a donc été ajouté au bilan d'énergie. L'existence d'une relation linéaire entre la vitesse laminaire de flamme et la surface totale développée par les particules impliquées dans le transfert radiatif a été démontrée, prouvant une nouvelle fois l'importance de la surface reactive. Une augmentation de vitesse laminaire de flamme atteignant 19% a notamment été observée en considérant la contribution des particules au transfert de chaleur par rayonnement. En effet, bien que l'influence du transfert thermique radiatif des nanoparticules a tendance à être négligée à cause d'une diffusion de Rayleigh, la contribution des micro-agglomérats subsistant après la dispersion doit être prise en compte.

Dans la dernière partie, la vitesse laminaire de flamme a été reconvertie en une vitesse de flamme turbulente à l'aide de modèles existants. Cependant, les valeurs calculées n'ont pas démontré une bonne cohérence avec les valeurs mesurées expérimentalement, montrant que la conversion de la vitesse laminaire de flamme vers une vitesse spatiale ou turbulence à partir des conditions de turbulence est loin d'être trivial pour les poussières.

Chapter 7: Conclusion

Conclusion (English)

This research work focuses on the adequacy of the standard methods to measure the ignition sensitivity and explosion severity of a dust. The impact of the chemical nature, primary particle size, agglomeration state, moisture content, ignition energy, dispersion procedure and ignition delay time on the explosion severity was notably analyzed through the example of four types of powders: nanocellulose, aluminum, carbon-coated silicon and carbon black. The aim of this work was to bring new insights on the influence of nanoparticles specificities on their explosivity in order to propose potential improvements and suggest alternative methods taking their specificities into account.

In the following sections, the main results obtained in this study are summarized, improved standard protocols are suggested, and some perspectives are discussed. In addition, some industrial cases are analyzed with regard to these results in Appendix 3.

7.1. Main results

The dust explosion phenomenon can be decomposed into three different parts: the dust dispersion, the ignition, and the explosion itself. This part presents the main results concerning each of these phenomena, and a fourth part is dedicated to the results obtained on the flame propagation study.

7.1.1. Dust dispersion

Due to their small size and high specific surface area, nanoparticles are prone to a reversible agglomeration through weak bonding (van der Waals, electrostatic and capillary forces). This agglomeration was notably highlighted through Scanning Electron Microscopy (SEM) analysis and particle size distribution (PSD) measurements by wet dispersion and dry sedimentation. In situ PSD analysis conducted in the 20L sphere, i.e. the standard apparatus to measure the explosion severity of a dust, evidenced that the high shear stress induced by the dust injection procedure leads to a fragmentation of these agglomerates, thus modifying the PSD of the dust cloud. Such fragmentation depends on the cohesion strength of the agglomerates and is thus different for each powder. Moreover, a preliminary preparation of the samples, such as sieving or mechanical agglomeration, can impact the PSD before and after the dispersion, and thus the explosion severity.

Therefore, the explosion severity measured using the standardized procedure is not related to the PSD measured before dispersion, but to the PSD of the dust cloud. The latter contains micro-agglomerates still subsisting after dispersion as well as small agglomerates in the nano-range, which can greatly affect the reactivity of the dust cloud. In order to accurately analyze the obtained values, this fragmentation must be kept in mind, especially for the development of models on the dust dispersion and dust cloud behavior. It should also be noted that the dispersion procedures in the 20L sphere is different from that of the apparatuses for ignition

sensitivity measurements (modified Hartmann tube, Godbert-Greenwald oven), which implies a different fragmentation of the agglomerates.

7.1.2. Dust ignition

Standards tests were performed to measure the ignition sensitivity of the chosen powders. Except for the carbon black, the considered powders are particularly sensitive and can be ignited by electrical sparks of several millijoules. However, according to EN 14034 standards, the ignition energy to apply when evaluating the explosion severity of a dust in the 20L sphere is 10 kJ, which can lead to an overdriving phenomenon, i.e. a perturbation of the flame propagation due to the excessive amount of energy provided. This phenomenon, already identified for micropowders, can be enhanced when testing dusts with a very low minimum ignition energy (MIE), such as aluminum that can be ignited by an electrical spark of 1 mJ, or even nanocellulose with an MIE of 5 mJ. Thus, the ignition energy should be adapted for the evaluation of the explosion severity of nanopowders, or this phenomenon should at least be better considered by assessing the additional energy.

Moreover, when testing very sensitive powders, generally metal-based powders (e.g. aluminum), a pre-ignition can occur during the pressurization of the dust container before the activation of the igniters. To avoid such phenomenon that leads to a misestimation of the pressure-time evolution in the 20L sphere and damages the apparatus, the dust could be placed directly in the combustion chamber and lifted by the air injection. It should be noted that, for such ignition sensitive powders, the injection using an inert gas in an oxygen enriched vessel to avoid the ignition during the pressurization should be avoided, due to a possible spontaneous ignition of the dust when in contact with the oxygen enriched atmosphere.

The effects of the moisture content of the powder and atmosphere on the ignition sensitivity of the powders were also investigated. Minimum ignition energy measurements on the raw and dried nanocellulose notably showed that the drying step increases the ignition sensitivity of the powder. The MIE of carbon black is higher than 1 J (Turkevitch et al., 2015), and the low MIE of metal-based powders does not allow a clear observation of variations when drying the powder. Nevertheless, organic powders should be dried under vacuum before the tests, at the temperature that does not degrade the product, in order to obtain the most conservative results.

Finally, it was shown through the examples of nanocellulose and carbon-coated silicon that the agglomeration tends to decrease the ignition sensitivity of the powders, even increasing the MIE from 5 mJ for the raw powder to higher than 1 J for the agglomerated samples. A mechanical agglomeration of the powders, for powder transport, for instance, could then be considered as an application of inherent safety principles. However, it should be kept in mind that during an industrial accident, several phenomena can lead to a fragmentation of the agglomerates, which may then exhibit an ignition sensitivity similar to the raw powder, i.e. the powder which was not mechanically agglomerated.

7.1.3. Dust explosion

Explosion severity tests were also performed in the standard 20L sphere in standard conditions and highlighted that nanopowders exhibits rather similar maximum overpressures with regard to microparticles. Indeed, this parameter is mainly affected by the thermodynamics and thus by amount of powder that reacts. For the same mass concentration, two powders of the same nature but different particle sizes should then lead to similar maximum overpressures. The same effect was notably evidenced when agglomerating the powder through the examples of nanocellulose and carbon-coated silicon.

On the contrary, the maximum rate of pressure rise is a parameter mainly affected by the kinetics. This contrast between the two explosion severity parameters was notably evidenced by assessing the influence of the moisture on the explosion severity. While the moisture content of the carbon black and nanocellulose did not affect the maximum overpressure, significant variations appeared in the maximum rate of pressure rise. Indeed, in the presence of humidity, water can play the role of a heat sink (in the case of nanocellulose) or react either with the powder or the pyrolysis gases to form hydrogen, thus modifying the reaction kinetics (notably in the case of aluminum and carbon black).

In a general way, for the same powder nature, higher maximum rates of pressure rise were obtained with nanoparticles with regard to microparticles. This can be explained by a modification in the kinetic limitation when decreasing the particle size to the nano-range. This kinetic variation was also observed when performing mechanical agglomeration, notably on carbon-coated silicon. Thus, a characterization of the dust cloud after dispersion is necessary in order to know exactly what explodes and be able to model the reaction kinetics. Moreover, since the combustion of organic powders is limited by the diffusion of the oxygen toward the particle, the surface concentration should be considered instead of the mass concentration.

The influence of the initial turbulence on the explosion severity was also investigated through modifications in the ignition delay time. It appeared that increasing the turbulence increases the mass transfer through flame stretching, which favorizes the propagation of the flame. However, a too high turbulence may lead to micro-scale flame quenching whereas a too low turbulence can lead to the segregation of the agglomerates.

7.1.4. Flame propagation

To overcome the influence of the operating conditions on the explosion severity parameters, the laminar burning velocity, an intrinsic property of the fuel-air mixture, was both experimentally and numerically investigated on nanocellulose. The experimental estimation was performed by flame visualization in two apparatuses, a flame propagation tube and a new vented 20L sphere. Considering a fast devolatilization of organic dusts, the relations between the spatial velocity, flame surface and flame stretching developed for gases were applied to the nanocellulose. In addition, a semi-empiric correlation based on the standard parameters

measured in the 20L was used. All three methods led to similar values of laminar burning velocity of nanocellulose, around 21 $cm.s^{-1}$.

This value was confirmed by a one-dimensional flame propagation model considering a propagation in quiescent conditions. The numerical system, composed of mass and energy balances equations and of mass reaction rates adapted to the combustion reactions, was resolved by the finite volume methods. Two approaches were compared: the dust combustion, considering the pyrolysis of the dust and the combustion of the emitted gases, and the combustion of the pyrolysis gases only. Similar values were obtained, validating the hypothesis of a fast devolatilization of the powder. In a second time, the radiative heat transfer was added to the energy balance, increasing the laminar burning velocity up to 19% depending on the particle size and concentration. These two parameters were combined to calculate a total reactive surface area. A linear relation between the laminar burning velocity and the total reactive surface area of the particles contributing to the radiation heat transfer was then evidenced. Depending on this contribution, laminar burning velocities from 17.5 to 20.8 $cm.s^{-1}$ were obtained, showing a good consistency between the experimental and numerical methods.

7.2. Come up to standard !

All along this work, some issues concerning the standard procedure for testing the explosion severity of nanopowders were evidenced through the example of powders of different natures. To overcome such issues, some refined procedures related to different points discussed by the standards EN 14034 are proposed in this section: sample preparation, dust dispersion system, test procedure, ignition source and test report. In addition, further considerations are discussed, notably concerning the ignition sensitivity measurements and the flame propagation.

7.2.1. Sample preparation

Due to the agglomeration phenomenon inherent to nanoparticles, the particle size distribution (PSD) is greatly modified before and after dispersion. Thus, the explosion severity measured in the 20L sphere may not correspond to the powder PSD measured before dispersion. When possible, the PSD of the dust cloud should then be measured after dispersion in similar conditions to that of the 20L sphere (high shear stress).

Since such estimation is difficult in practice due to the opacity of the standard 20L sphere, a correlation between the powder properties and the mean diameter after dispersion could be used. For instance, the relation established by dimensional analysis of the dispersion phenomenon in chapter 3 could be reinforced by complementary dispersion tests on different powders. Moreover, the PSD measurements should systematically be conducted in dry conditions to limit the influence of the solvent on the agglomeration state and improve the accuracy of the measured values.

Concerning the effects of humidity, it should be reminded that the presence of water does not necessarily decrease the explosion severity, notably due to the possible generation of hydrogen (e.g. with aluminum, silicon carbide). At least one test should then be conducted at the optimal concentration, i.e. the concentration leading to the most severe explosion, by modifying (decreasing or, if impossible, increasing) the moisture content of the powder to consider this possibility.

7.2.2. Test procedure

The standard test procedure consists in vacuuming the combustion chamber to 0.4 bara, and placing the required amount of dust in the dust container, which is then pressurized to an overpressure of 20 bar. The electrovalve then opens, starting the dispersion and reaching atmospheric pressure in the 20L sphere. The standard ignition delay time between the beginning of the dispersion and the activation of the two igniters of 5 kJ is of 60 ms. After the explosion, the pressure-time evolution is recorded, and, after cleaning, the procedure is repeated at different concentrations.

However, it was evidenced in this work that the low minimum ignition energy (MIE) of nanoparticles can have a strong impact on the explosion severity measured depending on the ignition energy, due to an overdriving phenomenon. Thus, the ignition energy should be chosen as a function of the MIE instead of being fixed to the highest value allowing the explosion.

Moreover, the agglomeration state of the powder can greatly affect the dust cloud characteristics: for instance, the presence of big agglomerates after the dispersion can, in addition to combustion mechanisms modifications, influence the initial turbulence level if the agglomerates do not follow the flow. Since this phenomenon is represented by the dimensionless Stokes number (St), it could be used to determine the injection procedure to apply during the tests. Coupling the Stokes number to the dustiness index (DI), characterizing the ability of a powder to release fine particles, would then provide information on the dust cloud behavior: if the powder easily releases nanoparticles, these particles will be present in the dust cloud, thus increasing its reactivity. Indeed, a relatively low Stokes number and high dustiness index characterize a weak agglomerate cohesion.

A proposal of standard procedure modifications is then presented in Figure 7-1. The critical values of MIE were fixed to 1 J and 3 mJ. Indeed, a MIE higher than 1 J traduces that the powder is almost insensitive to electrostatic ignition, implying that a high ignition energy, of several kilojoules for instance, may be required to ignite the powder. In contrast, a MIE lower than 3 mJ implies that the sample is extremely sensitive to electrostatic ignition (Janes et al., 2008). In such cases, to avoid a pre-ignition during the pressurization, a dispersion by dust lifting, i.e. by placing the dust directly in the 20L sphere, is preferred.

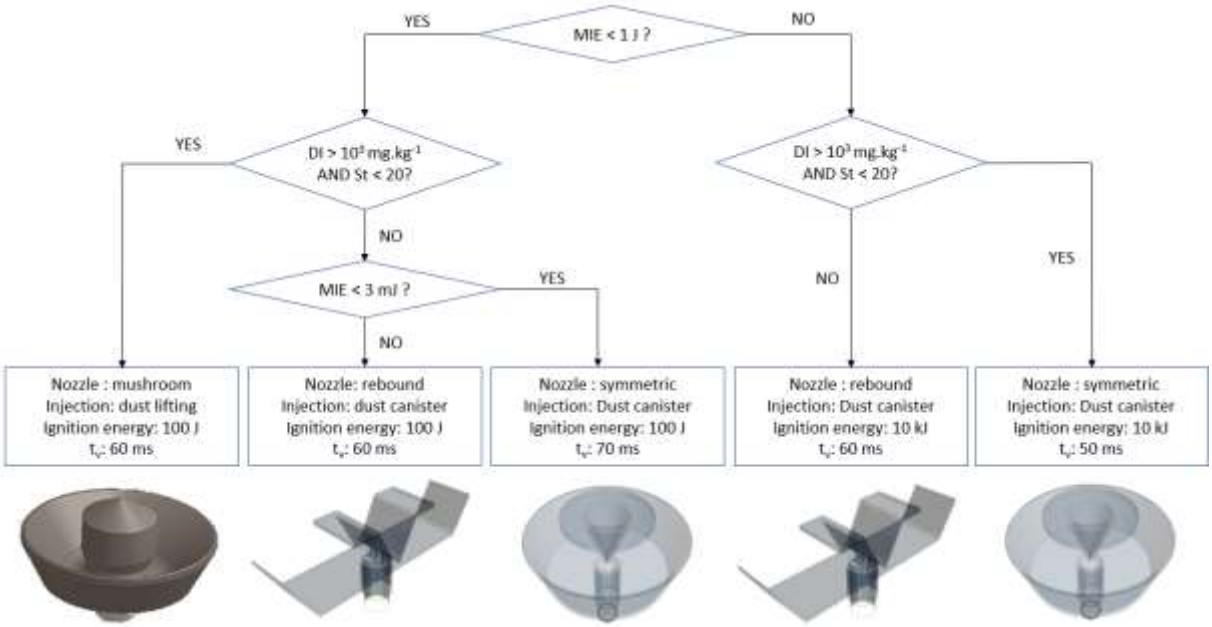

Figure 7-1 Proposal of standard procedures modifications for the determination of the explosion severity

Critical values of Stokes number and Dustiness Index were respectively set at 20 and 10^3 $mg.kg^{-1}$. Indeed, a St equal to 20 corresponds for instance to an agglomerate size of 70 µm for nanocellulose and 60 µm for carbon black. Such value then characterizes big agglomerates that does not follow the flow and must be broken in order to obtain the most conservative results: a standard injection, undergoing the pressurization and the high shear stress, is then preferred. On a similar way, a dustiness index lower than 1000 $mg.kg^{-1}$ implies that the powder does not easily release nanoparticles: a high shear stress is then once again required to decrease the agglomerates size and obtain the most conservative values. It should be noted that these values are proposed as indicators and can be debated. Experiments on different types of powders would then be necessary to validate or improve this method.

To provide the highest shear stress, a standard injection from the dust canister and through the rebound nozzle is considered. In case of dispersion by dust lifting, the mushroom nozzle (Krietsch et al., 2015) is preferred to the symmetric nozzle as its geometry can improve the dispersion efficacity, notably for low density powders.

Finally, the ignition delay time of 60 ms imposed by the current standards is maintained, except in two cases. First, when testing powders composed of big agglomerates (St > 20) or hardly releasing fine particles (DI < 10^3 $mg.kg^{-1}$) that are extremely sensitive to electrostatic ignition (MIE < 3 mJ), an injection from the dust container is preferred, but the ignition delay time is increased. Indeed, although such procedure would not prevent a pre-ignition during the pressurization, extremely sensitive powders can exhibit, especially for metal powders, a high explosion severity, which could lead to a propagation of the flame back to the dust canister. Increasing the ignition delay time then gives time to the electrovalve to close before the ignition, preventing the occurrence of this phenomenon. Secondly, using the symmetric nozzle to

improve the dust cloud homogeneity, the turbulence level is lower than with the rebound nozzle. The ignition delay time is then reduced to approach the turbulence level obtained with the rebound nozzle.

7.2.3. Test report

Complementary to the information already included in the test report according to EN 14034 standards, some elements should be added. Indeed, the report recipient should be alerted of the influence of the turbulence conditions and dust concentration on the explosion severity. Thus, instead of only providing the values of P_{max} and K_{St}, accent should be made on the evolution of P_m and $(dP/dt)_m$ with the dust concentration, highlighting the fact that the maximum values are not absolute values necessary attained during a dust explosion.

Moreover, as specified in the standard, two additional tests must be conducted at the concentrations around the optimal concentration. Instead of performing these tests at the same ignition delay time, it could be modified (e.g. ± 20 ms) in order to highlight the impact of the operating conditions on the explosion severity parameters.

7.2.4. Flame propagation

As discussed in chapter 6, the laminar burning velocity of the dust could be considered as a standard parameter describing the explosion severity of nanopowders, as it does not depend on the operating conditions. However, its experimental determination is not trivial, and the definition of a determination protocol is required. Measurements at low turbulence, allowed by the low sedimentation rate, tube could be conducted in a flame propagation and the flame propagation could be recorded using a high-speed video camera. To simplify the video analysis, the evolution of the flame front position could be considered instead of the flame surface to calculate the spatial velocity. A standard software should then be developed in order to estimate the laminar burning velocity from such experiments. Another solution relies on the use of a correlation relating the explosion severity parameters (P_{max}, dP/dt_{max}) to the laminar burning velocity, such as that developed by Silvestrini et al. (2008). However, this relation does not seem applicable for high concentrations. Experiments in a flame propagation tube could then be realized at different concentrations in order to reinforce the correlation.

7.2.5. Further considerations

The cube-root law, used to extrapolate the results from laboratory to industrial conditions, relies on different hypotheses. Among them, the flame thickness must be negligible with regard to the vessel radius but can be increased by the radiative heat transfer. Theoretically, the contribution of the radiative heat transfer for nanoparticles to the flame propagation is negligible due to a Rayleigh scattering. However, due to the agglomeration inherent to nanoparticles, agglomerates of a few micrometers are still present after dispersion, and can contribute to the flame propagation through Mie scattering. Such contribution would then

increase the flame thickness, and then invalidate the cube-root law. The influence of the radiative heat transfer on the flame propagation should then be further investigated, as discussed in section 7.4.

Finally, it should be noted that the ignition sensitivity measurements are conducted in different apparatuses than the explosion severity, implying a different dispersion procedure and thus, a different fragmentation efficiency. To obtain the most conservative values, a higher shear stress, improving the agglomerates breakage, should be considered. This point is further discussed in section 7.4. Concerning the determination of the LEL, the ignition energy to apply during the tests should be adapted on a similar way than for explosion severity experiments, i.e. depending on the MIE.

7.3. Perspectives for further works

The results of this work evidenced variations in the ignition sensitivity and explosion severity of powders when decreasing the particle size from the microscale to the nanoscale and led to some proposal concerning the standard procedure to follow when evaluating these parameters for nanopowders. However, further research is still necessary to define a standard procedure leading to reliable values in accordance with nanoparticles specificities.

Due to the influence of the powder characteristics on the properties of the dust cloud, notably highlighted in chapter 3, developing a single standard procedure to apply to every powder would not allow an accurate representation of their specificities. The determination of the 'optimal' dispersion conditions could be realized by the use of a Computational Fluid Dynamics (CFD), preferably at low concentration to reduce the calculation time. In a similar way than the laminar burning velocity, each powder would then exhibit its own optimal dispersion conditions as an intrinsic property, that could lead either to the values the most representative of an industrial accident or to the most conservative could be estimated.

The influence of the agglomeration on the ignition sensitivity and explosion severity was investigated on nanocellulose through powder sieving and mechanical agglomeration. However, the agglomerates generated by these methods were not strong enough to resist to the shear stress induced by the injection procedure in the 20L sphere, thus preventing from accurately evaluating the influence of the agglomeration level in the dust cloud on its explosion severity. Since the experiments conducted on the agglomerated carbon-coated silicon led to encouraging results on this subject, a similar agglomeration process than that used for such agglomeration could be applied to nanopowders of different nature to evaluate the effects of the agglomeration on each type of combustible powder.

Such experiments could be conducted in standard conditions, but also by modifying the injection procedure and the nozzle to represent different accidental conditions. More specifically, the slotted and perforated cylindrical nozzles, designed at the end of the experimental work, could be used to model a crack in a pipeline. An evaluation of the evolution of the turbulence with time within the 20L sphere would then be required to characterize the

related dust cloud, for instance through Particle Image Velocimetry (PIV) measurements. Moreover, since each nozzle induce a different fragmentation of the agglomerates, experiments could be performed at different ignition delay times to obtain the same initial turbulence in the 20L sphere. The influence of the turbulence being removed, the influence of the particle size distribution on the explosion severity could be isolated. Such consideration was unfortunately impossible by comparing the symmetric nozzle to the rebound nozzle due to a too similar fragmentation of the agglomerates.

The shear stress related to the dust dispersion in the 20L sphere was much discussed in this work, and it was attributed to the pressurization of the dust canister followed by the passage in the duct and electrovalve. However, such procedure is not applied to the modified Hartmann tube for the measurement of the minimum ignition energy. In addition to performing tests on a mechanically agglomerated powder as previously described to evaluate the influence of the agglomeration on the MIE, modifications could be realized in the dispersion procedure in the modified Hartmann tube. Thus, a dust container equipped with an electrovalve could be implemented to this apparatus to reproduce the turbulence and shear stress induced by the dispersion procedure in the 20L sphere. Nevertheless, it should be noticed that, since a pressurization of the container at 20 barg would probably damage the tube, this pressure should be adapted to the geometry of the apparatus. In addition, the ‘mushroom’ nozzle could be substituted by another nozzle, which could be a rebound nozzle to induce the same dispersion than in the 20L sphere.

The same procedure could also be applied to the flame propagation tube. Moreover, flame propagation experiments conducted on agglomerated powders could highlight the influence of the agglomeration on the laminar burning velocity. In addition, such tests could be conducted on powders of different nature, to investigate on the applicability of the models established for gases to powders. If not, new relations for the evaluation of the laminar burning velocity of dusts could be determined, notably relying on numerical models and requiring an estimation of the combustion reactions. Although the contribution of the radiative heat transfer was evidenced, an experimental determination would be interesting. Such estimation would notably be possible using an infrared camera coupled to a sapphire window.

Let us be clear: standards are essential. But when they face a grain of sand, they sometimes take a long time to adapt to a changing context. By being inherently more adaptive to different materials and industrial contexts, they would gain in reactivity. It’s time to gear up!

Conclusion (French)

Ce travail de thèse s'est focalisé sur l'évaluation des risques liés aux explosions de nanoparticules, et plus spécifiquement sur l'adéquation des méthodes standards pour la mesure de la sensibilité à l'inflammation et la sévérité d'explosion. L'impact de la nature chimique, du diamètre primaire de particule, de l'état d'agglomération, de la teneur en eau, de l'énergie d'inflammation, de la procédure de dispersion et du délai d'inflammation sur la sévérité d'explosion a notamment été analysé à travers l'exemple de quatre types de poudres : nanocellulose, aluminium, silicium enrobé de carbone et noir de carbone. L'objectif de ce travail était d'apporter de nouvelles connaissances concernant l'influence des spécificités des nanoparticules sur leur explosivité de manière à proposer des améliorations et méthodes alternatives adaptées à ces spécificités.

Dans les sections suivantes, les résultats principaux obtenus dans cette étude sont résumés, et quelques perspectives sont discutées.

Principaux résultats

Une explosion de poussière peut être décomposée en trois phénomènes différents : la dispersion de la poudre, l'inflammation, et l'explosion elle-même. Cette partie présente les principaux résultats concernant chacun de ces phénomènes, et une quatrième section est dédiée aux résultats obtenus lors de l'étude de propagation de flamme.

Dispersion de la poudre

Du fait de leur petite taille et grande surface spécifique, les nanoparticules ont tendance à s'agglomérer de manière réversible, par des liaisons faibles (forces de van der Waals, électrostatiques et capillaires). Cette agglomération a notamment été mise en évidence par des analyses par microscopie électronique à balayage (MEB) et mesures de distribution de tailles de particules (DTP) en voie liquide et par sédimentation en voie sèche. Des mesures in situ conduites dans la sphère de 20L, i.e. l'appareil standard de mesure de la sévérité d'explosion d'une poussière, ont démontré que le fort cisaillement induit par la procédure d'injection de la poudre conduit à la fragmentation partielle de ces agglomérats, modifiant ainsi la DTP du nuage. Cette fragmentation dépend de la contrainte de cohésion des agglomérats et est ainsi différente pour chaque poudre. De plus, une analyse préliminaire des échantillons, tels que du tamisage ou une agglomération mécanique, peut impacter la DTP avant et après dispersion, et par là même la sévérité d'explosion.

Il en résulte que la sévérité d'explosion mesurée en utilisant la procédure standard n'est pas liée à la DTP mesurée avant dispersion, mais à celle du nuage. Ce dernier contient des agglomérats micrométriques subsistant après la dispersion ainsi que des petits agglomérats nanométriques, ce qui peut fortement affecter la réactivité du nuage. Afin d'analyser de manière précise les valeurs obtenues, cette fragmentation devrait être gardée en mémoire, notamment lors du

développement de modèles concernant le phénomène de dispersion de poudre et les caractéristiques du nuage généré. Il est également à noter que la procédure de dispersion dans la sphère de 20L est différente de celle des appareils de mesure de sensibilité à l'inflammation (tube de Hartmann modifié, four de Godbert-Greenwald), ce qui implique une différente fragmentation des agglomérats.

Inflammation du nuage

Des essais standards ont été réalisés pour mesurer la sensibilité à l'inflammation des poudres considérées. A l'exception du noir de carbone, les poudres considérées sont particulièrement sensibles et peuvent être enflammées par des étincelles de quelques millijoules. Cependant, selon les standards EN 14034, l'énergie d'inflammation à appliquer lors de l'évaluation de la sévérité d'explosion d'une poudre dans la sphère de 20L est de 10 kJ, ce qui peut conduire à un phénomène dit « d'overdriving », i.e. une perturbation de la propagation de flamme à cause de la quantité excessive d'énergie fournie au nuage. Ce phénomène, déjà identifié pour les poudres micrométriques, peut être renforcé en testant des poudres présentant une énergie minimale d'inflammation (EMI) faible, telles que l'aluminium qui peut être enflammé par une étincelle de 1 mJ, ou même la nanocellulose qui présente une MIE de 5 mJ. Ainsi, l'énergie d'inflammation devrait être adaptée à l'évaluation de la sévérité d'explosion des nanopoudres, ou ce phénomène devrait au moins être mieux considéré en estimant l'énergie supplémentaire apportée.

De plus, en testant des poudres très sensibles, généralement des poudres à base métallique (e.g. aluminium), une pré-inflammation peut se produire durant la pressurisation du réservoir à poussière avant l'activation des inflammateurs. Afin d'éviter ce phénomène qui conduit à une mauvaise estimation de l'évolution de la pression avec le temps dans la sphère de 20L et peut endommager l'appareil, la poudre peut être placée directement dans la chambre de combustion et soulevée par l'injection d'air. Il est à noter que, pour ces poudres sensibles, l'injection par un gaz inerte dans une enceinte enrichie en oxygène afin d'éviter la pré-inflammation pendant la pressurisation est à proscrire, à cause d'une possible inflammation spontanée de la poudre lors du contact avec l'atmosphère enrichie en oxygène.

Les effets de la teneur en eau de la poudre et de l'atmosphère sur la sensibilité à l'inflammation des poudres ont aussi été investigués. Des mesures d'EMI sur la nanocellulose non modifiée et séchée ont notamment montré que le séchage accroit la sensibilité à l'inflammation de la poudre. En revanche, l'EMI du noir de carbone est supérieure à 1 J (Vignes, 2008) et la faible EMI des poudres à base métallique ne permet pas d'observer une variation claire en séchant la poudre. Cependant, les poudres organiques devraient être séchées avant les essais afin d'obtenir les valeurs les plus conservatives.

Enfin, il a été montré à travers des exemples de la nanocellulose et du silicium enrobé de carbone que l'agglomération tend à décroître la sensibilité à l'inflammation des poudres, augmentant même l'EMI de 5 mJ pour la poudre libre de silicium enrobé de carbone jusqu'à

plus d'un joule pour les échantillons agglomérés. L'agglomération mécanique des poudres, par exemple pour faciliter leur transport, peut ainsi être considérée comme une application des principes de sécurité intrinsèque. Cependant, il doit être gardé en mémoire que durant un accident industriel, différents phénomènes sont susceptibles de conduire à la fragmentation des agglomérats, qui présenteraient alors une sensibilité à l'inflammation similaire à la poudre libre, i.e. la poudre non agglomérée.

Explosion

Des essais de sévérité d'explosion ont aussi été réalisés dans la sphère de 20L dans les conditions définies par les standards internationaux EN 14034, et ont démontré que les nanopoudres présentent des surpressions maximales d'explosion similaires à celles des microparticles. En effet, ce paramètre est essentiellement affecté par la thermodynamique mise en jeu, et ainsi par la quantité de poudre qui réagit. Pour une même concentration massique, deux poudres de la même nature, mais présentant des tailles de particules différentes, devraient ainsi logiquement conduire à des surpressions maximales similaires. Le même effet a notamment été mis en lumière lors de l'agglomération de la poudre à travers les exemples de la nanocellulose et du silicium enrobé de carbone.

Au contraire, la vitesse maximale de montée en pression est un paramètre principalement affecté par la cinétique. Ce contraste entre les deux paramètres de sévérité d'explosion a notamment été mis en avant lors de l'étude de l'influence de la teneur en eau sur la sévérité d'explosion. Tandis que la teneur en eau du noir de carbone et de la nanocellulose n'a pas eu d'effet sur la surpression d'explosion, des variations significatives sont apparues dans les valeurs de vitesses de montée en pression. En effet, en présence d'eau, une partie de l'énergie peut être utilisée pour la vaporisation de l'eau (dans le cas de la nanocellulose) ou l'eau peut réagir pour former de l'hydrogène, modifiant ainsi la cinétique de réaction (notamment dans le cas de l'aluminium et du noir de carbone).

De manière générale, pour une même nature de poudre, des vitesses maximales de montée en pression plus élevées ont été obtenues pour des nanoparticules en comparaison avec les microparticules. Cela peut s'expliquer par une modification de limitation cinétique en diminuant la taille de particules jusqu'à l'échelle nanométrique. Cette variation cinétique a également été observée en réalisant une agglomération mécanique, notamment sur le silicium enrobé de carbone. Ainsi, une caractérisation du nuage après dispersion est nécessaire afin de savoir exactement ce qui explose et être à même de modéliser la cinétique de réaction. De plus, puisque la combustion des poudres organiques est limitée par la diffusion de l'oxygène vers la particule, la concentration surfacique devrait être considérée pour l'analyse à la place de la concentration massique.

L'influence de la turbulence initiale sur la sévérité d'explosion a également été investiguée à travers des modifications de délai d'inflammation. Il est apparu qu'augmenter la turbulence augmente le transfert de matière grâce à l'étirement de la flamme, ce qui favorise la propagation

de la flamme. Cependant, un niveau de turbulence trop élevé peut mener à une extinction de flamme tandis qu'un niveau de turbulence trop faible peut conduire à la sédimentation des agglomérats.

Propagation de flamme

Afin de s'affranchir de l'influence des conditions opératoires sur les paramètres de sévérité d'explosion, la vitesse laminaire de flamme, une propriété intrinsèque au mélange poussière-air, a été évalué à la fois de manière expérimentale et numérique pour la nanocellulose. La détermination expérimentale a été réalisée par visualisation de la propagation de la flamme dans deux appareils, un tube de propagation de flamme et une sphère éventée. En considérant une dévolatilisation rapide des poudres organiques, les relations entre la vitesse spatiale, la surface de flamme et l'étirement de la flamme développées pour les gaz ont été appliquées pour la nanocellulose. En complément, une corrélation semi-empirique basée sur les paramètres standards mesurés dans la sphère de 20L a été appliquée. Ces trois méthodes ont conduit à des valeurs similaires de vitesses laminaires de flamme pour la nanocellulose, aux environs de 21 $cm.s^{-1}$.

Cette valeur a été confirmée par un modèle de propagation de flamme en une dimension considérant un milieu non turbulent. Le système numérique, composé de bilans de masse et d'énergie et de vitesses de réactions adaptées aux réactions de combustion, a été résolu par la méthode des volumes finis. Deux approches ont été comparées : la combustion de la poudre d'une part, considérant à la fois la pyrolyse de la poudre et la combustion des gaz de pyrolyse, et la combustion directe des gaz de pyrolyse d'autre part. Des valeurs similaires ont été calculées, validant ainsi l'hypothèse d'une dévolatilisation rapide de la poudre. Dans un second temps, the transfert radiative a été ajouté au bilan d'énergie, augmentant alors la vitesse laminaire de flamme de la nanocellulose jusqu'à 19% en fonction de la concentration et de la taille des particules contribuant au rayonnement. Ces deux paramètres ont été combinés pour calculer une surface spécifique volumique, et l'existence d'une relation linéaire liant la vitesse laminaire de flamme à la surface spécifique volumique des particules contribuant au transfert radiatif a été soulignée. Selon cette contribution, des vitesses luminaires de flame de 17.5 à 20.8 $cm.s^{-1}$ ont été obtenues, démontrant ainsi une bonne cohérence entre les méthodes expérimentales et numériques.

Perspectives

Les résultats de ce travail ont montré des variations dans la sensibilité d'inflammation et la sévérité d'explosion des poudres lors de la diminution de la taille des particules de l'échelle micrométrique vers l'échelle nanométrique et ont mené à des propositions concernant les procédures standard à suivre lors de l'évaluation de ces paramètres pour des nanopoudres. Cependant, des recherches plus poussées sont toujours nécessaires afin de définir une procédure standard menant à des résultats fiables en accord avec les spécificités des nanoparticules.

Du fait de l'influence des caractéristiques des poudres sur les propriétés du nuage, notamment démontrée dans le chapitre 3, développer une unique procédure standard à appliquer à chaque poudre ne permettrait pas une représentation fidèle de leurs spécificités. La détermination de conditions « optimales » de dispersion pourrait être réalisée à l'aide de codes CFD, préférentiellement à faible concentration pour réduire le temps de calcul. D'une manière similaire à la vitesse laminaire de flamme, chaque poudre pourrait alors être associée à ses propres conditions optimales de dispersion, telle une propriété intrinsèque, qui pourraient mener soit aux valeurs les plus représentatives d'un accident industriel ou aux valeurs les plus conservatives.

L'influence de l'agglomération sur la sensibilité à l'inflammation et la sévérité d'explosion a été investiguée à travers la nanocellulose en tamisant la poudre et par agglomération mécanique. Cependant, les agglomérats générés par ces méthodes n'étaient pas assez solides pour résister au cisaillement induit par la procédure d'injection dans la sphère de 20L, empêchant ainsi d'évaluer précisément l'influence de l'état d'agglomération du nuage sur sa sévérité d'explosion. En revanche, puisque les essais conduits sur les agglomérats de silicium enrobé de carbone ont mené à des résultats encourageants, un procédé d'agglomération similaire à celui utilisé dans ce cas pourrait être appliqué à des nanopoudres de différentes natures afin d'évaluer les effets de l'agglomération sur chaque type de poudre combustible.

Ces essais pourraient être réalisés dans des conditions standard, mais aussi en modifiant la procédure d'injection et le disperseur afin de représenter différentes conditions industrielles. Plus précisément, les disperseurs fendus et perforés, fabriqués à la fin de la partie expérimentale de ce travail, pourraient être utilisés pour modéliser la rupture d'une canalisation. Une évaluation de l'évolution de la turbulence en fonction du temps dans la sphère de 20L serait alors requise pour caractériser le nuage généré, par exemple par des mesures par PIV. De plus, puisque chaque disperseur induit une fragmentation des agglomérats différente, des essais pourraient être réalisés pour différents délais d'inflammation afin d'obtenir la même turbulence initiale dans la sphère de 20L. L'influence de la turbulence étant supprimée, l'influence de la DTP sur la sévérité d'explosion pourrait être isolée. Une telle considération était malheureusement impossible en comparant le disperseur symétrique au disperseur standard à cause d'une fragmentation des agglomérats similaire.

Le cisaillement induit par la dispersion de la poudre dans la sphère de 20L a été beaucoup mentionné dans ce travail, et a été attribué à la pressurisation du réservoir à poudre suivi du passage par la conduite et l'électrovalve. Cependant, cette procédure n'est pas appliquée au tube de Hartmann modifié pour la mesure de l'énergie minimale d'inflammation. En complément de mesures d'EMI sur des poudres mécaniquement agglomérées selon le principe précédemment décrit afin d'évaluer l'influence de l'agglomération sur l'EMI, des modifications dans la procédure d'injection pourraient être réalisées sur le tube de Hartmann modifié. Ainsi, un réservoir à poudre équipé d'une électrovanne pourrait être implémenté à cet appareil afin de reproduire la turbulence et le cisaillement induits par la procédure de dispersion dans la sphère de 20L. Néanmoins, il est à noter que, puisque la pressurisation du réservoir à 20 bar

endommagerait probablement le tube, cette pression devrait être adaptée à la géométrie de l'appareil. De plus, le disperseur « champignon » pourrait être substitué par un autre disperseur, e.g. le disperseur standard de la sphère de 20L redimensionné afin d'introduire la même dispersion que dans la sphère de 20L.

La même procédure pourrait également être appliquée au tube de propagation de flamme. De plus, des essais expérimentaux de propagation de flame conduits sur des poudres agglomérées pourraient mettre en lumière l'influence de l'agglomération sur la vitesse laminaire de flamme. En complément, de tels tests pourraient être réalisés sur des poudres de différentes natures, afin d'investiguer sur l'applicabilité des modèles établis pour les gaz aux poudres. Si cela est impossible, de nouvelles relations pour l'évaluation de la vitesse laminaire de flamme des poussières pourraient être déterminées, notamment à l'aide de modèles numériques requérant une estimation des réactions de combustion. Bien que la contribution du transfert radiatif à la propagation de flamme a été numériquement estimée, une détermination expérimentale serait intéressante. Une telle évaluation serait notamment possible à l'aide d'une caméra infra-rouge couplée à une vitre en saphir, laissant traverser le rayonnement IR.

Une chose est sûre : les standards sont essentiels. Mais quand ils sont face à un grain de sable, ils prennent parfois un long moment à s'adapter à un contexte changeant. En étant, de manière inhérente, plus adaptables à différents matériaux et contextes industriels, ils gagneraient en réactivité. Il est temps de s'adapter !

Appendix 1: SEM images

Nanocellulose

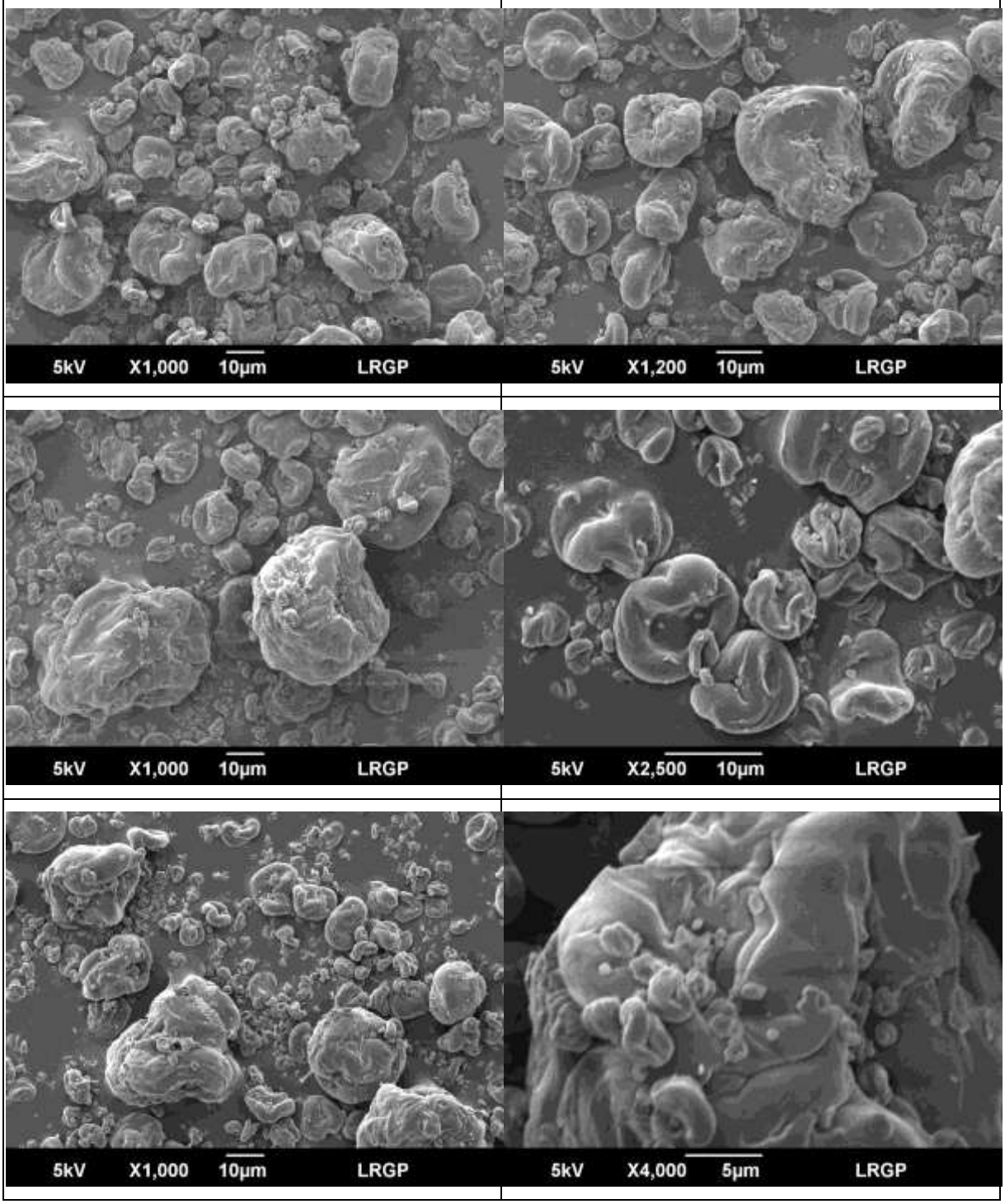

Carbon black

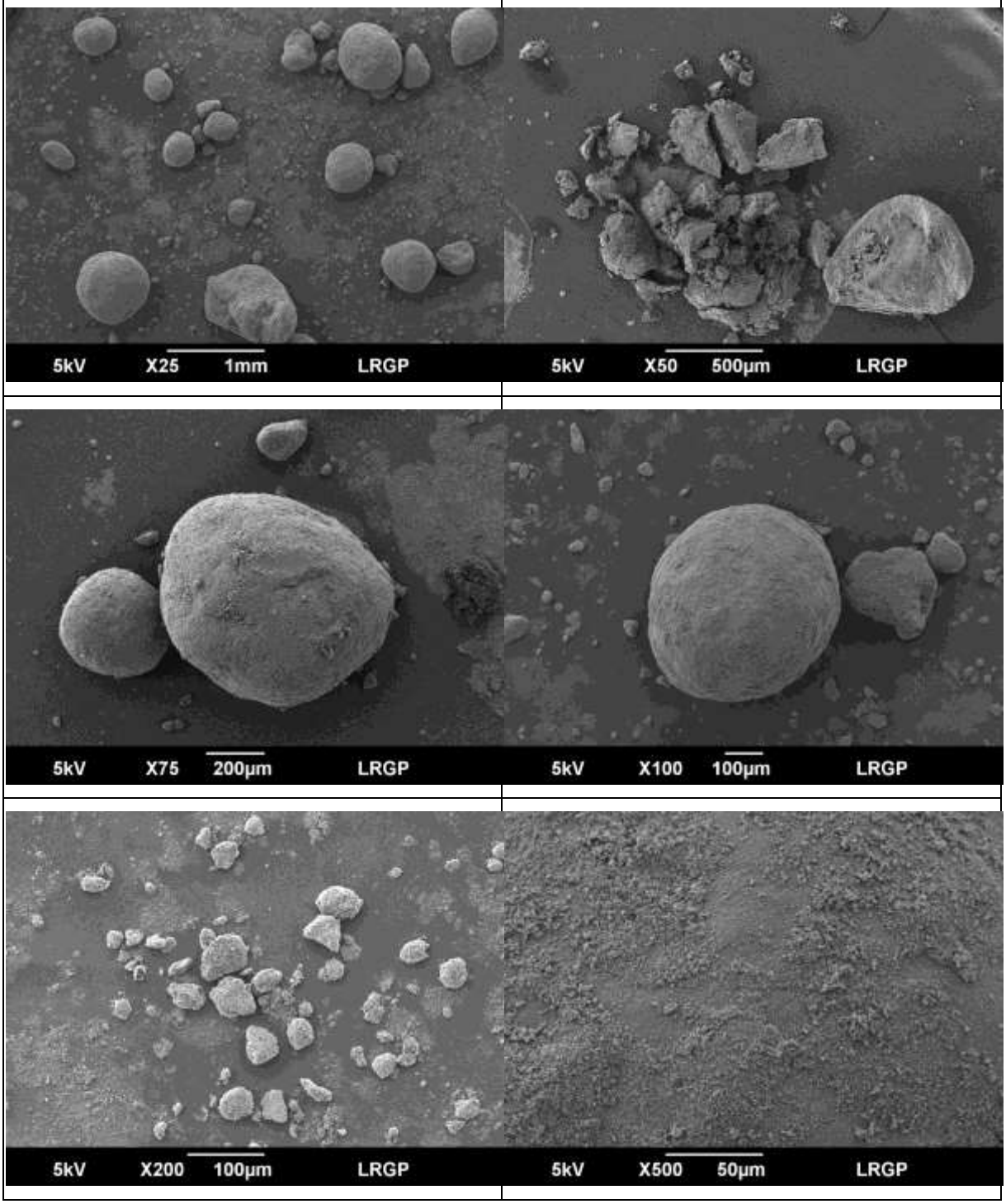

Carbon black

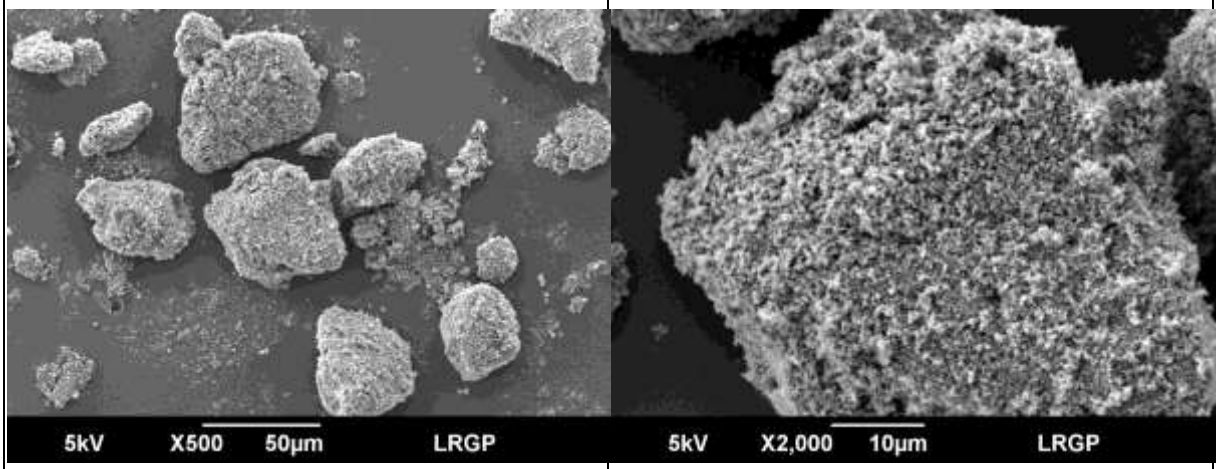

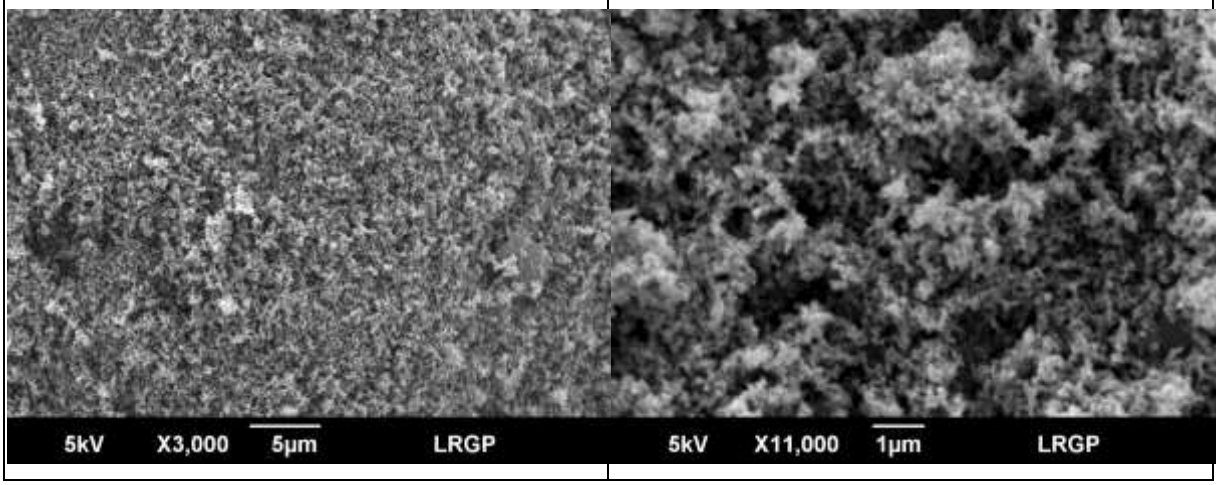

Dried carbon black (90°C under vacuum – Aw = 0.03)

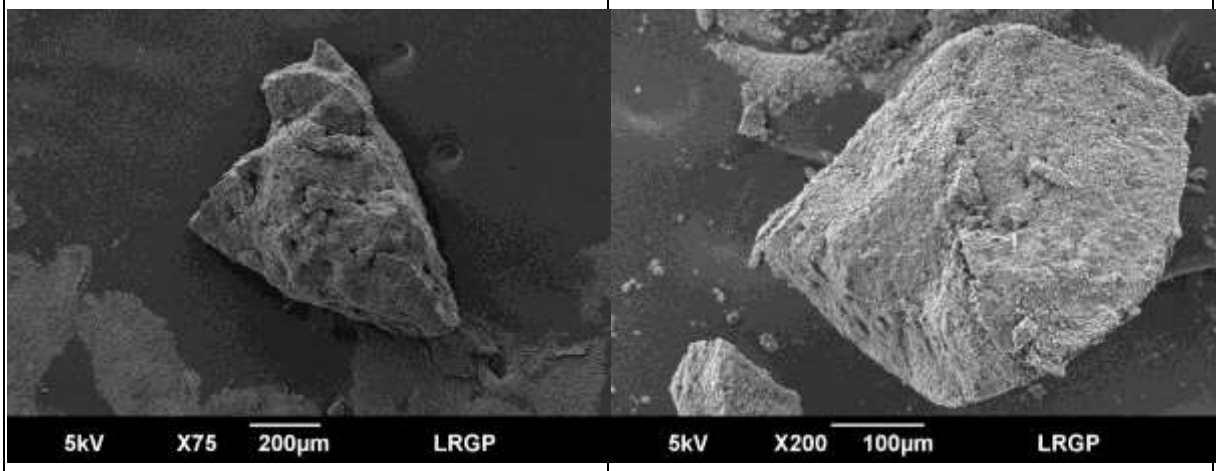

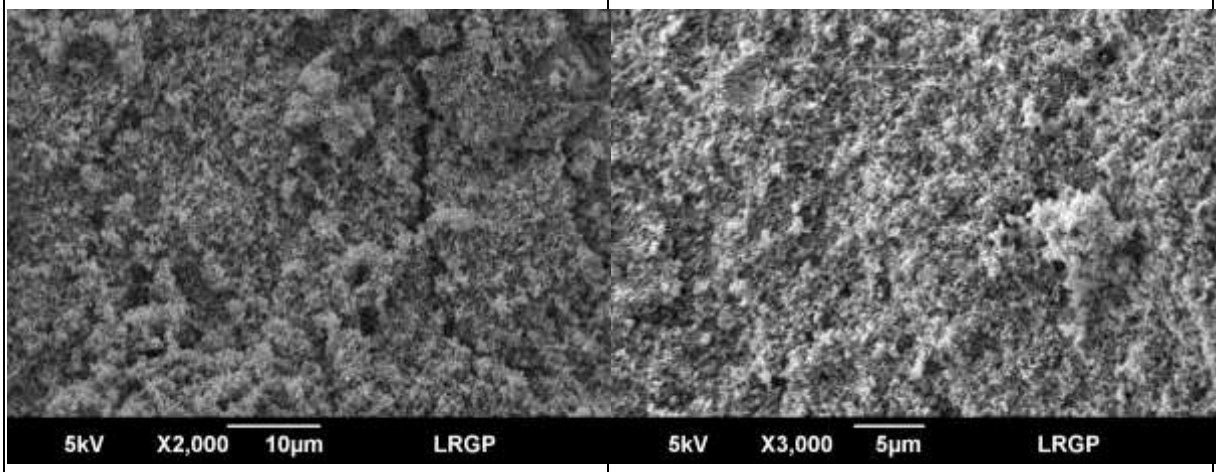

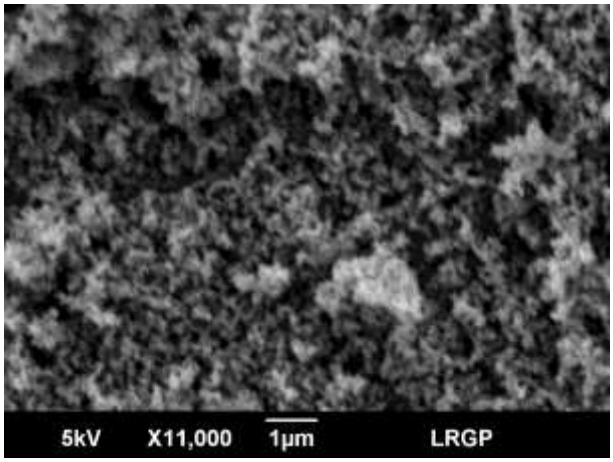

Aluminum 100 nm

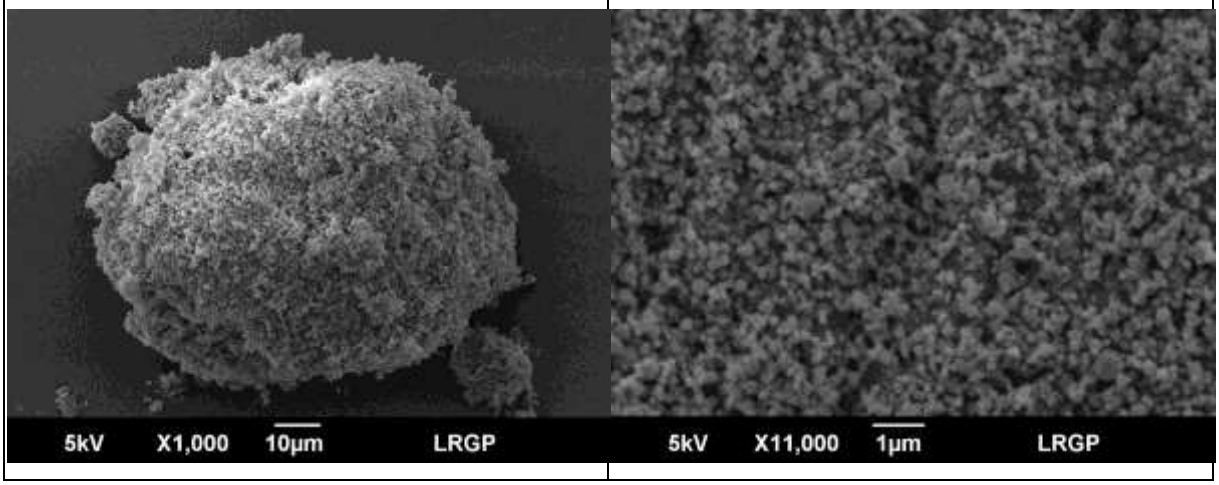

Aluminum 100 nm after explosion

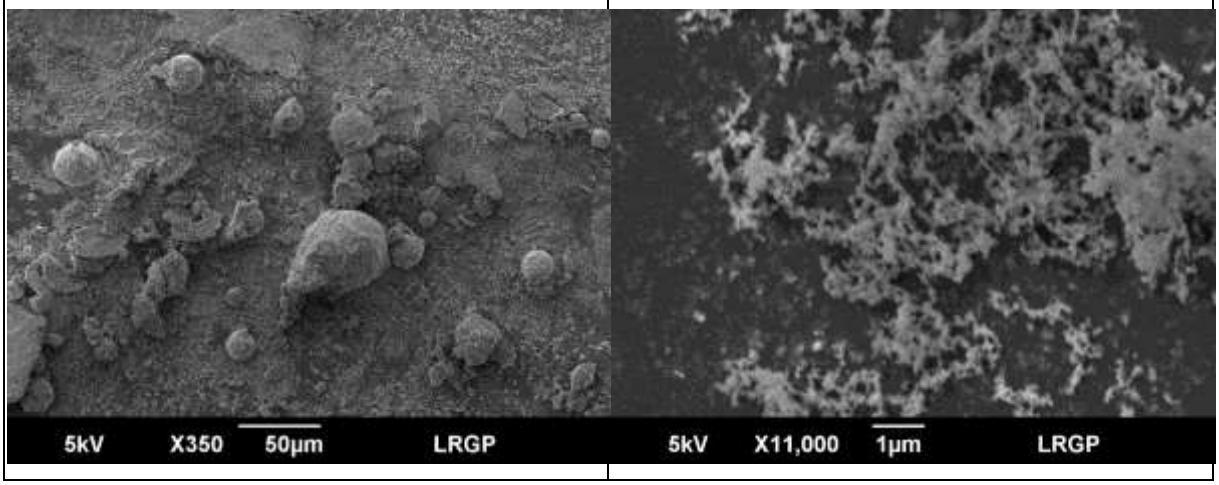

Aluminum 40-60 nm

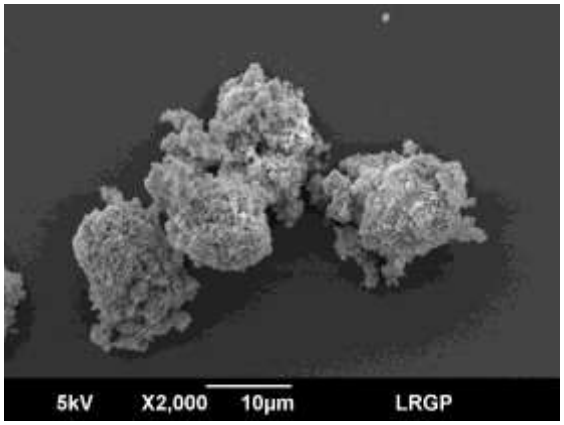

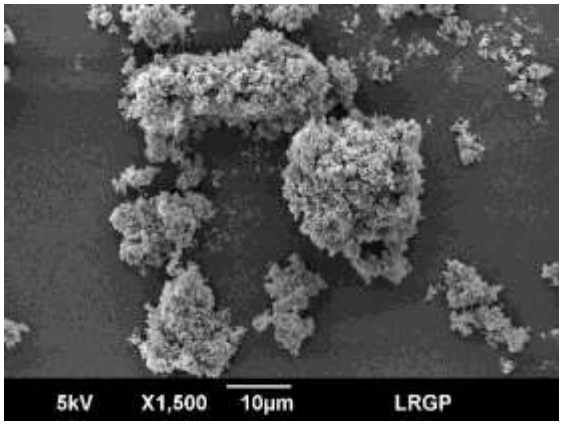

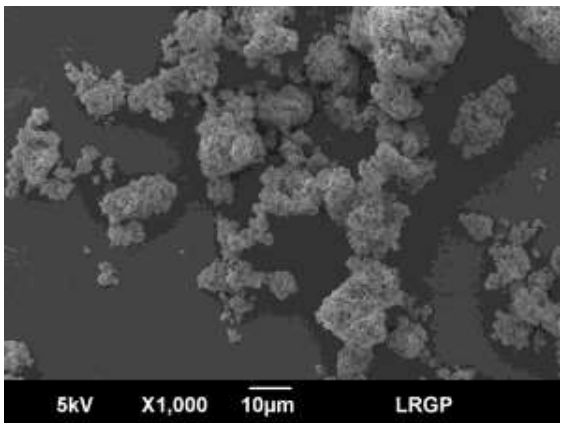

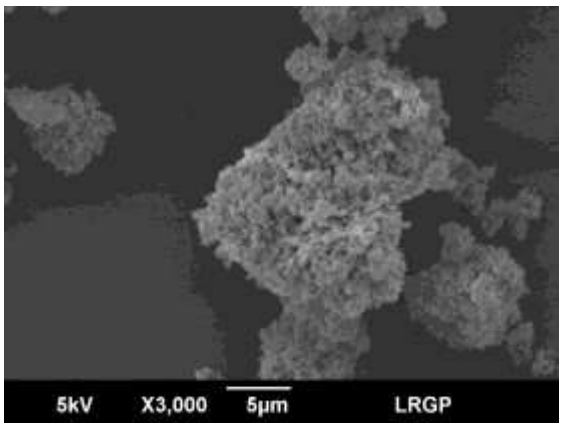

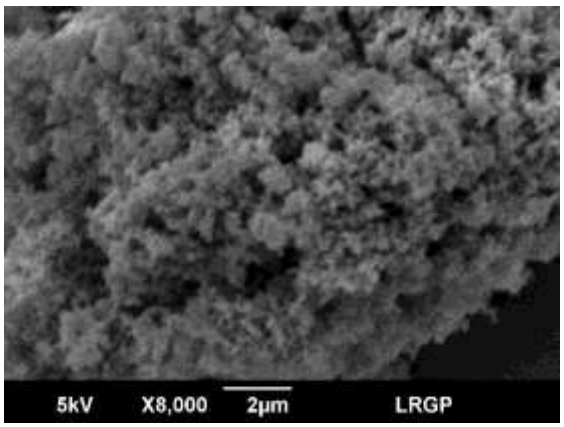

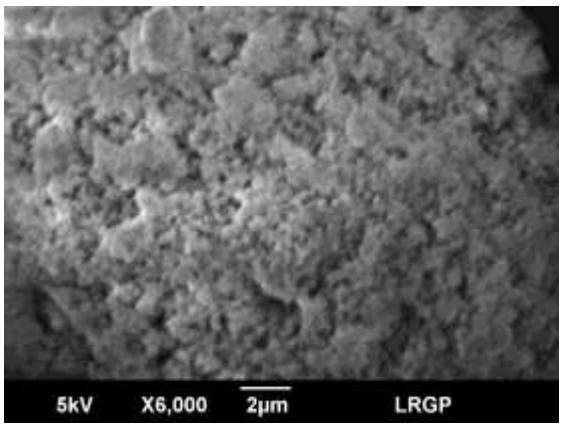

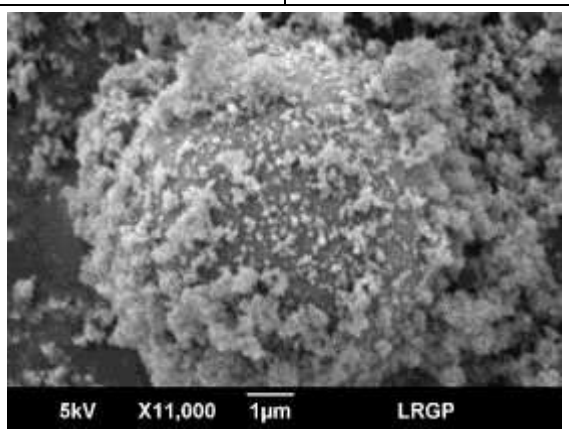

[201]

Carbon-coated silicon (raw powder)

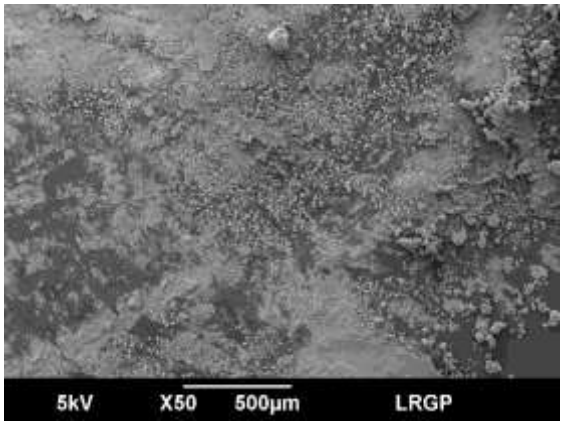

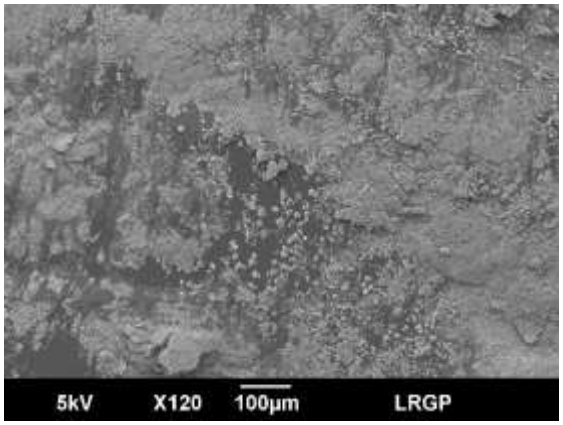

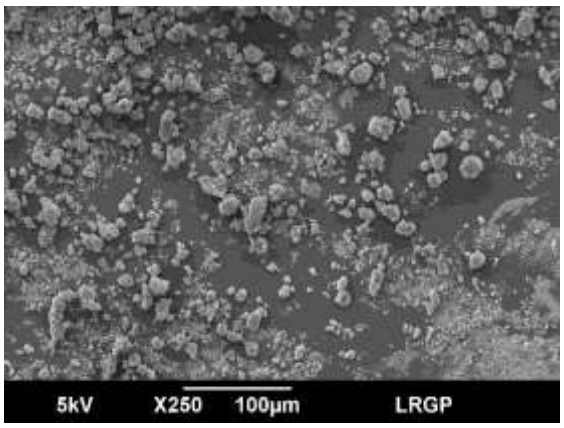

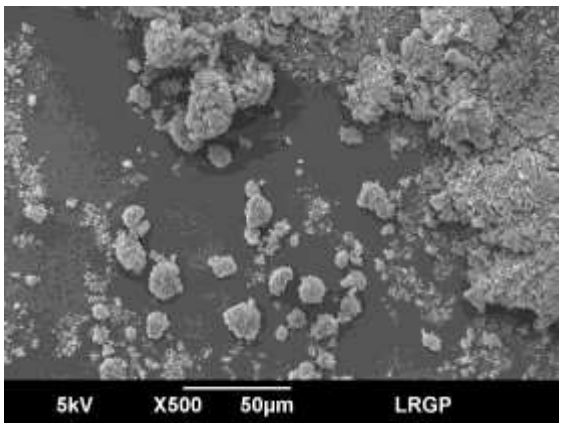

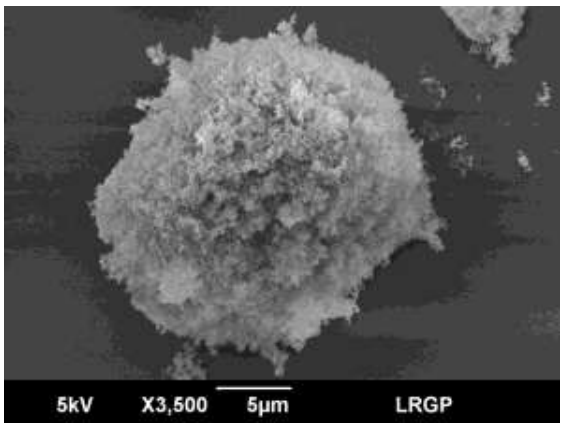

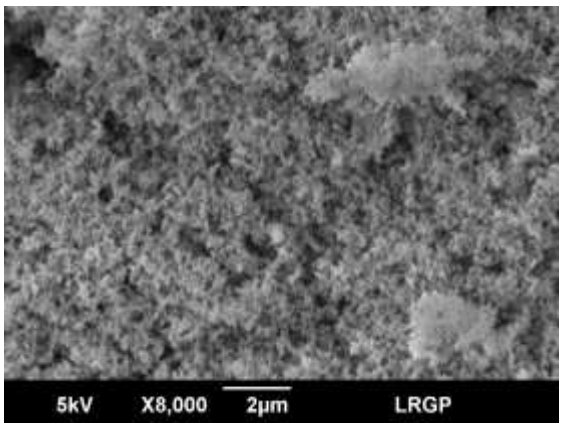

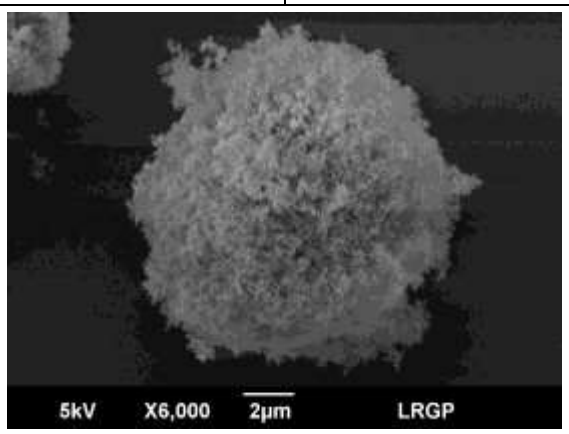

Carbon-coated silicon (agglomerated process A, 260 g.L^{-1})

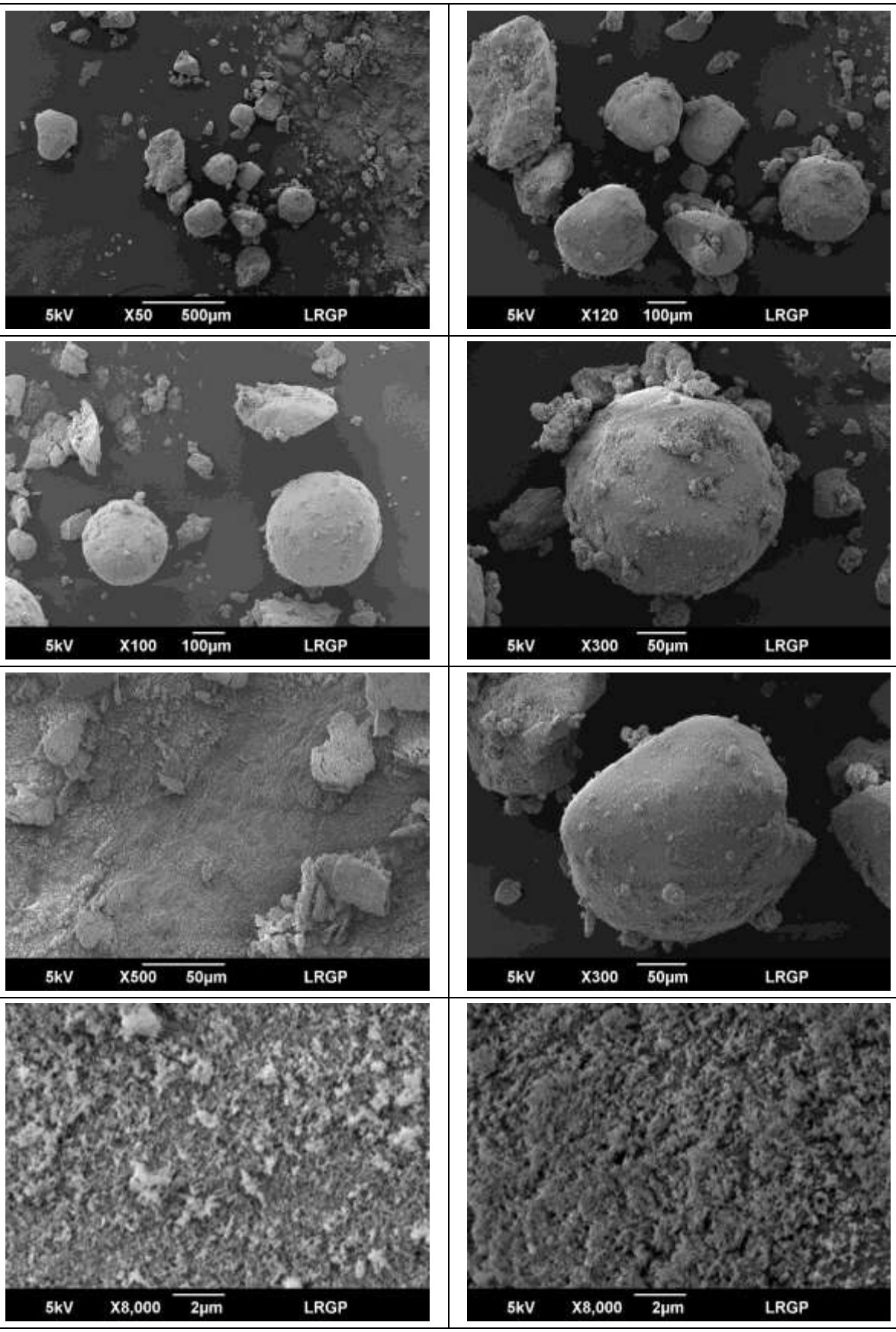

Carbon-coated silicon (agglomerated process A, 400 g.L^{-1})

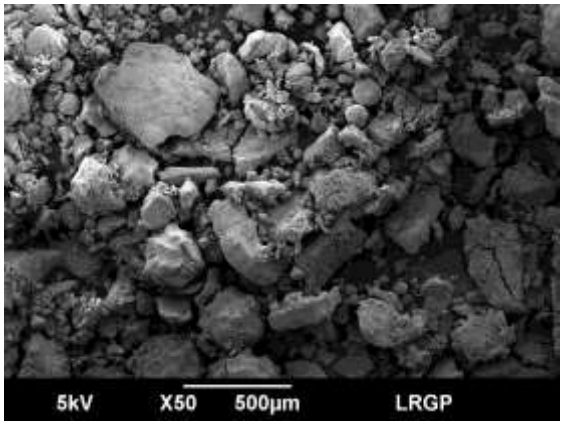

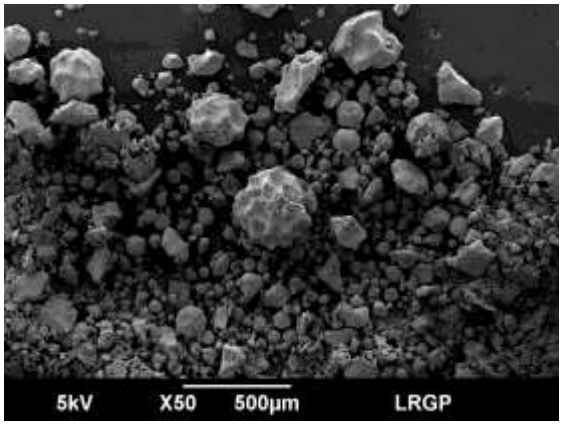

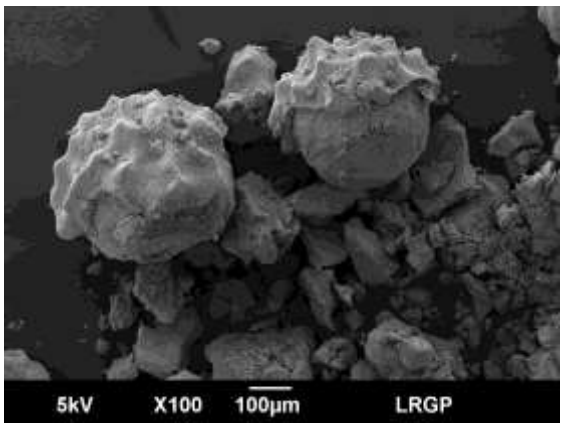

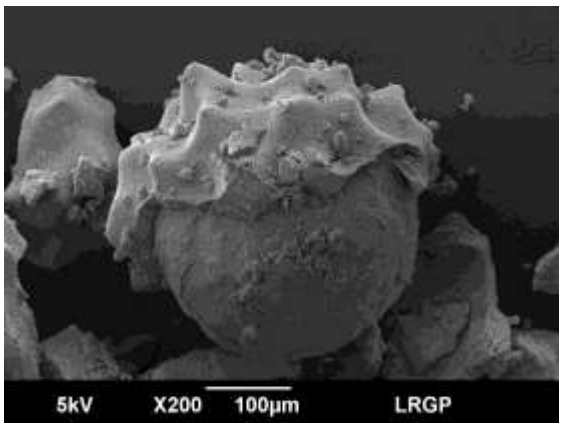

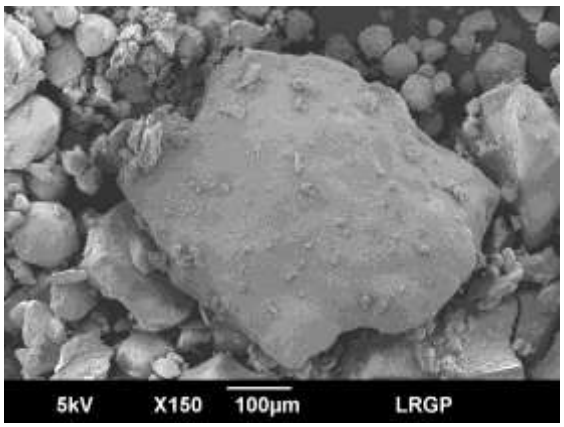

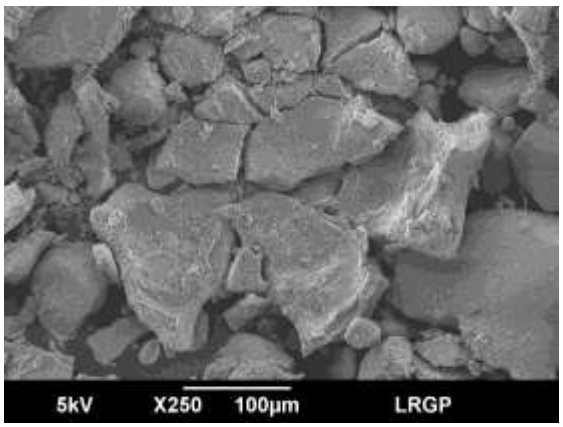

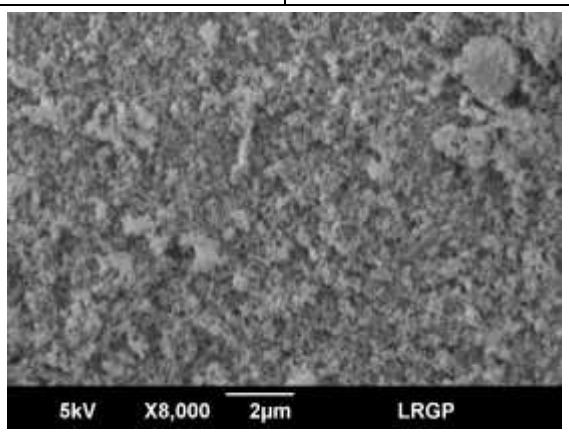

Carbon-coated silicon (agglomerated process B, 400 g.L-1)

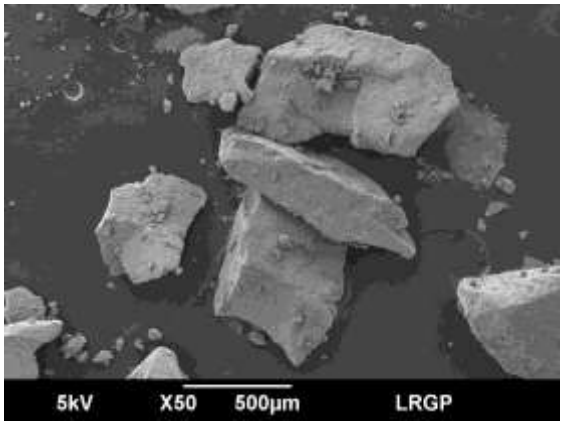

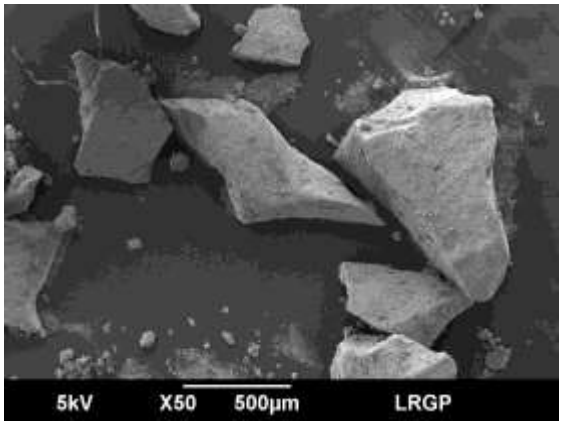

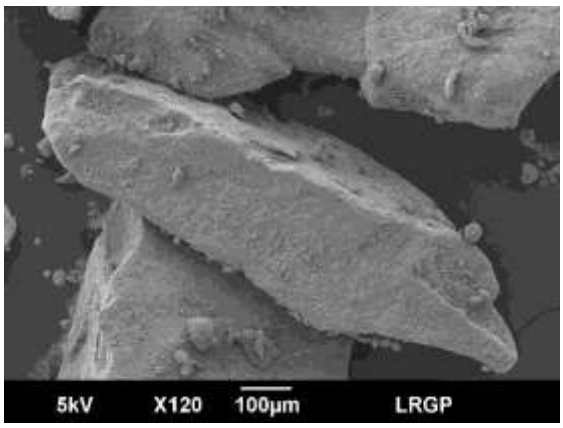

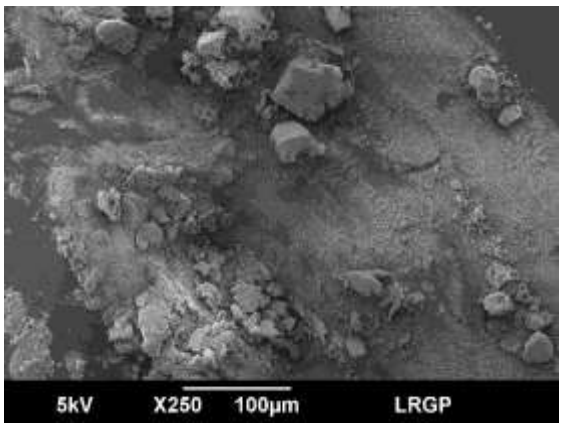

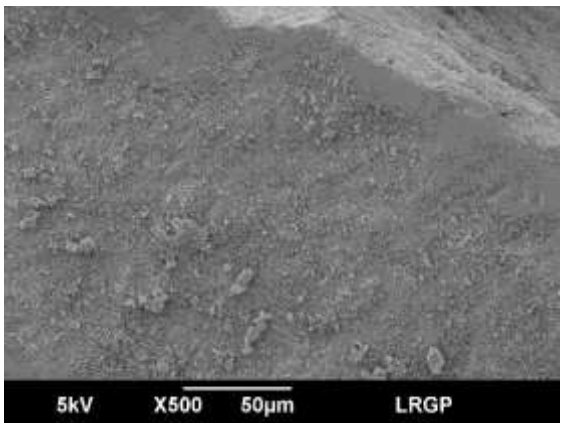

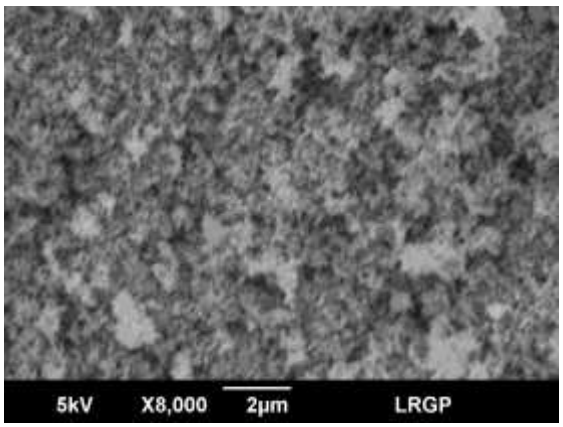

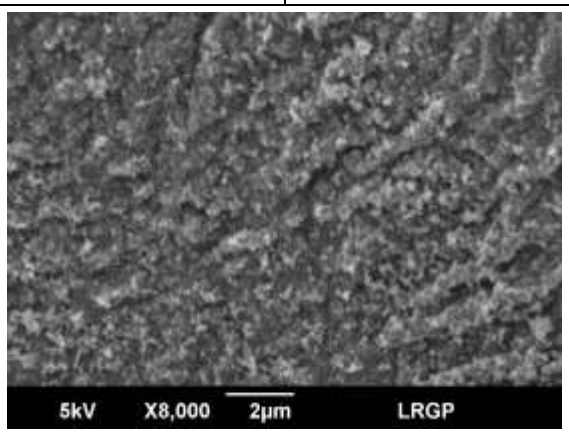

Appendix 2: A Monte Carlo Simulation

The aim of this study if to use Monte Carlo methods to evaluate the accessibility of the oxygen to the surface of agglomerates depending on their characteristics. The first step is then to form numerical agglomerates of different shapes, which is achieved by a random propagation of particles that agglomerate to each other when in contact. The generated agglomerates are then characterized, and oxygen molecules are sent toward its surface. The accessibility of oxygen to the agglomerate is then estimated by comparing the number of molecules received by an individual particle to the number of molecules received by the particle considering the steric hindrance of the other particles constituting the agglomerate.

Agglomerate generation and characterization

The first part of this study consists in generating agglomerates of different shapes to characterize and compare them. The mechanism used for their formation is very simplified in comparison to the real agglomeration mechanism and does not aim to represent it. All the particles within the agglomerate are considered spherical with the same diameter. A limiting volume is defined to limit calculation time, and the simulation starts with a particle at the center of the volume.

A particle is sent from a random point of the surface of the considered volume, in a random direction, and progresses in straight line. If the particle leaves the working volume without encountering another particle, a new one is sent. If a contact happens between the surface of two (or more) particles, the particle keeps its position, which is saved, and a new particle is sent (Figure A-1). The number of particles constituting the agglomerate is set as an input, and particles are sent into the volume until this number is reached.

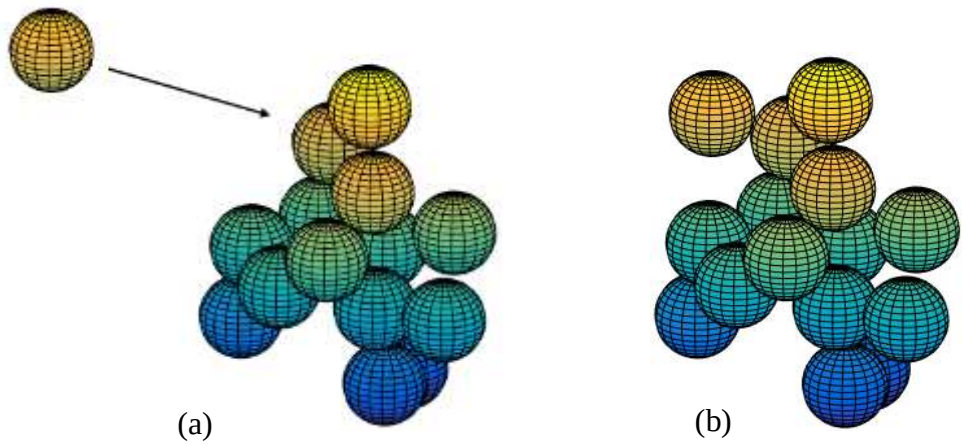

Figure A-1 a) Particle propagating toward an agglomerate and b) particle added to the agglomerate

For each generated agglomerate, the fractal dimension D_f was estimated to allow a comparison. This parameter varies with the number of particle within the agglomerate n_p, the primary particle diameter d_p and the gyration diameter d_g according to the following relation (Mandelbrot, 1983):

$$n_p = k_g\left(\frac{d_g}{d_p}\right)^{D_f} \quad \text{A-1}$$

$$d_g = \sqrt{\frac{4}{n_p}\sum_i {d_i}^2} \quad \text{A-2}$$

The fractal prefactor k_g is function of the nature of the particle and the fractal dimension and is difficult to evaluate (Sorensen and Roberts, 1997). A first approximation of the fractal dimension of each agglomerate is then calculated using relation (1) coupled with a correlation established by Gmachowski (2002) to estimate k_g:

$$k_g = \left(\left(1.56 - \left(1.728 - \frac{D_f}{2}\right)^2\right)^{\frac{1}{2}} - 0.228\right)^{D_f} \left(\frac{2+D_f}{D_f}\right)^{\frac{D_f}{2}} \quad \text{A-3}$$

This first estimation was performed to identify agglomerates with similar fractal dimension regardless of the particle number and diameter. Modifications of those parameters for agglomerates with the same fractal dimension then allow to linearize equation (1) to compare the real fractal dimensions of the agglomerates:

$$\log(n_p) = \log(k_g) + D_f \log\left(\frac{d_g}{d_p}\right) \quad \text{A-4}$$

It appears in Figure A-2 that Gmachowski's correlation allowed to obtain similar agglomerates in terms of fractal dimension by varying the particle number and diameter. Since agglomerates with different characteristics were generated, it is then possible to isolate the influence of the fractal dimension, particle number and particle diameter on the accessibility of oxygen to the agglomerate. Agglomerates of fractal dimension from 1 to 2.4, primary diameter from 4 to 10 nm and constituted by 15 to 100 particles were then studied.

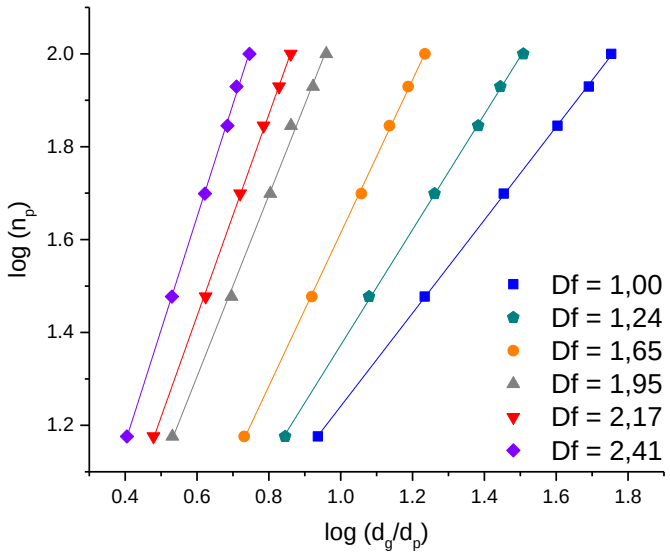

Figure A-2 Estimation of the fractal dimension of some generated agglomerates

Oxygen propagation

Once the agglomerate is generated, dioxygen molecules are sent toward it. Since the molecule propagates by turning on itself, to take the steric hindrance into account, it is considered to be a sphere with a diameter of 0.292 nm, which is the molecular diameter of the dioxygen molecule (Mukhopadhyay and Das, 1994). As previously, the molecule is sent from a random position of a defined volume around the agglomerate and propagates in a random direction. Since this simulation does not aim to represent the real adsorption phenomenon or molecule propagation, but only the accessibility of the molecule to the agglomerate, the random initial position and direction are considered sufficient to describe the Brownian motion of the molecules, which propagate in straight line.

During the molecule propagation, three situations can be encountered. First, if the molecule leaves the working volume, a new particle is sent with a new initial position and direction. Then, the molecule can get in contact with another molecule already adsorbed at the particle surface. Since the aim of the simulation is to evaluate the accessibility of the oxygen toward the agglomerate, it is considered that only one molecule can be adsorbed at the same spot. The propagating molecule is then reflected with the same plane and angle of incidence and keeps stepping forward in its new direction. In the final case, the molecule gets in contact with a particle of the agglomerate and is adsorbed at the particle surface. Its position is then saved and a new molecule is sent. The number of dioxygen molecules to receive on the whole agglomerate is fixed, and the generation stops when this number is reached. For each particle, the number of molecules on its surface is saved. Figure A-4 shows the agglomerate covered by molecules, represented by blue points.

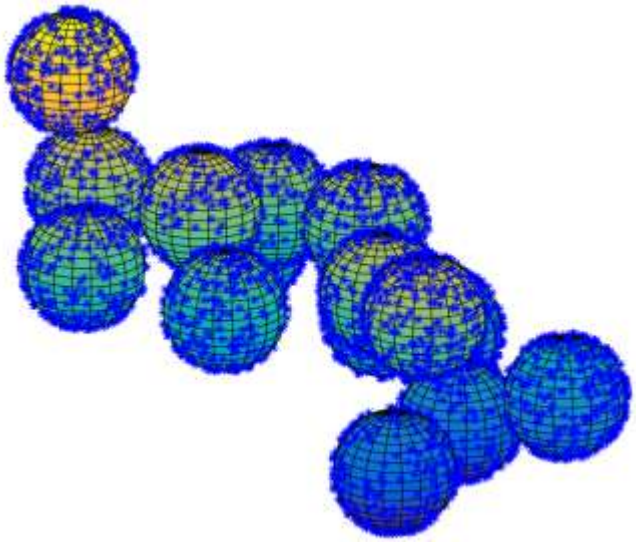

Figure A-3 Particles of an agglomerate (Df = 2) covered by dioxygen molecules

A second part consists in removing all particles from the agglomerate, except one, located at the same place in the working volume, and sending the exact same molecules than previously, in the same direction with the same initial position and angle. The number of molecules received by the individual particle is saved and compared to the number of molecules that the same particle received when being part of the agglomerate, i.e. when considering the hindrance of the agglomerate. This operation is carried out for each particle constituting the agglomerate and allows an estimation of the accessibility of the oxygen to each particle of the agglomerate. The algorithm flow chart of the oxygen propagation and adsorption is presented in Figure A-4.

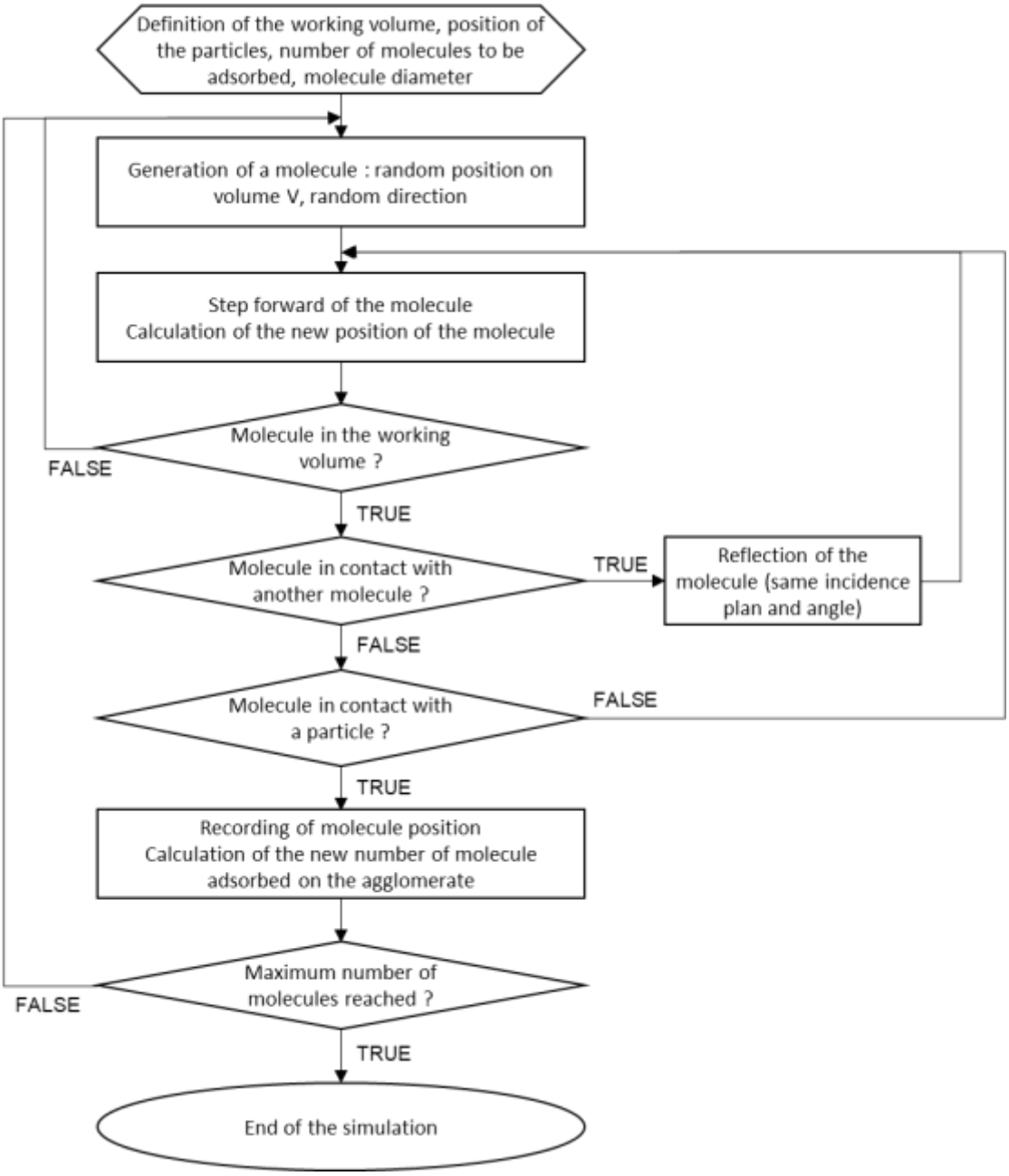

Figure A-4 Algorithm flow chart of the molecule propagation and adsorption to the agglomerate

Estimation of the accessibility of the oxygen to the agglomerate

The accessibility of oxygen to a particle is considered to be maximum when no other particle is present in the working volume to stop the propagation of oxygen. The number of oxygen molecules adsorbed at the surface of a particle in those conditions then represents an accessibility of 100% toward this particle. The ratio between the number of molecules adsorbed by a particle when considering the hindrance of the agglomerate to the number of molecules adsorbed by the same independent particle then leads to an estimation of the accessibility of the oxygen to the particle. The oxygen accessibility to the whole agglomerate is then calculated by meaning the accessibilities to the particles.

$$\text{Oxygen accessibility to one particle} = \frac{n_{ads} \text{ by the particle in the agglomerate}}{n_{ads} \text{ by the particle alone}} \quad \text{A-5}$$

Determination of the number of molecules to receive on the agglomerate

The arrangement of the particles being different for each agglomerate, fixing the total number of molecules to send would lead to significant discrepancies in the operating conditions, as different quantities of molecules would leave the working volume. Moreover, due to the calculation method to estimate the oxygen accessibility to the agglomerate, sending molecules until reaching a fixed value of accessibility is not suitable, as the condition could be reached by only sending a few molecules, which would lead to inaccurate results. Thus, as previously mentioned, the number of molecules to receive on the whole agglomerate was fixed to ensure the same conditions were set up for the different agglomerates and to eliminate the influence of the working volume on the results.

To determine the final value to set, simulations were performed on different agglomerates by varying the number of molecules to receive. Figure A-5 represents the results obtained for agglomerates of 15 particles with a primary diameter of 10 nm. It appears that the accessibility of oxygen to the agglomerate increases slowly with the number of molecules received by the agglomerate. Indeed, after being adsorbed on the easily accessible sites, molecules inevitably reach locations more difficult to access, ending up covering all the agglomerate if a sufficient number of molecules is sent. The aim of the simulation being to estimate how easily molecules can have access to the agglomerate's surface, the simulation was systematically stopped before this value was reached. Moreover, it appears in Figure A-5 that the difference of accessibility between agglomerates of different fractal dimensions is independent of the number of molecules received, inducing that fixing this number allows a reliable comparison of the accessibilities to the agglomerates. However, when less than 100 molecules are received on the agglomerate, the simulation does not converge to a reliable value, with an uncertainty up to 10%. From 500 molecules received, an uncertainty of less than 1% is observed, implying a sufficient number of molecules was received on the agglomerate. A compromise between accuracy and simulation time was realized by systematically setting the number of molecules to receive on the agglomerate to 5000, which provides an uncertainty always lower than 0.5%.

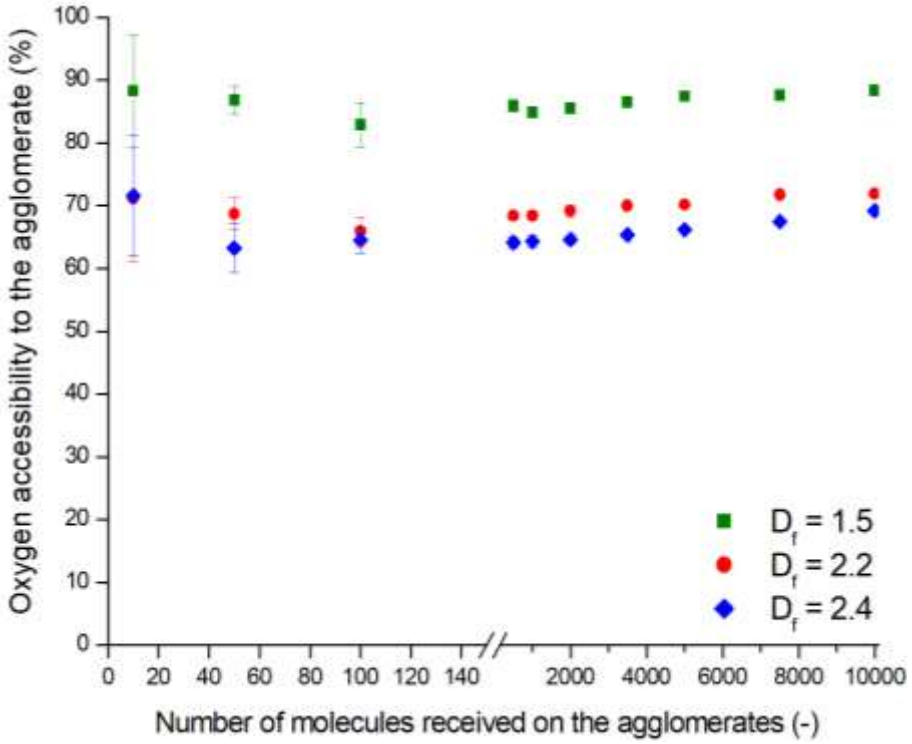

Figure A-5 Evolution of oxygen accessibility with the number of molecules received on the agglomerates of 15 particles with a primary diameter of 10 nm

Influence of the fractal dimension

Simulations were initially conducted by considering agglomerates constituted of 15 spherical particles with a primary diameter of 10 nm. The evolution of the oxygen accessibility to such agglomerates is presented in Figure A-6, and shows a decreasing tendency, from 84.1 ± 0.2% of accessibility to an agglomerate with a fractal dimension of 1 to 66.1 ± 0.4% for agglomerates presenting a fractal dimension of 2.41. An accessibility loss of 18% then appears when forming compact agglomerates with regard to rather linear ones. Although the accuracy of each obtained value is around 0.5%, agglomerates of fractal dimension around 2.1 exhibits accessibilities from 71.5 ± 0.3% to 76.1 ± 0.1%. This difference can be explained by the shape of such agglomerates. Indeed, agglomerates with a fractal dimension of 1 tend to be linear whereas agglomerates of fractal dimension equal to 3 tend be present a spherical shape. Between those extreme cases, different arrangement possibilities between the particles can lead to agglomerates with a fractal dimension equal to 2, which is not considered when calculating the fractal dimension, suggesting that an additional parameter may be necessary to fully characterize the agglomerates shape.

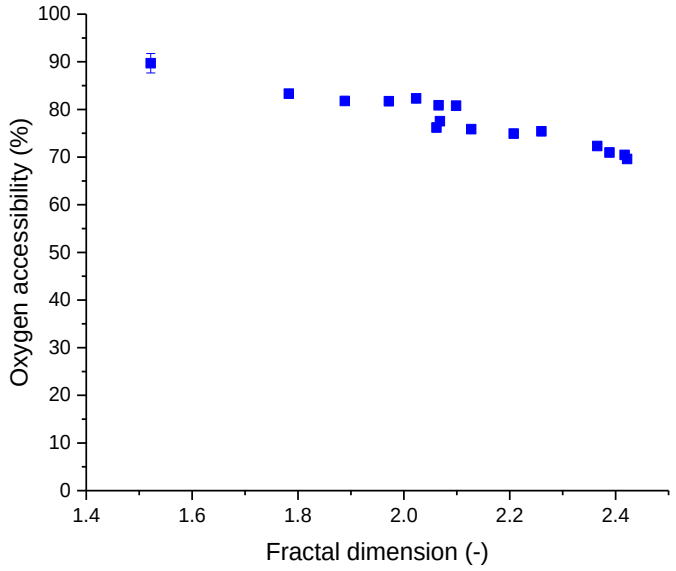

Figure A-6 Evolution of the oxygen accessibility toward agglomerates with the fractal dimension

Influence of the number of particles in the agglomerate

In practice, agglomerates are unlikely to be constituted of only 15 particles. Thus, the influence of the number of particles on the accessibility of oxygen to the agglomerate was investigated by varying the number of particles from 15 to 100 particles. In a first instance, the particle diameter was accordingly modified to keep the agglomerate total surface constant. The particle diameter then varied from 10 nm for 15 particles in an agglomerate to 3.8 nm for 100 particles. The simultaneous variation of the particle number and diameter in the agglomerates notably allowed the calculation of the actual fractal dimension previously presented in Figure A-2. It appears in Figure A-7 that, when increasing the number of particles, the accessibility of oxygen to the agglomerate decreases. However, this decrease is more important when considering compacted agglomerates than linear ones: when increasing the number of particles from 15 to 100 particles in agglomerates with fractal dimension of 1 and 2.4, the accessibility loss is respectively of 6.8% and 20.6%. Indeed, a higher number of particles implies more hindrance possibilities and can make difficult the access to particles in the center of the agglomerate.

Considering two powders constituted of agglomerates of different fractal dimension and their combustion limited by the diffusion of the oxygen to the agglomerate's surface, a slight difference in the ignition and explosion parameters could then be attributed to a different accessibility to the surface of the agglomerate.

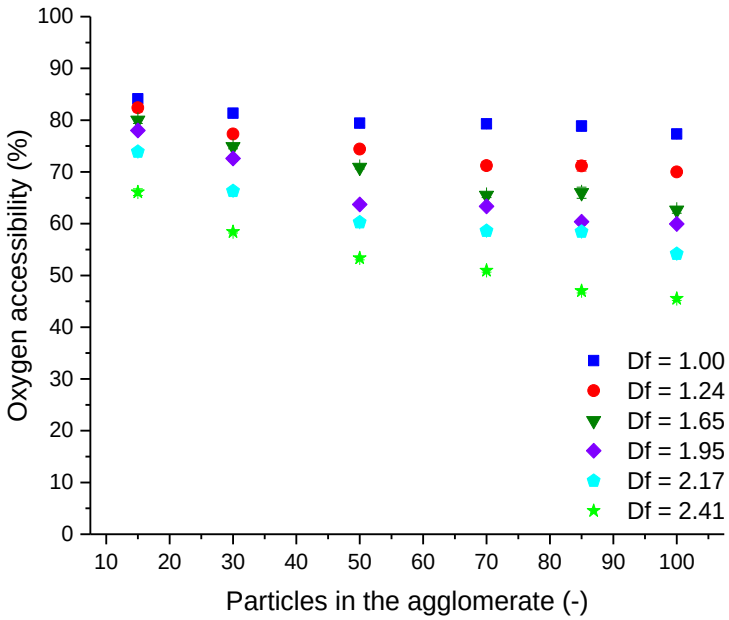

Figure A-7 Evolution of the oxygen accessibility with the number of particles in agglomerates of different fractal dimensions

Appendix 3: Case studies

Appendix 3: Case studies

The industrial situations in which nanoparticles could lead to an explosion are numerous and varied, and trying to report all of them would be illusory. Nevertheless, the four powders considered all along this manuscript will be placed in different industrial contexts based on the information presented by Chaineaux (2004).

Aluminum

Different types of dust collectors exist in industries in order to collect the particles from the air, for hygiene and safety reasons. These processes can be divided into two categories, depending on whether it operates in dry or humid atmosphere, and will be examined through the example of aluminum.

Among the dry dust collectors, a bag filter is constituted of a chamber in which sleeves are vertically placed, and of an aspiration. This aspiration leads to dust collection on the sleeves and allows air/dust separation. However, this aspiration can lead to the electrostatic charging of the particles and possibly to an ignition. Indeed, it should be noted that this type of electrostatic discharge generally releases an energy around 10 mJ, which is considerably higher than the minimum ignition energy (MIE) of aluminum nanopowders (< 1 mJ), and, to a further extent, of nanocellulose (5 mJ). To avoid an ignition, some measures must then be taken: for instance, anti-electrostatic dust bag filter cloths should be used, and electrical grounding of employees and plant should be considered. Moreover, if caking occurs on the sleeves, the agglomeration state of the powder is modified. When unclogging the filters, the PSD is then probably modified again, leading a different ignition sensitivity and explosion severity of the powder. These parameters should then be determined for different PSD to accurately assess the explosion risk.

Nanocellulose

As mentioned in chapter 2, cellulose nanocrystals are generally obtained by acid hydrolysis of different cellulose sources, implying that a drying step is necessary to retrieve a dry powder. The example of a spray drying is then considered in this part. This process is notably constituted of a spray tower supplied in hot air, a vibrating bed, and cyclones connected to a dust collector (Figure A-8).

Depending on the dustiness of the powder, the vibrating bed can release an important quantity of fine particles and generate an explosive atmosphere (ATEX). Due to the high ignition sensitivity of nanoparticles, such fine particles could be easily ignited, e.g. by a hot surface or the hot air, or an electrostatic discharge, provided that energy input is sufficient. Indeed, the minimum ignition temperature in cloud and energy of the nanocellulose respectively reached 420°C and 5 mJ for the dry powder. Thus, the dust deposit in the tower should be minimized, notably due to the high dustiness of nanopowders.

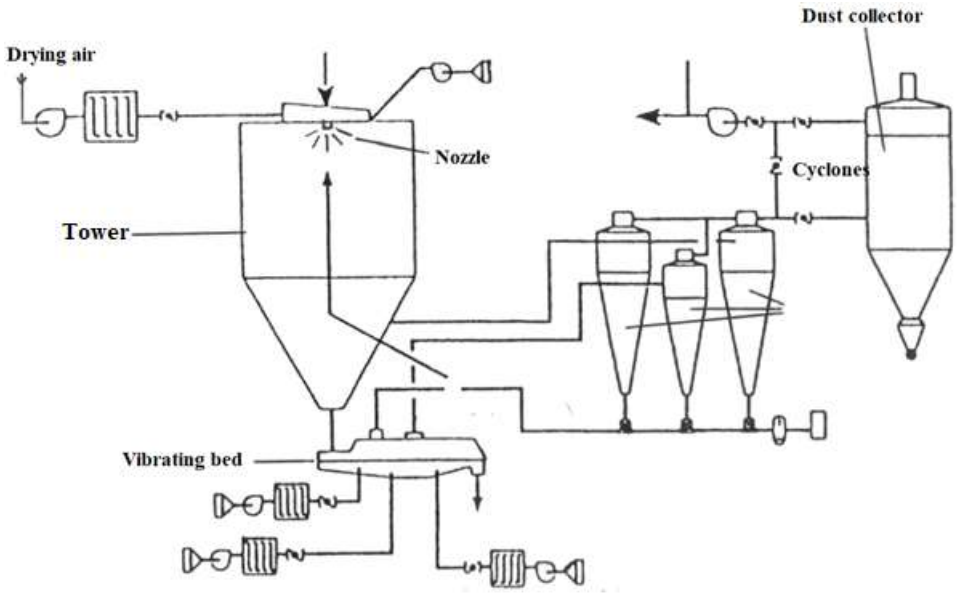

Figure A-8 Scheme of a co-current spray tower equipped with a vibrating bed (from Chaineaux (2004))

Moreover, the characteristics of the spray can affect the turbulence level in the tower, which can directly impact the explosion severity in case of explosion. In addition, right after going through the nozzle, the nanoparticles are not agglomerated yet, and will be very easy to ignite. However, the air is the hottest at this point, which considerably increases the explosion risk. The temperature of the air should then be lower than the MIT of the non-agglomerated nanoparticles, whereas the MIT measured by the standard method corresponds to the MIT of the agglomerates after dispersion in the Godbert-Greenwald oven. On the contrary, at the bottom of the tower, the powder is agglomerated, which will tend to decrease the ignition sensitivity and explosion severity of the powders. It should also be noted that the environment is very humid, which can, in case of explosion, lead to reactions between the water and the powder and increase the explosion severity, or, on the contrary, decrease it due to heat sink effects.

Concerning the vibrating bed, the risk generally considered is a fire, but it could evolve into an explosion when it comes to nanopowders, or micropowders releasing nanocrystals. Moreover, the use of cyclones is not recommended for the filtration of nanoparticles. Indeed, a cyclone separates the air from the particles by gravity, implying that the finest particles are not retained in the cyclone.

Carbon-coated silicon

The effectiveness of the mechanical agglomeration of the powder to decrease both its ignition sensitivity and explosion severity was evidenced through the example of the carbon-coated silicon. Moreover, the agglomeration of powders can reduce particle emissions in the air during handling facilitate the flowing of the product within industrial equipment and reduce cost of

transportation by increasing the bulk density of the powder. The agglomeration then limits the formation of the ATEX and decreases the ignition sensitivity of the powder, and thus the probability of ignition. Since such phenomenon does not modify the specific surface area, agglomeration can then be seen as an inherent safety solution. However, the conditions of handling and transporting must be carefully assessed as it may impact the level of fragmentation of the powder and reduce consequently the level of agglomeration of the powder. The influence of these conditions could be further assessed for instance by adjusting experimental conditions to better reproduce industrial conditions of interest.

Carbon black

An aging phenomenon of the carbon black due to a long storage of more than ten years was evidenced in chapter 5, and was notably attributed to the adsorption of water during this period. At a first sight, the storage of carbon black is not likely to generate an ATEX or, if so, this ATEX is not likely to be ignited without external intervention. However, the accident that recently occurred in New Mexico, United States in 2018, mentioned in chapter 2, indicates just the opposite with the collapsing of a silo holding more than 600 tons of coal that caused an explosion and a fire.

Moreover, when discharging the silo, the height between the hopper and the collect system should be as small as possible, since the turbulence level increases with the height. In a similar way, the explosion risk is increased when charging a silo from the top due to the high turbulence generated by the process.

Vent sizing is generally realized to protect from explosion scenarios. However, in such case, the turbulence may be higher or, at least, different than that of the experiments, whereas the cube-root law can be applied only if the turbulence temporal and spatial variations are similar in both enclosures. The extrapolation from the laboratory conditions to industrial may then be inaccurate, which could lead to an inadequate vent sizing.

References

References

2011/696/EU, 2011. Commission Recommendation of 18 October 2011 on the definition of nanomaterial (Text with EEA relevance). Off. J. Eur. Union 3.

Abbasi, T., Abbasi, S.A., 2007. Dust explosions–Cases, causes, consequences, and control. J. Hazard. Mater. 140, 7–44.

Abitbol, T., Rivkin, A., Cao, Y., Nevo, Y., Abraham, E., Ben-Shalom, T., Lapidot, S., Shoseyov, O., 2016. Nanocellulose, a tiny fiber with huge applications. Curr. Opin. Biotechnol., Systems biology - Nanobiotechnology 39, 76–88.

Abuswer, M., Amyotte, P., Khan, F., 2013. A quantitative risk management framework for dust and hybrid mixture explosions. J. Loss Prev. Process Ind. 26, 283–289.

Ali, M., Bonakdar, T., Ghadiri, M., Tinke, A., 2015. Particle Breakage in a Scirocco Disperser. Powder Technol., Pharmaceutical Particle Technology 285, 138–145.

Ali, M., Lin, L., Faisal, S., Ali, S.R., Ali, S.I., 2019. Let-down stability and screen printability of inks prepared using non-printing ink grades of carbon black pigment. Pigment Resin Technol. 48, 523–532.

American Institute of Chemical Engineers (Ed.), 2017. Guidelines for combustible dust hazard analysis, CCPS AIChE guidelines. CCPS, Center for Chemical Process Safety, New York, NY.

Amyotte, P.R., 2014. Some myths and realities about dust explosions. Process Saf. Environ. Prot. 92, 292–299.

Amyotte, P.R., Basu, A., Khan, F.I., 2003. Reduction of Dust Explosion Hazard by Fuel Substitution in Power Plants. Process Saf. Environ. Prot. 81, 457–462.

Amyotte, P.R., Chippett, S., Pegg, M.J., 1988. Effects of turbulence on dust explosions. Prog. Energy Combust. Sci. 14, 293–310.

Amyotte, P.R., Eckhoff, R.K., 2010. Dust explosion causation, prevention and mitigation: An overview. J. Chem. Health Saf. 17, 15–28.

Amyotte, P.R., Pegg, M.J., Khan, F.I., 2009. Application of inherent safety principles to dust explosion prevention and mitigation. Process Saf. Environ. Prot., 12th International Symposium of Loss Prevention and Safety Promotion in the Process Industries 87, 35–39.

Amyotte, P.R., Pegg, M.J., Khan, F.I., Nifuku, M., Yingxin, T., 2007. Moderation of dust explosions. J. Loss Prev. Process Ind. 20, 675–687.

Andersen, J., Rasmussen, C.L., Giselsson, T., Glarborg, P., 2009. Global Combustion Mechanisms for Use in CFD Modeling under Oxy-Fuel Conditions. Energy Fuels 23, 1379–1389.

Andrews, G.E., Bradley, D., 1972. Determination of burning velocities: A critical review. Combust. Flame 18, 133–153.

Andrews, G.E., Bradley, D., Lwakabamba, S.B., 1975. Turbulence and turbulent flame propagation—A critical appraisal. Combust. Flame 24, 285–304.

ASTM E1226-19, 2019. Standard Test Method for Explosibility of Dust Clouds. In: Annual Book of ASTM Standards. pp. 1–13.

ASTM E1491-06, 2012. Standard Test Method for Minimum Autoignition Temperature of Dust Clouds. In: Annual Book of ASTM Standards. pp. 1–11.

ASTM E1515-14, 2014. Standard Test Method for Minimum Explosible Concentration of Combustible Dusts. In: Annual Book of ASTM Standards. pp. 1–9.

References

ASTM E2019-03, 2007. Standard Test Method for Minimum Ignition Energy of a Dust Cloud in Air. In: Annual Book of ASTM Standards. pp. 1–8.

Babrauskas, V., Britton, L.G., 2018. Errors in the Compilations of Minimum Explosion Concentration Values for Dust Clouds. Fire Technol. 54, 37–55.

Bagaria, P., Zhang, J., Yang, E., Dastidar, A., Mashuga, C., 2016. Effect of dust dispersion on particle integrity and explosion hazards. J. Loss Prev. Process Ind. 44, 424–432.

Ballal, D.R., 1983. Flame Propagation Through Dust Clouds of Carbon, Coal, Aluminium and Magnesium in an Environment of Zero Gravity. Proc. R. Soc. Lond. Math. Phys. Sci. 385, 21–51.

Bartknecht, W., 1989. Dust-explosions: course, prevention, protection. Springer-Verlag.

Baudry, G., 2007. Etude de l'inflammabilité d'un nuage de particules d'aluminium partiellement oxydées.

Bazyn, T., Krier, H., Glumac, N., 2007. Evidence for the transition from the diffusion-limit in aluminum particle combustion. Proc. Combust. Inst. 31, 2021–2028.

Beeckmann, J., Hesse, R., Schaback, J., Pitsch, H., Varea, E., Chaumeix, N., 2019. Flame propagation speed and Markstein length of spherically expanding flames: Assessment of extrapolation and measurement techniques. Proc. Combust. Inst. 37, 1521–1528.

Belerrajoul, M., 2019. Modélisation multi-échelle de la combustion d'un nuage de particules (PhD Thesis). National Polytechnic Institute of Toulouse.

Ben Moussa, R., 2017. Contribution to thermal radiation to dust flame propagation : application to aluminium dust explosions (PhD Thesis). Université de Technologie de Compiègne.

Bergstroem, L., Meurk, A., Rowcliffe, D.J., Arwin, H., 1996. Estimation of Hamaker constants of ceramic materials from optical data using Lifshitz theory. J. Am. Ceram. Soc. 79.

Bews, I.M., Hayhurst, A.N., Richardson, S.M., Taylor, S.G., 2001. The order, Arrhenius parameters, and mechanism of the reaction between gaseous oxygen and solid carbon. Combust. Flame 124, 231–245.

Bidabadi, M., Azad, A.V., 2015. Effects of radiation on propagating spherical flames of dust–air mixtures. Powder Technol. 276, 45–59.

Bideau, D., 2010. Développement d'un modèle instationnaire pour l'étude de l'instabilité thermique de mélanges de solides pulvérulents - Application aux dépôts de poussières métalliques.

Boilard, S.P., Amyotte, P.R., Khan, F.I., Dastidar, A.G., Eckhoff, R.K., 2013. Explosibility of micron- and nano-size titanium powders. J. Loss Prev. Process Ind. 26, 1646–1654.

Bollinger, R.E., Crowl, D.A., 1997. Inherently safer chemical processes: a life cycle approach. Center for Chemical Process Safety of the American Institute of Chemical Engineers.

Bonakdar, T., Ali, M., Dogbe, S., Ghadiri, M., Tinke, A., 2016. A method for grindability testing using the Scirocco disperser. Int. J. Pharm. 501, 65–74.

Bonakdar, T., Ghadiri, M., 2017. Effect of Structure on Strength of Agglomerates using Distinct Element Method [WWW Document]. EPJ Web Conf. URL http://eprints.whiterose.ac.uk/119912/ (accessed 11.28.19).

Börjesson, M., Westman, G., 2015. Crystalline Nanocellulose — Preparation, Modification, and Properties. In: Poletto, M., Ornaghi, H.L. (Eds.), Cellulose - Fundamental Aspects and Current Trends. InTech.

Bouillard, J., Vignes, A., Dufaud, O., Perrin, L., Thomas, D., 2010. Ignition and explosion risks of nanopowders. J. Hazard. Mater. 181, 873–880.

References

Boutonnet Kizling, M., Gallas, J.P., Binet, C., Lavalley, J.C., 1992. Surface oxidation of silicon carbide: quantitative measurement and Rh effect. Mater. Chem. Phys. 30, 273–277.

Bradley, D., 2000. Flame Propagation in a Tube: The Legacy of Henri Guenoche. Combust. Sci. Technol. 158, 15–33.

Bradley, D., Chen, Z., Swithenbank, J.R., 1989. Burning rates in turbulent fine dust-air explosions. Symp. Int. Combust. 22, 1767–1775.

Bradley, D., Lawes, M., Mumby, R., 2017. Burning velocity and Markstein length blending laws for methane/air and hydrogen/air blends. Fuel 187, 268–275.

Bradley, D., Lee, J.H.S., 1984. . Proc. First Int. Colloq. Explos. Ind. Dusts 220–223.

Brequigny, P., Halter, F., Mounaïm-Rousselle, C., 2016. Lewis number and Markstein length effects on turbulent expanding flames in a spherical vessel. Exp. Therm. Fluid Sci., Special issue on Ninth Mediterranean Combustion Symposium 73, 33–41.

Brunauer, S., Emmett, P.H., Teller, E., 1938. Adsorption of Gases in Multimolecular Layers. J. Am. Chem. Soc. 60, 309–319.

BS EN 60529, 1992. Degrees of Protection Provided by Enclosures (IP Code).

Buckingham, E., 1914. On Physically Similar Systems; Illustrations of the Use of Dimensional Equations. Phys. Rev. 4, 345–376.

Calvert, G., Hassanpour, A., Ghadiri, M., 2013. Analysis of aerodynamic dispersion of cohesive clusters. Chem. Eng. Sci. 86, 146–150.

Cashdollar, K.L., Hertzberg, M., Zlochower, I.A., 1989. Effect of volatility on dust flammability limits for coals, gilsonite, and polyethylene. Symp. Int. Combust. 22, 1757–1765.

Cassel, H.M., Liebman, I., Mock, W.K., 1957. Radiative transfer in dust flames. Symp. Int. Combust., Sixth Symposium (International) on Combustion 6, 602–605.

CelluForce, 2016. Product Specification of CelluForce NCV100.

Center for Chemical Process Safety, 2004. Guidelines for Safe Handling of Powders and Bulk Solids: CCPS/Guidelines. John Wiley & Sons, Inc., Hoboken, NJ, USA.

Cesana, C., Siwek, R., 2001a. MIKE 3-Minimum Ignition Energy.

Cesana, C., Siwek, R., 2001b. Operating instructions 20L apparatus.

Chaineaux, J., 2004. Sécurité des procédés mettant en œuvre des pulvérulents combustibles. INERIS report Ω-14, 76p.

Chan, M., Chong, S.J., 2016. Dust explosion from coloured powder causing severe burns. ANZ J. Surg. 86, 103–104.

Chanut, C., 2018. Etude expérimentale de la propagation du front de flamme et de la vitesse de combustion d'une explosion de poussières d'aluminium (PhD Thesis). IMT Mines Alès.

Chen, Z., Ju, Y., 2007. Theoretical analysis of the evolution from ignition kernel to flame ball and planar flame. Combust. Theory Model. 11, 427–453.

Clavin, P., 1985. Dynamic behavior of premixed flame fronts in laminar and turbulent flows. Prog. Energy Combust. Sci. 11, 1–59.

Clavin, P., Williams, F.A., 1979. Theory of premixed-flame propagation in large-scale turbulence. J. Fluid Mech. 90, 589–604.

Cloney, C., 2018. 2018 Mid-Year Combustible Dust Incident Report - Version #1. DustEx Research Ltd.

References

Cloney, C., Snoeys, J., 2019. Chapter Three - Dust explosions: A serious concern. In: Amyotte, P.R., Khan, F.I. (Eds.), Methods in Chemical Process Safety, Dust Explosions. Elsevier, pp. 33–69.

Clouthier, M.P., Cormier, L., Hodapp, M., Ogungbemide, D., 2019. Dust explosions: Safety measures. In: Methods in Chemical Process Safety. Elsevier, pp. 193–228.

Condotta, R., 2005. Coulabilité des poudres cohésives : mesures aux faibles contraintes, granulaires humides et application à une poudre industrielle.

Cuervo, N., 2015. Influences of turbulence and combustion regimes on explosions of gas-dust hydrid mixtures (PhD Thesis). The University of Lorraine, France.

Cuervo, N., Dufaud, O., Perrin, L., 2017. Determination of the burning velocity of gas/dust hybrid mixtures. Process Saf. Environ. Prot. 109, 704–715.

Dagastine, R.R., Prieve, D.C., White, L.R., 2002. Calculations of van der Waals Forces in 2-Dimensionally Anisotropic Materials and Its Application to Carbon Black. J. Colloid Interface Sci. 249, 78–83.

Dahoe, A.E., 2000. Dust explosions: a Study of Flame Propagation (PhD Thesis). Delft University, Delft.

Dahoe, A. E., Cant, R.S., Pegg, M.J., Scarlett, B., 2001. On the transient flow in the 20-liter explosion sphere. J. Loss Prev. Process Ind. 14, 475–487.

Dahoe, A.E., Cant, R.S., Scarlett, B., 2001. On the Decay of Turbulence in the 20-Liter Explosion Sphere. Flow Turbul. Combust. 67, 159–184.

Dahoe, A.E., Hanjalic, K., Scarlett, B., 2002. Determination of the laminar burning velocity and the Markstein length of powder–air flames. Powder Technol., Special issue i in Honour of Prof Jimbo 122, 222–238.

Dahoe, A.E., Skjold, T., Roekaerts, D.J.E.M., Pasman, H.J., Eckhoff, R.K., Hanjalic, K., Donze, M., 2013. On the Application of the Levenberg–Marquardt Method in Conjunction with an Explicit Runge–Kutta and an Implicit Rosenbrock Method to Assess Burning Velocities from Confined Deflagrations. Flow Turbul. Combust. 91, 281–317.

Dahoe, A.E., Zevenbergen, J.F., Lemkowitz, S.M., Scarlett, B., 1996. Dust explosions in spherical vessels: The role of flame thickness in the validity of the ‘cube-root law.’ J. Loss Prev. Process Ind. 9, 33–44.

D’Amico, M., 2016. Étude expérimentale et modélisation des explosions hybrides solides/solides : application au cas des mélanges de poussières graphite/métaux (PhD Thesis). Université de Lorraine.

Damkoehler, G., 1947. The Effect of Turbulence on the Flame Velocity in Gas Mixtures.

Dastidar, A., 2019. Dust explosions: Test methods. In: Methods in Chemical Process Safety. Elsevier, pp. 71–122.

Dastidar, A., Amyotte, P., Going, J., Chatrathi, K., 2001. Inerting of coal dust explosions in laboratory- and intermediate-scale chambers. Fuel 80, 1593–1602.

Daubech, J., Leprette, E., Duclos, A., Proust, C., 2018. Accounting for turbulence in gas explosion venting design.

Dazon, C., Witschger, O., Bau, S., Payet, R., Beugnon, K., Petit, G., Garin, T., Martinon, L., 2017. Dustiness of 14 carbon nanotubes using the vortex shaker method. J. Phys. Conf. Ser. 838, 012005.

References

Debrincat, D.P., Solnordal, C.B., Van Deventer, J.S.J., 2008. Characterisation of inter-particle forces within agglomerated metallurgical powders. Powder Technol. 182, 388–397.

Deng, X., Huang, Z., Wang, W., Davé, R.N., 2016. Investigation of nanoparticle agglomerates properties using Monte Carlo simulations. Adv. Powder Technol. 27, 1971–1979.

Di Benedetto, A., Di Sarli, V., Russo, P., 2010. On the determination of the minimum ignition temperature for dust/air mixtures. Chem. Eng. Trans. 19, 189–194.

Di Benedetto, A., Garcia-Agreda, A., Dufaud, O., Khalili, I., Sanchirico, R., Perrin, L., Russo, P., 2011. Flame propagation of dust and gas-air mixtures in a tube. Proc. 7th Mediterr. Combust. Symp. 12.

Di Benedetto, A., Russo, P., 2007. Thermo-kinetic modelling of dust explosions. J. Loss Prev. Process Ind., Selected Papers Presented at the Sixth International Symposium on Hazards, Prevention and Mitigation of Industrial Explosions 20, 303–309.

Di Benedetto, A., Russo, P., Amyotte, P., Marchand, N., 2010. Modelling the effect of particle size on dust explosions. Chem. Eng. Sci. 65, 772–779.

Di Benedetto, A., Sanchirico, R., Di Sarli, V., 2019. Dust explosions: Emerging/unique scenarios. In: Methods in Chemical Process Safety. Elsevier, pp. 283–316.

Di Benedetto A., Russo, P., Sanchirico, R., Sarli, V.D., 2013. CFD simulations of turbulent fluid flow and dust dispersion in the 20 liter explosion vessel. AIChE J. 59, 2485–2496.

Di Blasi, C., Branca, C., 2001. Kinetics of Primary Product Formation from Wood Pyrolysis. Ind. Eng. Chem. Res. 40, 5547–5556.

Dufaud, O., 2011. Application des principes de la sécurité intrinsèque aux explosions de poussières : de la modération en toutes choses. (Habilitation à diriger des recherches Génie des Procédés et des Produits). INPL, Vandoeuvre-lès-Nancy.

Dufaud, O., Khalili, I., Cuervo-Rodriguez, N., Olcese, R.N., Dufour, A., Perrin, L., Laurent, A., 2012a. Highlighting the Importance of the Pyrolysis Step on Dusts Explosions.

Dufaud, O., Perrin, L., Traore, M., Chazelet, S., Thomas, D., 2009. Explosions of vapour/dust hybrid mixtures: A particular class. Powder Technol., Selection of Papers from the Symposium Powder Science and Technology - Powders and Sintered Material STP-PMF 2007 190, 269–273.

Dufaud, O., Poupeau, M., Khalili, I., Cuervo, N., Christodoulou, M., Olcese, R., Dufour, A., Perrin, L., 2012c. Comparing Pyrolysis Gases and Dusts Explosivities: A Clue to Understanding Hybrid Mixtures Explosions? Ind. Eng. Chem. Res. 51, 7656–7662.

Dufaud, O., Vignes, A., Henry, F., Perrin, L., Bouillard, J., 2011a. Ignition and explosion of nanopowders: something new under the dust. J. Phys. Conf. Ser. 304, 012076.

Eckhoff, R.K., 2002. Minimum ignition energy (MIE) — a basic ignition sensitivity parameter in design of intrinsically safe electrical apparatus for explosive dust clouds. J. Loss Prev. Process Ind. 15, 305–310.

Eckhoff, R.K., 2003. Dust Explosions in the Process Industries - 3rd Edition

Eckhoff, R.K., 2012. Does the dust explosion risk increase when moving from μm-particle powders to powders of nm-particles? J. Loss Prev. Process Ind. 25, 448–459.

Eckhoff, R.K., 2016. Dust Explosions. In: Explosion Hazards in the Process Industries. Elsevier, pp. 253–383.

Eckhoff, R.K., 2019a. Measuring hot-surface minimum ignition temperatures of dust clouds – History, present, future. J. Loss Prev. Process Ind. 59, 63–76.

References

Eckhoff, R.K., 2019b. Origin and development of the Godbert-Greenwald furnace for measuring minimum ignition temperatures of dust clouds. Process Saf. Environ. Prot. 129, 17–24.

Eckhoff, R.K., 2019c. Measurement of minimum ignition energies (MIEs) of dust clouds – History, present, future. J. Loss Prev. Process Ind. 61, 147–159.

Eckhoff, R.K., Randeberg, E., 2007. Electrostatic spark ignition of sensitive dust clouds of MIE<1mJ. J. Loss Prev. Process Ind., Selected Papers Presented at the Sixth International Symposium on Hazards, Prevention and Mitigation of Industrial Explosions 20, 396–401.

EN 1127-1, 2019. Explosive atmospheres. Explosion prevention and protection. Basic concepts and methodology.

EN 14034-1, 2004a. Determination of explosion characteristics of dust clouds — Part 1: Determination of the maximum explosion pressure Pmax of dust clouds.

EN 14034-2, 2006. Determination of explosion characteristics of dust clouds — Part 2: Determination of the maximum rate of explosion pressure rise (dp/dt)max of dust clouds.

EN 14034-3, 2006. Determination of explosion characteristics of dust clouds — Part 3: Determination of the lower explosion limit LEL of dust clouds.

EN 15051, 2006. Workplace Atmospheres: Measurement of the Dustiness of Bulk Materials - Requirements and Reference Test Methods.

EN 17199-5, 2019. Workplace exposure - Measurement of dustiness of bulk materials that contain or release respirabe NOAA or other respirable particles - Part 5: Vortex shaker method. p. 37.

EN 50281-2-1, 2000. Electrical apparatus for use in the presence of combustible dust. Test methods. Methods of determining minimum ignition temperatures.

Fan, Y., Fowler, G.D., Zhao, M., 2020. The past, present and future of carbon black as a rubber reinforcing filler – A review. J. Clean. Prod. 247, 119115.

Fayet, G., Rotureau, P., 2019. New QSPR Models to Predict the Flammability of Binary Liquid Mixtures. Mol. Inform. 38, 1800122.

Frankel, M.L., Sivashinsky, G.I., 1984. On Quenching of Curved Flames. Combust. Sci. Technol. 40, 257–268.

Frassoldati, A., Cuoci, A., Faravelli, T., Ranzi, E., Candusso, C., Tolazzi, D., 2009. Simplified kinetic schemes for oxy-fuel combustion. 1 St Int. Conf. Sustain. Foss. Fuels Future Energy – S4FE 2009.

Ghadiri, M., Zhang, Z., 2002. Impact attrition of particulate solids. Part 1: A theoretical model of chipping. Chem. Eng. Sci. 57, 3659–3669.

Ghaffari, M., Hoffmann, A.C., Skjold, T., Eckhoff, R.K., van Wingerden, K., 2019. A brief review on the effect of particle size on the laminar burning velocity of flammable dust: Application in a CFD tool for industrial applications. J. Loss Prev. Process Ind. 62, 103929.

Glorian, J., Gallier, S., Catoire, L., 2016. On the role of heterogeneous reactions in aluminum combustion. Combust. Flame 168, 378–392.

Gmachowski, L., 2002. Calculation of the fractal dimension of aggregates. Colloids Surf. Physicochem. Eng. Asp. 211, 197–203.

References

Going, J.E., Chatrathi, K., Cashdollar, K.L., 2000. Flammability limit measurements for dusts in 20-L and 1-m3 vessels. J. Loss Prev. Process Ind. 13, 209–219.

Goroshin, S., Tang, F.-D., Higgins, A.J., Lee, J.H.S., 2011. Laminar dust flames in a reduced-gravity environment. Acta Astronaut. 68, 656–666.

Grewer, T., 1991. The influence of chemical structure on exothermic decomposition. Thermochim. Acta 187, 133–149.

Griffith, A.A., 1921. The phenomena of rupture and flow in solids. Phil Trans R Soc Lond A 221, 163–198.

Gülder, Ö.L., 1991. Turbulent premixed flame propagation models for different combustion regimes. Symp. Int. Combust., Twenty-Third Symposium (International) on Combustion 23, 743–750.

Gustin, J.-L., 2004. Risques d'explosion de poussières - Caractérisation. Tech. Ing. Risques Explos. base documentaire : TIB157DUO.

Haghiri, A., Bidabadi, M., 2010. Modeling of laminar flame propagation through organic dust cloud with thermal radiation effect. Int. J. Therm. Sci. 49, 1446–1456.

Halter, F., 2005. Caractérisation des effets de l'ajout d'hydrogène et de la haute pression dans les flammes turbulentes de prémélange méthane/air (PhD Thesis). Université d'Orléans.

Harris, M.L., Sapko, M.J., Zlochower, I.A., Perera, I.E., Weiss, E.S., 2015. Particle size and surface area effects on explosibility using a 20-L chamber. J. Loss Prev. Process Ind. 37, 33–38.

Harris, R.J., 1983. The investigation and control of gas explosions in buildings and heating plant. E. & F.N. Spon in association with the British Gas Corp.

Hartley, P.A., Parfitt, G.D., Pollack, L.B., 1985. The role of the van der Waals force in the agglomeration of powders containing submicron particles. Powder Technol. 42, 35–46.

Hatakeyama, T., Nakamura, K., Hatakeyama, H., 1982. Studies on heat capacity of cellulose and lignin by differential scanning calorimetry. Polymer 23, 1801–1804.

Henry, F., 2013. Dynamique des systèmes nanodispersés: Application au cas de l'agglomération de nanoparticules (PhD Thesis). Université de Lorraine.

Hertzberg, M., Zlochower, A., Conti, R.S., Cashdollar, K.L., 1988. Thermokinetic transport control and structural microscopic realities in coal and polymer pyrolysis and devolatilization: their dominant role in dust explosions. Prepr Pap Am Chem Soc Div Fuel Chem U. S. 32:3.

Holbrow, P., Wall, M., Sanderson, E., Bennett, D., Rattigan, W., Bettis, R., Gregory, D., 2010. Fire and explosion properties of nanopowders.

Hong, S.-H., Winter, J., 2006. Size dependence of optical properties and internal structure of plasma grown carbonaceous nanoparticles studied by *in situ* Rayleigh-Mie scattering ellipsometry. J. Appl. Phys. 100, 064303.

Huang, Y., Risha, G.A., Yang, V., Yetter, R.A., 2007. Combustion of bimodal nano/micron-sized aluminum particle dust in air. Proc. Combust. Inst. 31, 2001–2009.

IEC 1241-2-1, 1994. Electrical apparatus for use in the presence of combustible dust - Part 2: Test methods - Section 1: Methods for determining the minimum ignition temperatures of dust.

IEC 60529, 2001. Degrés de protection procurés par les enveloppes (Code IP) = Degrees of protection provided by enclosures (IP Code). International Electrotechnical Commission, Geneva, Switzerland.

References

IEC TS 60079-32-1:2013+A1:2017, n.d. Explosive atmospheres - Part 32-1: Electrostatic hazards, guidance.

Iqbal, P., Preece, J.A., Mendes, P.M., 2012. Nanotechnology: The “Top-Down” and “Bottom-Up” Approaches. In: Supramolecular Chemistry. American Cancer Society.

ISO 6184/1, 1985. Explosion protection systems — part 1: Determination of explosion indices of combustible dusts in air. In: International Standards Organization. pp. 1–5.

ISO/IEC 80079-20-2, 2016. Explosive atmospheres — Part 20-2: Material characteristics — Combustible dusts test methods.

ISO/TS 80004-2, 2015. Nanotechnologies - Vocabulary - Part 2: Nano-objects.

Israelachvili, J.N., 2011. Chapter 13 - Van der Waals Forces between Particles and Surfaces. In: Intermolecular and Surface Forces (Third Edition). Academic Press, San Diego, pp. 253–289.

Ivanov, M.F., Kiverin, A.D., Liberman, M.A., 2015. Influence of radiation absorption by microparticles on the flame velocity and combustion regimes. J. Exp. Theor. Phys. 121, 166–178.

Jacobson, M., Cooper, A.R., Nagy, J., 1964. Explosibility of metal powders. DTIC Document.

Janes, A., Chaineaux, J., Carson, D., Le Lore, P.A., 2008. MIKE 3 versus HARTMANN apparatus: Comparison of measured minimum ignition energy (MIE). J. Hazard. Mater. 152, 32–39.

Janes, A., Lesné, P., Mauguen, G., Petit, J.M., Sallé, B., Marc, F., 2011. Mise en oeuvre de la réglementation relative aux atmosphères explosives (ATEX) - Brochure INRS, ED 945.

Jespen, T., 2016. ATEX—Explosive Atmospheres, Springer Series in Reliability Engineering. Springer International Publishing, Cham.

Jiang, K., Pinchuk, P., 2016. Temperature and size-dependent Hamaker constants for metal nanoparticles. Nanotechnology 27, 345710.

Jones, W.P., Lindstedt, R.P., 1988. Global reaction schemes for hydrocarbon combustion. Combust. Flame 73, 233–249.

Joulin, G., Clavin, P., 1979. Linear stability analysis of nonadiabatic flames: Diffusional-thermal model. Combust. Flame 35, 139–153.

Julien, P., Whiteley, S., Soo, M., Goroshin, S., Frost, D.L., Bergthorson, J.M., 2017. Flame speed measurements in aluminum suspensions using a counterflow burner. Proc. Combust. Inst. 36, 2291–2298.

Kalejaiye, O., Amyotte, P.R., Pegg, M.J., Cashdollar, K.L., 2010. Effectiveness of dust dispersion in the 20-L Siwek chamber. J. Loss Prev. Process Ind. 23, 46–59.

Karlovitz, B., Denniston, D.W., Wells, F.E., 1951. Investigation of Turbulent Flames. J. Chem. Phys. 19, 541–547.

Kee, R.J., Grcar, J.F., Smooke, M.D., Miller, J.A., Meeks, E., 1993. PREMIX: A FORTRAN Program for Modeling Steady Laminar One-Dimensional Premixed Flames.

Kendall, K., 1988. Agglomerate Strength. Powder Metall. 31, 28–31.

Keng, E.Y.H., 1969. Air and belium pycnometer. Powder Technol. 3, 179–180.

Khalili, I., Dufaud, O., Poupeau, M., Cuervo-Rodriguez, N., Perrin, L., 2012. Ignition sensitivity of gas–vapor/dust hybrid mixtures. Powder Technol. 217, 199–206.

Khan, F.I., Amyotte, P.R., 2003. How to Make Inherent Safety Practice a Reality. Can. J. Chem. Eng. 81, 2–16.

References

Klippel, A., Scheid, M., Krause, U., 2013. Investigations into the influence of dustiness on dust explosions. J. Loss Prev. Process Ind. 26, 1616–1626.

Klippel, A., Schmidt, M., Krause, U., 2015. Dustiness in workplace safety and explosion protection – Review and outlook. J. Loss Prev. Process Ind. 34, 22–29.

Krause, U., Kasch, T., 2000. The influence of flow and turbulence on flame propagation through dust-air mixtures. J. Loss Prev. Process Ind. 13, 291–298.

Krietsch, A., Romahn, T.-M., Scheid, M., Krause, U., 2013. Modified setup of 20-l-sphere for the determination of safety characteristics of nano powders. Chem. Eng. Trans. 805–810.

Krietsch, A., Scheid, M., Schmidt, M., Krause, U., 2015. Explosion behaviour of metallic nano powders. J. Loss Prev. Process Ind. 36, 237–243.

Kuai, N., Huang, W., Du, B., Yuan, J., Li, Z., Gan, Y., Tan, J., 2012. Effect of ignition energy on dust explosion behavior: Phenomena of under-driving and over-driving. AIChE Annu. Meet. Conf. Proc. 8 p.

Kwon, Y.-S., Gromov, A.A., Ilyin, A.P., Popenko, E.M., Rim, G.-H., 2003. The mechanism of combustion of superfine aluminum powders. Combust. Flame 133, 385–391.

Law, C.K., 2006. Combustion Physics by Chung K. Law. Camb. Core.

Le, H.D., 2018. Modelling of nanoparticles-laden jet from a conveying pipe leakage (PhD Thesis). Université de Toulouse, France.

Leason, D.B., 1951. Turbulence and flame propagation in premixed gases. Fuel 30, 233–239.

Lee, J., Peraldi, O., Knystautas, R., 1993. Microgravity combustion of dust suspension. In: 31st Aerospace Sciences Meeting. Presented at the 31st Aerospace Sciences Meeting, American Institute of Aeronautics and Astronautics, Reno,NV,U.S.A.

Lemkowitz, S.M., Pasman, H.J., 2014. A Review of the Fire and Explosion Hazards of Particulates. KONA Powder Part. J. 31, 53–81.

Levitas, V.I., 2013. Mechanochemical mechanism for reaction of aluminium nano- and micrometre-scale particles. Phil Trans R Soc A 371, 20120215.

Lewis, B., von Elbe, G., 1987. Combustion, Flames and Explosions of Gases. Elsevier.

Li, D., Sun, G., 2007. Coloration of textiles with self-dispersible carbon black nanoparticles. Dyes Pigments 72, 144–149.

Li, G., Yang, H.-X., Yuan, C.-M., Eckhoff, R.K., 2016. A catastrophic aluminium-alloy dust explosion in China. J. Loss Prev. Process Ind. 39, 121–130.

Liden, G., 2006. Dustiness Testing of Materials Handled at Workplaces. Ann. Occup. Hyg.

Lin, N., Dufresne, A., 2014. Nanocellulose in biomedicine: Current status and future prospect. Eur. Polym. J. 59, 302–325.

Lomba, R., 2016. Utilisation de la combustion métallique dans les machines thermiques (thesis). Orléans.

Lomba, R., Laboureur, P., Dumand, C., Chauveau, C., Halter, F., 2019. Determination of aluminum-air burning velocities using PIV and Laser sheet tomography. Proc. Combust. Inst. 37, 3143–3150.

Loryan, V.É., Borovinskaya, I.P., 2003. Aluminum Combustion in Nitrogen. Combust. Explos. Shock Waves 39, 525–533.

Lüttgens, G., Lüttgens, S., Schubert, W., 2017. Static Electricity: Understanding, Controlling, Applying | Wiley. Wiley-VCH.

References

Mallard, E., Chatelier, H.L., 1883. Recherches expérimentales et théoriques sur la combustion des mélanges gazeux explosives. H.Dunod et E. Pinat.

Markstein, G.H., 1964. Non-steady flame Propagation. P22 Pergarmon N. Y.

Mandelbrot, B., 1983. The Fractal Geometry of Nature. In: American Journal of Physics. p. 468

Marmo, L., Ferri, A., Danzi, E., 2019. Dust explosion hazard in the textile industry. J. Loss Prev. Process Ind. 62, 103935.

Martin, C., Comet, M., Schnell, F., Berthe, J.-E., Spitzer, D., 2018. Aluminum nanopowder: A substance to be handled with care. J. Hazard. Mater. 342, 347–352.

Mazumdar, A., 2013. Principles and Techniques of Schlieren Imaging Systems.

McBride, B.J., Gordon, S., 1996. Computer Program for Calculation of Complex Chemical Equilibrium Compositions and Applications II. Users Manual and Program Description. NASA. RP 1311.

Médout-Marère, V., 2000. A Simple Experimental Way of Measuring the Hamaker Constant A11 of Divided Solids by Immersion Calorimetry in Apolar Liquids. J. Colloid Interface Sci. 228, 434–437.

Miao, J., Leung, C.W., Huang, Z., Cheung, C.S., Yu, H., Xie, Y., 2014. Laminar burning velocities, Markstein lengths, and flame thickness of liquefied petroleum gas with hydrogen enrichment. Int. J. Hydrog. Energy 39, 13020–13030.

Mittal, M., 2014. Explosion characteristics of micron- and nano-size magnesium powders. J. Loss Prev. Process Ind. 27, 55–64.

Mohan, S., Ermoline, A., Dreizin, E.L., 2012. Pyrophoricity of nano-sized aluminum particles. J. Nanoparticle Res. 14, 723.

Mohan, S., Trunov, M.A., Dreizin, E.L., 2009. On possibility of vapor-phase combustion for fine aluminum particles. Combust. Flame 156, 2213–2216.

Mollenhauer, K., Tschöke, H., 2010. Handbook of Diesel Engines. Springer Science & Business Media.

Moosmüller, H., Arnott, W.P., 2009. Particle Optics in the Rayleigh Regime. J. Air Waste Manag. Assoc. 59, 1028–1031.

Moser, G., 2019. Combustion de particules métalliques pour la production d'énergie à faible impact environnemental.

Moussa, R.B., Guessasma, M., Proust, C., Saleh, K., Fortin, J., 2015. Thermal Radiation Contribution to Metal Dust Explosions. Procedia Eng., New Paradigm of Particle Science and Technology Proceedings of The 7th World Congress on Particle Technology 102, 714–721.

Mukhopadhyay, S.N., Das, D.K., 1994. Oxygen Responses, Reactivities, and Measurements in Biosystems. CRC Press.

Murillo, C., 2016. Experimental and numerical approaches to particles dispersion in a turbulent flow : application to dust explosions (PhD Thesis). Université de Lorraine, France.

Murillo, C., Amín, M., Bardin-Monnier, N., Muñoz, F., Pinilla, A., Ratkovich, N., Torrado, D., Vizcaya, D., Dufaud, O., 2018. Proposal of a new injection nozzle to improve the experimental reproducibility of dust explosion tests. Powder Technol. 328, 54–74.

Nagy, J., Verakis, H.C., 1983. Development and control of dust explosions.

Nanomakers, 2019. Nanomakers | Producer of Silicon and Silicon Carbide nanopowders [WWW Document]. Nanomakers Prod. Silicon Silicon Carbide Nanopowders. URL https://www.nanomakers.co (accessed 1.7.20).

References

Nazneen, N., Wang, Q., 2019. Evaluation of fire and explosion hazard of nanoparticles (NFPA report No. FPRF-2019-10). The Fire Protection Research Foundation.

Nichols, G., Byard, S., Bloxham, M.J., Botterill, J., Dawson, N.J., Dennis, A., Diart, V., North, N.C., Sherwood, J.D., 2002. A Review of the Terms Agglomerate and Aggregate with a Recommendation for Nomenclature Used in Powder and Particle Characterization. J. Pharm. Sci. 91, 2103–2109.

Nifuku, M., Koyanaka, S., Ohya, H., Barre, C., Hatori, M., Fujiwara, S., Horiguchi, S., Sochet, I., 2007. Ignitability characteristics of aluminium and magnesium dusts that are generated during the shredding of post-consumer wastes. J. Loss Prev. Process Ind. 20, 322–329.

Nowakowska, M., Herbinet, O., Dufour, A., Glaude, P.A., 2018. Kinetic Study of the Pyrolysis and Oxidation of Guaiacol. J. Phys. Chem. A 122, 7894–7909.

Oberdörster, G., Oberdörster, E., Oberdörster, J., 2005. Nanotoxicology: an emerging discipline evolving from studies of ultrafine particles. Environ. Health Perspect. 113, 823–839.

Palmer, K.N., 1973. Dust explosions and fires, Powder technology series. Chapman & Hall, London.

Pietraccini, M., Delon, E., Santandrea, A., Pacault, S., Glaude, P.-A., Dufour, A., Dufaud, O., 2020. Determination of reaction mechanisms for the gasification and explosion of organic powders. Submitt. 13th Int. Symp. Hazards Prev. Mitig. Ind. Explos. ISHPMIE.

Poinsot, T., Veynante, D., 2005. Theoretical and numerical combustion, 2nd ed. ed. Edwards, Philadelphia.

Popat, N.R., Catlin, C.A., Arntzen, B.J., Lindstedt, R.P., Hjertager, B.H., Solberg, T., Saeter, O., Van den Berg, A.C., 1996. Investigations to improve and assess the accuracy of computational fluid dynamic based explosion models. J. Hazard. Mater. 45, 1–25.

Proust, C., 2005. The usefulness of phenomenological tools to simulate the consequences of dust explosions. The experience of EFFEX (International ESMG Symposium “Process safety and industrial explosion protection”). Nuremberg, Germany.

Proust, C., 2006. Flame propagation and combustion in some dust-air mixtures. J. Loss Prev. Process Ind. 19, 89–100.

Proust, C., Ben Moussa, R., Guessasma, M., Saleh, K., Fortin, J., 2017. Thermal radiation in dust flame propagation. J. Loss Prev. Process Ind. 49, 896–904.

Proust, Ch., Accorsi, A., Dupont, L., 2007. Measuring the violence of dust explosions with the “20l sphere” and with the standard “ISO 1m3 vessel”: Systematic comparison and analysis of the discrepancies. J. Loss Prev. Process Ind., Selected Papers Presented at the Sixth International Symposium on Hazards, Prevention and Mitigation of Industrial Explosions 20, 599–606.

Przybyla, G., Ziolkowski, L., Szlęk, A., 2008. Performance of SI engine fuelled with LCV gas. Pol. Inst. Therm. Technol.

Pu, Y., Podfilipski, J., Jarosiński, J., 1998. Constant Volume Combustion of Aluminum and Cornstarch Dust in Microgravity. Combust. Sci. Technol. 135, 255–267.

Pu, Y.K., Jarosinski, J., Johnson, V.G., Kauffman, C.W., 1991. Turbulence effects on dust explosions in the 20-liter spherical vessel. Symp. Int. Combust., Twenty-Third Symposium (International) on Combustion 23, 843–849.

Rai, A., Park, K., Zhou, L., Zachariah, M.R., 2006. Understanding the mechanism of aluminium nanoparticle oxidation. Combust. Theory Model. 10, 843–859.

References

Rauscher, H., Mech, A., Gaillard, C., Stintz, M., Wohlleben, W., Weiler, S., Ghanem, A., Hodoroaba, D., Babick, F., Mielke, J., 2015. Recommendations on a Revision of the EC Definition of Nanomaterial Based on Analytical Possibilities (No. NanoDefine Technical Report D7.10), The EU FP7 NanoDefine Project. The NanoDefine Consortium.

Rauscher, H., Mech, A., Gibson, N., Gilliland, D., Held, A., Kestens, V., Koeber, R., Linsinger, T.P.J., Stefaniak, E.A., European Commission, Joint Research Centre, 2019a. Identification of nanomaterials through measurements: points to consider in the assessment of particulate materials according to the European Commission's Recommendation on a definition of nanomaterial.

Reynolds, G.K., Fu, J.S., Cheong, Y.S., Hounslow, M.J., Salman, A.D., 2005. Breakage in granulation: A review. Chem. Eng. Sci., Granulation across the length scales - 2nd International Workshop on Granulation 60, 3969–3992.

Roebben, G., Rauscher, H., Amenta, V., Aschberger, K., Boix Sanfeliu, A., Calzolai, L., Emons, H., Gaillard, C., Gibson, N., Holzwarth, U., Koeber, R., Linsinger, T., Rasmussen, K., Sokull-Klüttgen, B., Stamm, H., 2014. Towards a review of the EC Recommendation for a definition of the term "nanomaterial". JRC Science and policy reports, Report EUR 26744 EN.

Rotureau, P., Fayet, G., Marlair, G., Michot, C., Joubert, L., Adamo, C., 2010. Evaluation of chemicals explosive properties: from classical experimental methods to predictive methods combining statistical QSPR methodology and quantum chemistry. Actual. Chim. 51–58.

Rumpf, H., 1962. The strength of granules and agglomerates. In: Agglomeration. pp. 379–413.

Saeed, M.A., Farooq, M., Andrews, G.E., Phylaktou, H.N., Gibbs, B.M., 2019. Ignition sensitivity of different compositional wood pellets and particle size dependence. J. Environ. Manage. 232, 789–795.

Sanchirico, R., Di Sarli, V., Russo, P., Di Benedetto, A., 2015. Effect of the nozzle type on the integrity of dust particles in standard explosion tests. Powder Technol. 279, 203–208.

Santandrea, A., Bonamis, F., Pacault, S., Vignes, A., Perrin, L., Dufaud, O., 2019a. Influence of the Particle Size Distribution on Dust Explosion: How to Choose the Right Metrics? Chem. Eng. Trans. 77, 667–672.

Santandrea, A., Pacault, S., Perrin, L., Vignes, A., Dufaud, O., 2019b. Nanopowders explosion: Influence of the dispersion characteristics. J. Loss Prev. Process Ind.

Santandrea, A., Vignes, A., Krietsch, A., Perrin, L., Laurent, A., Dufaud, O., 2019c. Some Key Considerations when Evaluating Explosion Severity of Nanopowders. Chem. Eng. Trans. 77, 235–240.

Santandrea, A., Gavard, M., Pacault, S., Vignes, A., Perrin, L., Dufaud, O., 2020a. 'Knock on nanocellulose': Approaching the laminar burning velocity of powder-air flames. Process Saf. Environ. Prot. 134, 247–259.

Santandrea, A., Torrado, D., Pietraccini, M., Vignes, A., Perrin, L., Dufaud, O., 2020b. A flame propagation model for nanopowders. Submitt. 13th Int. Symp. Hazards Prev. Mitig. Ind. Explos. ISHPMIE.

Santandrea, A., Vignes, A., Krietsch, A., Brunello, D., Perrin, L., Laurent, A., Dufaud, O., 2020c. Evaluating the explosion severity of nanopowders: international standards versus reality. Process Saf. Environ. Prot. To be published.

References

Seville, J.P.K., Willett, C.D., Knight, P.C., 2000. Interparticle forces in fluidisation: a review. Powder Technol., Neptis Symposium on Fluidization- Present and Future 113, 261–268.

Shelkin, K.I., 1947. On Combustion in a Turbulent Flow [WWW Document]. J. Tech. Phys. Vol. 13 No 9-10. URL https://digital.library.unt.edu/ark:/67531/metadc64298/ (accessed 10.16.19).

Shi, Z., Phillips, G.O., Yang, G., 2013. Nanocellulose electroconductive composites. Nanoscale 5, 3194–3201.

Shkolnikov, E.I., Zhuk, A.Z., Vlaskin, M.S., 2011. Aluminum as energy carrier: Feasibility analysis and current technologies overview. Renew. Sustain. Energy Rev. 15, 4611–4623.

Silvestrini, M., Genova, B., Leon Trujillo, F.J., 2008. Correlations for flame speed and explosion overpressure of dust clouds inside industrial enclosures. J. Loss Prev. Process Ind. 21, 374–392.

Siwek, R., 1977. 20-l Laborapparatur für die Bestimmung der Explosionskenngrößen brennbarer Stäube (PhD Thesis). Technical University of Winterthur, Winterthur, Switzerland.

Siwek, R., 1995. Siwek 1995 Ignition behavior of dusts : meaning and interpretation.

Siwek, R., 1996. Determination of technical safety indices and factors influencing hazard evaluation of dusts. J. Loss Prev. Process Ind. 9, 21–31.

Skjold, T., 2003. Selected aspects of turbulence and combustion in 20-Litre explosion vessel (Master thesis). University of Bergen, Norway.

Skjold, T., 2007. Review of the DESC project. J. Loss Prev. Process Ind., Selected Papers Presented at the Sixth International Symposium on Hazards, Prevention and Mitigation of Industrial Explosions 20, 291–302.

Skjold, T., Hisken, H., Lakshmipathy, S., Atanga, G., Carcassi, M., Schiavetti, M., Stewart, J.R., Newton, A., Hoyes, J.R., Tolias, I.C., Venetsanos, A.G., Hansen, O.R., Geng, J., Huser, A., Helland, S., Jambut, R., Ren, K., Kotchourko, A., Jordan, T., Daubech, J., Lecocq, G., Hanssen, A.G., Kumar, C., Krumenacker, L., Jallais, S., Miller, D., Bauwens, C.R., 2018. Blind-prediction: Estimating the consequences of vented hydrogen deflagrations for homogeneous mixtures in 20-foot ISO containers. Int. J. Hydrog. Energy.

Smith, W.O., Foote, P.D., Busang, P.F., 1929. Packing of Homogeneous Spheres. Phys. Rev. 34, 1271–1274.

Soares, M.C.F., Viana, M.M., Schaefer, Z.L., Gangoli, V.S., Cheng, Y., Caliman, V., Wong, M.S., Silva, G.G., 2014. Surface modification of carbon black nanoparticles by dodecylamine: Thermal stability and phase transfer in brine medium. Carbon 72, 287–295.

Sokolov, S.V., Tschulik, K., Batchelor-McAuley, C., Jurkschat, K., Compton, R.G., 2015. Reversible or not? Distinguishing agglomeration and aggregation at the nanoscale. Anal. Chem. 87, 10033–10039.

Sorensen, C.M., Roberts, G.C., 1997. The Prefactor of Fractal Aggregates. J. Colloid Interface Sci. 186, 447–452.

Soundararajan, R., Amyotte, P.R., Pegg, M.J., 1996. Explosibility hazard of iron sulphide dusts as a function of particle size. J. Hazard. Mater. 51, 225–239.

References

Stark, W.J., Stoessel, P.R., Wohlleben, W., Hafner, A., 2015. Industrial applications of nanoparticles. Chem. Soc. Rev. 44, 5793–5805.

Sundaram, D.S., Puri, P., Yang, V., 2013. Pyrophoricity of nascent and passivated aluminum particles at nano-scales. Combust. Flame 160, 1870–1875.

Sundaram, D.S., Puri, P., Yang, V., 2016. A general theory of ignition and combustion of nano- and micron-sized aluminum particles. Combust. Flame 169, 94–109.

Tamanini, F., 1990. Turbulence effects on dust explosion venting. PlantOperations Prog. 9, 52–60.

Tanford, C., Pease, R.N., 1947. Theory of Burning Velocity. II. The Square Root Law for Burning Velocity. J. Chem. Phys. 15, 861–865.

Tang, F.-D., Goroshin, S., Higgins, A., Lee, J., 2009. Flame propagation and quenching in iron dust clouds. Proc. Combust. Inst. 32, 1905–1912.

Tascón, A., 2018. Influence of particle size distribution skewness on dust explosibility. Powder Technol. 338, 438–445.

Taylor, G.I., 1922. Diffusion by Continuous Movements. Proc. Lond. Math. Soc. s2-20, 196–212.

Theimer, O.F., 1973. Cause and prevention of dust explosions in grain elevators and flour mills. Powder Technol. 8, 137–147.

Thomas, A., Vignes, A., Le-Bihan, O., Santandrea, A., 2019. Quelques considérations sur la pulvérulence d'une poudre et les risques d'explosion associés. Presented at the SFGP 2019, Nantes.

Thompson, D.T., 2007. Using gold nanoparticles for catalysis. Nano Today 2, 40–43.

Tolias, I.C., Venetsanos, A.G., 2018. An improved CFD model for vented deflagration simulations – Analysis of a medium-scale hydrogen experiment. Int. J. Hydrog. Energy 43, 23568–23584.

Torrado, D., 2017. Effect of carbon black nanoparticles on the explosion severity of gas mixtures (PhD Thesis). Université de Lorraine, France.

Torrado, D., Buitrago, V., Glaude, P.-A., Dufaud, O., 2017a. Explosions of methane/air/nanoparticles mixtures: Comparison between carbon black and inert particles. Process Saf. Environ. Prot. 110, 77–88.

Torrado, D., Cuervo, N., Pacault, S., Glaude, P.-A., Dufaud, O., 2017b. Influence of carbon black nanoparticles on the front flame velocity of methane/air explosions. J. Loss Prev. Process Ind. 49, 919–928.

Torrado, D., Pinilla, A., Amin, M., Murillo, C., Munoz, F., Glaude, P.-A., Dufaud, O., 2018. Numerical study of the influence of particle reaction and radiative heat transfer on the flame velocity of gas/nanoparticles hybrid mixtures. Process Saf. Environ. Prot. 118, 211–226.

Traoré, M., Dufaud, O., Perrin, L., Chazelet, S., Thomas, D., 2009a. Dust explosions: How should the influence of humidity be taken into account? Process Saf. Environ. Prot., 12th International Symposium of Loss Prevention and Safety Promotion in the Process Industries 87, 14–20.

Turkevich, L.A., Dastidar, A.G., Hachmeister, Z., Lim, M., 2015. Potential explosion hazard of carbonaceous nanoparticles: Explosion parameters of selected materials. J. Hazard. Mater. 295, 97–103.

References

Turkevich, L.A., Fernback, J., Dastidar, A.G., Osterberg, P., 2016. Potential explosion hazard of carbonaceous nanoparticles: screening of allotropes. Combust. Flame 167, 218–227.

TÜV SÜD Schweiz AG, 2020. 20l Siwek sphere / Mike 3 [WWW Document]. URL https://www.tuev-sued.ch/ch-en/activity/testing-equipment/20l-siwek-sphere-mike-3 (accessed 3.9.20).

Upp, E.L., LaNasa, P.J., 2002. Fluid flow measurement: a practical guide to accurate flow measurement, 2nd ed. ed. Gulf Professional Pub, Boston.

U.S. Chemical Safety and Hazard Investigation Boart, 2009. Investigation report: sugar dust explosion and fire (14 killed, 36 injured), Imperial Sugar Company, Port Wentworth, Georgia, February 7, 2008 (No. 2008-05-I-GA). Washington, DC.

van der Wel, P.G.J., 1993. Ignition and propagation of dust explosions (PhD Thesis). Delft University, The Netherlands.

van der Wel, P.G.J., van Veen, J.P.W., Lemkowitz, S.M., Scarlett, B., van Wingerden, C.J.M., 1992. An interpretation of dust explosion phenomena on the basis of time scales. Powder Technol. 71, 207–215.

Varea, E., 2013. Experimental analysis of laminar spherically expanding flames (thesis). Rouen, INSA.

Vignes, A., 2008. Évaluation de l'inflammabilité et de l'explosivité des nanopoudres : une démarche essentielle pour la maîtrise des risques (PhD Thesis). Institut National Polytechnique de Lorraine, France.

Vignes, A., Muñoz, F., Bouillard, J., Dufaud, O., Perrin, L., Laurent, A., Thomas, D., 2012. Risk assessment of the ignitability and explosivity of aluminum nanopowders. Process Saf. Environ. Prot. 90, 304–310.

Vignes, A., Krietsch, A., Dufaud, O., Santandréa, A., Perrin, L., Bouillard, J., 2019. Course of explosion behaviour of metallic powders – From micron to nanosize. J. Hazard. Mater. 379, 120767.

Vijayaraghavan, G., 2004. Impact assessment, modelling, and control of dust explosions in chemical process industries (MTech Thesis). Department of Chemical Engineering, Coimbatore Institute of Technology.

Vizcaya, D., Pinilla, A., Amín, M., Ratkovich, N., Munoz, F., Murillo, C., Bardin-Monnier, N., Dufaud, O., 2018. CFD as an approach to understand flammable dust 20 L standard test: Effect of the ignition time on the fluid flow. AIChE J. 64, 42–54.

Wagman, D.D., Kilpatrick, J.E., Taylor, W.J., Pitzer, K.S., Rossini, F.D., 1945. Heats, free energies, and equilibrium constants of some reactions involving O2, H2, H2O, C, CO, CO2, and CH4. J. Res. Natl. Bur. Stand. 34, 143.

Walter, D., 2013. Primary Particles - Agglomerates - Aggregates. In: Deutsche Forschungsgemeinschaft DFG (Ed.), Nanomaterials. Wiley-VCH Verlag GmbH & Co. KGaA, Weinheim, Germany, pp. 9–24.

Weiler, C., Wolkenhauer, M., Trunk, M., Langguth, P., 2010. New model describing the total dispersion of dry powder agglomerates. Powder Technol. 203, 248–253.

Wengeler, R., Nirschl, H., 2007. Turbulent hydrodynamic stress induced dispersion and fragmentation of nanoscale agglomerates. J. Colloid Interface Sci. 306, 262–273.

Wohlleben, W., Mielke, J., Bianchin, A., Ghanem, A., Freiberger, H., Rauscher, H., Gemeinert, M., Hodoroaba, V.-D., 2017. Reliable nanomaterial classification of powders using the volume-specific surface area method. J. Nanoparticle Res. 19.

References

Wu, H.-C., Chang, R.-C., Hsiao, H.-C., 2009. Research of minimum ignition energy for nano Titanium powder and nano Iron powder. J. Loss Prev. Process Ind. 22, 21–24.

Wu, H.-C., Kuo, Y.-C., Wang, Y., Wu, C.-W., Hsiao, H.-C., 2010a. Study on safe air transporting velocity of nanograde aluminum, iron, and titanium. J. Loss Prev. Process Ind. 23, 308–311.

Wu, H.-C., Ou, H.-J., Hsiao, H.-C., Shih, T.-S., 2010b. Explosion Characteristics of Aluminum Nanopowders. Aerosol Air Qual. Res. 10, 38–42.

Wu, H.-C., Ou, H.-J., Peng, D.-J., Hsiao, H.-C., Gau, C.-Y., Shih, T.-S., 2010c. Dust Explosion Characteristics of Agglomerated 35 nm and 100 nm Aluminum Particles. Int. J. Chem. Eng. 2010, 1–6.

Xu, S., Liu, J., Cao, Wei, Li, Y., Cao, Weiguo, 2017. Experimental study on the minimum ignition temperature and combustion kinetics of coal dust/air mixtures. Powder Technol. 317, 154–161.

Yeap, S.P., 2018. Permanent agglomerates in powdered nanoparticles: Formation and future prospects. Powder Technol. 323, 51–59.

Yuan, J., Wei, W., Huang, W., Du, B., Liu, L., Zhu, J., 2014a. Experimental investigations on the roles of moisture in coal dust explosion. J. Taiwan Inst. Chem. Eng. 45, 2325–2333.

Yuan, Z., Khakzad, N., Khan, F., Amyotte, P., 2015. Dust explosions: A threat to the process industries. Process Saf. Environ. Prot. 98, 57–71.

Yuan, Z., Khakzad, N., Khan, F., Amyotte, P., Reniers, G., 2013. Risk-Based Design of Safety Measures To Prevent and Mitigate Dust Explosion Hazards. Ind. Eng. Chem. Res. 52, 18095–18108.

Zalosh, R., 2019. Dust explosions: Regulations, standards, and guidelines. In: Methods in Chemical Process Safety. Elsevier, pp. 229–282.

Zeldovich, Y.B., Barenblatt, G.I., 1959. Theorv of flame propagation. Combust. Flame 3, 61–74.

Zhang, Q., Zhang, B., 2015. Effect of ignition delay on explosion parameters of corn dust/air in confined chamber. J. Loss Prev. Process Ind. 33, 23–28.

Zhang, Z., Ghadiri, M., 2002. Impact attrition of particulate solids. Part 2: Experimental work. Chem. Eng. Sci. 57, 3671–3686.

Zhen, G., Leuckel, W., 1997. Effects of ignitors and turbulence on dust explosions. J. Loss Prev. Process Ind. 10, 317–324.

Zheng, Y.-P., Feng, C.-G., Jing, G.-X., Qian, X.-M., Li, X.-J., Liu, Z.-Yi., Huang, P., 2009. A statistical analysis of coal mine accidents caused by coal dust explosions in China. J. Loss Prev. Process Ind. 22, 528–532.

Par définition, les nanoparticules possèdent au moins une dimension inférieure à 100 nm. Cette petite taille induit une grande surface spécifique, qui procure des propriétés inédites, notamment chimiques, mécaniques, optiques ou biologiques, comparées aux particules micrométriques. Parmi ces nouvelles spécificités, les nanoparticules sont soumises à des forces de cohésion plus intenses, telles que des forces de van der Waals, électrostatiques ou capillaires, ce qui les amène à s'agglomérer de manière réversible. Cependant, une explosion de poussières nécessite une dispersion de la poudre dans l'air, ce qui peut mener à une fragmentation de ces agglomérats. L'objectif de ce travail est ainsi d'étudier l'influence des spécificités des nanoparticules, notamment de l'agglomération, sur leur sensibilité à l'inflammation et leur sévérité d'explosion, et d'évaluer l'adéquation des méthodes définies par les standards internationaux pour la détermination de ces paramètres concernant les nanoparticules.

Chapitre 2 : Généralités sur les explosions de poussières

Ce chapitre présente les premières étapes de l'évaluation des risques d'explosion liés à la production, au transport et à la manipulation de poudres nanométriques, et repose sur une revue bibliographique divisée en quatre parties.

Dans un premier temps, une analyse d'accidents impliquant différents types de poudres a souligné la réalité et la gravité du risque représenté par les explosions de poussières. Les deux directives européennes ATEX ont été introduites : la première, la directive 1999/99/CE classe les espaces de travail en zones selon la probabilité de formation d'une atmosphère explosive. Les équipements autorisés dans ces zones sont alors définis par la seconde directive, la directive 2014/34/UE. L'implémentation de mesures de sécurité pour prévenir et protéger contre les explosions de poussières est alors possible à partir de la connaissance des caractéristiques d'explosivité des poussières impliquées dans les procédés.

Dans une deuxième partie, la phénoménologie des explosions de poussières a été détaillée. D'abord, la distinction entre la sensibilité à l'inflammation, i.e. la probabilité qu'une poussière s'enflamme, et la sévérité d'explosion, qui concerne les effets de l'explosion, a été réalisée. Les paramètres décrivant l'inflammation (énergie minimale d'inflammation, température minimale d'inflammation, concentration minimale explosible) et l'explosion (surpression maximale d'explosion, vitesse maximale de montée en pression, vitesse de flamme) ont ensuite été détaillés, ainsi que les principaux facteurs influents, tels que la concentration en poussière, le taux d'humidité, l'énergie d'inflammation, la turbulence initiale et la taille de particules.

Ce travail se focalisant sur les nanoparticules, la troisième partie de ce chapitre a été dédiée à leurs spécificités. Plus précisément, le phénomène d'agglomération inhérent aux nanomatériaux a été analysé. En effet, les principales forces de cohésion, telles que les forces de van der Waals, électrostatiques et capillaires ont été détaillées, ainsi que les trois principaux modèles décrivant la fragmentation d'un agglomérat.

Enfin, l'influence des spécificités des nanoparticules sur le déroulement de leur combustion a été discutée. Certains auteurs ont observé que la sensibilité à l'inflammation tend à croître en

diminuant la taille de particules tandis que la sévérité d'explosion se stabilise (Vignes et al., 2019). Ce plateau peut être expliqué par l'agglomération des nanoparticules, qui présentent alors une sévérité d'explosion similaires aux microparticules. La transition d'une limitation diffusionnelle pour de grosses particules vers une limitation réactionnelle pour de petites particules a également été démontrée (Bouillard et al., 2010). Cette transition a été obtenue vers 10 à 100 µm pour des composés carbonés (Di Benedetto et al., 2010), vers 30 µm pour des composés organiques (Eckhoff, 2003) et vers 10 µm pour des particules métalliques (Glorian et al., 2016). Pour ces dernières, un comportement pyrophorique a également été mentionné, donnant lieu à une inflammation spontanée lors d'une exposition à l'air (Krietsch et al., 2015). De plus, en diminuant la taille de particules jusqu'à l'échelle nanométrique, la transition d'une diffusion de Mie vers une diffusion de Rayleigh induit des différences dans le transfert radiatif par rapport aux microparticules, impactant probablement la validité de la loi cubique.

Chapitre 3 : Caractérisation de la poudre et du nuage

Ce chapitre est dédié à la caractérisation des poudres et des nuages associés et divisé en trois parties.

D'abord, une présentation des poudres considérées dans ce travail a été réalisée : nanocellulose, noirs de carbone, silicium enrobé de carbone et deux poudres d'aluminium. Une méthode de classification basée sur le calcul d'une surface spécifique volumique couplée à une analyse d'image a été appliquée pour vérifier que les poudres peuvent être considérées comme des nanomatériaux selon la définition de la Commission Européenne. A l'exception de la nanocellulose, pour laquelle des tests complémentaires ont été réalisés par la suite, toutes les poudres étudiées sont classifiées en tant que nanomatériaux. Des mesures de distribution de tailles de particules (DTP) ont été réalisées en voie liquide, ce qui est pratique mais d'un intérêt limité quand il s'agit de tester des poudres dispersées dans l'air, ainsi que par sédimentation en voie sèche afin d'estimer la DTP des agglomérats soumis à un faible cisaillement. La présence de micro-agglomérats constitués de nanoparticules a alors été mise en avant.

Puisqu'une explosion de poussière nécessite la dispersion de la poudre, des mesures de DTP ont également été conduites après dispersion. D'abord, la pulvérulence du noir de carbone et de la nanocellulose a été mesurée, démontrant la capacité des deux poudres à émettre des nanoparticules. Des mesures de DTP ont été réalisées à l'aide d'un Fast Mobility Particle Sizer (FMPS) et d'un Scanning Mobility Particle Sizer (SMPS) et ont démontré la présence de nanoparticules jusqu'à deux minutes après dispersion. Des essais de dispersion ont aussi été conduits à l'aide d'un disperseur Scirocco et ont montré la fragmentation des agglomérats lors de la dispersion. Enfin, un granulomètre à diffraction laser couplé à une sphère de visualisation de 20L ont permis une estimation in situ de la DTP dans la chambre de combustion, au moment et à l'endroit de l'inflammation. Une différence nette est alors apparue entre les diamètres moyens mesurés par sédimentation et les diamètres mesurés après dispersion, à cause du fort cisaillement induit par le processus de dispersion. Le nuage est ainsi constitué de nano- et de micro-agglomérats. Ainsi, la considération de la DTP avant dispersion, mais aussi après

injection dans l'enceinte est essentielle lors de l'évaluation de la sévérité d'explosion des nanoparticules afin de savoir exactement ce qui explose. L'évolution du niveau de turbulence avec le temps après dispersion de la poudre dans la sphère de 20L a également été évaluée par Particle Image Velocimetry (PIV). Le délai d'inflammation préconisé par les standards internationaux se situant dans une zone de transition, une faible variation dans ce délai peut fortement modifier le niveau de turbulence, et ainsi la sévérité d'explosion de la poudre.

Cependant, la caractérisation visuelle du nuage de poussières ne peut être systématiquement effectuée à cause de l'opacité de la sphère standard et d'une limitation technique : actuellement, aucun appareil ne permet la mesure de nanoparticules à haute fréquence et forte concentration. Ainsi, une corrélation semi-empirique reliant les conditions opératoires et les caractéristiques de la poudre à un coefficient d'efficacité de fragmentation, défini par le ratio entre le diamètre moyen en surface avant et après dispersion, a été proposée et a montré des résultats encourageants.

Chapitre 4 : Evaluation standard de l'inflammabilité et explosivité

Ce chapitre est dédié à la détermination des paramètres standard de sécurité des poudres et à l'établissement de recommandations concernant ces paramètres.

D'abord, la sensibilité à l'inflammation des poudres a été évaluée par la mesure de l'énergie minimale d'inflammation, la température minimale d'inflammation et la concentration minimale explosible. Après une présentation des méthodes et appareils standards pour la mesure de ces éléments, les valeurs obtenues pour chaque poudre ont été discutées. Il apparait alors que les poudres considérées, à l'exception du noir de carbone, sont particulièrement sensibles comparées aux microparticules, notamment au niveau de l'énergie minimale d'inflammation. En effet, la nanocellulose et le silicium enrobé de carbone montrent des énergies minimales d'inflammation de 16 mJ et 4 mJ respectivement, alors que les deux poudres d'aluminium ont été enflammées par une étincelle de 1 mJ. Des mesures spécifiques pour éviter les décharges électrostatiques, telles qu'une mise à la terre des installations ou du personnel, doit alors être implémentée lors de la manipulation de ces nanopoudres. Les paramètres influençant la sensibilité à l'inflammation d'une poudre ont été détaillés à travers une analyse dimensionnelle décrivant la combustion d'un nuage de particules, mettant notamment en lumière les différentes limitations cinétiques lors de la combustion de micro- et de nanoparticules.

Dans une seconde partie, le protocole pour la mesure des caractéristiques de sévérité d'explosion, i.e. la surpression maximale d'explosion et la vitesse maximale de montée en pression, a été détaillé pour la sphère de 20L, et les valeurs déterminées ont été présentées. Les poudres organiques et carbonées ont alors été classées St1, ce qui traduit une explosivité modérée, tandis que les poudres métalliques, i.e. l'aluminium et le silicium enrobé de carbone, ont mené à des explosions bien plus sévères et ont été classées respectivement St3 et St2.

La dernière partie de ce chapitre se focalise sur les observations liées aux essais expérimentaux et à un questionnement concernant la validité des standards internationaux pour l'évaluation de la sensibilité à l'inflammation et la sévérité d'explosion des nanopoudres. En effet, à cause de leur forte sensibilité à l'inflammation, la pressurisation du réservoir avant l'injection de la poudre dans la sphère de 20L peut être suffisante pour enflammer la poudre avant l'activation des inflammateurs pyrotechniques. En résulte alors une mauvaise estimation de l'évolution de la pression en fonction du temps mesurée dans la chambre de combustion, et peut également endommager le matériel. De plus, la quantité d'énergie nécessaire pour enflammer ces poussières est assez faible (quelques millijoules), tandis que l'énergie d'inflammation standard dans la sphère de 20L est de 10 kJ, ce qui peut mener à un phénomène d'overdriving et influer sur la propagation de la flamme, menant une fois encore à des résultats erronés. Enfin, le fort cisaillement induit par la dispersion dans la sphère de 20L peut fragmenter les agglomérats, impliquant que la distribution de tailles de particules peut être différente avant et après la dispersion, ce qui n'est pas spécifiquement considéré dans les standards internationaux.

Chapitre 5 : Les standards versus la réalité

Les spécificités des nanopoudres (agglomération, propriétés d'adsorption, grande surface spécifique, etc.) induisent un comportement explosif parfois différent de celui observé pour les poudres micrométriques, ou, plus généralement, conduit à des tendances exacerbées. Ce chapitre est donc dédié à mettre en lumière ce genre de tendances à travers six parties et l'exemple de quatre poudres de différentes natures. Par exemple, les améliorations suivantes peuvent être suggérées :

i) Il est important de garder en mémoire que la distribution de tailles de particules (DTP) des poudres nanométriques est modifiée par désagglomération durant la dispersion, même si les techniques de mesures de DTP actuelles ne permettent pas de quantifier ce décalage. La DTP sera préférentiellement exprimée en surface à la place de la distribution volumique.

ii) Des disperseurs alternatifs permettent d'atteindre des valeurs plus élevées de sévérité d'explosion. Puisque l'objectif des standards n'est pas de reproduire les conditions industrielles, et que le disperseur standard ne mène pas systématiquement aux résultats les plus conservatifs, la priorité devrait être donnée à la fiabilité des résultats, notamment en choisissant des disperseurs permettant une meilleure homogénéité du nuage.

iii) La source d'inflammation devrait être adaptée à la faible énergie minimale d'inflammation des poudres nanométriques afin d'éviter un phénomène dit 'd'overdriving', ou, tout du moins, ce phénomène devrait être mieux caractérisé afin d'estimer l'énergie supplémentaire fournie au nuage pour la combustion.

iv) La pré-inflammation des nanopoudres particulièrement sensibles dans le réservoir à poussière peut être évitée par une injection sous azote (mais une inflammation

spontanée peut se produire dans la sphère), ou par simple soulèvement de la poudre, comme pour la détermination de l'énergie minimale d'inflammation. Cependant, du fait de leur vitesse de propagation rapide, le temps d'ouverture de l'électrovanne devrait être réduit afin d'éviter un retour de flamme dans le réservoir à poudres, ou le délai d'inflammation devrait être adapté.

v) Des modifications dans le délai d'inflammation peuvent être utiles afin d'obtenir les résultats les plus conservatifs possibles. Cependant, un niveau de turbulence trop faible (e.g. < 2 $m.s^{-1}$) peut conduire à la ségrégation des agglomérats, tandis qu'un niveau de turbulence trop élevé (e.g. > 6 $m.s^{-1}$) peut mener à des mécanismes de combustion alternatifs.

vi) Une attention particulière doit être porté aux conditions de stockage des nanopoudres et à l'humidité de l'air ambiant et de l'air d'injection. En effet, la présence d'eau peut modifier l'inflammabilité et l'explosivité des poudres en fonction de leur nature et de leur capacité à réagir avec l'eau.

Finalement, les résultats obtenus doivent être extrapolés à l'échelle industrielle, avec les mêmes limitations inhérentes à la loi cubique que celles rencontrées pour les poudres micrométriques. Une approche alternative serait d'utiliser les avantages des nanopoudres, en particulier leur faible vitesse de sédimentation, afin de déterminer leur vitesse laminaire de flamme, qui est un paramètre intrinsèque au mélange poussière/air qui peut être utilisé comme donnée d'entrée pour des codes CFD. Le chapitre suivant est ainsi dédié à l'évaluation de ce paramètre, notamment pour la nanocellulose.

Chapitre 6 : Etude de propagation de flamme

Afin de maîtriser l'influence des conditions opératoires sur les paramètres de sévérité d'explosion, les efforts se sont focalisés sur la détermination de la vitesse laminaire de flamme, un paramètre intrinsèque au mélange poussière-air. Ce chapitre est divisé en trois parties, respectivement dédiées à la détermination expérimentale et numérique de la vitesse laminaire de flamme de la nanocellulose, et à l'application des modèles de vitesses de flamme turbulentes.

Dans la première partie, la vitesse laminaire de flamme de la nanocellulose a été estimée par trois différentes méthodes. Les deux premières consistent en une visualisation directe de la propagation de flamme à faible turbulence dans un tube vertical de 1 m de long et dans une sphère de 20L éventée, couplée à l'application de relations liant la vitesse de la flamme et son étirement, tandis que la troisième méthode repose sur l'utilisation d'une corrélation basée sur l'évolution de la pression en fonction du temps durant un essai standard d'explosion. Ces trois méthodes ont mené à des valeurs similaires de vitesses laminaires de flamme pour la nanocellulose, d'environ 21 $cm.s^{-1}$. Il a notamment été souligné que ces analyses de propagation de flamme à faible turbulence peuvent aider au développement de corrélations semi-empiriques permettant une estimation de la vitesse laminaire de flamme à partir de la connaissance de l'évolution de la pression avec le temps dans la sphère de 20L.

La vitesse laminaire de flamme de la nanocellulose a également été déterminée à l'aide d'un modèle numérique de propagation de flamme en une dimension, déjà validé pour des mélanges hybrides. Le système numérique, composé d'équations de bilans de masse et d'énergie et de vitesses de réactions massiques adaptées aux réactions de combustion, a été résolu par la méthode des volumes finis, en considérant dans un premier temps une propagation par convection et conduction. Deux approches ont été comparées : une réaction simultanée de pyrolyse de la poudre et de combustion des gaz de pyrolyses d'un côté, et la combustion des gaz de pyrolyse, considérant une dévolatilisation rapide des poudres organiques (notamment discuté dans le chapitre 4) de l'autre. Les deux méthodes ont conduit à des valeurs similaires, avec une diminution de 19% dans la valeur de vitesse laminaire de flamme en considérant la réaction de pyrolyse, ce qui valide l'hypothèse d'une pyrolyse rapide ne limitant pas la combustion. Puisqu'en pratique, la dévolatilisation n'est pas instantanée, les particules qui n'ont pas encore réagi peuvent contribuer au transfert radiatif, qui a donc été ajouté au bilan d'énergie. L'existence d'une relation linéaire entre la vitesse laminaire de flamme et la surface totale développée par les particules impliquées dans le transfert radiatif a été démontrée, prouvant une nouvelle fois l'importance de la surface reactive. Une augmentation de vitesse laminaire de flamme atteignant 19% a notamment été observée en considérant la contribution des particules au transfert de chaleur par rayonnement. En effet, bien que l'influence du transfert thermique radiatif des nanoparticules a tendance à être négligée à cause d'une diffusion de Rayleigh, la contribution des micro-agglomérats subsistant après la dispersion doit être prise en compte.

Ce travail de thèse s'est focalisé sur l'évaluation des risques liés aux explosions de nanoparticules, et plus spécifiquement sur l'adéquation des méthodes standards pour la mesure de la sensibilité à l'inflammation et la sévérité d'explosion. L'impact de la nature chimique, du diamètre primaire de particule, de l'état d'agglomération, de la teneur en eau, de l'énergie d'inflammation, de la procédure de dispersion et du délai d'inflammation sur la sévérité d'explosion a notamment été analysé à travers l'exemple de quatre types de poudres : nanocellulose, aluminium, silicium enrobé de carbone et noir de carbone. L'objectif de ce travail était d'apporter de nouvelles connaissances concernant l'influence des spécificités des nanoparticules sur leur explosivité de manière à proposer des améliorations et méthodes alternatives adaptées à ces spécificités.

Une chose est sûre : les standards sont essentiels. Mais quand ils sont face à un grain de sable, ils prennent parfois un long moment à s'adapter à un contexte changeant. En étant, de manière inhérente, plus adaptables à différents matériaux et contextes industriels, ils gagneraient en réactivité. Il est temps de s'adapter !

Nouvelles considérations sur l'explosivité des nanopoudres: un nano-grain de sable dans les rouages des standards

Lorsqu'il s'agit de poudres combustibles, les analyses de risques et le zonage ATEX requièrent la connaissance de paramètres de sécurité obtenus à l'aide de procédures standards, initialement créées pour des poudres micrométriques et appliquées telles quelles aux nanopoudres. Cependant, leurs propriétés spécifiques (faible énergie minimale d'inflammation, distribution de tailles de particules allant des nanoparticules aux agglomérats micrométriques…) peuvent induire des déviations ou des erreurs de mesures en utilisant ces essais standards. Des tests ont été réalisés sur quatre nanopoudres en conditions standards et non-standards, démontrant que les normes ne mènent pas systématiquement aux paramètres de sécurité les plus conservatifs ni les plus représentatifs. Dès lors, une adaptation des standards est requise. Des propositions ont été faites concernant la préparation des échantillons, les procédures et équipements de mesure, ainsi que les paramètres de sécurité à considérer.

New insights on the explosion severity of nanopowders: a nano-grain of sand in the gears of the standards

When considering combustible dusts, hazard assessment studies and classification of ATEX zones require the knowledge of safety parameters obtained through standard procedures initially designed for micropowders. Currently, the same standards are applied, unchanged, for testing nanopowders. However, their specific properties (low minimum ignition energy, wide particle size distribution ranging from nanometric particles to micro-agglomerates…) can lead to deviations, or even measurement errors, when using these standardized tests. Therefore, tests were performed on four nanopowders under standard and non-standard conditions, demonstrating that standard conditions do not automatically lead to the most representative or conservative safety parameters. An adjustment of the international standards is then needed. Proposals are made concerning the samples preparation, the test procedure and equipment used for such characterization, and the more relevant safety parameters to be determined.